UNIVERSITY OF STRATHCLYDE

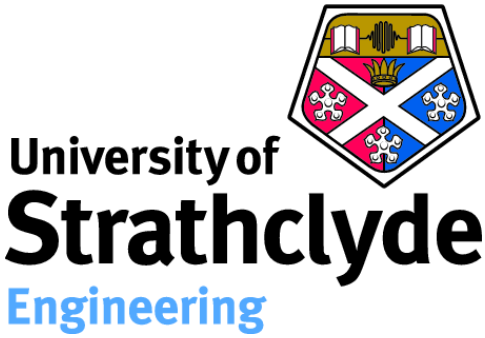

DOCTORAL THESIS

Molecular Simulations of the Interaction of Microwaves with Fluids

Author:
Javier CARDONA AMENGUAL

Academic supervisors:
Dr. Leo LUE
Dr. Martin SWEATMAN

A thesis submitted in fulfilment of the requirements for the degree of Doctor of Philosophy

in the

Department of Chemical and Process Engineering

7th December, 2016

Declaration of Authorship

This thesis is the result of the author's original research. It has been composed by the author and has not been previously submitted for examination which has led to the award of a degree.

Signed:

Date:

Acknowledgements

I would like to thank everyone who has helped and supported me during this long journey. Special thanks to my supervisors Dr Leo Lue and Dr Martin B. Sweatman. Leo, I cannot thank you enough, not only for everything I have learnt from you during this years, but also for being such a wonderful person. Martin, thank you for giving me the opportunity to start this PhD in the first place. Even in the distance, I have always felt your continuous support and your advice has always been very valuable to me. I hope we can keep in touch and work together in the future.

Thanks to the Department of Chemical and Process Engineering for funding my PhD and providing a nice atmosphere throughout the years. I would like to thank ARCHIE-WeSt High Performance Computer for facilitating my work, and my collaborators at the University of Edinburgh for supplying valuable experimental results.

Big thanks to all the friends I have made during these years. David, thanks for being always there but, even though it is great spending time with you, we have to stop doing this thing where we write theses together. Scott, Paul, thanks for all the various adventures. Alessia, thanks for all the random chats. Malaka, Dorin, thanks for the great times we had and will have together. Rab, thanks for all the mad nights. Carlota, moitas grazas por todo. Iván, gracias por las largas charlas. Maryam, thanks for always being so kind and supportive. Hrvojca, thanks for being there in the late nights. Carla, thanks for sharing the pain in the last few months. Thanasis, $\varepsilon\upsilon\chi\alpha\rho\iota\sigma\tau\acute{\omega}$ my green and white friend. Vitor, Craig, Joy, Francesco, Vincenzo, Daria, Andrew, Martin, Alexandra, Ruben, Teresa, Chris, Calum, Fraser, Kelly, Sirajadien, Manssor, Heba, thank you all for making these years so enjoyable.

Thank you to my new colleagues in CIDCOM and the ICT-CMAC project for your patience and comprehension during the last few months. I am really looking forward to working with you in this new journey that just started.

Lore, Vane, Mayka, Natalia, Mayte, Sergio, Carlos, todo empezó con vosotros. Todos esos años de mucho curro pero también muchos buenos ratos han hecho que esto fuera un poco más fácil. Muchas gracias a todos.

Y dejando lo más importante para el final, Mami, Puche, aunque la distancia no lo ponga fácil, sabéis que siempre vais a ser lo primero para mí. Muchas gracias por siempre estar ahí apoyándome. No habría podido llegar tan lejos sin vosotros.

Contents

List of Figures

List of Tables

Nomenclature

A	Aleatory property
A_0	Initial value of aleatory property
A_j	Intensity of relaxation process j
A_p	Area of parallel plate
$\mathbf{B}$	Magnetic induction
B	Property of the system that couples with external field
b_0	Equilibrium bond length
C	Capacitance
c	Speed of light in vacuum
C_i	Non-normalised correlation function
c_n	Parameters of Ryckaert-Bellemans torsional potential
c_P	Constant pressure heat capacity
$\mathbf{D}$	Dielectric displacement
$\mathbf{d}$	Unit vector in the direction of the electric field
d	Distance separating two fully conducting plates
$\mathbf{E}$	Electric field
E_0	Initial intensity of electric field
$E_{0\,\mathrm{ext}}$	Electric field intensity outside the dielectric material
$E_{0\,\mathrm{int}}$	Electric field intensity at the inner boundary of the dielectric material
E_{int}	Electric field distribution inside the dielectric material
$\mathrm{E}_{\mathrm{rms}}$	Root mean square of electric field intensity
$\mathbf{F}$	Vector function defining the dynamics of a system
$\mathcal{F}$	Fourier transform

f	Distribution of points in phase space
$\mathbf{F_e}$	Electrostatic force
$\mathbf{H}$	Magnetic field
H	Hamiltonian of the system
h	External perturbation
H_0	Initial intensity of magnetic field
$\mathrm{H_{rms}}$	Root mean square of magnetic field intensity
I	Electric current
$\mathbf{J}$	Current density
$\mathbf{k}$	Wave vector
k_B	Botzmann constant
k_b	Spring constant for bond stretching
k_θ	Spring constant for angle bending
$\mathcal{L}$	Liouvillean operator
$\mathbf{M}$	Dipole moment
$\mathcal{M}$	Magnetisation
m	Mass
n	Refractive index
N_{atom}	Number of atoms in molecule
N_{mol}	Number of molecules
$\mathbf{p}$	Momentum
$\mathbf{P}$	Polarisation
P	Power transmitted through the waveguide
$\dot{Q}$	Rate of heat dissipation from an electromagnetic field
Q, q	Point charges
$\dot{Q}_{abs}$	Energy absorption rate of the system from the electromagnetic wave
$\dot{Q}_{acc}$	Energy accumulation rate within the system

$\dot{Q}_{cond}$	Heat losses to the surroundings by conduction
$\dot{Q}_{conv}$	Heat losses to the surroundings by convection
$\mathbf{R}$	Position of reference point
$\mathbf{r}$	Position vector
R	Ideal gas constant
r	Distance between particles
$\mathbf{S}$	Poynting vector
$\mathcal{S}$	Time evolution operator
S_{11}	Reflection coefficient
T	Temperature
t	Time
T_{amb}	Ambient temperature
U	Overall heat transfer coefficient
u	Total electromagnetic energy
U_a	Angle bending potential
U_b	Bond stretching potential
U_d	Dihedral angle torsion potential
U_{LJ}	Potential energy for Lennerd-Jones potential
U_{nb}	Potential energy associated to non-bonded interactions
$\mathbf{v}$	Velocity
V	Volume
w_e	Total electrostatic energy
w_{em}	Electromagnetic rate of work
w_m	Total magnetic energy
x_{EtOH}	Mole fraction of ethanol in the mixture
Z	Characteristic impedance

α	Alpha parameter for the Cole-Cole and the Havriliak-Negami model
α_P	Thermal expansion coefficient
β_T	Thermodynamic beta $\beta_T = \frac{1}{k_B T}$
β	Beta parameter for the Cole-Davidson and the Havriliak-Negami model
β_i	Hyperpolarisabilities
χ	Electric susceptibility
χ_{AB}	Response function of the system
χ_m	Magnetic susceptibility
δ	Phase of the dielectric permittivity, dielectric loss angle
$\Delta G^{\#}$	Free energy of activation
$\Delta H^{\#}$	Free enthalpy of activation
δ_m	Phase of the magnetic permeability, magnetic loss angle
δ_p	Penetration depth
$\Delta S^{\#}$	Free entropy of activation
ΔH_{vap}	Heat of vaporization
ε	Dielectric permittivity
ε_{vac}	Vacuum permittivity
ε_0	Static dielectric constant
ϵ_{ij}	Depth of Lennard-Jones potential well
ε_∞	Infinite frequency dielectric permittivity
ε'	Real part of the dielectric permittivity
ε''	Imaginary part of the dielectric permittivity, dielectric loss
$\mathbf{\Gamma}$	Location in phase space
κ_T	Isothermal compressibility
λ	Wavelength of electromagnetic wave
λ_0	Free space wavelength
λ_g	Waveguide wavelength

μ	Magnetic permeability
μ_m	Molecular dipole moment
μ'	Real part of the magnetic permeability
μ''	Imaginary part of the magnetic permeability
μ_{vac}	Vacuum permeability
ν	Frequency of electromagnetic wave
ω	Angular frequency of electromagnetic wave
$\boldsymbol{\phi}$	Normalised autocorrelation function
$\boldsymbol{\phi_{\mathbf{box}}}$	Dipole moment autocorrelation function of simulation box
ϕ_d	Dihedral angle (zero-cis convention)
$\boldsymbol{\phi_{\mathbf{i}}}$	Dipole moment autocorrelation function of entire species i in mixture
$\boldsymbol{\phi_{\mathbf{mol\,i}}}$	Dipole moment autocorrelation function of individual molecules i in mixture
ϕ_v	Electric potential, voltage
ψ_d	Dihedral angle (zero-trans convention)
ρ	Density
ρ_e	Charge density
σ	Electric conductivity
σ_{ij}	Distance at which the Lennard-Jones potential becomes zero
τ_{CC}	Relaxation time for the Cole-Cole model
τ_{CD}	Relaxation time for the Cole-Davidson model
τ_D	Relaxation time for the Debye model
τ_{HN}	Relaxation time for the Havriliak-Negami model
τ_i	Relaxation time of relaxation process i ($i = 1, 2, 3, 4$)
θ	Angle between two bonds
θ_0	Equilibrium angle
φ	Phase shift of the electromagnetic wave
φ_{HN}	Additional parameter for the Havriliak-Negami model

List of Abbreviations

AC	**A**lternating **C**urrent
ACF	**A**uto**c**orrelation **F**unction
BDS	**B**roadband **D**ielectric **S**pectroscopy
BOBYQA	**B**ound **O**ptimisation **BY** **Q**uadratic **A**pproximation
CC	**C**ole-**C**ole
CD	**C**ole-**D**avidson
EPSRC	**E**ngineering and **P**hysical **S**ciences **R**esearch **C**ouncil
FDTD	**F**inite-**D**ifference **T**ime-**D**omain
FE	**F**inite **E**lements
GAFF	**G**eneralised **A**mber **F**orce **F**ield
HN	**H**avriliak-**N**egami
ISM	**I**ndustrial **S**cientific and **M**edical
LJ	**L**ennard-**J**ones
LINCS	**LIN**ear **C**onstraint **S**olver
MD	**M**olecular **D**ynamics
MEA	**M**ono**e**thanol**a**mine
MSD	**M**ean **S**quare **D**eviation
NPT	**N**umber of molecules, **P**ressure, **T**emperture
NRPB	**N**ational **R**adiation **P**rotection **B**oard
OPLS	**O**ptimised **P**otentials for **L**iquid **S**imulations
OU	**O**rnstein **U**hlenbeck
PME	**P**article-**M**esh **E**wald
PPPM	**P**article-**P**article **P**article-**M**esh
RDF	**R**adial **D**istribution **F**unction
RMSD	**R**oot **M**ean **S**quare **D**eviation
SPC	**S**imple **P**oint **C**harge
TEM	**T**ransverse **E**lectromagnetic **W**ave
TraPPE-UA	**Tra**nsferable **P**otentials for **P**hase **E**quilibria-**U**nited **A**tom
UK	**U**nited **K**ingdom
VOC	**V**olatile **O**rganic **C**ompound
WHO	**W**orld **H**ealth **O**rganisation
WLA	**W**etting **L**ayer **A**bsorption

Physical Constants

Botzmann constant	$k_B = 1.380\,648\,5 \times 10^{-23}\,\mathrm{J\,K^{-1}}$
Ideal gas constant	$R = 8.314\,\mathrm{J\,mol^{-1}\,K^{-1}}$
Planck's constant	$h = 6.626\,070\,040 \times 10^{-34}\,\mathrm{J\,s}$
Speed of Light	$c = 2.997\,924\,58 \times 10^{8}\,\mathrm{m\,s^{-1}}$
Vacuum permittivity	$\varepsilon_{vac} = 8.854 \times 10^{-12}\,\mathrm{F\,m^{-1}}$
Vacuum permeability	$\mu_{vac} = 1.2566 \times 10^{-6}\,\mathrm{H\,m^{-1}}$

UNIVERSITY OF STRATHCLYDE

Abstract

Faculty of Engineering
Department of Chemical and Process Engineering

Doctor of Philosophy

Molecular Simulations of the Interaction

of Microwaves with Fluids

by Javier CARDONA AMENGUAL

The interaction of electromagnetic radiation with matter has led to a large number of interesting applications. The propagation of electromagnetic waves within materials is described by Maxwell's equations. However, the fundamental understanding of the causes of the response of the material, defined by constitutive relations for its complex, frequency-dependent dielectric constant, can only be achieved through the study of processes occurring at the molecular scale. The fluctuation-dissipation theorem relates the frequency-dependent dielectric constant of a material to equilibrium fluctuations in its dipole moment. This fact can be used to determine dielectric properties from equilibrium molecular dynamics simulations for frequencies covering the microwave region of the electromagnetic spectrum (300 MHz – 300 GHz). In this work, the ability of current force fields to predict dielectric spectra of one component systems and mixtures is examined, showing accurate results when compared with experimental data for the systems under consideration. Additionally, the influence of temperature on the dielectric spectra is analysed, yielding equally satisfactory results. In the particular case of ethanol/water mixtures, the estimation of dielectric spectra at intermediate concentrations using molecular dynamics simulations outperforms the traditional use of mixing rules. The simulations of these systems reveal the importance of collaborative processes between groups of molecules, such as hydrogen bond networks, in the overall dielectric response. The reduction of the contribution of these processes as temperature increases confirms the weakening of these networks at high temperatures. The predicted dielectric properties are used in a heating model to estimate temperature profiles in microwave heating processes. Unexpected results are obtained which reveal the need for accurate determination of the electric field distribution within the workload in order to obtain representative heating profiles. In contrast, penetration depths are accurately determined from dielectric properties generated through molecular simulations.

Chapter 1

Introduction

The interaction of electromagnetic radiation with matter has been the subject of extensive research over the years. The interest on this topic ranges from the pure scientific explanation of the basic mechanisms behind this interaction to the exploitation of this knowledge to develop new applications and optimise current processes. The frequency of the electromagnetic radiation and the characteristics of the irradiated material dictate the nature of their interaction. Processes such as transitions between electronic states or the activation of vibrational and rotational modes in molecular systems can be achieved in this manner and can de detected by means of a range of spectroscopic techniques. At frequencies lower than 10^{12} Hz, the main mechanisms affected are the reorganisation of molecular dipoles in an attempt to follow the direction of the electric field and the displacement of free charges that generates an electric current. In both cases, absorption and dispersion phenomena are present. Microwave heating is in fact the result of dispersive processes generated during the coupling of the dynamics of molecular systems to electromagnetic radiation at microwave frequencies (3×10^8 – 3×10^{11} Hz).

The dynamics of electromagnetic fields is governed by the well-known Maxwell's equations. However, the macroscopic representation of the interaction between electromagnetic radiation and matter requires the introduction of so called constitutive relations in which the dielectric constant and the conductivity of the material describe the induced response of the system. The propagation of electromagnetic waves in different media has been studied extensively using computational electrodynamics. Numerical approximations to Maxwell's equations are used to design communication devices (antennas, radars, satellites) or develop medical imaging instruments (radiography, magnetic resonance imaging (MRI), endoscopy). Nevertheless, in order to achieve a fundamental understanding of wave propagation and absorption in dielectric media, it is necessary to study phenomena occurring at the molecular scale.

The objective of this thesis is to explore the physical mechanisms that originate the dielectric response of a system to electromagnetic radiation at the molecular level using molecular dynamics simulations. In particular, the focus is on the study of microwave heating processes the origin of which is not fully understood. In this work, it will be demonstrated that molecular dynamics simulations have the potential to predict dielectric properties of molecular systems through analysis of dipole moment fluctuations.

These properties are then used to estimate microwave heating rates.

In Chapter 2, a review is presented of some of the most important applications of microwave heating, together with a brief introduction to dielectric spectroscopy. The concept of microwave heating is introduced from a macroscopic point of view, and, starting from Maxwell's equations of Electromagnetism, an expression for the heating rate in microwave-driven processes is developed. Additionally, in this chapter the importance of accurate prediction of the dielectric constant for a satisfactory representation of microwave heating profiles is shown.

In Chapter 3, a method to obtain dielectric spectra of molecular systems using molecular dynamics simulations is described. The study of the interaction of electromagnetic fields and matter at the nanoscale, through the fluctuation dissipation theorem and linear response theory, leads to an expression relating the complex and frequency-dependent dielectric constant of a material to the fluctuations in its dipole moment. Molecular dynamics simulations are used to generate molecular trajectories and track the time evolution of the dipole moment of the system. Then the above-mentioned relationship between these fluctuations and the dielectric constant of the material is used to obtain dielectric spectra. The use of the 'ideal' Debye model and the more sophisticated Havriliak-Negami model in this procedure makes possible the physical interpretation of the results.

In Chapter 4, the application of the method developed in Chapter 3 is shown for the determination of the dielectric spectra of water, a series of alcohols and glycols, and monoethanolamine (MEA). Several different molecular force fields, that were originally developed for the prediction of thermodynamic properties, were tested to evaluate their performance in the prediction of a dynamic property such as the dielectric spectrum. The results are generally within reasonable agreement with experimental results, with at least one of the force fields providing satisfactory estimates of this property for every material. Some discrepancies were encountered in the prediction of the static (low frequency) dielectric constant, which is related to the magnitude of the dipole moment fluctuations. However, the frequency of these fluctuations is generally well predicted. In order to obtain more accurate representations of dielectric spectra, and avoid the need for complex recalibrations of molecular models, it was decided to use the experimental value of the static dielectric constant, instead of the one obtained through simulations.

In Chapter 5, we extend the prediction of dielectric spectra of single component systems performed in Chapter 4 to binary systems, in particular the ethanol/water mixture. Once again, we obtain satisfactory results with respect to experimental data for this particular binary system. In addition, we show how predictions obtained using molecular dynamics simulations outperform the ones generated through empirical mixing rules, which are solely based on the characteristics of the individual constituents of the mixture. In these systems, the final dielectric response results from a

combination of concentration-dependent relaxation mechanisms to which both components contribute simultaneously, rather than from individual contributions of each constituent. In order to obtain a deeper insight into the origin of these different relaxation mechanisms, both the individual contribution of each component of the mixture to the dielectric response of the system and the importance of cross-correlation between components are studied.

The results presented in Chapter 4 and Chapter 5 have been obtained at ambient conditions. In Chapter 6, we analyse the influence of another important variable, temperature, on the dielectric spectra of water, ethanol, MEA, and ethanol/water mixtures. The accurate prediction of microwave heating rates relies on an adequate representation of this dependency since the dielectric properties of the material will vary as the temperature increases during the microwave heating process. This is not a topic that is widely covered in the literature, even from an experimental point of view. The force fields employed in this work are shown to provide a good estimation of the temperature dependence of dielectric properties. Additionally, the effect of temperature on the different relaxation processes that contribute to the global dielectric response is studied, as well as the influence this variable has on the dynamic response of individual molecules.

In Chapter 7 we apply the concepts developed in the previous chapters for the estimation of macroscopic quantities at the most common microwave frequency, 2.45 GHz. Based on the good prediction of dielectric properties at this particular frequency, we show how it is possible to obtain accurate predictions of penetration depths. This is an important parameter in the design of microwave heating processes since it determines the depth of propagation of the electromagnetic wave inside the dielectric material. Despite the high accuracy in the estimation of dielectric properties, it is not possible to obtain an adequate prediction of microwave heating profiles in irradiated dielectric materials without a careful consideration of the electric field distribution inside the sample. The appropriate estimation of microwave heating profiles can be a powerful tool for the optimisation of microwave heating processes.

Finally, in Chapter 8 the main findings of this thesis are summarised and indications for future lines of research that could carry forward the work developed here are provided.

Chapter 2

Microwave Heating: Applications and Foundations

Microwave heating is a complex phenomenon derived from the interaction of electromagnetic fields with matter. The rapid oscillations of electric and magnetic fields at microwave frequencies cause molecular motion in dipolar systems and generate a flow of current in conductive materials. Both phenomena cause heat dissipation and lead to a temperature increase which extent will depend on the dielectric properties of the irradiated material.

This chapter starts with an introduction to electromagnetic radiation. A short description of the different means that radiation interacts with matter is provided through the electromagnetic spectrum. Predominant attention is given to radiation at microwave frequencies, including the general mechanisms by which microwave heating occurs. Then, we review the main applications of microwave heating in chemical processing. This includes a brief tour through the history of microwave heating followed by a review of some of the most recent advances and challenges in this field. Next, the foundations of dielectric heating are defined from a macroscopic point of view. Taking Maxwell's equations of electromagnetism as a starting point, we derive an expression for the rate of heat dissipation in microwave heating. This gives the opportunity to model microwave heating profiles at larger scales. To conclude this chapter, we discuss how the dielectric constant of a material determines its response to electromagnetic radiation. Broadband dielectric spectroscopy is an experimental technique developed to analyse the frequency-dependency of this property from macroscopic quantities. We briefly show the evolution of this technique and present some applications of particular interest.

2.1 Interactions of electromagnetic radiation with matter

This section describes the basic principles of microwave heating. We provide a definition of electromagnetic radiation and describe the way in which it interacts with matter in order to generate heat.

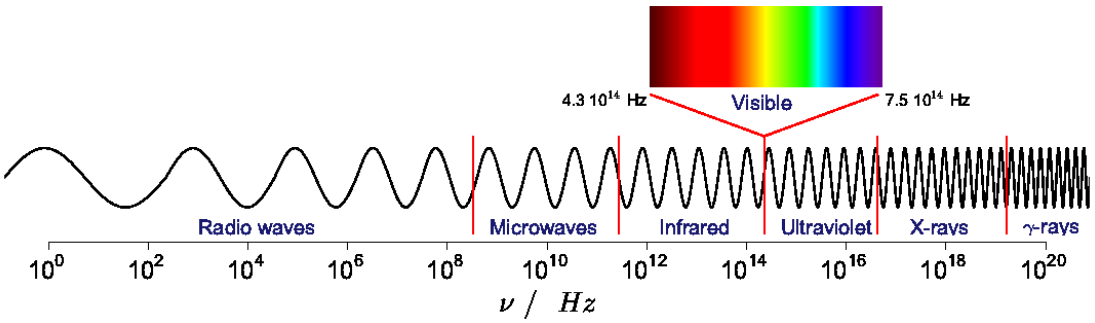

FIGURE 2.1: Electromagnetic spectrum.

2.1.1 Electromagnetic radiation

Electromagnetic radiation essentially originates from the acceleration of charged particles. The resulting synchronised fluctuations of electric and magnetic fields give rise to electromagnetic waves which propagate perpendicularly to both the fields, that are simultaneously perpendicular to each other. In vacuum the propagation of these waves occurs at the speed of light. Electromagnetic waves are fundamentally characterized by their intensity and their frequency ν or wavelength λ, and have been classified according to these last properties in what is called the electromagnetic spectrum (see Fig. 2.1). When subject to electromagnetic radiation, matter interacts in different ways depending on the frequency of the wave. From lower to higher frequency (longer to shorter wavelength), the electromagnetic spectrum is composed by:

- Radio waves (ν = 3 kHz - 300 MHz, λ = 100 km - 1 m): conduction of charge carriers or plasma oscillation.
- Microwaves (ν = 300 MHz - 300 GHz, λ = 1 m - 1 mm): molecular rotation, plasma oscillation.
- Infrared radiation (ν = 300 GHz - 400 THz, λ = 1 mm - 760 nm): molecular rotation, molecular vibration, plasma oscillation in metals.
- Visible radiation (ν = 400 THz - 790 THz, λ = 760 nm - 380 nm): electron excitation.
- Ultraviolet radiation (ν = 790 THz - 30 PHz, λ = 380 nm - 10 nm): excitation and ejection of molecular and atomic valence electrons.
- X-rays (ν = 30 PHz - 30 EHz, λ = 10 nm - 10 pm): excitation and ejection of core atomic electrons, Compton scattering (for low atomic numbers).
- Gamma rays (ν > 30 EHz, λ < 10 pm): excitation and ejection of core atomic electrons in heavy elements, excitation and dissociation of atomic nuclei, Compton scattering, creation of particle-antiparticle pairs.

In this work, we are particularly interested in how matter interacts with electromagnetic radiation in the microwave and high-frequency radio wave region. One of

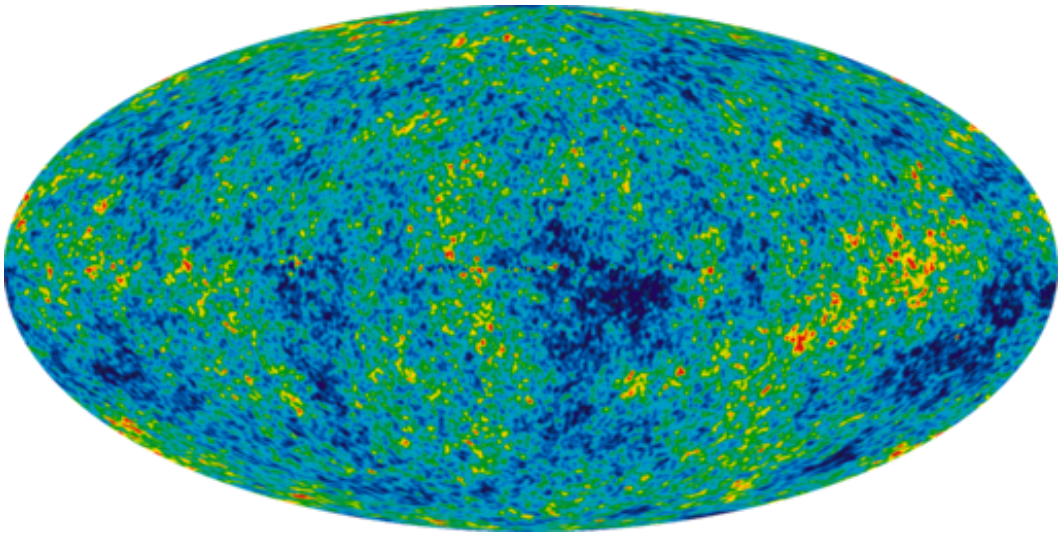

FIGURE 2.2: Cosmic microwave background. Detailed, all-sky picture of the infant universe created from nine years of WMAP data. The image reveals 13.77 billion year old temperature fluctuations (shown as color differences) that correspond to the seeds that grew to become the galaxies. The signal from our Galaxy was subtracted using the multi-frequency data. This image shows a temperature range of $\pm$ 200 microKelvin. Image and caption obtained from NASA's WMAP Science Team.

the most remarkable examples of this type of radiation is the cosmic microwave background [1], which is considered to be evidence of the Big Bang model of the universe. In the early stages of its formation, the universe was composed of a hot and dense plasma. As the universe expanded, it became cooler and allowed the formation of neutral atoms through the combination of protons and electrons. At that point, the neutral atoms were no longer able to absorb thermal radiation by proton and electron scattering, and it escaped the original plasma in the form of photons or electromagnetic radiation. The expansion of the universe has increased the wavelength of the original radiation, and now it reaches the Earth in the form of microwave radiation at a frequency distributed around 160.2 GHz, which can be detected by means of radio telescopes (see Fig. 2.2). The artificial generation of electromagnetic radiation in the microwave region has led to a broad range of applications that include telecommunications, radar technology, spectroscopy or heating. In the particular case of chemical processing, microwave heating is becoming more and more widely used as will be described in section 2.2

2.1.2 Mechanisms of microwave heating

At microwave frequencies, electromagnetic waves have the ability to influence particle motion, such as molecular rotation or ionic translation, but do not affect the molecular structure. There are two ways to convert electromagnetic energy from microwaves into heat in fluids:

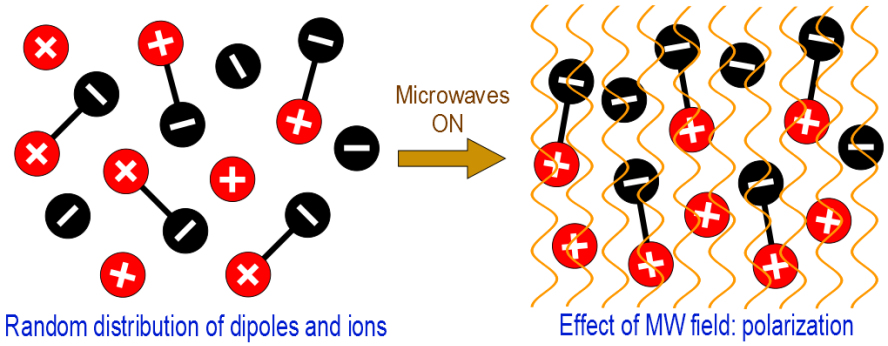

FIGURE 2.3: Interaction of electromagnetic fields with matter at microwave frequencies: dielectric polarization and ionic conduction.

- Dielectric polarization (see Fig. 2.3): Molecular dipoles in dielectric materials tend to align with the external electric field. The alternating nature of the electric field in microwaves results in a maintained oscillation of the dipoles as they attempt to realign with the field. Heat is generated due to the mechanical friction caused by dipolar motion between and within molecules. Power absorption is however a frequency-dependent phenomenon. The response of a dipolar system to an electric field is related to its natural motion in the absence of an external field. Different species have different response which results in shifted power absorption peaks in the frequency spectrum [2].

- Ionic translation (see Fig. 2.3): Ionic species can travel in the direction of the alternating electric field producing an electric current. In a molecular system, the movement of charged species encounters resistance due to their collision with other molecules and atoms, which thereby results in heat dissipation [3].

Both types of heating result in a volumetric heating of the material which makes heating processes more independent of the thermal conductivity and surface temperature of the materials involved. This highly efficient way of heating has led to the development of a significant number of applications in chemical processing [4].

2.2 Microwave Heating in Chemical Processing

The now widely used microwave oven was an accidental discovery [5]. In 1946, when he was conducting research on the use of magnetrons in radar technology for World War II, the American engineer Percy Lebaron Spencer noticed how a candy bar he had in his pocket had melted. He correctly assumed that this effect was caused by the microwaves he was working with. Astonished by his discovery, he decided to run some experiments with other types of food. He started by successfully cooking popcorn, and later caused the first — but clearly not last — explosion of an egg in a microwave oven. Subsequent research on the topic led to the production of the first

commercial microwave oven in 1954. However, the large dimensions and high cost of the equipment made it only suitable for some specific applications. It was not until 1967 that the first domestic microwave oven was produced by Amana, a division of The Raytheon Corporation, where Spencer used to work.

Since then, microwave heating has seen a significant development with applications in the processing of food, ceramics, polymers, minerals or waste materials [6, 7]. Some major results have also been achieved in the acceleration of reactions in organic chemistry or in separation technologies [4], as we show below.

2.2.1 Applications

Food industry

The main uses of microwave heating in food processing include cooking, drying and pasteurisation [8]. The large heating rates achieved lead to faster processes in comparison with conventional conductive heating [9]. For this reason, microwave heating is widely spread in this sector, although more research is necessary in order to deal with some unresolved issues. The non-uniform temperature distribution associated with this type of heating has raised some safety concerns due to the impossibility of guaranteeing complete sterilisation at cold spots [10]. One possible solution is the combination of conventional and microwave heating which has shown to improve heat uniformity [11]. Additionally, important efforts have been made towards the development of techniques that allow an appropriate heat distribution in purely microwave-driven processes [12–14].

Ceramics

Ceramics processing is one of the fields that has benefited the most from the use of microwaves. The main applications involve synthesis and sintering of this type of materials [6, 15–17]. The synthesis of ceramics is carried out through reactions that are generally temperature-dependent. The volumetric effect of microwave heating results in rapid heating because it avoids the relatively slow heat transfer from the surface to the interior in this kind of materials. This is also the case in sintering or joining of ceramics [18]. An example is the microwave sintering of WC-Co composites, used in cutting and drilling operations due to their hardness and strength [15]. The production of this composite is generally lengthy and is carried out at high temperatures, but the use of microwaves [19, 20] leads to a decrease in the operating temperature and a reduction in the cycle time from 12-24 hours to less than 90 min. In addition, a more homogeneous product is obtained with improved mechanical characteristics. However, in general, the industrial application of microwave technologies in the ceramics sector still depends greatly on the wider development of continuous processes.

Polymers

In the polymers field, the number of publications related to microwave-assisted processes has seen a big increase in the last 15 years [21]. Several applications have shown the importance of using microwaves in the acceleration of polimerisation reactions and polymer processing [4]. These include step-growth polimerisation, free radical polimerisation and ring-opening polimerisation [22–24]. In most cases higher reaction rates and enhancement of the properties of the final product by avoiding side-reactions have been reported [25]. However, the causes for this positive effect remain generally unknown, and research in this area is expected to grow in the near future.

Environmental applications

Microwave heating has also been implemented to solve problems in environmental engineering [26]. Examples of this include waste treatment [27], soil remediation [28–30] and regeneration of spent adsorbents [31–34]. One of the areas in which microwave heating has seen a wider implementation is wastewater treatment [35], with applications in the treatment of biological sewage sludges [36], pharmaceutical residues [37] or pulp mill waste sludges [38].

Organic chemistry

In organic synthesis, microwave heating has shown to have the ability to accelerate reactions and improve the product yield in a wide range of applications [4, 39–41]. A few examples include improvements in rate and product selectivity for Suzuki cross-coupling reactions [42, 43], a significant acceleration on the reaction rate of the oxidation of benzyl alcohol to benzaldehyde [44], or the optimisation of the synthesis of ionic liquids [45]. Langa et al. [46] provide an extensive review on organic reactions that have benefited from the use of microwave heating, and discuss the controversial possibility of the existence of specific non-thermal effects in the interaction of microwaves with matter. Until recently, most of the microwave-enhanced processes have only been studied at laboratory scale. However, an important aspect to consider if this technology wants to be implemented in industrial applications is the scale-up of the processing equipment [47].

Separation technologies

Over the years, important breakthroughs have also been obtained in a variety of separation processes [4]. Knowing the importance of this area of chemical processing in a large number of industries, any advance should be considered with interest.

Microwave-assisted extraction has been applied to recover essential oils and antioxidants from plants [48, 49], sometimes with the help of ionic liquids [50], or to extract

graphene from carbon fibers [51]. One of the main benefits of the rapid microwave-assisted extraction processes is that the valuable components are exposed to high temperatures for shorter times, and their properties are not greatly affected.

In adsorption-desorption cycles, the effectiveness and duration of the desorption step is one of the most important factors in the evaluation of the efficiency of the entire cycle. In some cases, microwave-assisted processes can clearly help achieving high regeneration yields in shorter times, if compared with other technologies such as pressure-swing or temperature-swing desorption [52]. This has been proved in the regeneration of zeolites [53], or in the desorption of VOCs (Volatile Organic Compounds) [54] and methylene blue [55] from activated carbons. Additionally, it has been observed that, generally, the adsorption capacity of the adsorbent materials is not substantially affected by microwave regeneration [55, 56].

Although fewer examples can be found in the literature, microwave-enhanced distillation can be an interesting option, especially when the substances to be separated have significantly different dielectric properties [57]. Going a step forward, the combination of the positive effects of dielectric heating on reaction and separation processes make reactive distillation an excellent candidate for good results. In this sense Altman et al. studied the synthesis of n-propyl propionate by microwave-enhanced reactive distillation [58]. They clearly observed an increase in the volatility of the component with lower boiling point. However, they showed how this effect is only obtained when the microwave radiation is focused directly on the vapour-liquid interface. When only the bulk liquid is exposed, no improvement is noticed. The influence of the interface had already been reported on previous studies of the boiling point elevation of several substances [59, 60].

Finally, membrane technology has also benefited from the use of microwave heating. Examples of this are the membrane permeation [61] and the microwave-assisted pervaporation of ethanol/water mixtures [62]. In this last case the dielectric properties of the mixture had a strong influence on the efficiency of the microwave induced process. It was concluded that the effect of dielectric heating was more significant for higher concentrations of ethanol due to the increase of the dielectric loss of this component with temperature. When water – for which the dielectric loss decreases with temperature – is predominant, the effect is not so important.

2.2.2 Non-thermal effects

Thermal effects due to the exposure of a material to microwave radiation are generally well known and characterised. In condensed phases, heat dissipation originates from relaxation processes caused by the frictional damping of dipoles as they intend to align with the electromagnetic field. However, a big debate exists in the scientific community on whether there exist specific non-thermal effects of the interaction of electromagnetic fields at microwave frequencies with matter [52, 63–65]. There are still some phenomena, particularly the enhancement of chemical reaction rates or the effect

on phase equilibrium, for which the physical mechanisms are not totally clear. Several authors claim that any deviation from the results obtained by conventional heating can still be explained as a thermal or relaxation process, and that the same effect could be achieved through conventional heating if it were possible to reproduce the same process conditions [66]. In other words, microwave heating processes also follow Arrhenius behaviour, although the volumetric nature of microwave heating allows for higher heating rates. This has been proven in most cases, and even authors who initially attributed unusual results to the non-thermal effect of microwave heating have rectified later [46, 67]. Additionally, a large number of claims of non-thermal effects have been discarded due to the inaccuracy in the temperature measurements [68, 69].

Dudley et al. [70] provide a novel interpretation in the case of chemical reactions, in which they suggest the classification of microwave effects should be divided into relaxation and resonant processes. As mentioned above, relaxation phenomena appear due to the delay in the response of the system due to dipolar friction. Resonant processes would only take place if the rotational modes of the dipoles were activated and these had complete rotational freedom, which leads to the response of the system being in phase with the incident electromagnetic wave. However, this is much more unlikely to occur, especially in condensed phases. In addition, an alternative way to generate chemical reactions is the activation of electronic and vibrational modes, but the frequency of microwaves would not be high enough to affect these processes.

Having said that, there are still some cases that cannot be explained following this reasoning [46]. Dudley et al. also discuss the concept of selective heating [71–73] in microwave heating by which absorbing species in a solution can reach higher temperatures than the average temperature of the medium. If the solute is a reactant, the situation may lead to higher reaction rates than the ones expected at that average temperature. The process would still be Arrhenius, but it would take place at higher temperatures, leading to higher rates. This is a phenomenon that would not occur in conventional heating and can be considered as a microwave-specific effect. In this context, it is important to consider the influence of the solvent. Heat transfer will be maximised in systems for which reactants have stronger dielectric absorption than the solvent, because, locally, the temperature difference between solute and solvent will be higher. It follows from this discussion that the mechanisms of microwave heating still remain somehow unclear, and this is a relatively unexplored field in which additional research should be conducted.

2.2.3 Challenges in microwave heating

Along with the study of the physical mechanisms that give rise to microwave heating, several challenges need to be overcome to achieve a widespread implementation of this technology in chemical processing, especially at an industrial level. Although a large number of applications have been found at laboratory scale, and some can be

directly performed at larger volumes using the same operating conditions [74], generally, the scale-up of the equipment is not necessarily straightforward. In recent years the design of microwave heating equipment has evolved rapidly [4]. From the traditional single-mode and multimode cavity systems, where no control exists over the electromagnetic field distribution, experimental setups have developed into equipment where the field distribution can be controlled and even optimised [75, 76]. This translates into processes with a more efficient use of microwave energy and that provide more reproducible results.

In order to help with this transition, modelling can be an important tool. In particular electromagnetic simulations that predict the field distribution in the equipment can facilitate the design [77–80]. Software developed with this goal is mainly based on the solution of Maxwell's equations using the finite-difference time-domain (FDTD) method [81, 82].

Another interesting aspect to consider is the extension to frequencies other than the common 2.45 GHz. As explained below, the use of microwaves is limited to specific frequencies, that do not necessarily correspond with the optimum operating conditions according to the dielectric characteristics of the system under consideration. The unrestricted utilisation of additional frequencies could lead to significant improvements in the efficiency of microwave-driven processes. The only limitation would be the cost of the equipment insulation, which would be required to avoid the escape of radiation.

Although dielectric properties have been obtained for a large number of systems, an even more extensive database would be desirable. This can be complemented by modelling tools such as molecular simulations, which can be certainly helpful, as we will show in this thesis. Dielectric properties of mixtures have also been successfully estimated by means of mixing rules that depend on the dielectric properties of the individual components and the composition of the mixture [83].

Finally, an important challenge to address, and probably the only one over which little control is possible, is the electricity cost [4]. In the current, situation the generation of microwaves depends entirely on electricity generated in fossil-fuelled power plants, which is not the most efficient and affordable energy source, and, additionally, can have associated environmental costs. This would theoretically be compensated by the increase in efficiency of microwave-assisted processes with respect to conventional processes, although the overall energy efficiency has to be evaluated with care. However, if the energy source for microwaves was to be more sustainable, the benefits would be even more important.

2.2.4 Safety and operational limitations

According to the World Health Organisation (WHO) [84], the short-term exposure to low intensity microwaves has not been shown to have any adverse effect on human health. Some studies postulate possible damaging effects of long-term exposure which could lead the development of cancer [85]. While other authors do not discount this

TABLE 2.1: Occupational and general public reference levels for continuous whole body exposure to electromagnetic fields.

	Occupational			General public		
Frequency range	E_{rms} (V m^{-1})	H_{rms} (A m^{-1})	Power dens. (W m^{-2})	E_{rms} (V m^{-1})	H_{rms} (A m^{-1})	Power dens. (W m^{-2})
400 - 2000 MHz	$3\sqrt{\nu}$	$0.008\sqrt{\nu}$	$\nu/40$	$1.375\sqrt{\nu}$	$0.0037\sqrt{\nu}$	$\nu/200$
2 - 300 GHz	137	0.36	50	61	0.16	10

ν is the frequency in MHz

possibility, they state that there are insufficient data to undoubtedly reach this conclusion [86, 87]. At higher field intensities, microwaves have shown to cause serious internal burns, particularly in tissues in which heat transfer is not efficient enough to quickly carry heat away. In the specific case of the microwave oven, this is avoided by appropriately insulating the equipment so the radiation is always contained within it.

As shown in Table 2.1, the UK Government, through the NRPB (National Radiological Protection Board), has set reference levels for continuous whole body exposure to electromagnetic fields that depend on the frequency of the radiation [88]. Occupational limits are usually high as they refer to individuals working under controlled conditions, and for which personal protection measures can be implemented if necessary. The general public includes population of any age and condition for which the exposure occurs under uncontrolled conditions and are not necessarily aware of possible risks.

In terms of operability, only a few specific frequencies are allowed in what are called the ISM (Industrial, Scientific and Medical) bands [89]. The reason behind this is to avoid interferences with telecommunications, and special permission is required to operate outside those frequencies. In the microwave range, the available bands are 915 ± 25 MHz, 2.45 ± 0.05 GHz, 5.800 ± 0.075 GHz and 24.125 ± 0.125 GHz, 2.45 GHz being the most common one. However, for some specific processes these particular frequencies may not coincide with the optimum operating conditions. In those cases, different frequencies could be used provided that the equipment was properly insulated and the adequate permissions had been requested. It has been shown that in order to avoid interference with radio communication, the electric field strength should not exceed 100 μV/m [2], which is a limit well bellow the safe exposure levels shown in table 2.1. In general, heating applications deal with power densities in the order of 10^3 to 10^6 W m^{-2}, which correspond to electric field intensities of 0.6 to 20 kV m^{-1} in vacuum. These levels are considerably higher and the appropriate protection measures have to be implemented. Nevertheless, these are still relatively low in comparison with the voltages necessary to reach dielectric breakdown of air, which are in the order of 3000 kV m^{-1}, although this phenomenon could still occur for particular geometries of the interface between air and a dielectric material [2].

2.2.5 Summary

Even though the use of microwaves for heating purposes has been known for more than 60 years, it is still a relatively new technology for which widespread industrial application is still to be seen. We showed a number of applications in sectors such as food, ceramics and polymer processing, together with examples of its implementation in environmental engineering, organic chemistry and several separation processes. The physical origin of the thermal component of microwave heating is generally well known. However, some controversy exists over the possible existence of non-thermal effects rising from the interaction of electromagnetic fields with matter at microwave frequencies. This, together with the design and optimisation of new microwave-enhanced processes and equipments, are probably the main challenges in this sector. Once the potential of microwave heating has been discussed, in the following section, we describe in more detail the physical mechanisms behind this phenomenon.

2.3 Foundations of Microwave Heating

The theoretical understanding of electromagnetic phenomena can generally be derived from the well-known Maxwell's equations. We start by briefly describing the two basic components of electromagnetic fields: the electric field and the magnetic field. Then, we consider the interaction between these fields through Maxwell's equations. This theoretical framework gives us the opportunity to develop the laws of conservation of charges and energy for electromagnetic systems. From that point, we work out an expression for the rate of heat dissipation in a material under the influence of electromagnetic radiation, which can be used to predict heating profiles in microwave heating processes. This expression will clearly depend on the characteristics of both the material and the incident electromagnetic wave.

2.3.1 Electric and magnetic fields

According to Coulomb's law, the electrostatic force $\mathbf{F_e}$ acting on a charge q due to the presence of another charge Q separated by a distance r is given in SI units by:

$$\mathbf{F_e} = \frac{1}{4\pi\varepsilon_{vac}} \frac{Qq}{r^2} \mathbf{r} \tag{2.1}$$

where $\mathbf{r}$ is a unit vector pointing from Q to q, in the direction of the force, and ε_{vac} is the vacuum permittivity ($\varepsilon_{vac} = 8.854 \times 10^{-12}\, Fm^{-1}$).

The electric field $\mathbf{E}$ generated by a charge Q is defined as the expected electrostatic force, per unit charge, exerted by Q on a charge q placed at a distance r:

$$\mathbf{E} = \frac{\mathbf{F_e}}{q} = \frac{1}{4\pi\varepsilon_{vac}} \frac{Q}{r^2} \mathbf{r} \tag{2.2}$$

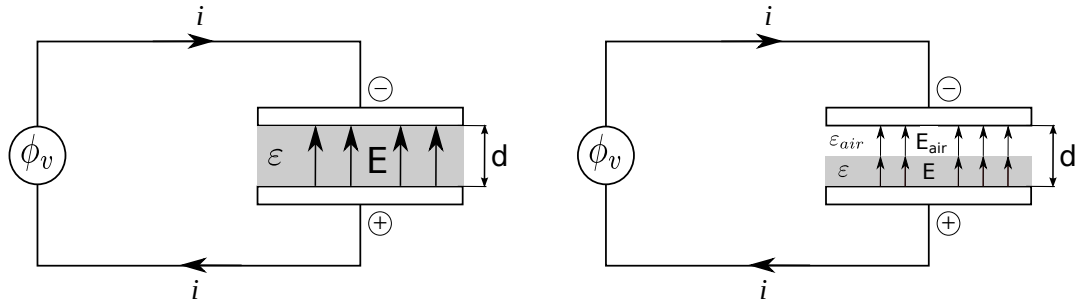

(a) Capacitor filled with dielectric material

(b) Capacitor filled with a slab of dielectric material

FIGURE 2.4: Electric field in a capacitor.

As an illustration, we consider a system formed by two fully conducting plates separated by a distance d, and coupled to a voltage source ϕ_v (see Fig. 2.4a). The electric field between the charged plates is given by:

$$\mathbf{E} = \frac{\phi_v}{d}\,\mathbf{d} \tag{2.3}$$

where $\mathbf{d}$ is a unit vector in the direction of the field. In this case, where the plates are considered as perfect conductors, the electric field is a vector for which the components tangential to the surface of the plates must be zero. The result is that the direction of the electric field is normal to the surfaces and indicates the path a charged particle would follow if it happened to be between the two plates.

When a voltage difference is applied to a parallel-plate capacitor, it has the ability to store electrical charge. The capacity of a material to build charge is quantified by the capacitance C which is defined as:

$$C = \frac{Q}{\phi_v} \tag{2.4}$$

where Q is the charge stored on the capacitor.

The capacitance is a function of the geometry of the capacitor and the permittivity of the material situated between the plates:

$$C = \frac{\varepsilon_{vac}\,\varepsilon\,A_p}{d} \tag{2.5}$$

where ε is the relative permittivity of the material between the plates with respect to vacuum and A_p is the area of one of the plates.

If there is an infinitesimal change in the voltage applied between the plates, it will

generate a change in the charge accumulated on the capacitor determined by the differential capacitance:

$$C = \frac{dQ}{d\phi_v} \tag{2.6}$$

Knowing that the electric current I is defined as the rate at which charge flows through a conductive surface:

$$I = \frac{dQ}{dt} \tag{2.7}$$

We can combine the previous definitions to obtain:

$$I = C\frac{d\phi_v}{dt} = \frac{\varepsilon_{vac}\,\varepsilon A}{d}\,\frac{d\phi_v}{dt} = \varepsilon_{vac}\,\varepsilon A\,\frac{dE}{dt} = A\,\frac{dD}{dt} \tag{2.8}$$

where $D = \varepsilon_{vac}\,\varepsilon E$ is known as the displacement current or dielectric displacement.

This expression clearly states how the time variation of the electric field in a capacitor gives rise to an electric current. Additionally, Œrstd discovered that when a conductor carries an electric current, as in this case, it generates a magnetic field H in its surroundings. Therefore, in the case of a parallel-plate capacitor, a time-varying electric field is associated to the generation of a magnetic field in its vicinity.

2.3.2 Constitutive relations

The constitutive relations define the interaction of radiation with matter. Precisely, they establish the relationship between dielectric displacement $\mathbf{D}$ and electric field $\mathbf{E}$, as well as the equivalent link between magnetic induction $\mathbf{B}$ and magnetic field $\mathbf{H}$. These relations are necessary if one wants to solve Maxwell's equations, and can be derived from the definition of dielectric displacement and magnetic induction, respectively:

$$\mathbf{D}(t) = \varepsilon_{vac}\mathbf{E}(t) + \mathbf{P}(t) \tag{2.9}$$

$$\mathbf{B}(t) = \mu_{vac}\mathbf{H}(t) + \mathcal{M}(t) \tag{2.10}$$

Here the polarisation $\mathbf{P}(t)$ and magnetisation $\mathcal{M}(t)$ represent the response of a dielectric material to the presence of external electric and magnetic fields, respectively. μ_{vac} is the vacuum permeability ($\mu_{vac} = 1.2566 \times 10^{-6}\,Hm^{-1}$).

When a time-dependent electromagnetic field is applied to a dielectric material, it has an influence on time-dependent processes within the material, such as atomic or molecular vibration, dipole rotation, or ionic conduction. As a consequence, the material requires a certain time to react to the incident field. Therefore, the transfer function, which relates the response of the system to the incident field must reflect this delay. In this context, the polarisation can be defined as follows:

$$\mathbf{P}(t) = \varepsilon_{vac}\int_{-\infty}^{t} dt'\;\chi(t-t')\;\mathbf{E}(t) \tag{2.11}$$

Equivalently:

$$\mathcal{M}(t) = \mu_{vac} \int_{-\infty}^{t} dt' \; \chi_m(t - t') \; \mathbf{H}(t) \tag{2.12}$$

where $\chi(t)$ and $\chi_m(t)$ are called electric and magnetic susceptibility. This expression describes polarisation and magnetisation as convolutions of electric and magnetic fields at previous times, respectively. The causality expressed through this relation implies that $\chi(t) = 0$ and $\chi_m(t) = 0$ for $t < 0$.

A time varying signal can be considered as a sum of sinusoidal signals. For relatively weak electric and magnetic fields the response of the system tends to be linear with the respective fields. This implies that these sinusoidal signals can be treated independently of each other. Based on the convolution theorem, it is useful to employ Fourier transforms:

$$\hat{f}(\omega) = \int dt \; e^{i\omega t} \; f(t) \tag{2.13}$$

$$f(t) = \int \frac{d\omega}{2\pi} \; e^{-i\omega t} \; \hat{f}(\omega) \; , \tag{2.14}$$

to convert the integrals defined in Eqs.(2.11) and (2.12) into simple products in the frequency domain:

$$\mathbf{P}(\omega) = \varepsilon_{vac} \, \hat{\chi}(\omega) \, \mathbf{E}(\omega) \tag{2.15}$$

$$\mathcal{M}(\omega) = \mu_{vac} \, \hat{\chi}_m(\omega) \, \mathbf{H}(\omega) \tag{2.16}$$

where the "$\hat{}$" symbol denotes the Fourier transform operation and ω is the angular frequency of the perturbing wave ($\omega = 2\pi\nu$).

For stronger fields, non-linear effects may appear and these linear relations would not hold any more. As an example, the non-linear behaviour of the polarisation can be expressed as [90]:

$$\mathbf{P}(\omega) = \varepsilon_{vac} \, \hat{\chi}(\omega) \, \mathbf{E}(\omega) + \sum_{i=1 \cdots odd} \beta_i \, E^{i+1} \, \mathbf{E} \tag{2.17}$$

where the parameters β_i receive the name of hyperpolarisabilities. However, in the following we decide to discard non-linear effects due to the weak nature of the electromagnetic fields considered in this work.

For linear response, the definitions of dielectric displacement (Eq. (2.9)) and magnetic induction (Eq. (2.10)) lead to linear dependencies between $\mathbf{D}$ and $\mathbf{E}$, and $\mathbf{B}$ and $\mathbf{H}$ defined as constitutive relations::

$$\mathbf{D} = \varepsilon_{vac} \, \mathbf{E} + \varepsilon_{vac} \, \hat{\chi}(\omega) \, \mathbf{E} = \varepsilon_{vac} \, \hat{\varepsilon}(\omega) \, \mathbf{E} \tag{2.18}$$

$$\mathbf{B} = \mu_{vac} \, \mathbf{H} + \mu_{vac} \, \hat{\chi}_m(\omega) \, \mathbf{H} = \mu_{vac} \, \hat{\mu}(\omega) \, \mathbf{H} \tag{2.19}$$

where $\hat{\varepsilon}(\omega) = \hat{\chi}(\omega)+1$ and $\hat{\mu}(\omega) = \hat{\chi}_m(\omega)+1$ are the dielectric permittivity and magnetic permeability of the material, respectively.

An additional constitutive equation relates the current density $\mathbf{J}$ to the electric field through Ohm's law:

$$\mathbf{J}(\omega) = \hat{\sigma}(\omega)\mathbf{E}(\omega) \tag{2.20}$$

where $\hat{\sigma}(\omega)$ is the electric conductivity.

An important fact to point out is that both incident ($\mathbf{E}(\omega)$ and $\mathbf{H}(\omega)$) and response ($\mathbf{D}(\omega)$, $\mathbf{B}(\omega)$ and $\mathbf{J}(\omega)$) fields are vectors, which means that $\hat{\varepsilon}(\omega)$, $\hat{\mu}(\omega)$ and $\hat{\sigma}(\omega)$ have to be considered as tensors. This is particularly important in the case of anisotropic systems.

2.3.3 The complex nature of dielectric permittivity and magnetic permeability

In the case of an electric field in the form of a periodic disturbance $E(t,\omega) = E_0\, e^{-i\omega t}$, the response is a dielectric displacement $D(t,\omega)$ (Eq. (2.18)), such as:

$$D(t,\omega) = \varepsilon_{vac}\,\hat{\varepsilon}(\omega)\,E_0\,e^{-i\omega t} \tag{2.21}$$

The transfer function corresponds to the dielectric permittivity, which is a complex quantity that can be expressed as:

$$\hat{\varepsilon}(\omega) = |\varepsilon|\,e^{i\delta} = |\varepsilon|\,(\cos\delta + i\sin\delta) \tag{2.22}$$

where $|\varepsilon|$ and δ are the magnitude and phase of the dielectric permittivity, respectively. This leads to:

$$D(t,\omega) = \varepsilon_{vac}\,|\varepsilon|\,E_0\,e^{-i\omega t+\delta} \tag{2.23}$$

, showing the phase shift or delayed response with respect to the electric field.

Analogously, a similar analysis can be carried out when the perturbation is caused by a periodic magnetic field $H(t,\omega) = H_0\,e^{-i\omega t}$. In this case the response would be given as a magnetic induction of the form:

$$B(t,\omega) = \mu_{vac}\,|\mu|\,H_0\,e^{-i\omega t+\delta_m} \tag{2.24}$$

where δ_m corresponds to the delay in the response to the magnetic field.

In both cases, the complex nature of the transfer functions can be expressed in terms of their real and imaginary parts:

$$\hat{\varepsilon}(\omega) = \varepsilon'(\omega) + i\,\varepsilon''(\omega) \tag{2.25}$$

$$\hat{\mu}(\omega) = \mu'(\omega) + i\,\mu''(\omega) \tag{2.26}$$

where the real parts (ε' and μ') are associated to reversible energy storage and the imaginary parts (ε'' and μ'') are related to energy dissipation (losses) within the material. Real and imaginary components are related through the Kramers-Kronig relations [90, 91] and, in principle, one can be determined from the other. The use of a complex quantity as transfer function allows the specification of a phase shift between the signals that corresponds to the delayed response. Note that for a non-lossy material there would be no delay in the response ($\delta = \delta_m = 0$) and, according to Eq. (2.22), the imaginary parts of dielectric permittivity and magnetic permeability would vanish.

In certain contexts, some magnitudes that are often used are the dielectric and magnetic loss angles. These can be obtained combining equations (2.22), (2.25) and (2.26) as:

$$\delta = \tan^{-1}\left[\frac{\varepsilon''(\omega)}{\varepsilon'(\omega)}\right] \tag{2.27}$$

$$\delta_m = \tan^{-1}\left[\frac{\mu''(\omega)}{\mu'(\omega)}\right] \tag{2.28}$$

Loss angles can be a useful representation of the lossiness of a material.

2.3.4 Maxwell's Equations

The example of a parallel-plate capacitor is a specific case showing the relationship between electric and magnetic fields. The importance of Maxwell's equations resides in the generalization of this interaction between time-varying electric and magnetic fields to any electromagnetic phenomena. They define the propagation of electromagnetic waves in space and time. For a more detailed discussion on this set of equations, we refer the reader to the abundant literature on this topic [92–96]. Here we limit ourselves to show the renowned equations in their differential form, in SI units, and with the only assumption that no magnetic dipoles are present in the system:

Gauss's law	$\nabla \cdot \mathbf{D} = \frac{\rho_e}{\varepsilon_{vac}}$	(2.29)
Gauss's law for magnetism	$\nabla \cdot \mathbf{B} = 0$	(2.30)
Maxwell-Faraday's law	$\nabla \times \mathbf{E} = -\frac{\partial \mathbf{B}}{\partial t}$	(2.31)
Maxwell-Ampère's law	$\nabla \times \mathbf{H} = \mathbf{J} + \frac{\partial \mathbf{D}}{\partial t}$	(2.32)

where ρ_e is the charge density.

The physical meaning of Gauss's law (Eq. (2.29)) is that positive charges act as a source of electric fields in which the field lines diverge away from the charge, while negative charges result in a sink of electric fields. Gauss's law applied to magnetism in a system with no magnetic monopoles (Eq. (2.30)) states that magnetic fields neither diverge from the charge nor converge on it, and therefore tend to form closed loops

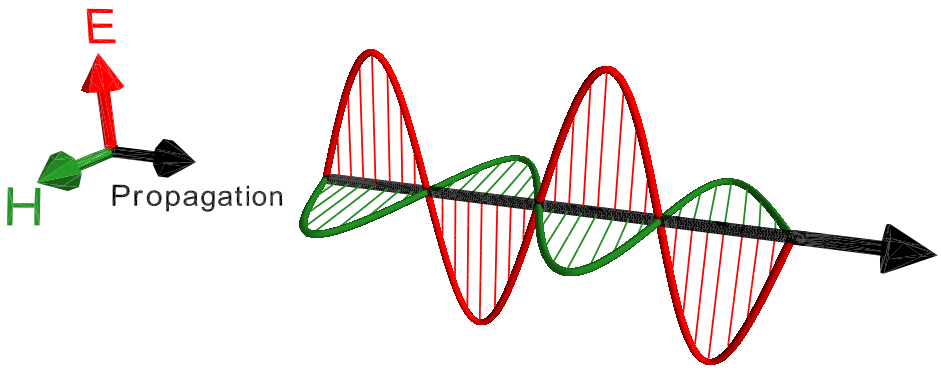

FIGURE 2.5: Electromagnetic wave.

around the charge. Maxwell-Faraday's law (Eq. (2.31)) expresses the fact that a time-varying magnetic field generates an electric field, where the curl of the voltage is proportional to the rate of change of the magnetic field with time. As a consequence, electric fields can be generated in two different ways: from static electric charges or from time-varying magnetic fields. Finally Maxwell-Ampère's law (Eq. (2.32)) shows how both an electric current and a time-varying electric field give rise to a magnetic field circulating around the surface the electric field breaks through. The second term in this equation is Maxwell's main contribution, and is the reason why the set of equations is named after him. It generalized Ampère's law, which was only valid for steady-state situations, to time-dependent problems, setting the base for the study of electromagnetic phenomena.

Plane wave solution to Maxwell's equations and boundary conditions

Depending on the characteristics of the system under consideration, the solution to Maxwell's equations can become extremely complicated. Analytical solutions can only be obtained for simple shapes, while more convoluted geometries require the use of numerical methods such as finite-difference time-domain (FDTD) [97] or finite elements (FE) [98, 99].

Plane waves are a particularly useful tool to visually understand electromagnetic phenomena. They consist of functions with constant frequency and constant amplitude. An example of this type of function is the cosine function:

$$A(\mathbf{r}, t) = A_0 \cos\left(\mathbf{k} \cdot \mathbf{r} - \omega t + \varphi\right) \tag{2.33}$$

where $A(\mathbf{r}, t)$ is the magnitude of the function at a specific position $\mathbf{r}$ and time t, A_0 is the amplitude of the signal, and ω and φ are the angular frequency and the phase shift of the wave, respectively. $\mathbf{k}$ represents the wave vector which components are the

wave numbers $\frac{2\pi}{\lambda}$ in the three spatial directions (x, y, z), where λ is the wavelength of the signal.

The solution of Maxwell's equations for plane waves is shown in Fig. 2.5. It consists of electric and magnetic field vectors orthogonal to each other, and simultaneously orthogonal to the direction of propagation of the wave ($\mathbf{k}$). Mathematically, the solution can be represented as:

$$E(\mathbf{r}, t) = E_y = E_0 \cos(kz - \omega t) \tag{2.34}$$

$$H(\mathbf{r}, t) = H_x = H_0 \cos(kz - \omega t) \tag{2.35}$$

where the electric field has only a component in the y direction and the magnetic field only points into the x direction, being z the direction of propagation of the wave. This type of wave is called transverse electromagnetic wave (TEM).

As for any other set of differential equations, the boundaries of the system have a significant role on the final solution. The most common boundary conditions are the following:

- The component of the electric field tangential to a perfectly conducting surface is always zero.
- The component of the magnetic field normal to a perfectly conducting surface is always zero.
- When two different dielectric materials are present in a system, there must exist continuity of displacement current across the boundary between the materials. This condition is especially important in electromagnetic heating because it determines the intensity of the electric field inside the heated workload. If we consider the system depicted in Fig. 2.4b, in which a slab of dielectric material with permittivity ε is introduced between the plates of a capacitor, the continuity in displacement current translates into:

  $$\mathbf{D} = \varepsilon_{vac}\,\varepsilon\,\mathbf{E} = \varepsilon_{vac}\,\varepsilon_{air}\,\mathbf{E_{air}}\,, \tag{2.36}$$

  and therefore:

  $$\mathbf{E} = \frac{\varepsilon_{air}}{\varepsilon}\,\mathbf{E_{air}} \approx \frac{\mathbf{E_{air}}}{\varepsilon} \tag{2.37}$$

  As a consequence, for materials with high dielectric permittivity, the electric field inside the material can be significantly smaller than in the surroundings.

The ratio of amplitudes between electric and magnetic field is called the characteristic impedance Z. For propagation in free space, its magnitude is related to the vacuum

permittivity and permeability as:

$$Z_0 = \frac{E_0}{H_0} = \sqrt{\frac{\mu_{vac}}{\varepsilon_{vac}}} = 377\,\Omega \tag{2.38}$$

This value can be significantly modified when the wave propagates through a dielectric or ferromagnetic material. In this case:

$$Z = \frac{E_0}{H_0} = \sqrt{\frac{\mu_{vac}\,\hat{\mu}}{\varepsilon_{vac}\,\hat{\varepsilon}}} \tag{2.39}$$

where $\hat{\varepsilon}$ and $\hat{\mu}$ are complex quantities in a lossy medium.

When a wave propagates through two media with different characteristic impedance, a reflected wave is generated at the interface between the two materials. The amplitude of this reflected wave becomes more important when the difference in characteristic impedance between the two materials increases. For large mismatches, it can result in significant power losses, as well as being a risk for the wave generator.

2.3.5 Conservation of Charge

Maxwell's equations can be used to prove the conservation of charges in a system. By taking the divergence on both sides of Maxwell-Ampère's law (Eq. (2.32)), we obtain:

$$\nabla \cdot (\nabla \times \mathbf{H}) = \nabla \cdot \mathbf{J} + \frac{\partial}{\partial t}\left(\nabla \cdot \mathbf{D}\right) \tag{2.40}$$

Then taking into account that the divergence of a curl is always zero, and using Gauss's law (Eq. (2.29)), we reach the law of conservation of charges in the form of a continuity equation:

$$\boxed{\frac{1}{\varepsilon_{vac}}\frac{\partial \rho_e}{\partial t} + \nabla \cdot \mathbf{J} = 0} \tag{2.41}$$

This equation states that a change in the charge density of a system can only occur if a current flows into or out of the system.

Rewriting Eq. (2.41) in Fourier space and defining again the charge density in terms of dielectric displacement through Gauss's law, we obtain:

$$i\omega\,\nabla \cdot \mathbf{D} + \nabla \cdot \mathbf{J} = 0 \tag{2.42}$$

We now introduce the constitutive relations for dielectric displacement (Eq. (2.18)) and current density (Eq. (2.20)):

$$i\omega\varepsilon_{vac}\hat{\varepsilon}\,\nabla \cdot \mathbf{E} + \hat{\sigma}\,\nabla \cdot \mathbf{E} = 0 \tag{2.43}$$

which leads to a final relation between complex dielectric permittivity and conductivity:

$$\hat{\sigma}(\omega) = -i\omega\varepsilon_{vac}\hat{\varepsilon}(\omega) \tag{2.44}$$

2.3.6 Conservation of Energy

For a point charge q, the force $\mathbf{F_e}$ exerted by an electromagnetic field on the charged particle is given by:

$$\mathbf{F_e} = q\left(\mathbf{E} + \mathbf{v} \times \mathbf{B}\right) \tag{2.45}$$

where $\mathbf{v}$ is the velocity of the particle. This is the well-known Lorentz force. In the case of a continuous charge distribution in an infinitesimal element of volume dV, the force becomes:

$$d\mathbf{F_e} = dq\left(\mathbf{E} + \mathbf{v} \times \mathbf{B}\right) \tag{2.46}$$

where the term dq/dV corresponds to the charge density ρ_e. Therefore:

$$d\mathbf{F_e} = \rho_e dV\left(\mathbf{E} + \mathbf{v} \times \mathbf{B}\right) \tag{2.47}$$

The integration of this equation over the volume of the charge distribution leads to the total force exerted by the electromagnetic field on the charge distribution:

$$\mathbf{F_e} = \int_V dV \rho_e\left(\mathbf{E} + \mathbf{v} \times \mathbf{B}\right) \tag{2.48}$$

The rate of work w_{em} done by the electromagnetic field is given by:

$$w_{em} = \frac{\mathbf{F_e} \cdot d\mathbf{r}}{dt} = \mathbf{F_e} \cdot \mathbf{v} = \int_V dV \rho_e\left[\mathbf{E} \cdot \mathbf{v} + (\mathbf{v} \times \mathbf{B}) \cdot \mathbf{v}\right] \tag{2.49}$$

where $(\mathbf{v} \times \mathbf{B}) \cdot \mathbf{v} = 0$, and if we introduce at this point the definition of current density $\mathbf{J} = \rho_e \mathbf{v}$, we obtain:

$$w_{em} = \int_V dV\ \mathbf{J} \cdot \mathbf{E} \tag{2.50}$$

The work done by the electromagnetic field corresponds to a transformation of electromagnetic energy into mechanical or thermal energy. In order to reach energy conservation, this work 'lost' by the electromagnetic field must be compensated by a rate of reduction of the energy of the field itself. Maxwell's modification of Ampère's law (Eq. (2.32)) can be used to express this balance explicitly:

$$\int_V dV\ \mathbf{J} \cdot \mathbf{E} = \int_V dV \left(\nabla \times \mathbf{H} - \frac{\partial \mathbf{D}}{\partial t}\right) \cdot \mathbf{E} \tag{2.51}$$

$$\int_V dV\ \mathbf{J} \cdot \mathbf{E} = \int_V dV \left[\mathbf{E} \cdot (\nabla \times \mathbf{H}) - \mathbf{E} \cdot \frac{\partial \mathbf{D}}{\partial t}\right] \tag{2.52}$$

where:

$$\nabla \cdot (\mathbf{E} \times \mathbf{H}) = \mathbf{H} \cdot (\nabla \times \mathbf{E}) - \mathbf{E} \cdot (\nabla \times \mathbf{H}) \tag{2.53}$$

Thus:

$$\int_V dV\ \mathbf{J}\cdot\mathbf{E} = -\int_V dV\left[\nabla\cdot(\mathbf{E}\times\mathbf{H}) + \mathbf{E}\cdot\frac{\partial\mathbf{D}}{\partial t} - \mathbf{H}\cdot(\nabla\times\mathbf{E})\right] \tag{2.54}$$

If we introduce Maxwell-Faraday equation (Eq. (2.31)), we reach:

$$\int_V dV\ \mathbf{J}\cdot\mathbf{E} = -\int_V dV\left[\nabla\cdot(\mathbf{E}\times\mathbf{H}) + \mathbf{E}\cdot\frac{\partial\mathbf{D}}{\partial t} + \mathbf{H}\cdot\frac{\partial\mathbf{B}}{\partial t}\right] \tag{2.55}$$

Let us assume at this point that, even for time-varying fields, the total electromagnetic energy u is the sum of the total electrostatic energy w_e and the total magnetic energy w_m:

$$u = w_e + w_m = \frac{1}{2}\left(\mathbf{E}\cdot\mathbf{D} + \mathbf{H}\cdot\mathbf{B}\right) \tag{2.56}$$

And therefore:

$$\frac{\partial u}{\partial t} = \frac{1}{2}\left(\mathbf{E}\cdot\frac{\partial\mathbf{D}}{\partial t} + \mathbf{D}\cdot\frac{\partial\mathbf{E}}{\partial t} + \mathbf{H}\cdot\frac{\partial\mathbf{B}}{\partial t} + \mathbf{B}\cdot\frac{\partial\mathbf{H}}{\partial t}\right) \tag{2.57}$$

If we now consider the medium has linear electric and magnetic response, we can use the constitutive relations (2.18) and (2.19) to obtain:

$$\frac{\partial u}{\partial t} = \mathbf{E}\cdot\frac{\partial\mathbf{D}}{\partial t} + \mathbf{H}\cdot\frac{\partial\mathbf{B}}{\partial t} \tag{2.58}$$

Introducing this equation back into Eq. (2.55):

$$-\int_V dV\ \mathbf{J}\cdot\mathbf{E} = \int_V dV\left[\nabla\cdot(\mathbf{E}\times\mathbf{H}) + \frac{\partial u}{\partial t}\right] \tag{2.59}$$

Expressing this equation in the form of a differential continuity equation, the law of conservation of energy, also known as Poynting's Theorem, is finally given by:

$$\boxed{\frac{\partial u}{\partial t} + \nabla\cdot\mathbf{S} = -\mathbf{J}\cdot\mathbf{E}} \tag{2.60}$$

where we define the Poynting vector as $\mathbf{S} = \mathbf{E}\times\mathbf{H}$.

The physical meaning of this energy balance is that the negative value of the total work done by the electromagnetic field on the charge distribution (energy dissipation), per unit of time and per unit of volume, is given by the sum of the rate of change of the electromagnetic energy with time (accumulation), and the energy flow leaving a certain volume per unit of time (convection or propagation), given by the Poynting vector. The right-hand side of this expression represents then the power losses from the electromagnetic field into the material that is being irradiated by the field, which would correspond to the rate of heat absorbed by a material in dielectric heating.

2.3.7 Rate of Heat Dissipation in Dielectric Heating

The capacitor example

If an ideal capacitor is connected to a sinusoidal AC (Alternating Current) source, the build-up of charge (dQ) with an applied potential ($d\phi_v$) is determined by the capacitance of the capacitor [2]:

$$\frac{dQ}{d\phi_v} = C \tag{2.61}$$

$$\frac{dQ}{dt} = C\frac{d\phi_v}{dt} \tag{2.62}$$

$$I = C\frac{d\phi_v}{dt} \tag{2.63}$$

which in Fourier representation results in:

$$I = -i\omega\, C\phi_v \tag{2.64}$$

This means that the current sinusoidal signal leads the voltage signal by 90°. As a consequence, in an ideal capacitor there is no component of the current in phase with the voltage and no power dissipation is observed.

For a real parallel-plate capacitor filled with a dielectric material, such as the one shown in Fig. 2.4a, the capacitance is given by Eq. (2.5), and therefore the current density J results in:

$$J = \frac{I}{A_p} = -i\omega\frac{\varepsilon_{vac}\,\hat{\varepsilon}(\omega)}{d}\,\phi_v \tag{2.65}$$

where in this case we define $\hat{\varepsilon}(\omega) = \varepsilon'(\omega) + i\varepsilon''(\omega)$ as a complex quantity to account for possible losses. This leads to:

$$J = \omega\frac{\varepsilon_{vac}}{d}\,\left[-i\varepsilon'(\omega) + \varepsilon''(\omega)\right]\phi_v \tag{2.66}$$

According to this expression, the imaginary part of the current will be ahead of the voltage by 90° and, as mentioned before, will not contribute to power dissipation. It is the real component of the current, which is in phase with the voltage, the one that is responsible for power dissipation or losses given by:

$$\dot{Q} = Re\,(\phi_v I) = Re\,(\phi_v J A_p) = \omega\frac{\varepsilon_{vac}\,A_p}{d}\,\varepsilon''(\omega)\,\phi_v^2 \tag{2.67}$$

Remembering that in a capacitor the electric field inside the dielectric material between the plates is $E = \phi_v/d$, and knowing the volume of material is $V = A\,d$, the power dissipation can be defined as:

$$\dot{Q} = \omega\varepsilon_{vac}\varepsilon''(\omega)\,E^2\,V \tag{2.68}$$

The generalized dielectric heating equation

As mentioned previously in section 2.3.6 (Eqs. (2.50) and (2.60)), the rate of heat dissipation from an electromagnetic field $\dot{Q}$ is given by:

$$\dot{Q} = \int_V dV \; \mathbf{J} \cdot \mathbf{E} \tag{2.69}$$

However, for harmonic fields such as the ones we can find at microwave frequencies, current density and electric field are complex vectors, and some care has to be taken when handling these quantities. In this case, we can decompose the time-dependent electric field into a linear combination of sinusoidal functions, such as:

$$\mathbf{E}(\mathbf{r}, t) = \int d\omega \; \mathbf{E}(\mathbf{r}) \; e^{-i\omega t} \tag{2.70}$$

where the entire time-dependence of the field is contained in the term $e^{-i\omega t}$, while the spatial-dependence is included in $\mathbf{E}(\mathbf{r})$. Considering only an individual frequency, this can also be expressed as:

$$\mathbf{E}(\mathbf{r}, t) = Re\left\{\mathbf{E}(\mathbf{r})\, e^{-i\omega t}\right\} = \frac{1}{2}\left[\mathbf{E}(\mathbf{r})\, e^{-i\omega t} + \mathbf{E}^*(\mathbf{r})\, e^{i\omega t}\right] \tag{2.71}$$

where $\mathbf{E}^*(\mathbf{r})$ is the complex conjugate of $\mathbf{E}(\mathbf{r})$.

Using this expression, the product $\mathbf{J} \cdot \mathbf{E}$ becomes:

$$\mathbf{J}(\mathbf{r}, t) \cdot \mathbf{E}(\mathbf{r}, t) = \frac{1}{4}\left[\mathbf{J}(\mathbf{r})\, e^{-i\omega t} + \mathbf{J}^*(\mathbf{r})\, e^{i\omega t}\right] \cdot \left[\mathbf{E}(\mathbf{r})\, e^{-i\omega t} + \mathbf{E}^*(\mathbf{r})\, e^{i\omega t}\right] \tag{2.72}$$

, which can be shown to be equivalent to:

$$\mathbf{J}(\mathbf{r}, t) \cdot \mathbf{E}(\mathbf{r}, t) = \frac{1}{2} Re\left\{\mathbf{J}^*(\mathbf{r}) \cdot \mathbf{E}(\mathbf{r}) + \mathbf{J}(\mathbf{r}) \cdot \mathbf{E}(\mathbf{r})\, e^{-2i\omega t}\right\} \tag{2.73}$$

For time averages over one period of the electromagnetic wave, the second term in this expression vanishes, and replacing this in Eq. (2.69), the power dissipation in harmonic fields can be written as:

$$\dot{Q} = \int_V dV \; \frac{1}{2} Re\left\{\mathbf{J}^*(\mathbf{r}) \cdot \mathbf{E}(\mathbf{r})\right\} \tag{2.74}$$

For electric field strengths falling into the linear regime, if we use the constitutive relation given by Eq. (2.20) combined with Eq. (2.44), we obtain:

$$\dot{Q} = \frac{1}{2} \int_V dV \; Re\left\{[-i\omega\, \varepsilon_{vac}\, \hat{\varepsilon}(\omega)\; \mathbf{E}(\mathbf{r})]^* \cdot \mathbf{E}(\mathbf{r})\right\} \tag{2.75}$$

$$\dot{Q} = \frac{1}{2}\, \omega\, \varepsilon_{vac} \int_V dV \; Re\left\{\left[-i\varepsilon'(\omega) + \varepsilon''(\omega)\right]^* \; \mathbf{E}^*(\mathbf{r}) \cdot \mathbf{E}(\mathbf{r})\right\} \tag{2.76}$$

where $\mathbf{E}^*(\mathbf{r}) \cdot \mathbf{E}(\mathbf{r}) = |\mathbf{E}|^2$, being $|\mathbf{E}|$ the peak magnitude of the electric field. Therefore:

$$\dot{Q} = \frac{1}{2}\,\omega\,\varepsilon_{vac} \int_V dV\ Re\left\{\left[\varepsilon''(\omega) + i\varepsilon'(\omega)\right]\ |\mathbf{E}|^2\right\} \tag{2.77}$$

$$\dot{Q} = \frac{1}{2}\,\omega\,\varepsilon_{vac} \int_V dV\ \varepsilon''(\omega)\ |\mathbf{E}|^2 \tag{2.78}$$

In terms of RMS electric field, $|\mathbf{E}| = \sqrt{2}\,|\mathbf{E_{rms}}|$. Thus:

$$\dot{Q} = \omega\,\varepsilon_{vac} \int_V dV\ \varepsilon''(\omega)\ |\mathbf{E_{rms}}|^2 \tag{2.79}$$

Assuming $\varepsilon''(\omega)$ and $|\mathbf{E}|$ are independent from position:

$$\boxed{\dot{Q} = \omega\,\varepsilon_{vac}\,\varepsilon''(\omega)\,|\mathbf{E_{rms}}|^2\,V} \tag{2.80}$$

This is the final expression for the rate of heat dissipation from an electromagnetic field into the material that is being irradiated by the field. From an engineering perspective, if we want to establish the rate at which a sample absorbs heat from an electromagnetic field, it is essential to determine the frequency-dependence of the complex dielectric permittivity, as well as the intensity of the electric field inside the sample. All other quantities, such as the frequency of the wave or the volume of the sample, can be known a priori. The electric field inside the dielectric material is determined by the conservation of displacement current at the boundary, and by the penetration depth of the wave inside the sample. These issues will be discussed later in Chapter 7, where we use Eq. (2.80) to predict microwave heating rates for several materials.

In the next section, we review the main experimental techniques involved in the determination of the complex permittivity and we present some recent applications. As the main topic of this thesis, in Chapter 3, we explore the possibility of using molecular dynamics simulations to predict dielectric permittivities and to analyse the main molecular mechanisms that lead to its frequency-dependence. Subsequent chapters show the usefulness of this method through some specific applications.

2.4 Broadband Dielectric Spectroscopy

Broadband dielectric spectroscopy (BDS) can be defined as the study of the dielectric properties of a material in the frequency range extending from 10^{-6} to 10^{12} Hz [90]. In this broad frequency domain, electromagnetic fields interact with matter at different levels, including polarization effects such as dipole fluctuations in molecules or groups of molecules and conduction of charge carriers. Figure. 2.6 shows the common frequency-dependence of the real and imaginary parts of the dielectric permittivity. Generally, at low frequencies charged particles have the possibility to be transported within the medium. The increase in the conductivity of the material at lower frequencies is directly associated to power loss, which translates into a rise in the imaginary

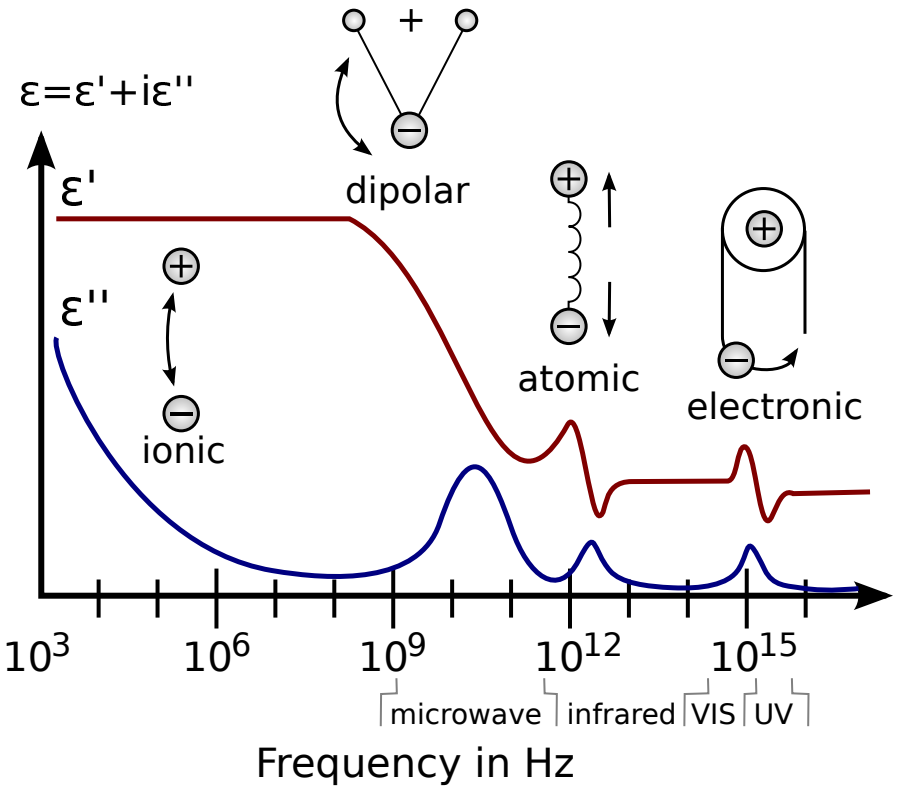

FIGURE 2.6: General shape of a dielectric spectrum showing different modes of interaction between electromagnetic waves and matter. Image by Beau Lambert from Dr. Kenneth A. Mauritz's research group [100].

part of the dielectric permittivity. At microwave frequencies, electromagnetic fields mainly influence dipolar fluctuations, which is manifested as a decay in the real part of the dielectric permittivity with an associated absorption peak in the imaginary part. For more complex systems, additional features may appear in the spectrum corresponding to collective dipolar dynamics. Processes occurring at higher frequencies (molecular vibration and electronic polarization) are also shown in Fig. 2.6 but are out of the scope of broadband dielectric spectroscopy. Experimental techniques covering different parts of the vast range of frequencies studied in BDS were initially pioneered in the late nineteenth century and saw their development during the twentieth century. The first methods were based on transient current and AC bridges and could only reach frequencies up to 10^7 Hz. In that case, samples can be treated as parallel or serial circuits formed by a capacitor and an ohmic resistor. This is an acceptable approximation because at those frequencies, wavelengths are significantly longer than the size of the sample. At higher frequencies, geometrical considerations become important, and different techniques are required. In the 1940's, the use of distributed circuit methods allowed the study of microwave frequencies (3×10^8 to 3×10^{11} Hz). The highest frequencies analysed by BDS (3×10^{11} to 3×10^{12} Hz) only became accessible in the 1970's, when novel spectroscopic techniques were developed. However, despite the large amount of data generated during those years, most of these methods were

only able to perform measurements one frequency at a time, which made them particularly time-consuming. The development of new instruments, such as impedance measuring devices, network analysers, time-domain reflectometers or laser spectrometers, together with the evolution of computational resources, allowed the automation of measurements and data analysis. This led to a revolution in the field, and nowadays it is possible to find experimental techniques that cover the entire range of frequencies that define BDS (10^{-6} to 10^{12} Hz).

Broadband dielectric spectroscopy has been used to study a large variety of systems, ranging from simple molecules to more complex systems, such as polymers, in which a multi-scale dielectric response is expected. As in many other areas, the characteristics of pure water and aqueous solutions are among the most studied systems in dielectric spectroscopy. Several authors [101–104] have shown how, in liquid water, dipole rotation translates into a single and ideal dielectric relaxation process over a wide range of temperatures, despite the presence of hydrogen bonding. The effect of adding different solutes on the strength of this hydrogen bonding network has also been analysed for various aqueous solutions [105]. Short alcohols start to show small deviations from ideality at high frequencies, while the deviations in larger alcohols are more significant. The hydroxyl groups in alcohols can relax freely in the gas phase, but the presence of hydrogen bonding in the liquid phase limits the rotation of these groups [106]. This is signalled by the appearance of multiple contributions to the dielectric absorption spectrum, which occasionally show as shoulders or distinct absorption peaks [107–111]. A similar effect has been observed in water/ethanol mixtures, which show a distribution of relaxation times, as opposed to the single relaxation phenomenon observed for the pure components [112]. As for more complex systems, research has been conducted on the dielectric properties of ferroelectric materials [113, 114] and semiconductors [115]. In addition, the mobility of charge carriers in electrolytes [116, 117] and polyelectrolytes [118–121] has also been studied for applications in battery technology. Recently, there has been interest in the dielectric properties of glass-forming materials, with the aim of interpreting the different frequency-dependent features observed in those systems [90, 122, 123]. These processes can be associated to phenomena such as the relaxation of side-groups in a polymer, and appear as shoulders, or occasionally peaks, in dielectric spectra [124]. Examples of polymeric glassy systems include: polystyrene [125, 126], poly(vinyl acetate), poly(vinyl methyl ether), poly(vinyl chloride) and poly(o-chlorostyrene) [127], propylene glycol [128], poly(alkylene oxides) [129], polyisoprene [130–132]. Some of these materials have important applications in fields such as optics. Another important topic of research is the dynamics of polymers in confined spaces [133], which has significant applications in nanotechnology (thin films on surfaces, diffusion in nanopores or nanodroplets).

2.5 Conclusions

In this chapter we introduce the concept of electromagnetic radiation and describe its different modes of interaction with matter with particular interest on radiation at microwave frequencies. Additionally, we enumerate some of the main applications of microwave heating in chemical processing. Then, we proceed to define the theoretical foundations of dielectric heating from a macroscopic point of view. Maxwell's equations, which describe the propagation of electromagnetic radiation in a dielectric medium, are combined with linear constitutive relations, that determine the interaction of radiation with matter, to obtain an expression for the rate of heat dissipation in microwave heating processes. This expression shows the importance of the characteristics of the electromagnetic wave and the dielectric properties of the material in these processes. The determination of the frequency-dependent dielectric permittivity is a key aspect in the characterisation of the dielectric response. To close this chapter, we expose how broadband dielectric spectroscopy experimental techniques are nowadays an established way to obtain dielectric spectra. However, some of the frequency-dependent features that appear on those results remain difficult to explain. In the following chapters, we show how molecular dynamics simulations can be a very useful tool to predict dielectric spectra, and to facilitate the understanding of the molecular mechanisms leading to a particular dielectric response.

Chapter 3

Molecular Simulations for the Prediction of Dielectric Response

In Chapter 2, we enumerated some of the main applications of microwave heating and described the theoretical foundations of this phenomenon from a macroscopic point of view. We showed how it is the dielectric constant of a material that defines its response to external electromagnetic fields. In this chapter, we demonstrate how this important quantity is related to the fluctuations in the dipole moment of the material, and how this relationship can be determined through the fluctuation-dissipation theorem and linear response theory. We explain how molecular simulations, in particular molecular dynamics (MD) simulations, and dielectric relaxation models can be used to exploit this relationship and predict dielectric spectra.

3.1 Background

Since Debye [134] stated that the phenomenon of dielectric relaxation originates from the reorganisation of molecular dipoles, with associated dispersion and absorption mechanisms, the theoretical understanding of the interaction of electromagnetic fields with matter has evolved considerably [90]. Initial efforts were directed towards finding a relationship between the dynamics of systems under the influence of external fields and the evolution of unperturbed systems. However, this task proved to be arduous, especially for complex systems. It was not until Kubo demonstrated that the frequency-dependent conductivity $\hat{\sigma}(\omega)$ is related through Fourier transformation to both the mean-squared displacement of charges with time and their velocity autocorrelation function in the unperturbed system [135], that the field clearly evolved. In order to reach this result, Kubo made use of linear response theory and time-dependent statistical mechanics. Based on these findings, the equivalent relationship between dielectric permittivity $\hat{\varepsilon}(\omega)$ and the time autocorrelation function of the dipole moment of the system was established by Glarum [136] and Cole [137]. Some years later, Neumann and Steinhauser adapted these expressions for their use in computer simulations of non-polarisable [138] and polarisable [139] systems, in cases where the perturbed dynamics do not depend explicitly on time.

In general, time correlation functions are a key element in the previous derivations. The link between theory and experiments can be made through the determination of transport coefficients and other properties obtained by means of a wide range of spectroscopic techniques, which can be predicted theoretically through various correlation functions. Moreover, computer simulations have the ability to use these and other correlation functions, that are not accessible experimentally, to determine material properties while providing a deeper understanding of processes depending on molecular dynamics [140]. The fluctuation-dissipation theorem covers all these considerations and can be applied to a wide variety of properties ranging from self-diffusion coefficients derived from velocity autocorrelation functions to viscosities obtained from shear stress correlation functions, or to the relationship between the dielectric constant and dipole moment fluctuations studied in this work.

Molecular simulations are becoming more and more important in the study of systems under the influence of external electric fields [141]. This tool has reached a stage in which it can be used confidently in the design of processes and materials that benefit from the interaction with external fields, while providing an atomistic and molecular level understanding of these processes. Molecular simulations have already been used in fields such as dielectric heating, estimation of structural, thermodynamic and dielectric properties, the study of the influence of external electric fields on protein dynamics and chemical reactions, and improving the understanding of spectroscopic techniques. Furthermore, a quick expansion to additional fields is expected in the near future [141].

In this chapter, we first show how the fluctuation-dissipation theorem coupled with linear response theory can be used to develop an expression that relates the dielectric constant of a material to the equilibrium fluctuations of its dipole moment. After describing the basic principles of molecular dynamics (MD) simulations, we explain how the molecular trajectories generated through this simulation technique can be used to exploit the previous relationship and predict dielectric spectra. Additionally, we introduce some of the most common models employed to describe dielectric relaxation phenomena.

3.2 The fluctuation-dissipation theorem

The fluctuation-dissipation theorem [142, 143] relates the response of a system to the influence of an external perturbation (e.g. mechanical forces, electric fields) to the natural internal fluctuations of the system at equilibrium [90, 144]. Within the framework of linear response theory, it is presupposed that perturbations are not strong enough to alter relaxation rates, and the response to external fields is identical to the relaxation of internal equilibrium fluctuations within the system. This enables the determination of properties (e.g. self-diffusion coefficient, dielectric constant) from equilibrium molecular dynamics simulations.

3.2.1 Hamilton's equations of motion

The state of the system is fixed by specifying the values of a set of generalized coordinates $\mathbf{r}_k$ and momenta $\mathbf{p}_k$. This corresponds to a location in the phase space of the system. Collectively, we will refer to a location in phase space as $\mathbf{\Gamma}$.

In general the dynamics of a system through its phase space can be written as a set of first order differential equations

$$\frac{\partial \mathbf{\Gamma}}{\partial t} = \mathbf{F}(\mathbf{\Gamma}, t) \tag{3.1}$$

where the vector function $\mathbf{F}$ on the right-hand side of the equation defines the dynamics of the system. In principle, this function can also include stochastic terms (e.g., a random forcing function, as in the case of Langevin equation), so the dynamics do not need to be deterministic.

The energy of the system is given by a function of its phase space coordinates H (i.e. $H(\mathbf{\Gamma}, t)$). We refer to this energy function as the Hamiltonian of the system. Note that the Hamiltonian may also depend explicitly on time.

One special class of systems are Hamiltonian systems. For Hamiltonian systems, there are two sets of dynamical variables: (generalized) coordinates and momenta. For each coordinate variable $\mathbf{r}_k$, there is an associated conjugate momentum $\mathbf{p}_k$. The time evolution of these systems through their phase space is governed by the Hamiltonian:

$$\dot{\mathbf{r}}_k = \frac{\partial H}{\partial \mathbf{p}_k} \tag{3.2}$$

$$\dot{\mathbf{p}}_k = -\frac{\partial H}{\partial \mathbf{r}_k} \tag{3.3}$$

where $\dot{x}$ denotes the rate of change of variable x with time (i.e. $\partial x/\partial t$).

3.2.2 Evolution of the properties of a system with time

In general, we are not interested in the motion of the individual particles of a system, but rather the evolution of its overall properties. Typically, these properties will depend on the state of the system (location in phase space $\mathbf{\Gamma}$) and possibly on time. That is $A(\mathbf{\Gamma}, t)$. For example, the net dipole moment $\mathbf{M}$ of a system is given by:

$$\mathbf{M}(\mathbf{\Gamma}, t) = \sum_k q_k \mathbf{r}_k(t). \tag{3.4}$$

The time variation of the value of a property will depend on how the system evolves through phase space:

$$\frac{d}{dt}A(\mathbf{\Gamma}(t),t) = \dot{\mathbf{\Gamma}} \cdot \frac{\partial}{\partial \mathbf{\Gamma}} A(\mathbf{\Gamma}(t),t) + \frac{\partial}{\partial t} A(\mathbf{\Gamma}(t),t) \tag{3.5}$$

$$= \sum_k \left[\dot{\mathbf{r}}_k \cdot \frac{\partial}{\partial \mathbf{r}_k} A(\mathbf{\Gamma}(t),t) + \dot{\mathbf{p}}_k \cdot \frac{\partial}{\partial \mathbf{p}_k} A(\mathbf{\Gamma}(t),t) \right] + \frac{\partial}{\partial t} A(\mathbf{\Gamma}(t),t) \tag{3.6}$$

We can use the above expression to examine the time evolution of the Hamiltonian (total energy) of the system. In this case, we find:

$$\frac{d}{dt}H(\mathbf{\Gamma}(t),t) = \sum_k \left[\dot{\mathbf{r}}_k \cdot \frac{\partial H}{\partial \mathbf{r}_k} + \dot{\mathbf{p}}_k \cdot \frac{\partial H}{\partial \mathbf{p}_k} \right] + \frac{\partial H}{\partial t} \tag{3.7}$$

$$= \sum_k \left[\frac{\partial H}{\partial \mathbf{p}_k} \cdot \frac{\partial H}{\partial \mathbf{r}_k} - \frac{\partial H}{\partial \mathbf{r}_k} \cdot \frac{\partial H}{\partial \mathbf{p}_k} \right] + \frac{\partial H}{\partial t} \tag{3.8}$$

$$= \frac{\partial H}{\partial t} \tag{3.9}$$

If the dynamics of the system is derivable from a Hamiltonian that does not explicitly depend on time, then its Hamiltonian is conserved.

3.2.3 The Liouville equation

Often, we are interested in tracking the evolution of an ensemble of systems, rather than just the evolution of a single system. Let us consider an initial distribution $f(\mathbf{\Gamma})$ of points in phase space. We want to know how this distribution evolves with time (i.e. $f(\mathbf{\Gamma}, t)$. This is given by the Liouville equation:

$$\frac{\partial f}{\partial t} + \dot{\mathbf{\Gamma}} \cdot \frac{\partial f}{\partial \mathbf{\Gamma}} = 0 \tag{3.10}$$

$$\frac{\partial f}{\partial t} = -\mathcal{L} f \tag{3.11}$$

where $\mathcal{L}$ is the Liouvillean operator, which is defined as:

$$\mathcal{L} = \dot{\mathbf{\Gamma}} \cdot \frac{\partial}{\partial \mathbf{\Gamma}} \tag{3.12}$$

The evolution of the property with time across this ensemble of systems is:

$$\langle A(t) \rangle = \int d\mathbf{\Gamma} A(\mathbf{\Gamma}, t) f(\mathbf{\Gamma}, t) \tag{3.13}$$

We can define a time evolution operator $\mathcal{S}(t, t_0)$ which acts on the distribution f to transform it from its form at time t_0 to its form at time t:

$$f(\mathbf{\Gamma}, t) = \mathcal{S}(t, t_0) f(\mathbf{\Gamma}, t_0). \tag{3.14}$$

By substituting the definition of the time evolution operator into the equation of motion (Eq.(3.11)), we obtain a differential equation for the time evolution operator:

$$\frac{\partial}{\partial t}\mathcal{S}(t,t_0) = -\mathcal{L}(t)\mathcal{S}(t,t_0) \tag{3.15}$$

We can determine a formal expression for the time evolution operator by integrating this equation:

$$\mathcal{S}(t,t_0) = 1 - \int_{t_0}^{t} dt_1 \mathcal{L}(t_1)\mathcal{S}(t_1,t_0) \tag{3.16}$$

This equation can be repeatedly iterated by substituting the left side of the equation in to the integrand in the right side of the equation to obtain:

$$\begin{aligned}\mathcal{S}(t,t_0) = 1 - \int_{t_0}^{t} dt_1 \mathcal{L}(t_1) + \int_{t_0}^{t} dt_1 \int_{t_0}^{t_1} dt_2 \mathcal{L}(t_1)\mathcal{L}(t_2) \\ - \int_{t_0}^{t} dt_1 \int_{t_0}^{t_1} dt_2 \int_{t_0}^{t_2} dt_3 \mathcal{L}(t_1)\mathcal{L}(t_2)\mathcal{L}(t_3) + \cdots\end{aligned} \tag{3.17}$$

Therefore, formally, the time evolution operator corresponds to a power series that can be written as:

$$\mathcal{S}(t,t_0) = e^{-\int_{t_0}^{t} dt_1 \mathcal{L}(t_1)} \tag{3.18}$$

And, for a time independent Liouville operator:

$$\mathcal{S}(t,t_0) = e^{-(t-t_0)\mathcal{L}} \tag{3.19}$$

3.2.4 The Dyson equation

Now we are interested in how a perturbation can alter the dynamics of a system. Let us divide the right side of the dynamic equation (Eq. (3.1)) as:

$$\mathbf{F}(\mathbf{\Gamma},t) = \mathbf{F}_0(\mathbf{\Gamma},t) + \mathbf{F}_1(\mathbf{\Gamma},t) \tag{3.20}$$

where $\mathbf{F}_0$ defines the initial dynamics of the unperturbed system, and $\mathbf{F}_1$ represents the perturbation. For a Hamiltonian system, this is equivalent to splitting the Hamiltonian as:

$$H(\mathbf{\Gamma},t) = H_0(\mathbf{\Gamma},t) + H_1(\mathbf{\Gamma},t) \tag{3.21}$$

where H_0 is the Hamiltonian of the unperturbed system, and H_1 is the perturbation.

We divide the Liouvillean of the system into a reference contribution $\mathcal{L}_0$ and a perturbation $\mathcal{L}_1$:

$$\begin{aligned}\mathcal{L} &= \mathbf{F}_0 \cdot \frac{\partial}{\partial \mathbf{\Gamma}} + \mathbf{F}_1 \cdot \frac{\partial}{\partial \mathbf{\Gamma}} \\ &= \mathcal{L}_0 + \mathcal{L}_1\end{aligned} \tag{3.22}$$

Then, we define a time evolution operator $\mathcal{S}_I$ for the interaction of the perturbation with the original system such as:

$$\mathcal{S}_I(t,t_0) = \mathcal{S}_0^{-1}(t,t_0)\mathcal{S}(t,t_0) \tag{3.23}$$

$$\frac{\partial}{\partial t}\mathcal{S}_I = \frac{\partial \mathcal{S}_0^{-1}}{\partial t}\mathcal{S} + \mathcal{S}_0^{-1}\frac{\partial \mathcal{S}}{\partial t} \tag{3.24}$$

However:

$$\begin{aligned}
\mathcal{S}_0\mathcal{S}_0^{-1} &= 1 \\
\frac{\partial}{\partial t}[\mathcal{S}_0\mathcal{S}_0^{-1}] &= 0 \\
\frac{\partial \mathcal{S}_0}{\partial t}\mathcal{S}_0^{-1} + \mathcal{S}_0\frac{\partial \mathcal{S}_0^{-1}}{\partial t} &= 0 \\
\frac{\partial \mathcal{S}_0^{-1}}{\partial t} &= -\mathcal{S}_0^{-1}\frac{\partial \mathcal{S}_0}{\partial t}\mathcal{S}_0^{-1} \\
\frac{\partial \mathcal{S}_0^{-1}}{\partial t} &= \mathcal{S}_0^{-1}\mathcal{L}_0\mathcal{S}_0\mathcal{S}_0^{-1} \\
\frac{\partial \mathcal{S}_0^{-1}}{\partial t} &= \mathcal{S}_0^{-1}\mathcal{L}_0
\end{aligned}$$

Therefore:

$$\begin{aligned}
\frac{\partial}{\partial t}\mathcal{S}_I &= \mathcal{S}_0^{-1}\mathcal{L}_0\mathcal{S} - \mathcal{S}_0^{-1}\mathcal{L}\mathcal{S} \\
&= -\mathcal{S}_0^{-1}\mathcal{L}_1\mathcal{S} \\
&= -\mathcal{S}_0^{-1}\mathcal{L}_1\mathcal{S}_0\mathcal{S}_0^{-1}\mathcal{S} \\
\frac{\partial}{\partial t}\mathcal{S}_I &= -[\mathcal{S}_0^{-1}\mathcal{L}_1\mathcal{S}_0]\mathcal{S}_I
\end{aligned} \tag{3.25}$$

This implies that the time evolution operator in the interaction representation can be written as:

$$\mathcal{S}_I(t,t_0) = 1 - \int_{t_0}^{t} dt_1 \left[\mathcal{S}_0^{-1}(t_1,t_0)\mathcal{L}_1\mathcal{S}_0(t_1,t_0)\right]\mathcal{S}_I(t_1,t_0) \tag{3.26}$$

Assuming the initial state of the system is time independent and applying the free streaming operator $\mathcal{S}_0$ to both sides of the equation, yields the Dyson equation:

$$\mathcal{S}(t,t_0) = \mathcal{S}_0(t,t_0) - \int_{t_0}^{t} dt_1 \mathcal{S}_0^{-1}(t_1,t_0)\mathcal{S}_0(t,t_0)\mathcal{L}_1\mathcal{S}(t_1,t_0) \tag{3.27}$$

$$\mathcal{S}(t,t_0) = \mathcal{S}_0(t,t_0) - \int_{t_0}^{t} dt_1 \mathcal{S}_0^{-1}(t_1,t_0)\mathcal{S}_0(t,t_1)\mathcal{S}_0(t_1,t_0)\mathcal{L}_1\mathcal{S}(t_1,t_0) \tag{3.28}$$

$$\mathcal{S}(t,t_0) = \mathcal{S}_0(t,t_0) - \int_{t_0}^{t} dt_1 \mathcal{S}_0(t,t_1)\mathcal{L}_1\mathcal{S}(t_1,t_0) \tag{3.29}$$

The physical interpretation of this expression is that the time evolution of the system can be represented by the sum of the evolution of the unperturbed system and the iterative effects of an increasing number of perturbations on this unperturbed path.

3.2.5 Linear response theory

Let us assume that there is a spatially homogeneous and time varying external field $h(t)$ that perturbs our system and couples linearly to a property $B(\mathbf{\Gamma}, t)$ of the system. The interaction of this field with the system is given by:

$$H_1(\mathbf{\Gamma}, t) = B(\mathbf{\Gamma}, t)\ h(t) \tag{3.30}$$

For example, we can perturb the system with a uniform, time varying electric field $\mathbf{E}_0(t)$ which couples with the dipole moment of the system $\mathbf{M}(\mathbf{\Gamma}, t)$ such as:

$$\begin{aligned} H_1(\mathbf{\Gamma}, t) &= \sum_k q_k \phi_0(\mathbf{r}_k, t) \\ &\approx \sum_k q_k [\phi_0(\mathbf{R}, t) + (\mathbf{r}_k - \mathbf{R}) \cdot \nabla \phi_0(\mathbf{R}, t) + \cdots] \\ &\approx -\sum_k q_k (\mathbf{r}_k - \mathbf{R}) \cdot \mathbf{E}_0(t) \\ &\approx -\mathbf{M}(\mathbf{\Gamma}, t) \cdot \mathbf{E}_0(t) \end{aligned} \tag{3.31}$$

where $\mathbf{R}$ is some fixed reference position in the system and $\phi_0(\mathbf{R}, t)$ represents the electric potential at that position.

The phase-space probability density that defines the dynamics of the system at equilibrium is given by: $f_{\text{eq}}(\mathbf{\Gamma}) = e^{-\hat{\beta} H_0(\mathbf{\Gamma})}$, with $\beta_T = 1/k_B T$, where $k_B = 1.3806485 \times 10^{-23} JK^{-1}$ is the Botzmann constant. Applying the Liouvillean operator of the perturbation (Eq. (3.22)) to this function:

$$\begin{aligned} \mathcal{L}_1 f_{\text{eq}}(\mathbf{\Gamma}) &= \mathbf{F}_1 \cdot \frac{\partial}{\partial \mathbf{\Gamma}} f_{\text{eq}}(\mathbf{\Gamma}) \\ &= \sum_k \left[\frac{\partial H_1}{\partial \mathbf{p}_k} \cdot \frac{\partial f_{\text{eq}}}{\partial \mathbf{r}_k} - \frac{\partial H_1}{\partial \mathbf{r}_k} \cdot \frac{\partial f_{\text{eq}}}{\partial \mathbf{p}_k} \right] \\ &= -\beta_T f_{\text{eq}} \sum_k \left[\frac{\partial H_1}{\partial \mathbf{p}_k} \cdot \frac{\partial H_0}{\partial \mathbf{r}_k} - \frac{\partial H_1}{\partial \mathbf{r}_k} \cdot \frac{\partial H_0}{\partial \mathbf{p}_k} \right] \\ &= \beta_T f_{\text{eq}} \sum_k \left[\frac{\partial H_0}{\partial \mathbf{p}_k} \cdot \frac{\partial H_1}{\partial \mathbf{r}_k} - \frac{\partial H_0}{\partial \mathbf{r}_k} \cdot \frac{\partial H_1}{\partial \mathbf{p}_k} \right] \\ \mathcal{L}_1 f_{\text{eq}}(\mathbf{\Gamma}) &= \beta_T f_{\text{eq}}(\mathbf{\Gamma})\ \mathcal{L}_0 H_1(\mathbf{\Gamma}, t) \end{aligned}$$

Introducing the perturbation as defined in Eq.(3.30), we obtain:

$$\begin{aligned}\mathcal{L}_1 f_{\text{eq}}(\mathbf{\Gamma}) &= \beta_T f_{\text{eq}}(\mathbf{\Gamma})\ \mathcal{L}_0 B(\mathbf{\Gamma}, t)\ h(t) \\ &= \beta_T h(t)\ f_{\text{eq}}(\mathbf{\Gamma})\ \mathcal{L}_0 B(\mathbf{\Gamma}, t) \\ \mathcal{L}_1 f_{\text{eq}}(\mathbf{\Gamma}) &= \beta_T h(t)\ f_{\text{eq}}(\mathbf{\Gamma})\ \dot{B}(\mathbf{\Gamma}, t)\end{aligned} \tag{3.32}$$

If this external field is quite weak, we can linearise the time evolution operator given by the Dyson equation (Eq. (3.29)) as:

$$\mathcal{S}(t, t_0) \approx \mathcal{S}_0(t, t_0) - \int_{t_0}^{t} dt_1\ \mathcal{S}_0(t, t_1)\mathcal{L}_1(t_1)\mathcal{S}_0(t_1, t_0) + \cdots \tag{3.33}$$

Applying this linearised time evolution operator to the phase-space distribution at equilibrium, we can obtain the time evolution of the phase-space probability density:

$$\mathcal{S}(t, t_0) f_{\text{eq}}(\mathbf{\Gamma}, t) \approx \mathcal{S}_0(t, t_0) f_{\text{eq}}(\mathbf{\Gamma}, t) - \int_{t_0}^{t} dt_1\ \mathcal{S}_0(t, t_1)\mathcal{L}_1(t_1)\mathcal{S}_0(t_1, t_0) f_{\text{eq}}(\mathbf{\Gamma}, t_1) + \cdots$$

$$f(\mathbf{\Gamma}, t) \approx f_{\text{eq}}(\mathbf{\Gamma}, t) - \int_{t_0}^{t} dt_1\ \mathcal{S}_0(t, t_1)\mathcal{L}_1(t_1) f_{\text{eq}}(\mathbf{\Gamma}, t_1) + \cdots$$

If we introduce here the result given by Eq. (3.32):

$$f(\mathbf{\Gamma}, t) \approx f_{\text{eq}}(\mathbf{\Gamma}, t) - \beta_T \int_{t_0}^{t} dt_1\ \mathcal{S}_0(t, t_1)\ f_{\text{eq}}(\mathbf{\Gamma}, t_1)\ \dot{B}(\mathbf{\Gamma}, t_1)\ h(t_1) + \cdots \tag{3.34}$$

Once the evolution of the distribution of points in phase space with time is known, it is possible to determine how a a property A of the system evolves with time. Through Eq. (3.13), we obtain:

$$\langle A(t) \rangle \approx \int d\mathbf{\Gamma} A(\mathbf{\Gamma}, t) \left[f_{\text{eq}}(\mathbf{\Gamma}, t) - \beta_T \int_{t_0}^{t} dt_1\ \mathcal{S}_0(t, t_1)\ f_{\text{eq}}(\mathbf{\Gamma}, t_1)\ \dot{B}(\mathbf{\Gamma}, t_1)\ h(t_1) + \cdots \right]$$

$$\langle A(t) \rangle \approx \langle A(t) \rangle_{\text{eq}} - \beta_T \int d\mathbf{\Gamma} A(\mathbf{\Gamma}, t) \int_{t_0}^{t} dt_1\ \mathcal{S}_0(t, t_1)\ f_{\text{eq}}(\mathbf{\Gamma}, t_1)\ \dot{B}(\mathbf{\Gamma}, t_1)\ h(t_1) + \cdots$$

which leads to the general expression of the fluctuation-dissipation theorem:

$$\langle A(t) \rangle = \langle A(t) \rangle_{\text{eq}} - \beta_T \int_{t_0}^{t} dt_1 \langle A(t) \dot{B}(t - t_1) \rangle_{\text{eq}}\ h(t_1) \tag{3.35}$$

For a time-translationally invariant system (e.g. equilibrium system), we have:

$$\langle A(t) \rangle = \langle A(t) \rangle_{\text{eq}} + \beta_T \int_{t_0}^{t} dt_1 \left[\frac{\partial}{\partial t_1} \langle A(t) B(t - t_1) \rangle_{\text{eq}} \right]\ h(t_1) \tag{3.36}$$

In general, we define a response function $\chi_{AB}(t, t_1)$

$$\langle A(t)\rangle = \langle A(t)\rangle_{\text{eq}} + \int_{t_0}^{t} dt_1 \; \chi_{AB}(t, t_1) \; h(t_1) \tag{3.37}$$

Therefore, we can identify:

$$\chi_{AB}(t, t_1) = -\beta_T \langle A(t)\dot{B}(t - t_1)\rangle_{\text{eq}} = \beta_T \frac{\partial}{\partial t_1}\langle A(t)B(t - t_1)\rangle_{\text{eq}} \tag{3.38}$$

3.2.6 Application to systems perturbed by weak external electric fields

The expressions above define the effect of a perturbation on the expected value of a property of the system. In this thesis, we are interested in predicting the interaction of external electric fields with matter. As mentioned previously in Eq. (3.31), the perturbation due to the presence of a uniform, time varying electric field $\mathbf{E}_0(t)$ is given by:

$$H_1(\mathbf{\Gamma}, t) \approx -\mathbf{M}(\mathbf{\Gamma}, t) \cdot \mathbf{E}_0(t) \tag{3.39}$$

In this case, the electric field couples with the dipole moment of the system, which is the property for which we want to analyse the influence of the perturbation. Therefore, by comparison with the general case:

$$\begin{aligned} A(t) &= \mathbf{M}(t) \\ B(t) &= \mathbf{M}(t) \\ h(t) &= -\mathbf{E}_0(t) \end{aligned} \tag{3.40}$$

Applying the result given by the fluctuation-dissipation theorem (Eq. (3.37)) to this particular three-dimensional case, we obtain:

$$\langle \mathbf{M}(t)\rangle = \langle \mathbf{M}(t)\rangle_{\text{eq}} + \frac{\beta_T}{3} \int_{t_0}^{t} dt_1 \left[\frac{\partial}{\partial t_1}\langle \mathbf{M}(t) \cdot \mathbf{M}(t - t_1)\rangle_{\text{eq}}\right] [-\mathbf{E}_0(t_1)] \tag{3.41}$$

where the average dipole moment of the unperturbed system is zero ($\langle \mathbf{M}(t)\rangle_{\text{eq}} = 0$), therefore:

$$\langle \mathbf{M}(t)\rangle = -\frac{\beta_T}{3} \int_{t_0}^{t} dt_1 \left[\frac{\partial}{\partial t_1}\langle \mathbf{M}(t) \cdot \mathbf{M}(t - t_1)\rangle_{\text{eq}}\right] \mathbf{E}_0(t_1) \tag{3.42}$$

We introduce at this point the concept of normalized autocorrelation function $\boldsymbol{\phi}(t)$. In the case of the dipole moment it is defined as:

$$\boldsymbol{\phi}(t - t_1) = \frac{\langle \mathbf{M}(t) \cdot \mathbf{M}(t - t_1)\rangle}{\langle \mathbf{M}(t - t_1) \cdot \mathbf{M}(t - t_1)\rangle} = \frac{\langle \mathbf{M}(t) \cdot \mathbf{M}(t - t_1)\rangle}{\langle \mathbf{M}^2\rangle} \tag{3.43}$$

which leads to:

$$\langle \mathbf{M}(t)\rangle = -\frac{\beta_T}{3} \; \langle \mathbf{M}^2\rangle \int_{t_0}^{t} dt_1 \; \frac{\partial \boldsymbol{\phi}(t - t_1)}{\partial t_1} \; \mathbf{E}_0(t_1) \tag{3.44}$$

From this expression, the polarisation $\mathbf{P}(t)$ of a volume V of perturbed system results in:

$$\langle \mathbf{P}(t) \rangle = \frac{\langle \mathbf{M}(t) \rangle}{3V} = -\frac{\beta_T \, \langle \mathbf{M}^2 \rangle}{V} \int_{t_0}^{t} dt_1 \, \frac{\partial \boldsymbol{\phi}(t - t_1)}{\partial t_1} \, \mathbf{E}_0(t_1) \tag{3.45}$$

This expression describes the polarisation as a convolution of electric fields at previous times. According to the convolution theorem, the equivalent expression in the Fourier domain is given by:

$$\hat{\mathbf{P}}(\omega) = -\frac{\beta_T \, \langle \mathbf{M}^2 \rangle}{3V} \, \mathcal{F}\left[\frac{\partial \boldsymbol{\phi}(t)}{\partial t}\right] \, \hat{\mathbf{E}}_0(\omega) \tag{3.46}$$

where $\mathcal{F}$ denotes a Fourier transform operation. For the term containing the dipole moment autocorrelation function:

$$\mathcal{F}\left[\frac{\partial \boldsymbol{\phi}(t)}{\partial t}\right] = \int_{-\infty}^{\infty} dt \left[\frac{\partial}{\partial t}\boldsymbol{\phi}(t)\right] e^{i\omega t}$$

Note that $\phi(t) = 0$ if $t < 0$, therefore:

$$\begin{aligned}
\mathcal{F}\left[\frac{\partial \boldsymbol{\phi}(t)}{\partial t}\right] &= \int_{0}^{\infty} dt \left[\frac{\partial}{\partial t}\boldsymbol{\phi}(t)\right] e^{i\omega t} \\
&= \boldsymbol{\phi}(t) \, e^{i\omega t} \Big|_0^{\infty} - \int_0^{\infty} dt \; \boldsymbol{\phi}(t) \; i\omega \; e^{i\omega t} \\
&= \boldsymbol{\phi}(\infty) - \boldsymbol{\phi}(0) - i\omega \; \hat{\boldsymbol{\phi}}(\omega) \\
\mathcal{F}\left[\frac{\partial \boldsymbol{\phi}(t)}{\partial t}\right] &= -1 - i\omega \; \hat{\boldsymbol{\phi}}(\omega)
\end{aligned}$$

Then, the polarisation results in:

$$\hat{\mathbf{P}}(\omega) = \frac{\beta_T \, \langle \mathbf{M}^2 \rangle}{3V} \, \left[1 + i\omega \; \hat{\boldsymbol{\phi}}(\omega)\right] \, \hat{\mathbf{E}}_0(\omega) \tag{3.47}$$

However, from Chapter 2 we know that, at the macroscopic level, the polarisation of a system due to the presence of an external electric field is governed by the dielectric constant of the material. For weak electric fields, the response tends to be linear:

$$\hat{\mathbf{P}}(\omega) = (\hat{\varepsilon}(\omega) - 1) \; \varepsilon_{vac} \, \hat{\mathbf{E}}_0(\omega) \tag{2.15}$$

Combining the previous expressions, we obtain:

$$\hat{\varepsilon}(\omega) - 1 = \frac{\beta_T \, \langle \mathbf{M}^2 \rangle}{\varepsilon_{vac} \, 3V} \, \left[1 + i\omega \; \hat{\boldsymbol{\phi}}(\omega)\right] \tag{3.48}$$

The fact that $\lim_{\omega \to \infty} 1 + i\omega\hat{\boldsymbol{\phi}}(\omega) = 0$ and $\lim_{\omega \to 0} -\hat{\dot{\boldsymbol{\phi}}}(\omega) = \lim_{\omega \to 0} -\mathcal{F}\left[\frac{\partial \boldsymbol{\phi}(t)}{\partial t}\right] = 1$ leads to:

$$\varepsilon_\infty = 1$$

$$\frac{\beta_T \, \langle \mathbf{M}^2 \rangle}{\varepsilon_{vac} \, 3V} = \varepsilon_0 - \varepsilon_\infty$$

where ε_∞ is the infinite frequency relative permittivity and ε_0 is the zero-frequency or static dielectric constant given by:

$$\varepsilon_0 = \varepsilon_\infty + \frac{\beta_T}{\varepsilon_{vac}\, 3V} \langle \mathbf{M}^2 \rangle \tag{3.49}$$

Replacing these findings in Eq. (3.48), we finally obtain:

$$\boxed{\frac{\hat{\varepsilon}(\omega) - \varepsilon_\infty}{\varepsilon_0 - \varepsilon_\infty} = 1 + i\omega\, \hat{\boldsymbol{\phi}}(\omega)} \tag{3.50}$$

This expression relates the frequency-dependent dielectric constant of a system with the fluctuations of its dipole moment, and allows the determination of this property provided an accurate knowledge of the dynamics of the system.

3.3 Molecular Dynamics Simulations

Molecular Dynamics (MD) Simulations are an interesting tool to exploit the relationship given by Eq. (3.50) since they have the potential to generate dipole moment fluctuations in molecular systems. In this section, we introduce the basic concepts that define MD simulations, leaving their particular implementation for determination of dielectric spectra for section 3.4.

3.3.1 General concepts

In MD simulations, atoms and molecules are allowed to interact with each other, generating trajectories which are the result of the integration of Newton's equations of motion [145]. Any equilibrium or transport property to be determined through MD simulations has to be a function of the positions and momenta of the particles in the system. In a first instance, a system with a predefined number of particles is prepared by assigning an initial position and velocity to each particle. Then classical molecular dynamics simulate the evolution of a many-body system by integrating the laws of classical mechanics. An initial equilibration step is always required in order to allow the system to reach a steady state, in which the average of the properties of interest does not suffer any variation with time. At this point, equilibrium is reached, and it is possible to start recording those properties. As it is the case in real experiments, "measurements" in MD simulations are subject to statistical noise and to obtain accurate results it is necessary to take averages over a long period of time [146].

In this work we perform MD simulations using the GROMACS package [147]. This open source software was developed at the University of Groningen and is one the fastest and most popular MD codes currently available. It was originally designed for the simulation of large systems such as proteins, lipids or nucleic acids, but it is perfectly applicable to smaller molecules such us the ones studied here.

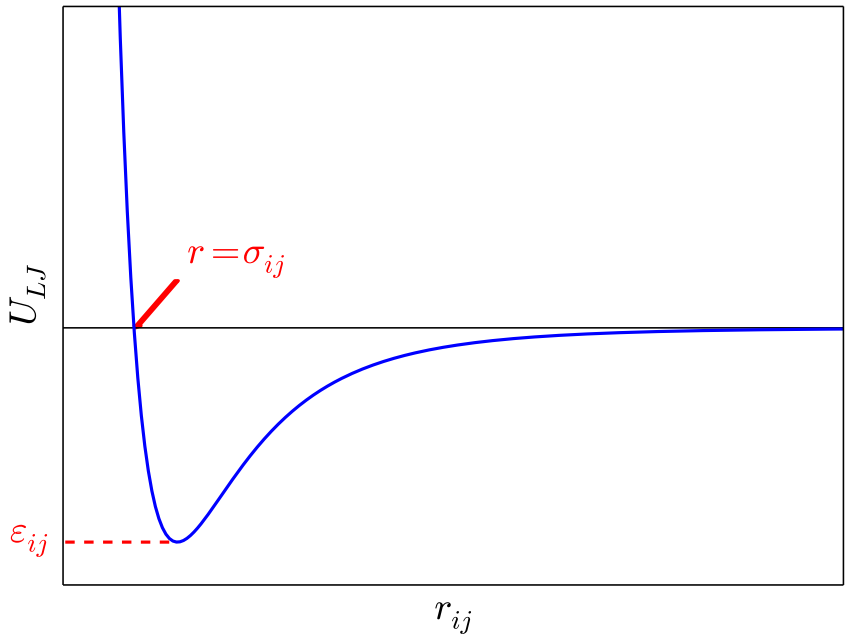

FIGURE 3.1: The Lennard-Jones potential.

3.3.2 Particle interactions in MD simulations

One of the most important aspects to consider in MD simulations is the short-range and long-range interactions between particles. The forces acting within the system are defined through parameterised sets of equations called force fields. Below we present the most common interactions considered in the definition of force fields for MD simulations.

Non-bonded interactions

Non-bonded interactions are defined as the interactions occurring between atoms which are not linked by covalent bonds. This includes dispersion and repulsion terms, coulombic electrostatic interactions, hydrogen bonds or salt bridges among others. One of the most common expressions to account for the potential energy U_{nb} associated to non-bonded interactions is the following:

$$U_{nb}(r_{ij}) = 4\epsilon_{ij}\left[\left(\frac{\sigma_{ij}}{r_{ij}}\right)^{12} - \left(\frac{\sigma_{ij}}{r_{ij}}\right)^{6}\right] + \frac{q_i q_j}{4\pi\epsilon_{vac} r_{ij}} \tag{3.51}$$

where r_{ij} is the distance between the atoms i and j, ϵ_{ij} is the depth of the potential well, and σ_{ij} is the distance at which the intermolecular potential is zero, as shown in Fig. 3.1.

The first term in Eq. (3.51) corresponds to the Lennard-Jones (LJ) potential which is a mathematical model describing the interaction between neutral atoms or

molecules [148]. The r_{ij}^{-12} term expresses the Pauli repulsion at short distances caused by overlapping of electron orbitals while the r_{ij}^{-6} term represents the long range attraction due to van der Waals or dispersion forces. The different pairs of particles constituting the system will tend to exert forces on each other to try to reach the distance corresponding to the energy well observed in Fig. 3.1. However, thermal energy caused by collisions between particles makes unlikely the total coexistence of particle pairs at their lowest potential energy level. Even though more sophisticated models exist, the computational simplicity of the Lennard-Jones potential makes it useful in a large number of cases. Every type of atom is assigned a value of σ and ϵ. For dissimilar atoms, the values of these parameters are obtained using the approximation given by combination rules, of which, one of the most common is the Lorentz-Berthelot formulas [149, 150]:

$$\sigma_{ij} = \frac{1}{2}(\sigma_i + \sigma_j) \tag{3.52}$$

$$\epsilon_{ij} = (\epsilon_i \epsilon_j)^{\frac{1}{2}}. \tag{3.53}$$

To further reduce the computational time of this method, in MD simulations the Lennard-Jones potential is often truncated and shifted at a cut-off distance r_c [151] so that:

$$U_{LJtrunc}(r) = \begin{cases} U_{LJ}(r) - U_{LJ}(r_c) & for \quad r \leq r_c \\ 0 & for \quad r > r_c \end{cases} \tag{3.54}$$

The second term in Eq. (3.51) represents the electrostatic interactions, where q_i and q_j are the charges of particles i and j, respectively. The Lennard-Jones potential describes a significant part of the interactions between particles but Coulomb's law is necessary to model the forces created between electrical charges. Coulomb stated in 1785 that "the force of attraction or repulsion between two point charges is directly proportional to the product of magnitude of each charge and indirectly proportional to the square of distance between them" [152], which corresponds to the potential shown in Eq. (3.51). The electrostatic force between charged particles is repulsive if their charges have the same sign while an attractive interaction will occur if the charges have opposite sign.

In general, interactions between atoms separated by less than three bonds in a molecule are not included as non-bonded interactions because they receive a specific treatment as we will show below. Interactions between atoms separated by exactly three bonds (also called 1–4 interactions) follow different rules that depend on the force field under consideration.

Bond stretching interactions

Different functions exist to describe the potential energy within a bond but the most common approximation is to represent the bond stretching potential U_b as a harmonic

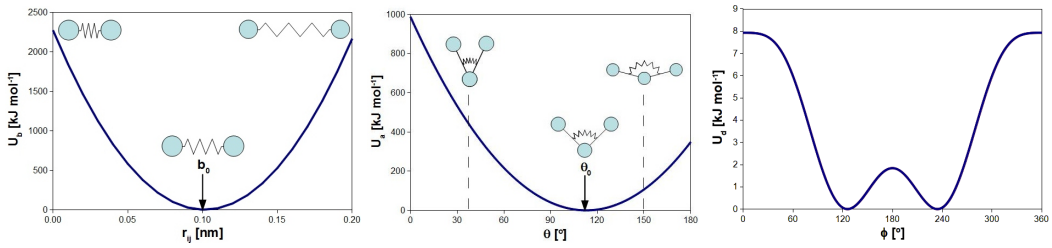

(a) Bond stretching (b) Angle bending (c) Dihedral torsion

FIGURE 3.2: Examples of bonded interactions

potential in an analogy to the behaviour of a system formed by a mass connected to a spring:

$$U_b(r_{ij}) = \frac{1}{2}k_b(r_{ij} - b_0)^2 \tag{3.55}$$

where k_b is the spring constant of the system and b_0 is the equilibrium bond length. The shape of this potential is shown in Fig. 3.2a in which the lowest energy corresponds to a situation in which the bond has reached its equilibrium length.

In many cases it is decided to constrain the bond length to a specific value. This is accomplished by applying an algorithm that ensures the distance between atoms stays at the desired value.

Angle bending interactions

In a similar manner to the bond stretching potential, angle bending in a molecule can be represented using a harmonic potential U_a:

$$U_a(\theta) = \frac{1}{2}k_\theta(\theta - \theta_0)^2 \tag{3.56}$$

where k_θ is the spring constant of the system and θ_0 is the equilibrium angle. This potential has a similar shape to the bond stretching potential as shown in Fig. 3.2b. Although it is a less common feature, in some cases it may be interesting to constrain the angle to a specific value (i.e. benzene).

Dihedral torsion interactions

The last of the bonded interactions usually considered is the one corresponding to the internal torsion of the molecule. The potential related to the dihedral angle between four consecutive atoms in a molecule U_d can be described by several expressions, of which, one of the most common is the Ryckaert-Bellemans function:

$$U_d(\phi_d) = \sum_{n=0}^{5} c_n \cos^n(\psi_d) \tag{3.57}$$

where $\psi_d = \phi_d - 180°$, with ϕ_d being the dihedral angle (zero-cis convention), and c_n the different constants defining the model.

As it can be seen in Fig. 3.2c, a more complex function is obtained in this case. Several low energy states are observed, corresponding to the most probable configurations of the molecule.

Long-range electrostatics

Long-range interactions are considered those which spatial interactions fall off slower than r^{-d}, where d is the dimensionality of the system. This is the case of charge-charge ionic interactions ($\sim r^{-1}$) and dipole-dipole molecular interactions ($\sim r^{-3}$). The range of action of these forces, which is larger than half the length of the typical molecular simulation boxes, represents a significant problem from the point of view of computer simulations. One of the options to solve this problem is to increase the size of the simulation box to reduce the effective range of the potentials using the screening effect of neighbours. However, this would require long simulation times proportional to N^2, where N is the number of molecules in the system [153]. Another option to avoid these expensive calculations is to use truncations as in non-bonded interactions. But this solution is not valid for Coulombic and dipolar interactions as it leads to high inaccuracies in the results. The most widely used method to deal with long-range electrostatic interactions is the Ewald summation [154] which simulation times are proportional to $N^{3/2}$, being still extremely expensive for large systems. To further reduce this computational effort, several approaches have been suggested such as the Particle-Particle Particle-Mesh PPPM method by Eastwood and Hockney [155] or the Particle-Mesh Ewald (PME) method proposed by Darden [156], which simulation times in both cases scale as $N \log N$ [146]. Lekner method [157] is a more accurate alternative but may also be expensive for large systems. In this work, it has been decided to use the PME method to account for the long-range electrostatics due to its balance between accuracy and efficiency and its availability in GROMACS MD simulation package.

3.4 Determination of Dielectric Spectra via Molecular Dynamics Simulations

In this section we present the method developed to predict the dielectric spectrum of a system using molecular dynamics simulations. The procedure is explained in more detail below but a summary is shown in Fig. 3.3.

3.4.1 The Dipole Moment Time Series

Trajectories obtained during molecular dynamics simulations can be used to track the evolution of the dipole moment of an entire simulation box or single molecules with time.

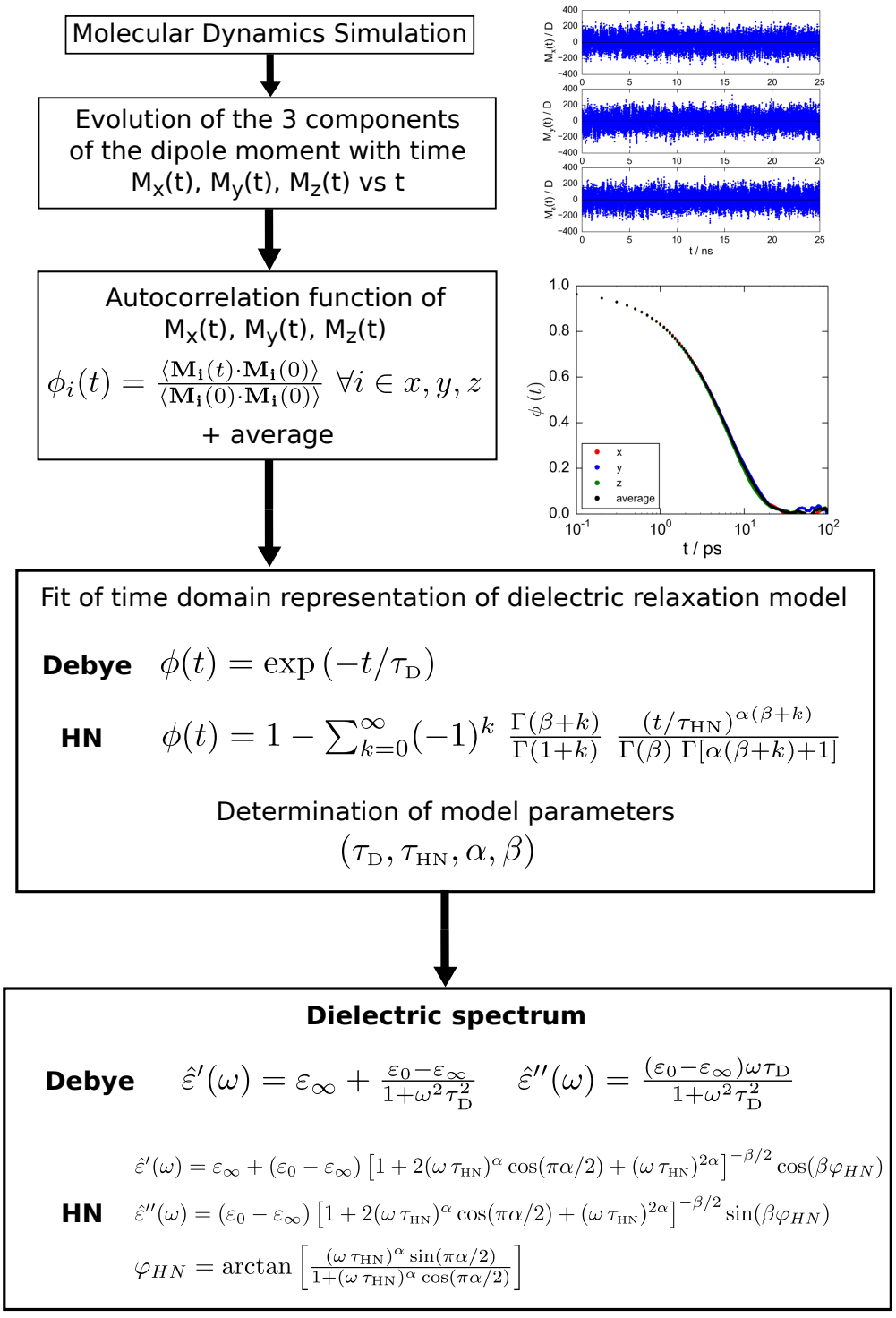

FIGURE 3.3: Determination of the frequency-dependent dielectric constant via molecular dynamics simulations.

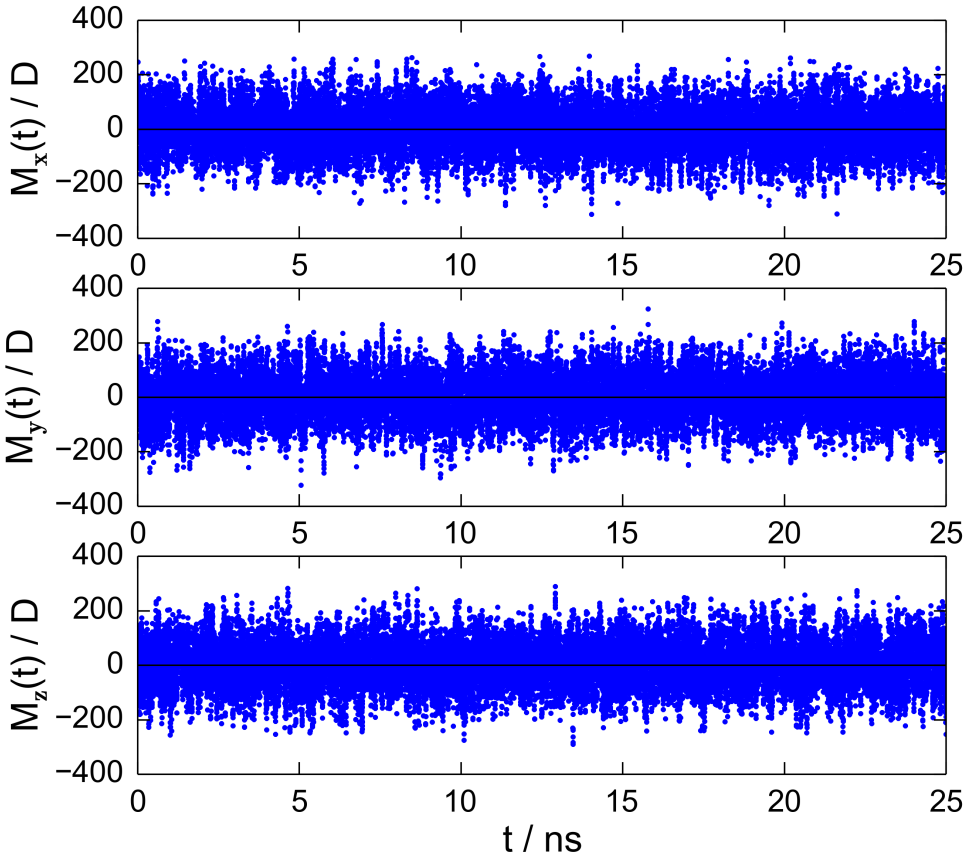

FIGURE 3.4: Time series of the three components of the dipole moment of SPC water [158] at 298 K and 1 bar.

The dipole moment vector of an entire system of N_{mol} molecules at a particular instant t is calculated as:

$$\mathbf{M}(t) = (M_x(t), M_y(t), M_z(t)) = \sum_{j}^{N_{mol}} \sum_{\alpha}^{N_{atom}} \left[\mathbf{r_{\alpha j}}(t) - \mathbf{r_{0j}}(t)\right] \; q_{\alpha j} \tag{3.58}$$

which three components are given by:

$$M_x(t) = \sum_{j}^{N_{mol}} \sum_{\alpha}^{N_{atom}} \left[x_{\alpha j}(t) - x_{0j}(t)\right] \; q_{\alpha j} \tag{3.59}$$

$$M_y(t) = \sum_{j}^{N_{mol}} \sum_{\alpha}^{N_{atom}} \left[y_{\alpha j}(t) - y_{0j}(t)\right] \; q_{\alpha j} \tag{3.60}$$

$$M_z(t) = \sum_{j}^{N_{mol}} \sum_{\alpha}^{N_{atom}} \left[z_{\alpha j}(t) - z_{0j}(t)\right] \; q_{\alpha j} \tag{3.61}$$

where N_{atom} is the number of atoms in molecule j, $q_{\alpha j}$ is the charge of atom α, $\mathbf{r}_{\alpha \mathbf{j}}(t)$ is the position vector of atom α with components $x_{\alpha j}(t)$, $y_{\alpha j}(t)$ and $z_{\alpha j}(t)$, and $\mathbf{r_{0j}}(t)$ is

the position of a reference atom in molecule j with coordinates $x_{0j}(t)$, $y_{0j}(t)$ and $z_{0j}(t)$.

If we want to analyse the average molecular dipole moment at every time step, then the three components are calculated as:

$$M_x(t) = \frac{1}{N_{mol}} \sum_{j}^{N_{mol}} \sum_{\alpha}^{N_{atom}} \left[x_{\alpha j}(t) - x_{0j}(t)\right] \; q_{\alpha j} \tag{3.62}$$

$$M_y(t) = \frac{1}{N_{mol}} \sum_{j}^{N_{mol}} \sum_{\alpha}^{N_{atom}} \left[y_{\alpha j}(t) - y_{0j}(t)\right] \; q_{\alpha j} \tag{3.63}$$

$$M_z(t) = \frac{1}{N_{mol}} \sum_{j}^{N_{mol}} \sum_{\alpha}^{N_{atom}} \left[z_{\alpha j}(t) - z_{0j}(t)\right] \; q_{\alpha j} \tag{3.64}$$

As an example, Fig. 3.4 shows the time series of the dipole moment of an entire equilibrated system of water molecules at 298 K using the SPC model [158]. As expected from a homogeneous system, the three components of the dipole moment fluctuate around an average value of zero, and have a similar magnitude. The dielectric properties of the system are closely related to the characteristics of these fluctuations. In this context, autocorrelation functions can be a powerful tool to identify patterns hidden in these signals.

3.4.2 Dipole Moment Autocorrelation Function

The cross-correlation of a signal with itself provides the resemblance between data points as the time interval between them increases. In our case the autocorrelation function of the dipole moment is given by:

$$\boldsymbol{\phi}(\tau) = \frac{\langle \mathbf{M}(\tau) \cdot \mathbf{M}(0) \rangle}{\langle \mathbf{M}(0) \cdot \mathbf{M}(0) \rangle} \tag{3.65}$$

which, for the three components of the dipole moment results in:

$$\phi_x(\tau) = \frac{\langle M_x(\tau) \cdot M_x(0) \rangle}{\langle M_x(0) \cdot M_x(0) \rangle} \tag{3.66}$$

$$\phi_y(\tau) = \frac{\langle M_y(\tau) \cdot M_y(0) \rangle}{\langle M_y(0) \cdot M_y(0) \rangle} \tag{3.67}$$

$$\phi_z(\tau) = \frac{\langle M_z(\tau) \cdot M_z(0) \rangle}{\langle M_z(0) \cdot M_z(0) \rangle} \tag{3.68}$$

where τ is the lag time between samples, and in this case $\langle \cdots \rangle$ represents an average over all available samples. Figure 3.5 shows the procedure followed to calculate an autocorrelation function. It is clearly seen how the number of samples decreases as the lag time increases, and as a consequence the quality of the data will be poorer at longer time intervals. When the lag time between samples is zero, the average will

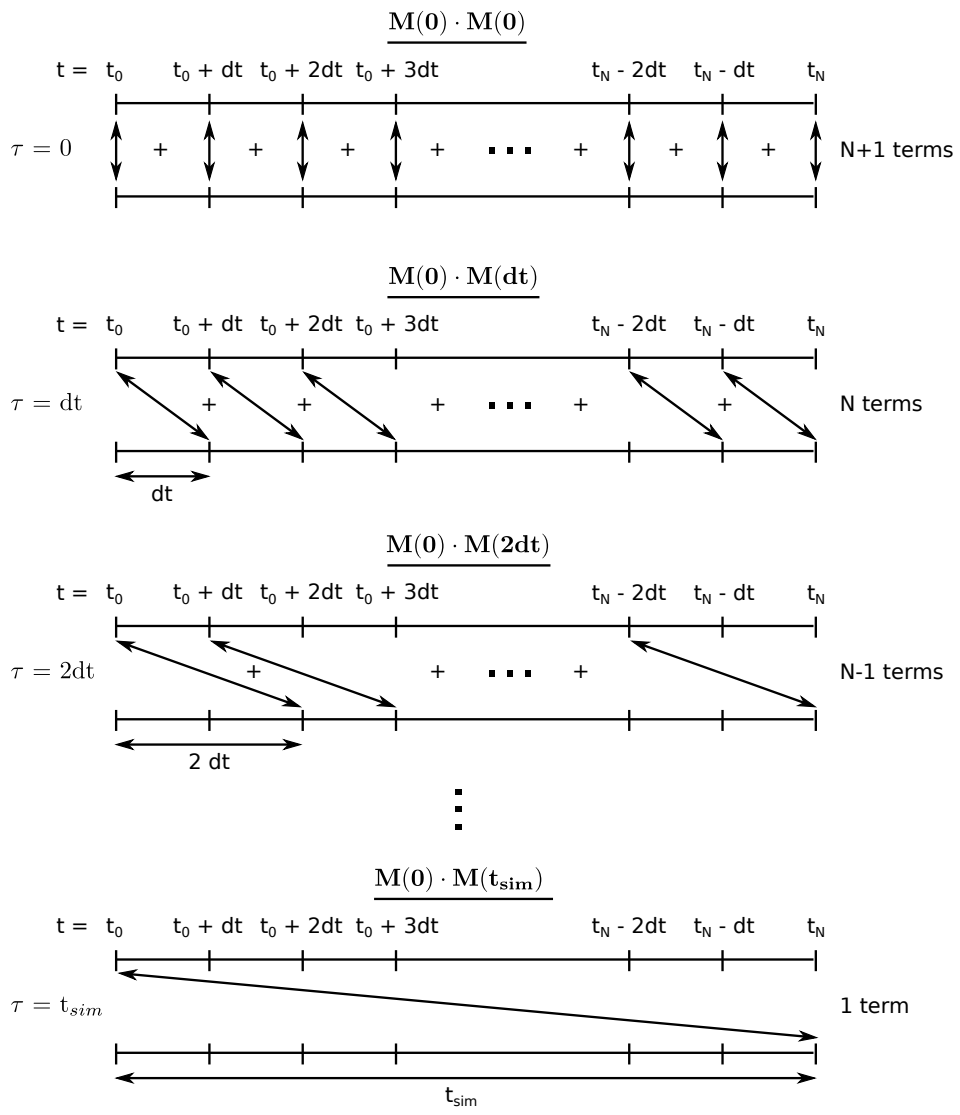

FIGURE 3.5: Procedure for the calculation of autocorrelation functions. N is the last element of the time frame counter, which starts at zero. Therefore, the data set contains $N + 1$ samples.

be performed over all possible samples, while when the time coincides with the total simulation time, only one term contributes to the average.

Once the three components of the dipole moment autocorrelation function have been obtained, and assuming we have an homogeneous system, we can perform an average between these three contributions. For heterogeneous systems, the three components would have a different behaviour, which would lead to a heterogeneous dielectric response. In general, at long correlation times, not enough data are available to obtain appropriate statistics and therefore the three contributions cannot be considered

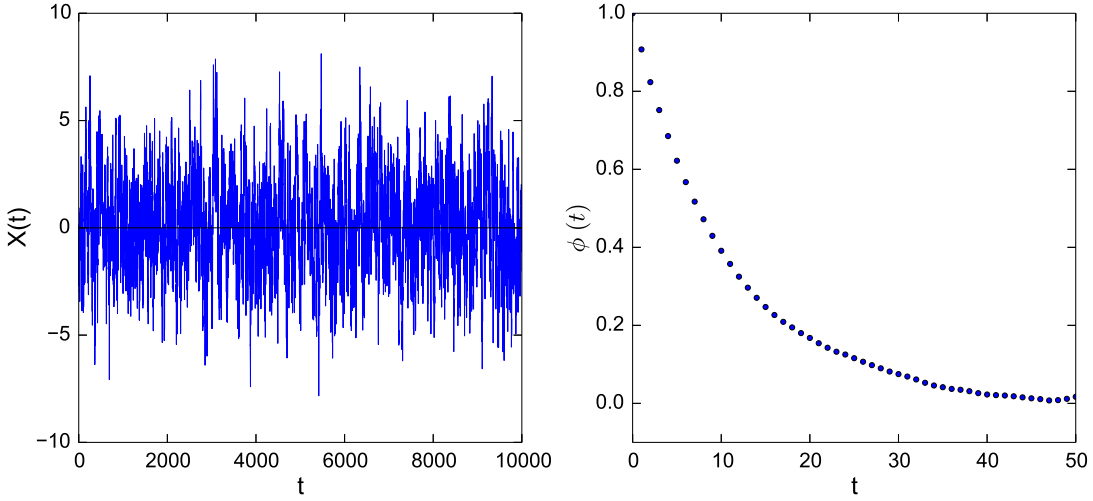

(a) Time series (b) Autocorrelation function

FIGURE 3.6: Sample of exponentially correlated data: (a) time series and (b) autocorrelation function.

identical. To take this fact into account, a normalised average is implemented:

$$\phi(\tau) = \frac{N}{N - N_\tau}\left[\frac{C_x(0)}{C_x(0)+C_y(0)+C_z(0)}\,\phi_x(\tau) + \frac{C_y(0)}{C_x(0)+C_y(0)+C_z(0)}\,\phi_y(\tau) + \frac{C_z(0)}{C_x(0)+C_y(0)+C_z(0)}\,\phi_z(\tau)\right] \tag{3.69}$$

where N is the total number of time frames, and N_τ is the frame number corresponding to τ, where $N_\tau = 0$ for $\tau = 0$ and $N_\tau = N - 1$ for $\tau = t_{sim}$.

In order to show the effect of data availability, we study the results obtained for randomly generated data. Following the procedure described by Gillespie [159], using the Ornstein-Uhlenbeck (OU) process, we generate exponentially correlated data perturbed with 'Gaussian white noise' $X(t)$ such as:

$$X(t + dt) = X(t) + X(t)(\bar{\mu} - 1) + \sigma_X\, n \tag{3.70}$$

where $\bar{\mu} = e^{-dt/\tau}$ is the expected value of the exponential decay with relaxation time τ, $\sigma_X = \left[1/2\; c\tau\left(1 - \bar{\mu}^2\right)\right]^{1/2}$ is the standard deviation of the signal, with c being the diffusion constant of the process, and n is a sample of the unit normal random distribution $\mathcal{N}(0, 1)$, with mean 0 and standard deviation 1. In Fig. 3.6 we show an example of exponentially correlated data, and its corresponding autocorrelation function. In analogy to the three components of the dipole moment, we generate three independent samples, and we obtain the average for three different values of τ. Since we are always using the same total number of data points, this means that we are studying systems that include data that accounts for different amounts of correlation lengths. An example of this is shown in Fig. 3.7.

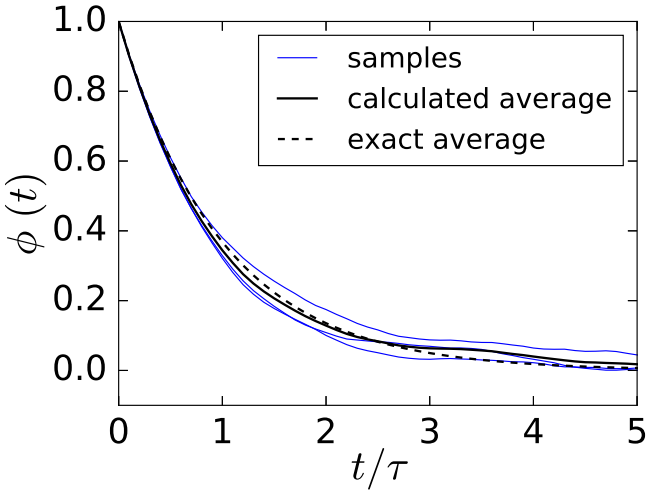

(a) $t_{sim}/\tau = 1000$

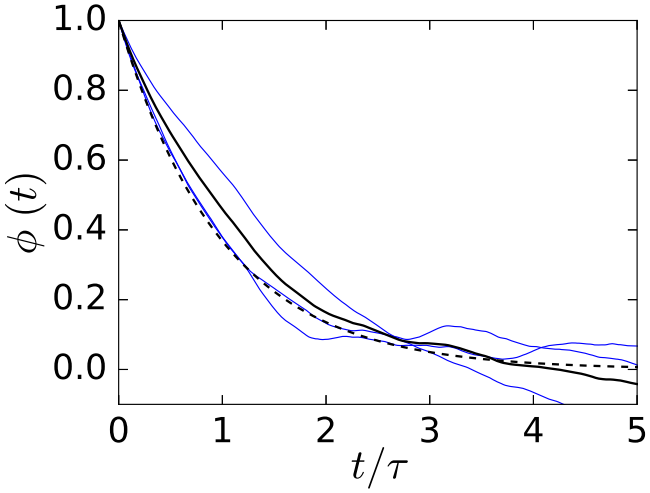

(b) $t_{sim}/\tau = 100$

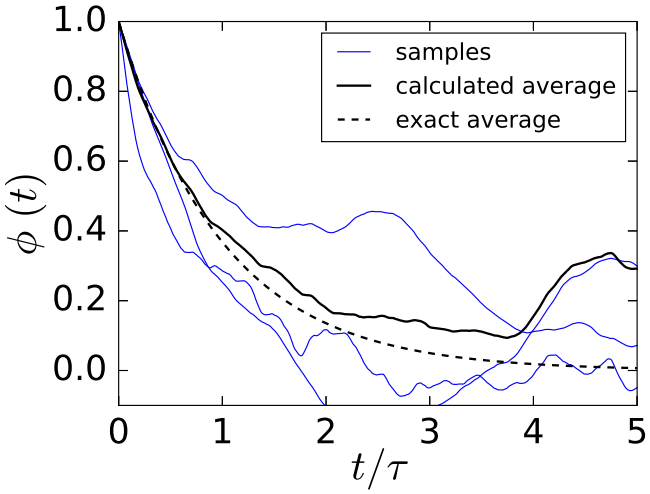

(c) $t_{sim}/\tau = 10$

FIGURE 3.7: Influence of data availability on the accuracy of average correlation functions of three samples of exponentially correlated data.

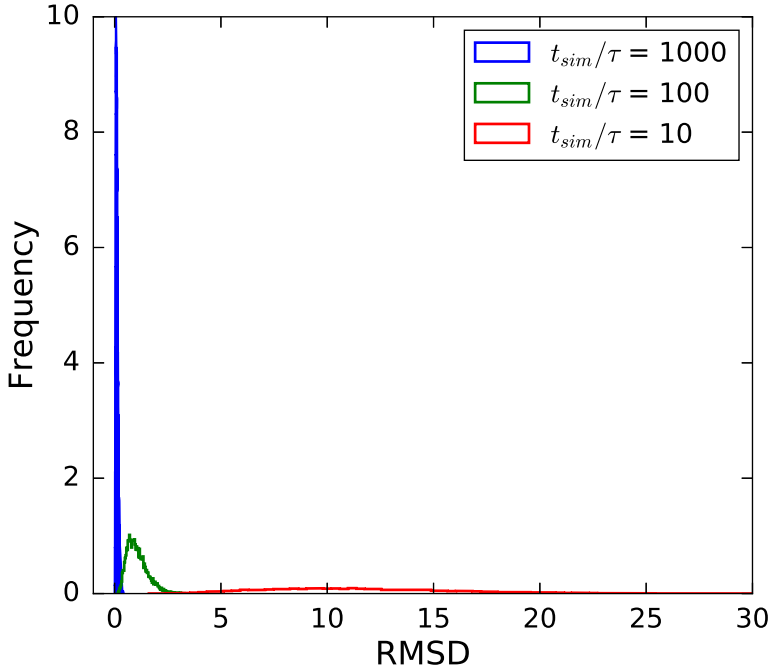

FIGURE 3.8: Histogram of the RMSD of average correlation functions with respect to the expected exponential decay for different availability of exponentially correlated data.

In order to evaluate the effect of the amount of correlation lengths covered by the available data on the final result, we repeat this procedure 10000 times and obtain the root mean square deviation (RMSD) with respect to the exact solution:

$$RMSD = \sqrt{\sum_{t=0}^{t_{sim}} [\phi_{ave}(t) - \phi_{exact}(t)]^2} \tag{3.71}$$

The average and standard deviation of the RMSD for different t_{sim}/τ is presented in Table 3.1, while a histogram of the RMSD is shown in Fig. 3.8. In general, we observe how the larger t_{sim}/τ, and so the more correlation lengths covered by the available data, the smaller the RMSD and then the closer is the average to the exact solution. This confirms the results obtained for a single repetition (Fig. 3.7). We observe that when we have data that covers 1000 correlation lengths there is no significant difference with the exact solution. However, as the number of correlation lengths covered by the available data decreases, the deviations tend to become important. An example of the application of this procedure to dipole moment autocorrelation functions is shown in Fig. 3.9, in which we anticipate some results for water and glycerol systems. A more detailed discussion will follow in subsequent chapters, but at this point we observe how for systems with shorter correlation times, such as water, the three components of the autocorrelation function differ less than for the ones with longer relaxation times, such as glycerol. This is because in the case of glycerol, the simulation time is insufficient to cover an acceptable number of correlation lengths as we will show in Chapter 4.

TABLE 3.1: Average and standard deviation of the root mean square deviation of the average of three samples of exponentially correlated noise with respect to the expected exponential decay for different availability of uncorrelated data.

t_{sim}/τ	RMSD
1000	0.1057 ± 0.0005
100	1.064 ± 0.005
10	11.82 ± 0.05

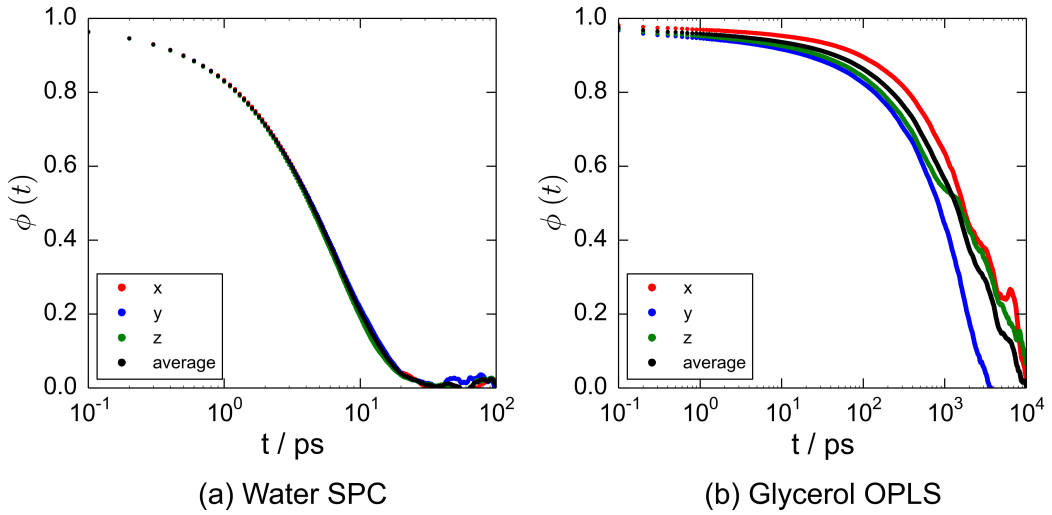

FIGURE 3.9: Three components and average autocorrelation functions for: (a) water SPC [158] and (b) glycerol OPLS [160, 161].

3.4.3 Models for dielectric relaxation

The relationship between dipole moment fluctuations and dielectric constant expressed through Eq. (3.50) has been explained from a theoretical point of view for idealised systems by means of the Debye model. Based on this model, several empirical models have been developed to account for deviations observed in more complex systems. These models are particularly useful for the characterisation of dielectric spectra, as they facilitate the study of the evolution of this property with variables such as composition and temperature.

The Debye model

According to the Debye model [162], the different dipoles forming the dielectric medium interact with each other only through random collisions, captured through a relaxation time. The resulting complex dielectric permittivity is given by:

$$\frac{\hat{\varepsilon}(\omega) - \varepsilon_\infty}{\varepsilon_0 - \varepsilon_\infty} = \frac{1}{1 - i\,\omega\tau_D} \tag{3.72}$$

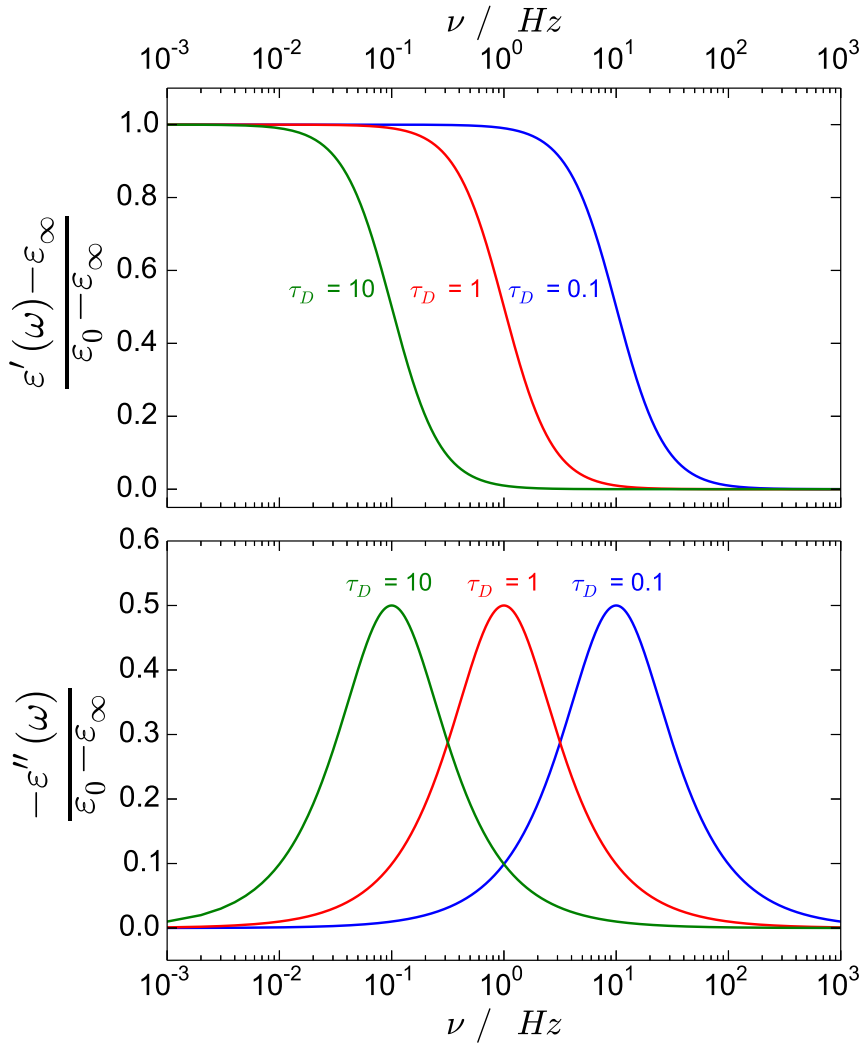

FIGURE 3.10: Effect of τ_D on the dielectric spectrum according to the Debye model.

where τ_D is the dielectric relaxation time.

The real and imaginary part of the dielectric permittivity, as derived from Eq. (3.72), result in:

$$\begin{aligned} \frac{\hat{\varepsilon}'(\omega)-\varepsilon_\infty}{\varepsilon_0-\varepsilon_\infty} &= \frac{1}{1+\omega^2\tau_D^2} \\ \frac{\hat{\varepsilon}''(\omega)}{\varepsilon_0-\varepsilon_\infty} &= \frac{\omega\tau_D}{1+\omega^2\tau_D^2} \end{aligned} \tag{3.73}$$

Figure 3.10 shows the effect of the relaxation time τ_D on the characteristics of the dielectric spectrum. For larger relaxation times, the decay in real permittivity and the dominant peak in dielectric loss are shifted to lower frequencies.

The Debye model is generally valid for gases and liquids formed by small molecules, but it tends to fail for more sophisticated systems.

The Havriliak-Negami model

In order to capture the behaviour of more complex systems, such as polymers, it is typically necessary to introduce modifications to the Debye model. To this effect, the Cole-Cole model [163] considers the broadness of the signal, while the Cole-Davidson [164] model accounts for its asymmetry. Later, Havriliak and Negami [165] decided to combine both contributions in a single model. The following expressions represent the application of the previous models to dielectric relaxation processes:

$$\begin{aligned} \text{Cole-Cole (CC) model} \qquad & \frac{\hat{\varepsilon}(\omega)-\varepsilon_\infty}{\varepsilon_0-\varepsilon_\infty} = \frac{1}{1+(-i\omega\tau_{\text{CC}})^{\alpha}} \\ \text{Cole-Davidson (CD) model} \qquad & \frac{\hat{\varepsilon}(\omega)-\varepsilon_\infty}{\varepsilon_0-\varepsilon_\infty} = \frac{1}{[1+(-i\omega\tau_{\text{CD}})]^{\beta}} \\ \text{Havriliak-Negami (HN) model} \qquad & \frac{\hat{\varepsilon}(\omega)-\varepsilon_\infty}{\varepsilon_0-\varepsilon_\infty} = \frac{1}{[1+(-i\omega\tau_{\text{HN}})^{\alpha}]^{\beta}} \end{aligned} \tag{3.74}$$

where τ_{CC}, τ_{CD} and τ_{HN} are the relaxation times characterising the different models, and α and β are parameters related to the broadness and the asymmetry of the signal, respectively.

It is evident that the Havriliak-Negami model reduces to the Cole-Cole model when β = 1, and to the Cole-Davidson model when α = 1. Furthermore when both α = 1 and β = 1, the HN model is equivalent to the Debye model.

In the case of the general Havriliak-Negami model, the real and imaginary parts of the dielectric permittivity are given by:

$$\begin{aligned} \frac{\hat{\varepsilon}'(\omega)-\varepsilon_\infty}{\varepsilon_0-\varepsilon_\infty} &= \left[1-2(\omega\,\tau_{\text{HN}})^{\alpha}\cos\left(\frac{\pi\alpha}{2}\right)+(\omega\,\tau_{\text{HN}})^{2\alpha}\right]^{-\beta/2}\cos(-\beta\varphi_{HN}) \\ \frac{\hat{\varepsilon}''(\omega)}{\varepsilon_0-\varepsilon_\infty} &= \left[1-2(\omega\,\tau_{\text{HN}})^{\alpha}\cos\left(\frac{\pi\alpha}{2}\right)+(\omega\,\tau_{\text{HN}})^{2\alpha}\right]^{-\beta/2}\sin(-\beta\varphi_{HN}) \end{aligned} \tag{3.75}$$

with:

$$\varphi_{HN} = \arctan\left[-\frac{(\omega\,\tau_{\text{HN}})^{\alpha}\sin(\pi\alpha/2)}{1-(\omega\,\tau_{\text{HN}})^{\alpha}\cos(\pi\alpha/2)}\right] \tag{3.76}$$

Figure 3.11 shows the effect of α and β on the shape of the dielectric spectrum for τ_{HN} = 1. If β = 1 (i.e. Cole-Cole model), the deviation from the ideal behaviour predicted by the Debye model (α = 1) results in a symmetric broadening in the distribution of relaxation times. In the case in which α = 1 (i.e. Cole-Davidson model), the deviation from the Debye model (β = 1) is observed as an asymmetry of the distribution of relaxation times towards the high frequency end of the spectrum. The combination of the previous effects allows the HN model to fit relatively complex features in dielectric spectra.

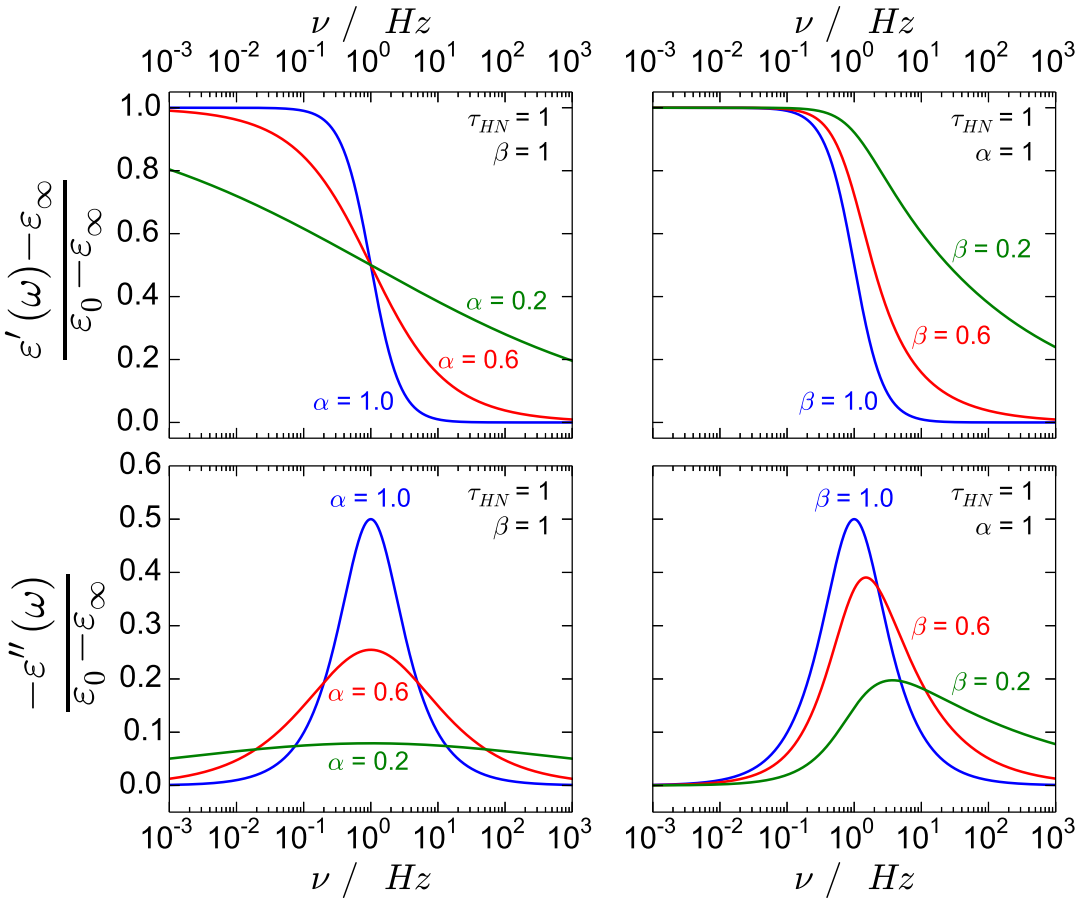

FIGURE 3.11: Effect of α and β on the shape of the dielectric spectrum according to the Havriliak-Negami model.

3.4.4 Determination of Dielectric Spectrum

To determine the frequency-dependent dielectric constant $\hat{\varepsilon}(\omega)$ from Eq. (3.50), it is necessary to obtain the Fourier transform of the dipole moment autocorrelation function $\phi(t)$. However, this becomes straightforward if we make use of the predefined models for dielectric relaxation presented in section 3.4.3. By deriving the time domain representation of these models, we can fit their characteristic parameters to reproduce dipole moment time autocorrelation functions obtained from MD simulations. Then it is simple to obtain the frequency-dependence of the dielectric constant from the frequency domain representation of the models. The fitting procedure aims to reduce the sum of squares of the difference between simulation data and model predictions, and is performed using the NLopt C++ library, particularly the BOBYQA algorithm developed by M.J.D. Powell [166] which is based on derivative-free bound-constrained optimisation using a quadratic approximation of the objective function built through iteration. This procedure has the disadvantage that it assumes the number of relaxation processes is known a priori. In principle, an infinite number of processes can be

superposed using this methodology. Nevertheless, it is important to consider that the fitting procedure becomes significantly tedious when we increase the number of relaxation processes, due to the large number of parameters employed in the fit. However, the systems we consider in this study are generally characterised by a single dominant relaxation process, and in any case, no more than three processes are required to obtain a good fit.

We present below the expressions of the dipole moment autocorrelation function as given by the Debye and the Havriliak-Negami models in the time domain, including the extension to multiple relaxation processes. More details on the derivation of these equations can be found in Appendix A.

Single Debye relaxation As defined in section 3.4.3, the single debye relaxation in the frequency domain is given by the expression:

$$\frac{\hat{\varepsilon}(\omega) - \varepsilon_\infty}{\varepsilon_0 - \varepsilon_\infty} = \frac{1}{1 - i\,\omega\tau_{\mathrm{D}}} \tag{3.72}$$

with real and imaginary parts:

$$\begin{aligned} \hat{\varepsilon}'(\omega) &= \varepsilon_\infty + \frac{\varepsilon_0 - \varepsilon_\infty}{1 + \omega^2\tau_{\mathrm{D}}^2} \\ \hat{\varepsilon}''(\omega) &= \frac{(\varepsilon_0 - \varepsilon_\infty)\,\omega\tau_{\mathrm{D}}}{1 + \omega^2\tau_{\mathrm{D}}^2} \end{aligned} \tag{3.77}$$

As shown in Appendix A, the resulting time representation of the Debye model is expressed as:

$$\phi(t) = \exp\left(-\frac{t}{\tau_{\mathrm{D}}}\right) \tag{3.78}$$

Multiple Debye relaxation The extension of the Debye model to multiple relaxation processes is given by the following expression in the frequency domain:

$$\frac{\hat{\varepsilon}(\omega) - \varepsilon_\infty}{\varepsilon_0 - \varepsilon_\infty} = \sum_{j=1}^{n} \frac{A_j}{1 - i\omega\tau_{\mathrm{D}j}} \tag{3.79}$$

with real and imaginary parts:

$$\begin{aligned} \varepsilon'(\omega) &= \varepsilon_\infty + (\varepsilon_0 - \varepsilon_\infty) \sum_{j=1}^{n} \frac{A_j}{1 + \omega^2\,\tau_{\mathrm{D}j}^2} \\ \varepsilon''(\omega) &= (\varepsilon_0 - \varepsilon_\infty) \sum_{j=1}^{n} \frac{A_j\,\omega\,\tau_{\mathrm{D}j}}{1 + \omega^2\,\tau_{\mathrm{D}j}^2} \end{aligned} \tag{3.80}$$

In this case, the time domain representation of Eq. (3.79) is given by:

$$\phi(t) = \sum_{j=1}^{n} A_j \exp\left(-\frac{t}{\tau_{\mathrm{D}j}}\right) \qquad \text{with: } \sum_{j=1}^{n} A_j = 1\,;\; A_j > 0\;\forall j \tag{3.81}$$

Single HN relaxation For a single relaxation, the form of the model in the frequency-domain is the following (see section 3.4.3):

$$\frac{\hat{\varepsilon}(\omega) - \varepsilon_\infty}{\varepsilon_0 - \varepsilon_\infty} = \frac{1}{\left[1 + (-i\omega\tau_{\mathrm{HN}})^{\alpha}\right]^{\beta}} \tag{3.74}$$

which real and imaginary parts are given by:

$$\begin{aligned}
\hat{\varepsilon}'(\omega) &= \varepsilon_\infty + (\varepsilon_0 - \varepsilon_\infty)\left[1 - 2(\omega\,\tau_{\mathrm{HN}})^{\alpha}\cos\left(\frac{\pi\alpha}{2}\right) + (\omega\,\tau_{\mathrm{HN}})^{2\alpha}\right]^{-\beta/2}\cos(-\beta\varphi_{HN}) \\
\hat{\varepsilon}''(\omega) &= (\varepsilon_0 - \varepsilon_\infty)\left[1 - 2(\omega\,\tau_{\mathrm{HN}})^{\alpha}\cos\left(\frac{\pi\alpha}{2}\right) + (\omega\,\tau_{\mathrm{HN}})^{2\alpha}\right]^{-\beta/2}\sin(-\beta\varphi_{HN})
\end{aligned} \tag{3.82}$$

with:

$$\varphi_{HN} = \arctan\left[-\frac{(\omega\,\tau_{\mathrm{HN}})^{\alpha}\sin(\pi\alpha/2)}{1 - (\omega\,\tau_{\mathrm{HN}})^{\alpha}\cos(\pi\alpha/2)}\right] \tag{3.83}$$

In Appendix A, we show how the time representation of the HN model is given by:

$$\phi(t) = 1 - \sum_{k=0}^{\infty}(-1)^k\,\frac{\Gamma(\beta+k)}{\Gamma(1+k)}\,\frac{(t/\tau_{\mathrm{HN}})^{\alpha(\beta+k)}}{\Gamma(\beta)\,\Gamma\left[\alpha(\beta+k)+1\right]} \tag{3.84}$$

Multiple HN relaxation The form of the HN model when extended to multiple relaxation processes in the frequency domain is the following:

$$\frac{\hat{\varepsilon}(\omega) - \varepsilon_\infty}{\varepsilon_0 - \varepsilon_\infty} = \sum_{j=1}^{n} \frac{A_j}{\left[1 + (-i\omega\tau_{\mathrm{HN}j})^{\alpha_j}\right]^{\beta_j}} \tag{3.85}$$

which, real and imaginary parts are given by:

$$\begin{aligned}
\varepsilon'(\omega) &= \varepsilon_\infty + (\varepsilon_0 - \varepsilon_\infty)\sum_{j=1}^{n} A_j\big[1 + 2(\omega\,\tau_{\mathrm{HN}j})^{\alpha_j}\cos\left(\frac{\pi\alpha_j}{2}\right) \\
&\quad + (\omega\,\tau_{\mathrm{HN}j})^{2\alpha_j}\big]^{-\beta_j/2}\cos(\beta_j\varphi_{HN\,j}) \\
\varepsilon''(\omega) &= (\varepsilon_0 - \varepsilon_\infty)\sum_{j=1}^{n} A_j\big[1 + 2(\omega\,\tau_{\mathrm{HN}j})^{\alpha_j}\cos\left(\frac{\pi\alpha}{2}\right) \\
&\quad + (\omega\,\tau_{\mathrm{HN}j})^{2\alpha_j}\big]^{-\beta_j/2}\sin(\beta_j\varphi_{HN\,j})
\end{aligned} \tag{3.86}$$

with:

$$\varphi_{HN\,j} = \arctan\left[\frac{(\omega\,\tau_{\mathrm{HN}j})^{\alpha_j}\sin(\pi\alpha_j/2)}{1 + (\omega\,\tau_{\mathrm{HN}j})^{\alpha_j}\cos(\pi\alpha_j/2)}\right] \tag{3.87}$$

From this expression, it can be shown that the equivalent time domain equation is given by:

$$\phi(t) = 1 - \sum_{j=1}^{n} A_j \left[\sum_{k=0}^{\infty} (-1)^k \frac{\Gamma(\beta_j + k)}{\Gamma(1+k)} \frac{(t/\tau_{\mathrm{HN\,j}})^{\alpha_j(\beta_j+k)}}{\Gamma(\beta_j)\,\Gamma\left[\alpha_j(\beta_j+k)+1\right]} \right] \tag{3.88}$$

1 HN + 1 Debye relaxation The combination of Havriliak-Negami and Debye relaxations can be useful in cases in which multiple processes are required, and the use of multiple HN relaxations becomes computationally expensive. The expression corresponding to a 1 HN + 1 Debye model is given by:

$$\frac{\hat{\varepsilon}(\omega) - \varepsilon_\infty}{\varepsilon_0 - \varepsilon_\infty} = \frac{A_1}{\left[1 + (-i\omega\tau_1)^\alpha\right]^\beta} + \frac{A_2}{1 - i\,\omega\tau_2} \tag{3.89}$$

which real and imaginary parts are given by:

$$\begin{aligned}
\hat{\varepsilon}'(\omega) &= \varepsilon_\infty + (\varepsilon_0 - \varepsilon_\infty) \left\{ A_1 \left[1 - 2(\omega\,\tau_1)^\alpha \cos\left(\frac{\pi\alpha}{2}\right) + (\omega\,\tau_1)^{2\alpha} \right]^{-\beta/2} \cos(-\beta\varphi_{HN}) \right. \\
&\quad \left. + \frac{A_2}{1 + \omega^2\,\tau_2^2} \right\} \\
\hat{\varepsilon}''(\omega) &= (\varepsilon_0 - \varepsilon_\infty) \left\{ A_1 \left[1 - 2(\omega\,\tau_1)^\alpha \cos\left(\frac{\pi\alpha}{2}\right) + (\omega\,\tau_1)^{2\alpha} \right]^{-\beta/2} \sin(-\beta\varphi_{HN}) \right. \\
&\quad \left. + \frac{A_2\,\omega\,\tau_2}{1 + \omega^2\,\tau_2^2} \right\}
\end{aligned} \tag{3.90}$$

with:

$$\varphi_{HN} = \arctan\left[-\frac{(\omega\,\tau_1)^\alpha \sin(\pi\alpha/2)}{1 - (\omega\,\tau_1)^\alpha \cos(\pi\alpha/2)} \right] \tag{3.91}$$

The time representation of the 1 HN + 1 Debye model results in:

$$\phi(t) = 1 - A_1 \sum_{k=0}^{\infty} (-1)^k \frac{\Gamma(\beta+k)}{\Gamma(1+k)} \frac{(t/\tau_1)^{\alpha(\beta+k)}}{\Gamma(\beta)\,\Gamma\left[\alpha(\beta+k)+1\right]} - A_2 \left[1 - \exp\left(-\frac{t}{\tau_2}\right) \right] \tag{3.92}$$

1 HN + 2 Debye relaxation Adding a second Debye relaxation to the model, the frequency-dependent dielectric constant becomes:

$$\frac{\hat{\varepsilon}(\omega) - \varepsilon_\infty}{\varepsilon_0 - \varepsilon_\infty} = \frac{A_1}{\left[1 + (-i\omega\tau_1)^\alpha\right]^\beta} + \frac{A_2}{1 - i\,\omega\tau_2} + \frac{A_3}{1 - i\,\omega\tau_3} \tag{3.93}$$

which real and imaginary parts are given by:

$$\begin{aligned}\hat{\varepsilon}'(\omega) &= \varepsilon_\infty + (\varepsilon_0 - \varepsilon_\infty)\left\{A_1\left[1 - 2(\omega\,\tau_1)^\alpha \cos\left(\frac{\pi\alpha}{2}\right) + (\omega\,\tau_1)^{2\alpha}\right]^{-\beta/2}\cos(-\beta\varphi_{HN})\right. \\ &\left. + \frac{A_2}{1+\omega^2\,\tau_2^2} + \frac{A_3}{1+\omega^2\,\tau_3^2}\right\} \\ \hat{\varepsilon}''(\omega) &= (\varepsilon_0 - \varepsilon_\infty)\left\{A_1\left[1 - 2(\omega\,\tau_1)^\alpha \cos\left(\frac{\pi\alpha}{2}\right) + (\omega\,\tau_1)^{2\alpha}\right]^{-\beta/2}\sin(-\beta\varphi_{HN})\right. \\ &\left. + \frac{A_2\,\omega\,\tau_2}{1+\omega^2\,\tau_2^2} + \frac{A_3\,\omega\,\tau_3}{1+\omega^2\,\tau_3^2}\right\}\end{aligned} \tag{3.94}$$

with:

$$\varphi_{HN} = \arctan\left[-\frac{(\omega\,\tau_1)^\alpha \sin(\pi\alpha/2)}{1-(\omega\,\tau_1)^\alpha\cos(\pi\alpha/2)}\right] \tag{3.95}$$

And finally, the 1 HN + 2 Debye model in the time domain results in:

$$\begin{aligned}\phi(t) = 1 &- A_1\sum_{k=0}^{\infty}(-1)^k\,\frac{\Gamma(\beta+k)}{\Gamma(1+k)}\,\frac{(t/\tau_1)^{\alpha(\beta+k)}}{\Gamma(\beta)\,\Gamma\left[\alpha(\beta+k)+1\right]} \\ &- A_2\left[1-\exp\left(-\frac{t}{\tau_2}\right)\right] - A_3\left[1-\exp\left(-\frac{t}{\tau_3}\right)\right]\end{aligned} \tag{3.96}$$

3.4.5 Range of validity of our results

In our analysis of results, although we use simulation time steps of about 1 fs, we only sample the trajectory of the molecules every 100 fs due to data storage limitations. This means a sampling frequency of 10^{13} Hz. According to Nyquist-Shannon sampling theorem [167], in order to completely determine a phenomenon occurring at a frequency ν_0, the frequency of sampling must be at least $2\nu_0$. Therefore for the sampling frequency used in our simulations, we can only fully determine phenomena occurring at frequencies lower than 5×10^{12} Hz. In order to be on the safe side, in our results we will only consider frequencies below 10^{12} Hz, which are well into the microwave region of the electromagnetic spectrum.

In addition, as evidenced by Figs. 3.7 and 3.8, the number of correlation lengths that the available data can cover is an important factor to take into account. As a result, we decided to only consider as representative systems for which $t_{sim}/\tau \geq 100$ (i.e. if a simulation has a length of 100ns, only systems with relaxation times lower than 1 ns can be considered).

3.5 Conclusions

After describing the basic principles of dielectric heating at the macroscale in Chapter 2, in this chapter we study the theoretical foundation of this phenomenon at the molecular level. Within the framework of the fluctuation-dissipation theorem and linear response theory, we show how the response of a system to external perturbations, such as an electromagnetic field, is related to the internal equilibrium fluctuations of the system, provided the perturbation is weak. In the case of dielectric heating, this result can be applied to the determination of the complex and frequency-dependent dielectric permittivity of a material from the equilibrium fluctuations of its dipole moment. Using this relationship, we describe how molecular dynamics simulations are a useful tool to predict dielectric spectra. We develop a methodology to extract dipole moment fluctuations from molecular dynamics simulations, and obtain dielectric spectra by means of the dipole moment autocorrelation function and the use of previously developed models for dielectric response, in particular the Debye and the Havriliak-Negami models.

In the following chapters we apply this methodology for the determination of dielectric spectra of one component systems (Chapter 4) and mixtures (Chapter 5). Additionally, we examine the influence of temperature on the dielectric spectra of these systems (Chapter 6).

Chapter 4

Dielectric Spectra of One Component Systems

This chapter has been published in *Molecular Simulation*, 42, 5 (2016), 370–390 (see Appendix B)
Authors: J. Cardona, R. Fartaria, M. Sweatman, L. Lue

The response of molecular systems to electromagnetic radiation in the microwave region (0.3–300 GHz) has been principally studied experimentally, using broadband dielectric spectroscopy. However, relaxation times corresponding to reorganisation of molecular dipoles due to their interaction with electromagnetic radiation at microwave frequencies are within the scope of modern molecular simulations. In previous chapters, we discussed the importance of microwave heating processes and dielectric spectroscopy; and we introduced a method to predict dielectric spectra from fluctuations of the dipole moment of molecular systems, obtained through molecular dynamics simulations. In this chapter, we apply this method to determine the dielectric spectra of water, a series of alcohols and glycols, and monoethanolamine. Although the force fields employed in this study have principally been developed to describe thermodynamic properties, most them give fairly good predictions of this dynamical property for these systems. However, the inaccuracy of some models and the long simulation times required for the accurate estimation of the static dielectric constant can sometimes be problematic. We show that the use of the experimental value for the static dielectric constant in the calculations, instead of the one predicted by the different models, yields satisfactory results for the dielectric spectra, and hence the heat absorbed from microwaves, avoiding the need for extraordinarily long simulations or re-calibration of molecular models.

4.1 Introduction

Despite the relatively large literature on microwave heating and dielectric spectroscopy, the vast majority of the work in this area has been experimental, while there is relatively little computational work. Nevertheless, Rick, Stuart, and Berne [168] and later English and MacElroy [169, 170] determined the dielectric spectrum of water via equilibrium molecular dynamics simulations using the relationship between dipole

moment fluctuations and the frequency-dependent dielectric constant initially developed by Neumann and Steinhauser [138, 139]. Non-equilibrium molecular dynamics simulations have also been performed in order to model the microwave heating of water [171–173], the kinetics of methane hydrate crystallization [174] and dissociation [175, 176], and the effects of an external electromagnetic field on the conductivity of molten sodium chloride [177], rutile TiO_2 [178], nanoconfined fluids [179] and binary dimethylimidazolium-based ionic liquid/water solutions [180–183]. Additionally, recent work has been carried out on dielectric spectroscopy of more complex systems such as protein solutions [184–186]. The paucity of simulation work can probably be explained by the fact that usual relaxation times corresponding to the reorganization of molecular dipoles due to their interaction with electromagnetic radiation at microwaves frequencies are on the order of nanoseconds, or even microseconds for larger molecules. This requires long, computationally expensive simulations in order to obtain statistically accurate results. Another cause for this scarcity in simulation work could be that most atomistic force fields for molecular simulations have been developed to reproduce thermodynamic rather than dynamic properties. Thus, it is unclear how reliably they will be able to reproduce the dynamic dielectric properties of a material.

In this chapter, we examine the ability of several different force fields to reproduce the dielectric spectra of relatively small molecules, such as water, alcohols, glycols and monoethanolamine (MEA). In order to do so, we perform equilibrium molecular dynamics simulations for these systems and apply the methodology developed in Chapter 3 to obtain their frequency-dependent complex permittivity. Ultimately, one of our aims is to apply the results of this work to the estimation of heating rates in microwave heating processes. Equations (2.80) and (3.50) indicate this requires good prediction of the dielectric spectra of the materials involved in the process, including the static dielectric constant.

The following section gives the details of the potential models used to describe the different molecules and explains the simulation methodology we have employed. The results of the simulations are presented and discussed in Sec. 4.3. We find that the force fields examined in this work show generally good predictions of dielectric spectra. The estimation of the static dielectric constant can sometimes be problematic though, due to the inaccuracy of some models and the long simulation times required. In this study, we obtain satisfactory results by employing the experimental value of this parameter in our calculations, instead of the one predicted by the models. This improves the prediction of dielectric spectra while significantly reducing the simulation times required, and hence, will result in more realistic estimations of the heat a dielectric material can absorb from microwaves. Finally, in Sec. 4.4, we summarize the main findings of the work and provide directions for future studies.

4.2 Molecular Dynamics Simulations

The molecular systems studied in this work include water, a series of alcohols and glycols (i.e. ethanol, ethylene glycol, propylene glycol, and glycerol), and monoethanolamine (MEA). In this section, we present the force fields used to describe these systems, and we give details of the main characteristics of the molecular dynamics simulations we perform.

4.2.1 Molecular models and interactions

Force fields For water, three rigid models (SPC [158], TIP4P [187], and SPC/E [188]) and two flexible models (F-SPC [189] and Fw-SPC [190]) are examined. For alcohols and glycols, three force fields are used: Transferable Potentials for Phase Equilibria - United Atom (TraPPE-UA) [191, 192], Optimized Potentials for Liquid Simulations (OPLS) [160, 161] and Generalized Amber Force Field (GAFF) [161, 193]. Finally, to model MEA we use the MEAa force field [194] along with the transferable OPLS and GAFF force fields. In the following, we summarize the main characteristics of the different force fields. The parameters used in our simulations are mainly taken from the original sources, and their values can be found in Appendix C.

Nonbonded interactions Nonbonded interactions between atoms are represented as the sum of a Lennard-Jones (LJ) 12-6 pair potential and an electrostatic interaction as defined previously in Eq. (3.51):

$$U_{nb}(r_{ij}) = 4\,\epsilon_{ij}\left[\left(\frac{\sigma_{ij}}{r_{ij}}\right)^{12} - \left(\frac{\sigma_{ij}}{r_{ij}}\right)^{6}\right] + \frac{q_i q_j}{4\pi\varepsilon_{vac} r_{ij}} \tag{3.51}$$

where r_{ij} is the distance between atoms i and j, ϵ_{ij} is the depth of the potential well, and σ_{ij} is the distance at which the LJ potential becomes zero. In the second term, q_i and q_j are the charges of atoms i and j, respectively.

Nonbonded interactions apply to all intermolecular interactions, but, for intramolecular interactions, they never apply to atoms separated by two or less bonds and always apply to the ones separated by four or more bonds. In the particular case of atoms separated by precisely 3 bonds (1-4 interactions), different models have different criteria, as discussed below.

The Lorentz-Berthelot combination rules are used in the TraPPE-UA, GAFF and MEAa force fields to calculate the interatomic parameters ϵ_{ij} and σ_{ij} from the atomic parameters ϵ_i and σ_i:

$$\begin{aligned} \sigma_{ij} &= \frac{1}{2}(\sigma_i + \sigma_j) \\ \epsilon_{ij} &= (\epsilon_i \epsilon_j)^{1/2}. \end{aligned} \tag{4.1}$$

Alternatively, the OPLS force field employs a geometric average:

$$\begin{aligned} \sigma_{ij} &= (\sigma_i \sigma_j)^{1/2} \\ \epsilon_{ij} &= (\epsilon_i \epsilon_j)^{1/2}. \end{aligned} \tag{4.2}$$

Bonded interactions Bond stretching interactions between atoms separated by one bond are modelled by means of a harmonic potential:

$$U_b(r_{ij}) = \frac{1}{2} k_b (r_{ij} - b_0)^2 \tag{4.3}$$

where k_b is the spring constant, and b_0 is the equilibrium bond length. This applies only to bonds in the F-SPC and Fw-PSC water models and the MEAa force field, because the remaining molecular models use rigid bonds with a fixed bond length b_0.

Similarly to the bond stretching potential, bending of the angle between two adjacent bonds can be represented using a harmonic potential:

$$U_a(\theta) = \frac{1}{2} k_\theta (\theta - \theta_0)^2 \tag{4.4}$$

where k_θ is the spring constant for bond angle bending, and θ_0 is the equilibrium bond angle.

The last of the bonded interactions considered in most models is the internal molecular torsion. In the force fields employed in this work, the potential related to the dihedral angle between four consecutive atoms in a molecule is described either by a Ryckaert-Bellemans or a Fourier function:

Ryckaert-Bellemans dihedral:

$$U_d(\phi) = \sum_{n=0}^{3} c_n \, \cos^n(\phi - 180^\circ) \tag{4.5}$$

Fourier dihedral:

$$U_d(\phi) = \frac{1}{2} \left\{ C_1 \left[1 + \cos(\phi)\right] + C_2 \left[1 - \cos(2\phi)\right] + C_3 \left[1 + \cos(3\phi)\right] \right\} \tag{4.6}$$

where ϕ is the dihedral angle (zero-cis convention), and c_n and C_n are the different constants defining the models.

Particularities of the molecular models We analyse the performance of five of the most common water models: the simple point charge (SPC) model [158], the TIP4P model [187], the SPC/E model [188], the Flexible SPC (F-SPC) model [189] and the Fw-SPC model [190] (see Fig. 4.1). More details on the models can be found in Appendix C. The rationale behind the selection of these particular water force fields was not that of performing an exhaustive study on the dielectric properties of water, which have already been analysed extensively. We rather want to compare our results with

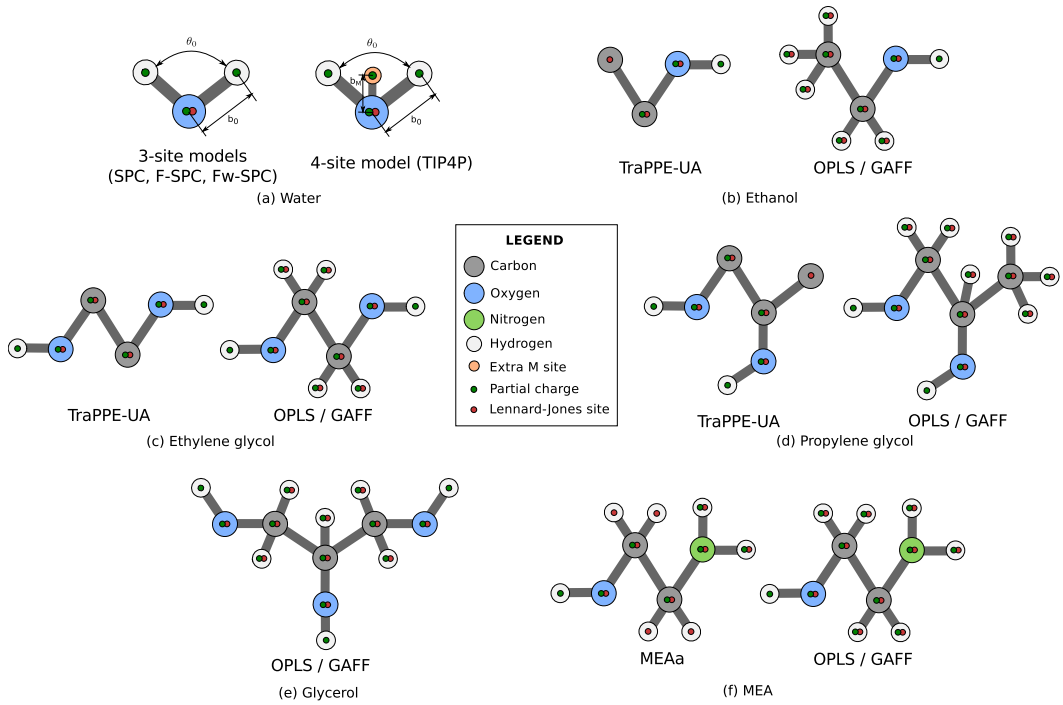

FIGURE 4.1: Molecular models used in this study. Carbon, Oxygen, Nitrogen and Hydrogen atoms are represented as grey, blue, green and white circles, respectively. The extra site in the TIP4P water model is shown as a light orange circle. Partial charges appear as dark green dots while Lennard-Jones interaction sites are represented as red dots.

previous simulation work [169, 170] in order to validate our methods and extend them to additional systems.

For the remaining molecules, more generalized force fields are used. The Transferable Potentials for Phase Equilibria (TraPPE) force field is parameterised to describe phase equilibria and structural properties of a wide range of compounds. Its United Atom version (TraPPE-UA) [191, 192], in which the atomic interactions of a group of atoms are condensed into a single pseudo-atom, is used to model ethanol, ethylene glycol and propylene glycol. While the first two molecules have been tested by the original authors, there is no evidence of previous work carried out with propylene glycol. Nevertheless, based on TraPPE parameters, we decided to build our own TraPPE-UA model for propylene glycol. Glycols require a repulsive potential of the form:

$$U_{rep}(r_{ij}) = \frac{a}{r_{ij}^{12}}, \tag{4.7}$$

between hydroxyl hydrogens and oxygens situated four bonds away, where $a = 6.2 \times 10^{-7}$ kJ mol^{-1} nm^{12} [192]. This is needed to avoid the hydrogen atom, not originally protected by a LJ potential, overlapping the oxygen atom which has an opposite charge and will tend to attract it. Both OPLS [160, 161] and GAFF [161, 193] force fields are all-atom models which consider alkyl hydrogens explicitly. In this work, they have

been used to model every studied compound (except water), although model parameters for ethylene and propylene glycols could not be found in the literature, and so their topologies are built based on similar molecules (ethanol and glycerol). Finally the MEAa [194] force field is again an all-atom model. It is mainly based on GAFF's MEA model but some corrections in the charge distribution, the bond flexibility and the O-C-C-N, C-C-O-H and C-C-N-H dihedrals were introduced by the authors. This was done in order to improve the prediction of intramolecular interactions, which are believed to have an important effect on the properties of MEA in the liquid phase.

The 1-4 nonbonded interactions are treated differently by the various force fields. The TraPPE-UA model generally excludes these interactions, but in the particular case of ethylene and propylene glycol, coulombic interactions between atoms separated by three bonds are included, although scaled by a factor of 0.5. OPLS, GAFF and MEAa force fields include both LJ and coulombic 1-4 interactions with different scaling factors. The OPLS model only considers half of the magnitude of these interactions. The same strategy is used by the GAFF force field regarding LJ interactions, however, coulombic interactions are scaled by a factor of 5/6 in this case. Finally MEAa fully considers all 1-4 nonbonded interactions.

Figure 4.1 shows the distribution of charges and LJ interaction sites for the models under consideration. As mentioned previously, the parameters defining the different molecular interactions used in our simulations can be found in Appendix C.

4.2.2 Simulation details

Molecular dynamics (MD) simulations are carried out using the GROMACS 4.6.3 [147] package to study the performance of the different force fields in the prediction of dielectric spectra. All systems consist of simulation boxes containing 1000 molecules and are simulated for 25 to 100 ns, depending on the time required to obtain a converged value for the static dielectric constant. Starting from independent and equilibrated configurations, four simulations are carried out for every molecular system. The results are analysed according to the procedure introduced in section 3.4, and averaged across those four samples to improve statistics. The equations of motion are integrated by means of the leap-frog algorithm [195] with a time step of 1 fs for rigid (SPC, TIP4P, and SPC/E) and semi-flexible models (TraPPE-UA, OPLS and GAFF), and 0.2 fs for flexible force fields (F-SPC, Fw-SPC and MEAa). The trajectory of the molecules is read every 100 fs while the energy configuration is recorded every 50 fs. The simulations are performed with the NPT ensemble at 298 K and 1 bar, except for MEA for which a temperature of 293 K is used, due to the larger availability of experimental data at that temperature. The Nosé-Hoover thermostat [196, 197], with a time constant of 0.1 ps, is used for temperature coupling while the pressure is controlled by means of a Parrinello-Rahman barostat [198, 199] with a compressibility of 4.5×10^{-5} bar^{-1} and a time constant of 1.0 ps. The LINCS algorithm [200] is responsible for constraining the bond length when necessary. A cut-off radius of 0.85 nm is used for the Lennard-Jones

interactions in all the systems, except when the TraPPE-UA or the MEAa force fields are used; for those models, the LJ interaction is truncated at $1.40\,\text{nm}$ and $1.00\,\text{nm}$, respectively. Long-range electrostatics are treated with the particle mesh Ewald (PME) method [156] with a truncation at the same distance as the LJ cut-off, and a spacing for the PME grid of $0.12\,\text{nm}$. Analytical tail corrections in potential energy are used to compensate for the truncation in LJ interactions. Finally, cubic and tin-foil periodic boundary conditions are used in every case, where the system and its periodic images are assumed to be immersed in a perfectly conducting medium (infinite dielectric constant) [201].

4.3 Results and Discussion

4.3.1 Thermodynamic properties

Table 4.1 summarizes several thermodynamic properties for the systems we study, as determined from molecular dynamics simulations [153, 161]:

$$\rho = \frac{M}{\langle V \rangle} \tag{4.8}$$

$$\alpha_P = \frac{\langle \delta V \delta H \rangle}{k_B T^2 \langle V \rangle} \tag{4.9}$$

$$\kappa_T = \frac{\langle \delta V^2 \rangle}{k_B T \langle V \rangle} \tag{4.10}$$

$$\Delta H_{vap} = E_{pot\ vap} + k_B T - E_{pot\ liq} \tag{4.11}$$

where ρ is the density of the fluid and M and V are the mass and volume of the system, respectively. The thermal expansion coefficient α_P is calculated from volume (δV) and enthalpy (δH) fluctuations, and $\langle V \rangle$ is the average volume across the entire simulation. The isothermal compressibility is obtained from fluctuations in the volume squared (δV^2). Finally, the heat of vaporization (ΔH_{vap}) is determined as the difference between potential energy of vapour ($E_{pot\ vap}$) and liquid ($E_{pot\ liq}$) phases, where $E_{pot\ vap}$ is obtained from a separate simulation of a single molecule in the same conditions as the liquid phase.

Although thermodynamic properties are not the main focus of this work, we provide these results as a benchmark for the validity of our simulations. The standard errors for the different properties are obtained by averaging across the values obtained for each of the four independent simulations for every system. Most of the force fields used in this study are developed for the prediction of thermodynamic properties. Therefore, as expected, the results are generally in good agreement with experimental data. They are also consistent with previous simulation work by Caleman and coworkers [161], where the overprediction of the heat capacities is also observed and thought to be due to the neglect of quantum corrections in the calculation of enthalpy fluctuations.

TABLE 4.1: Summary of thermodynamic properties (density ρ, thermal expansion coefficient α_P, isothermal compressibility κ_T, constant pressure heat capacity c_P, heat of vaporization ΔH_{vap}). Simulations are run at 298 K and 1 bar, except for the case of MEA for which the temperature is 293 K

	ρ (kg/m^3)	10^3 α_P (K^{-1})	κ_T (GPa^{-1})	c_P (J mol^{-1} K^{-1})	ΔH_{vap} (kJ mol^{-1})
Water					
SPC	978.93 ± 0.02	0.733 ± 0.002	0.529 ± 0.002	83.6 ± 0.1	44.168 ± 0.001
TIP4P	998.88 ± 0.04	0.552 ± 0.003	0.512 ± 0.001	87.9 ± 0.1	43.920 ± 0.001
SPC/E	1000.14 ± 0.03	0.506 ± 0.004	0.459 ± 0.001	87.1 ± 0.2	49.239 ± 0.001
F-SPC	995.01 ± 0.02	0.528 ± 0.006	0.457 ± 0.001	112.0 ± 0.2	51.710 ± 0.001
Fw-SPC	1009.70 ± 0.04	0.459 ± 0.006	0.431 ± 0.002	114.1 ± 0.4	46.252 ± 0.002
Experiment	997.1 [202]	0.256 [203]	0.4525 [204]	75.29 [205]	43.87 [206]
Ethanol					
TraPPE-UA	782.4 ± 0.2	1.149 ± 0.006	1.263 ± 0.006	114.4 ± 0.4	46.891 ± 0.004
OPLS	793.21 ± 0.06	1.419 ± 0.004	1.002 ± 0.005	219.0 ± 0.4	45.455 ± 0.003
GAFF	794.16 ± 0.05	1.272 ± 0.005	0.976 ± 0.007	211.7 ± 0.4	47.514 ± 0.003
Experiment	784.8 [207]	1.09 [207]	1.15 [207]	112 [207]	42.32 [207]
Ethylene glycol					
TraPPE-UA	1129.78 ± 0.05	0.62 ± 0.02	0.411 ± 0.002	199 ± 3	80.862 ± 0.007
OPLS	1075.77 ± 0.05	0.80 ± 0.02	0.386 ± 0.003	261 ± 2	69.664 ± 0.005
GAFF	1176.52 ± 0.07	0.709 ± 0.008	0.241 ± 0.002	263.8 ± 0.3	83.911 ± 0.008
Experiment	1113.1 [208]	0.631 [209]	0.3686 [210] [a]	148.3425 ± 1.48467 [211]	65.99 ± 0.25 [212]
Propylene glycol					
TraPPE-UA	1042.0 ± 0.2	0.70 ± 0.02	0.591 ± 0.003	238 ± 5	78.85 ± 0.03
OPLS	1097.5 ± 0.2	0.98 ± 0.04	0.390 ± 0.007	334 ± 4	84.69 ± 0.02
GAFF	1120.06 ± 0.04	0.92 ± 0.03	0.307 ± 0.005	344 ± 4	82.318 ± 0.009
Experiment	1032.79 [213]	0.714 [214] [b]	—	190.54 ± 3.81 [215]	64.47 ± 0.18 [212]
Glycerol					
OPLS	1251.7 ± 0.2	0.80 ± 0.02	0.273 ± 0.004	361 ± 4	97.57 ± 0.03
GAFF	1302.9 ± 0.4	0.49 ± 0.02	0.166 ± 0.006	332 ± 8	102.57 ± 0.07
Experiment	1257.98 [216]	0.46 [217] [c]	0.24 [161] [c]	218.9 ± 0.2 [218]	91.7 ± 0.9 [218]
Monoethanolamine					
MEAa	1053.56 ± 0.02	1.01 ± 0.02	0.356 ± 0.002	376 ± 2	54.140 ± 0.004
OPLS	1024.12 ± 0.06	1.061 ± 0.006	0.457 ± 0.002	280.9 ± 0.6	59.222 ± 0.002
GAFF	1130.6 ± 0.1	0.75 ± 0.02	0.234 ± 0.003	289 ± 3	85.765 ± 0.008
Experiment	1018.0 [219]	0.801 ± 0.016 [220]	0.378 ± 0.038 [220]	144 [221]	64.03 [222]

[a] at 320K, [b] at 0.8bar, [c] at 293.15K

TABLE 4.2: Summary of dielectric properties: mean molecular dipole moment μ_m, relaxation time τ_D corresponding to the Debye model, relaxation time τ_{HN} and parameters α and β corresponding to the Havriliak-Negami model, static dielectric constant ε_0 and infinite frequency dielectric constant ε_∞. Simulations are run at 298 K and 1 bar, except for the case of MEA for which the temperature is set to 293 K. * Experimental relaxation times τ_D are obtained fitting the experimental data in Fig. 4.6 to the Debye model.

		Debye		*Havriliak-Negami*					
	μ_m (D)	τ_D (ps)	MSD	τ_{HN} (ps)	α	β	MSD	ε_0	ε_∞
Water									
SPC	2.2740	6.41 ± 0.05	0.102	7.1 ± 0.2	1.0	0.911 ± 0.008	0.013	66.6 ± 0.4	–
TIP4P	2.1775	5.51 ± 0.03	0.162	6.32 ± 0.02	1.0	0.890 ± 0.004	0.026	44.5 ± 0.3	–
SPC/E	2.3506	10.5 ± 0.2	0.145	11.6 ± 0.2	0.992 ± 0.007	0.915 ± 0.003	0.010	70.6 ± 0.6	–
F-SPC	2.4580 ± 0.0001	13.1 ± 0.3	0.090	13.9 ± 0.7	0.99 ± 0.01	0.95 ± 0.02	0.015	94 ± 1	–
Fw-SPC	2.3949 ± 0.0001	13.2 ± 0.1	0.110	14.7 ± 0.4	1.0	0.91 ± 0.02	0.014	80.2 ± 0.8	–
Experiment	2.9 ± 0.6 [223]	8.22*	–	–	–	–	–	78.54 [224]	1.77686 [221]
Ethanol									
TraPPE-UA	2.2625 ± 0.0001	118 ± 6	1.352	190 ± 20	1.0	0.71 ± 0.02	0.178	18.1 ± 0.5	–
OPLS	2.3746 ± 0.0001	43 ± 2	2.373	78 ± 5	1.0	0.62 ± 0.03	0.103	17.9 ± 0.3	–
GAFF	2.1234 ± 0.0002	76 ± 3	1.175	113 ± 5	1.0	0.73 ± 0.01	0.150	15.6 ± 0.4	–
Experiment	3.43 [225]	187*	–	–	–	–	–	25 [219]	1.85349 [221]
Ethylene glycol									
TraPPE-UA	3.43 ± 0.02	870 ± 90	1.736	1300 ± 200	0.97 ± 0.03	0.74 ± 0.05	0.143	36 ± 2	–
OPLS	2.482 ± 0.005	52.4 ± 0.9	0.806	72 ± 4	1.0	0.76 ± 0.03	0.066	20.3 ± 0.2	–
GAFF	3.209 ± 0.007	370 ± 12	1.296	580 ± 40	1.0	0.71 ± 0.02	0.073	35.6 ± 0.5	–
Experiment	4.02 [225]	123*	–	–	–	–	–	40.86 [226]	2.05005 [221]
Propylene glycol									
TraPPE-UA	3.28 ± 0.02	1210 ± 60	2.318	2100 ± 100	0.99 ± 0.02	0.65 ± 0.02	0.082	22.8 ± 0.9	–
OPLS	4.04 ± 0.02	2600 ± 500	2.924	5000 ± 2000	1.0	0.64 ± 0.07	0.363	46 ± 3	–
GAFF	3.13 ± 0.02	520 ± 40	2.405	940 ± 90	0.98 ± 0.02	0.64 ± 0.02	0.068	25.1 ± 0.6	–
Experiment	3.60 [227]	342*	–	–	–	–	–	28.373 ± 0.004 [228]	2.05349 [221]
Glycerol									
OPLS	4.453 ± 0.003	2300 ± 300	2.364	4000 ± 300	0.97 ± 0.03	0.67 ± 0.05	0.204	33 ± 3	–
GAFF	3.45 ± 0.03	11000 ± 2000	10.533	19900 ± 900	1.0	0.56 ± 0.04	0.209	28 ± 5	–
Experiment	4.21 [225]	933*	–	–	–	–	–	42.54 [229]	2.17445 [221]
Monoethanolamine									
MEAa	1.994 ± 0.004	30.6 ± 0.6	2.760	55 ± 2	0.99 ± 0.02	0.61 ± 0.02	0.058	10.5 ± 0.2	–
OPLS	3.462 ± 0.008	83 ± 3	0.203	96 ± 5	1.0	0.88 ± 0.02	0.037	50.7 ± 0.9	–
GAFF	3.002 ± 0.004	1140 ± 60	2.358	1800 ± 300	0.94 ± 0.04	0.72 ± 0.07	0.113	40.9 ± 0.9	–
Experiment	2.60 [227]	162*	–	–	–	–	–	34.20 [230]	2.11441 [221]

4.3.2 The average molecular dipole moment

The molecular dipole moment μ_m results from averaging this variable over all the N_{mol} molecules in the system and over the entire trajectory:

$$\mu_m = \left\langle \frac{1}{N_{mol}} \sum_{j}^{N_{mol}} \boldsymbol{\mu}_j \cdot \boldsymbol{\mu}_j \right\rangle^{\frac{1}{2}} \tag{4.12}$$

where $\langle \cdots \rangle$ represents an average over all time frames of the simulation, and $\boldsymbol{\mu}_j$ is the dipole moment of molecule j defined as:

$$\boldsymbol{\mu}_j = \sum_{\alpha}^{N_{atom}} \left(\mathbf{r}_{\alpha j} - \mathbf{r}_{0j}\right) \; q_{\alpha j} \tag{4.13}$$

This property fluctuates due to the flexible nature of most of the molecular models under consideration, as shown in Table 4.2. In general, the values obtained by the models used in this study differ significantly from the corresponding experimental values. Within condensed phases, in addition to flexibility, polarization effects have a significant effect on the molecular dipole moment, as compared to the gas phase [231]. Therefore, polarisable force fields would be required if one wanted to obtain more accurate values of the liquid phase dipole moment. However, the additional computational cost associated with this type of force fields would deem infeasible the long simulations required to properly estimate dielectric spectra, particularly for larger systems.

4.3.3 Dynamic response: the dipole moment autocorrelation function

The relaxation times corresponding to the rotational and translational modes of a molecule, or group of atoms within a larger molecule, can be determined from the analysis of the time evolution of the dipole moment. The influence of an external electric field on these processes is believed to be the basis for the microwave heating mechanism. In this context, the dipole moment autocorrelation function is a powerful tool to study the dynamics of molecular systems.

Following the procedure explained in section 3.4.2, we determine the dipole moment autocorrelation function of the different systems we have simulated. Figure 4.2a shows an example of the results obtained in the case of ethanol, using the TraPPE-UA force field. As previously stated, we perform four simulations for every system, obtaining four independent autocorrelation functions. Next, we fit separately both the Debye (Eq. (3.78)) and the Havriliak-Negami (Eq. (3.84)) models to these data, and obtain four independent sets of parameters for the models. An example of this fitting procedure, for one of the runs shown in Fig. 4.2a, is presented in Fig. 4.2b, where we can clearly see how the HN model outperforms the Debye model. The flexibility introduced by the parameters α and β in the HN model allows the use of more complex shapes with regard to the simple exponential decay given by the Debye model.

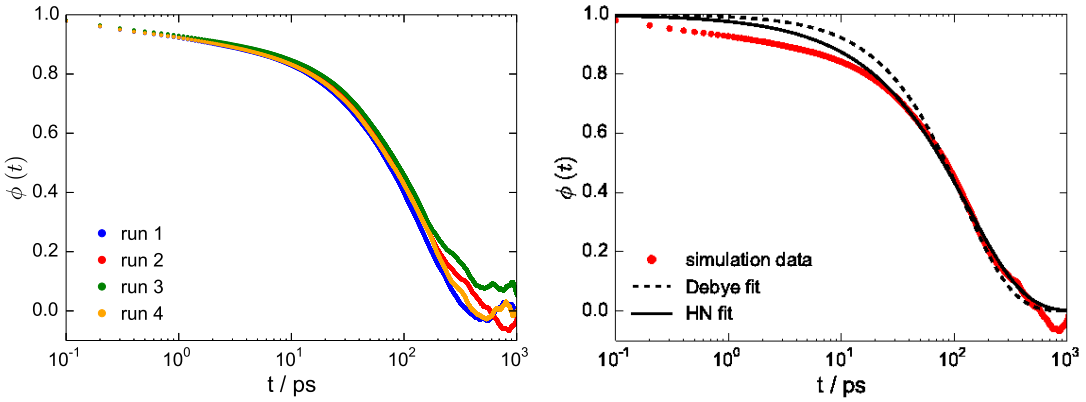

(a) Four independent runs

(b) Debye and HN fits for run 2

FIGURE 4.2: Dipole moment autocorrelation function of ethanol as given by the TraPPE-UA force field, at 298 K and 1 bar.

Once the fitting procedure is completed, we average these parameters across the four runs to obtain the final values shown in Table 4.2. In Table 4.2 we also show the goodness of the fit calculated as the mean square deviation (MSD) between the value of dipole moment autocorrelation function obtained in the simulations (ϕ_{sim}) and the one predicted by the models (ϕ_{model}):

$$MSD = \frac{1}{N_t} \sum_{j}^{N_t} \left[\phi_{model}(t) - \phi_{sim}(t)\right]^2 , \tag{4.14}$$

where N_t is the number of time intervals included in the fit.

The analysis of the MSD results confirms the better performance of the HN model in every case. The increased complexity of this model improves the characterisation of non-ideal responses. In Fig. 4.3 we present and compare the average dipole moment autocorrelation functions for all the systems under consideration, according to the time domain representation of both the Debye and the HN models.

Studying the results in Table 4.2 and Fig. 4.3, we can conclude that water is the only system for which the Debye model produces a satisfactory prediction. The remaining systems show a behaviour that approaches the Cole-Davidson model, since for most α is significantly close to one. The values of β for systems other than water oscillate between 0.55 and 0.90, indicating different levels of asymmetry of the response with respect to the purely exponential behaviour. In general, we consider that the extension of the Debye model into the Havriliak-Negami model is clearly necessary to analyse these specific systems. Therefore, in the following, we will always interpret our results in relation to the latter, knowing that the former is included as a particular case when $\alpha = 1$ and $\beta = 1$.

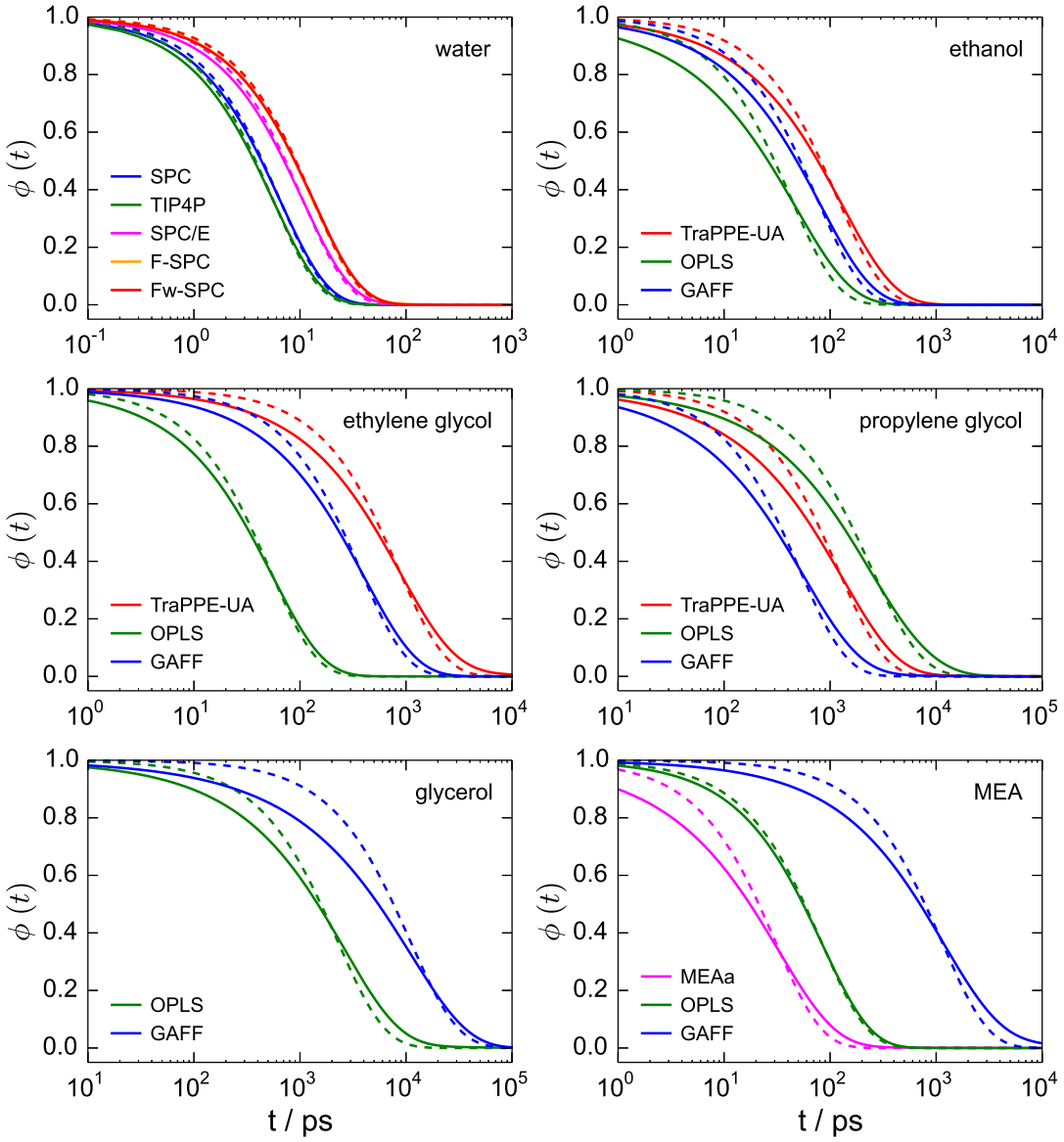

FIGURE 4.3: Average dipole moment autocorrelation function at 298 K and 1 bar. For monoethanolamine (MEA), the results are obtained at 293 K. Solid lines represent the results obtained using the Havriliak-Negami model to fit the simulation data, while dashed lines where obtained using the Debye model.

In the case of water, the flexible models (F-SPC and Fw-SPC) show longer relaxation times than the rigid models (SPC, TIP4P and SPC/E), which would indicate that the introduction of flexibility translates into a slower reorganisation of dipoles. The slight increase of the atomic charges in the SPC/E force field with respect to the original SPC model also results in slowing the dipole dynamics. For the remaining substances, the OPLS force field seems to provide the faster response (smaller relaxation times) with the exception of propylene glycol. In all cases, the GAFF force field generates faster relaxation than the TraPPE-UA force field. In the particular case of MEA,

the MEAa model shows faster dynamics than both OPLS and GAFF force fields. In Table 4.2, for every system, we have highlighted the force field that provides the best estimation of relaxation times, in comparison with experimental results: SPC model for water; TraPPE-UA for ethanol; OPLS for ethylene glycol; GAFF for propylene glycol; OPLS for glycerol; and OPLS for MEA. According to these results, none of the force fields shows a consistently better performance across species. Nevertheless, this was expected since these force fields have been developed on the base of thermodynamic properties and dynamic properties were not involved in their calibration. Even though, for every system, one model, at least, provides satisfactory results. This will become more obvious when we present below their prediction of dielectric spectra as compared with experimental data.

The dynamic response of the system given by the dipole moment autocorrelation function can also be studied in the frequency domain. Figure 4.4 shows the Fourier transform of the dipole moment autocorrelation function $\hat{\phi}(\omega)$ as given by the Havriliak-Negami model (Eq. (A.27) in Appendix A), for all the systems under consideration. This figure includes experimental data obtained using Eq. (3.50) to calculate the real and imaginary parts of $\hat{\phi}(\omega)$ from the experimental dielectric spectra, shown later in Fig. 4.6:

$$\frac{\hat{\varepsilon}(\omega) - \varepsilon_\infty}{\varepsilon_0 - \varepsilon_\infty} = 1 + i\omega\, \hat{\phi}(\omega) \tag{3.50}$$

$$\boxed{\begin{aligned} \hat{\phi}'(\omega) &= \frac{\hat{\varepsilon}''(\omega)}{\omega\,(\varepsilon_0 - \varepsilon_\infty)} \\ \hat{\phi}''(\omega) &= \frac{1}{\omega} - \frac{\hat{\varepsilon}'(\omega) - \varepsilon_\infty}{\omega\,(\varepsilon_0 - \varepsilon_\infty)} \end{aligned}} \tag{4.15}$$

Experimental values for ε_0 and ε_∞ can be found in Table 4.2. At high frequencies, it can be derived from Maxwell's equations [232] that the dielectric constant is related to the refraction index n through:

$$\sqrt{\varepsilon_\infty} = \frac{ck}{\omega} = n \tag{4.16}$$

where c is the speed of light in vacuum. Since ω/k represents the speed of light in a medium, the refractive index (always greater than one) expresses that waves always propagate slower in a medium than in vacuum.

The frequency response is mainly manifested by the presence of low frequency phenomena such as the decay in $\hat{\phi}'(\omega)$ and the corresponding peak in $\hat{\phi}''(\omega)$. In the case of water, it is clear that the flexible models and the SPC/E model overestimate both $\hat{\phi}'(\omega)$ and $\hat{\phi}''(\omega)$ in the microwave region, while SPC and TIP4P models underpredict the response. At higher frequencies, the characteristics of the different models seem to have less influence on the frequency dependence of the dynamic response. The rigid models clearly outperform the flexible ones, with the SPC model showing the best performance. For the remaining systems, Fig. 4.4 confirms the models to which

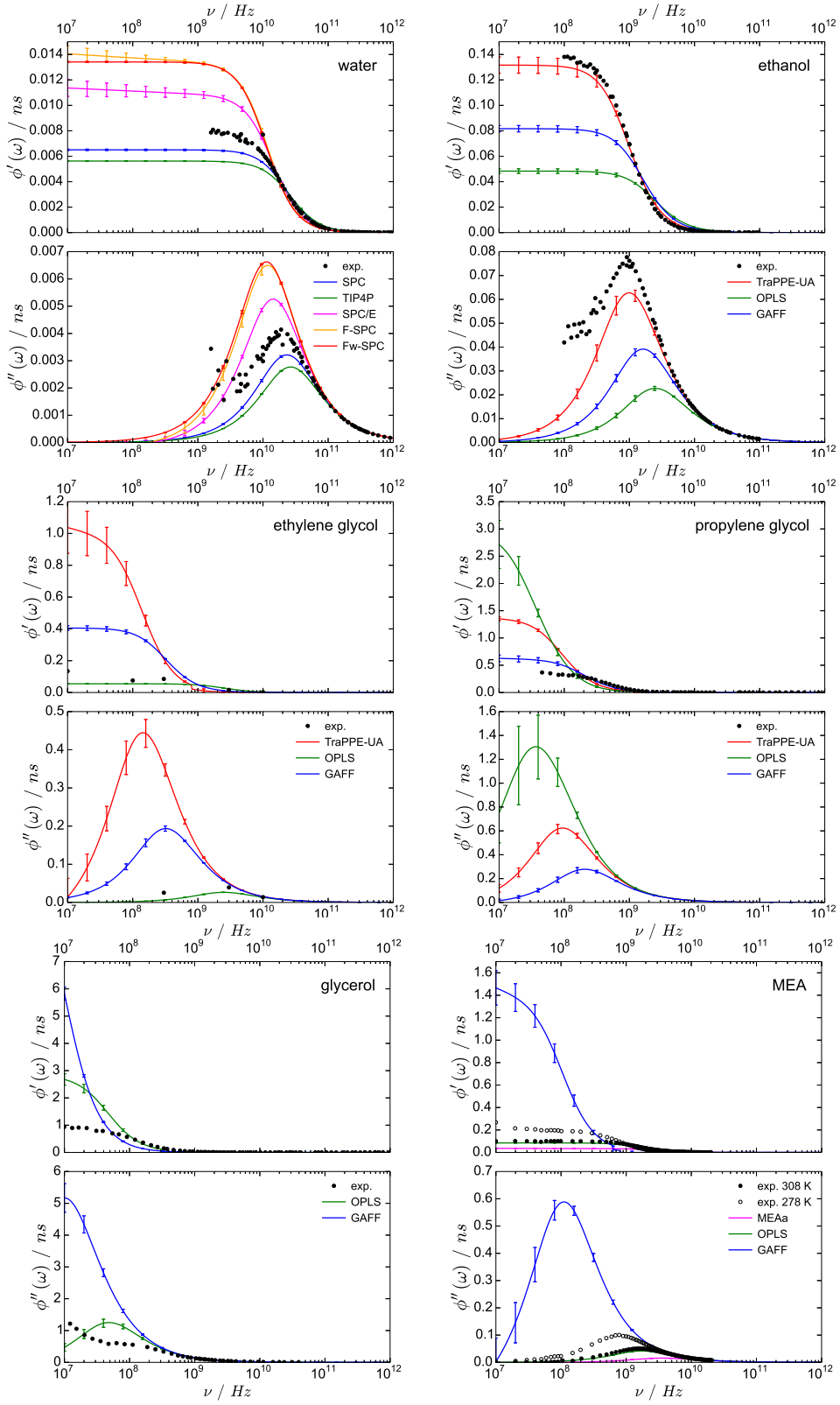

FIGURE 4.4: Dynamic response of several organic compounds at 298 K and 1 bar through the dipole moment autocorrelation function in the frequency domain. For monoethanolamine (MEA), the simulations are performed at 293 K. Solid lines represent the results obtained in our simulations using the different force fields introduced in the text. Black circles represent experimental values obtained from Eq. (3.50) using dielectric spectrum data from different sources for the following systems: water [102–105], ethanol [110–112, 233, 234], ethylene glycol [235], propylene glycol [123], glycerol [122, 124, 236, 237]. For MEA, black open and filled circles are experimental values at 278 K [238] and 308 K [239], respectively.

we attributed a better performance based on the closer similarity to the experimental relaxation time in Table 4.2. This is because the frequency response of a molecular system is purely dependent on this parameter in the range of frequencies we are studying. For ethanol, the TraPPE-UA force field provides a surprisingly good prediction of the experimental results, while in the case of ethylene glycol and propylene glycol, the best performance is shown by the OPLS and the GAFF models, respectively. In addition, the results corroborate that the frequency response of both glycerol and MEA is better predicted by the OPLS force field, although for the former the region where the main features appear is poorly characterised due to the insufficient length of the simulations we have carried out for this system (100 ns which corresponds to a frequency of 10^7 Hz).

Once the dynamic response of the different systems has been obtained through the dipole moment autocorrelation function, the dielectric response is achieved through Eq. (3.50), or, in our case, using the Havriliak-Negami representation of the dielectric permittivity given by Eq. (3.82). To obtain an accurate description of dielectric spectra, it becomes essential to have a good estimate of the static dielectric constant ε_0. The importance of the selection of this parameter is discussed in the following sections.

4.3.4 The Static Dielectric Constant

The long correlation times in the fluctuations of total dipole moment make the calculation of the static dielectric constant difficult. Previous work has shown the importance of selecting the appropriate block length for the correct calculation of this property of water [240, 241].

The static dielectric constant is calculated using Neumann's formula [138, 153] which relates this magnitude to the fluctuations of the total dipole moment of the system. Two alternative versions of this formula are usually considered:

$$\varepsilon_0 = \varepsilon_\infty + \frac{\beta_T}{\varepsilon_{vac}\, 3V} \langle \mathbf{M} \cdot \mathbf{M} \rangle \tag{4.17}$$

$$\varepsilon_0 = \varepsilon_\infty + \frac{\beta_T}{\varepsilon_{vac}\, 3V} \left(\langle \mathbf{M} \cdot \mathbf{M} \rangle - \langle \mathbf{M} \rangle \cdot \langle \mathbf{M} \rangle \right) \tag{4.18}$$

where $k_B = 1.38064852 \times 10^{-23}\,\mathrm{m^2\,kg\,s^{-2}\,K^{-1}}$ is the Boltzmann constant, T is the temperature and V is the volume of the system.

In Eq. (4.17) it is assumed that the average dipole moment is zero ($\langle \mathbf{M} \rangle = 0$) at any time. This would mean that the dipole moment data are always uncorrelated. However, if simulation times are not long enough to allow dipole moment data to decorrelate, this generates a bias in the calculations. By introducing the term $\langle \mathbf{M} \rangle \cdot \langle \mathbf{M} \rangle$ in Eq. (4.18), we take this fact into account. At long times, and only when the simulation is long enough to obtain uncorrelated data, both alternatives are equivalent since the term $\langle \mathbf{M} \rangle \cdot \langle \mathbf{M} \rangle$ vanishes. Therefore, we need either simulations longer than dipole moment correlation times, or different simulations of about the length of the dipole

moment correlation time, but independent from each other. In our case, this is achieved through an annealing procedure by which we generate four independent samples.

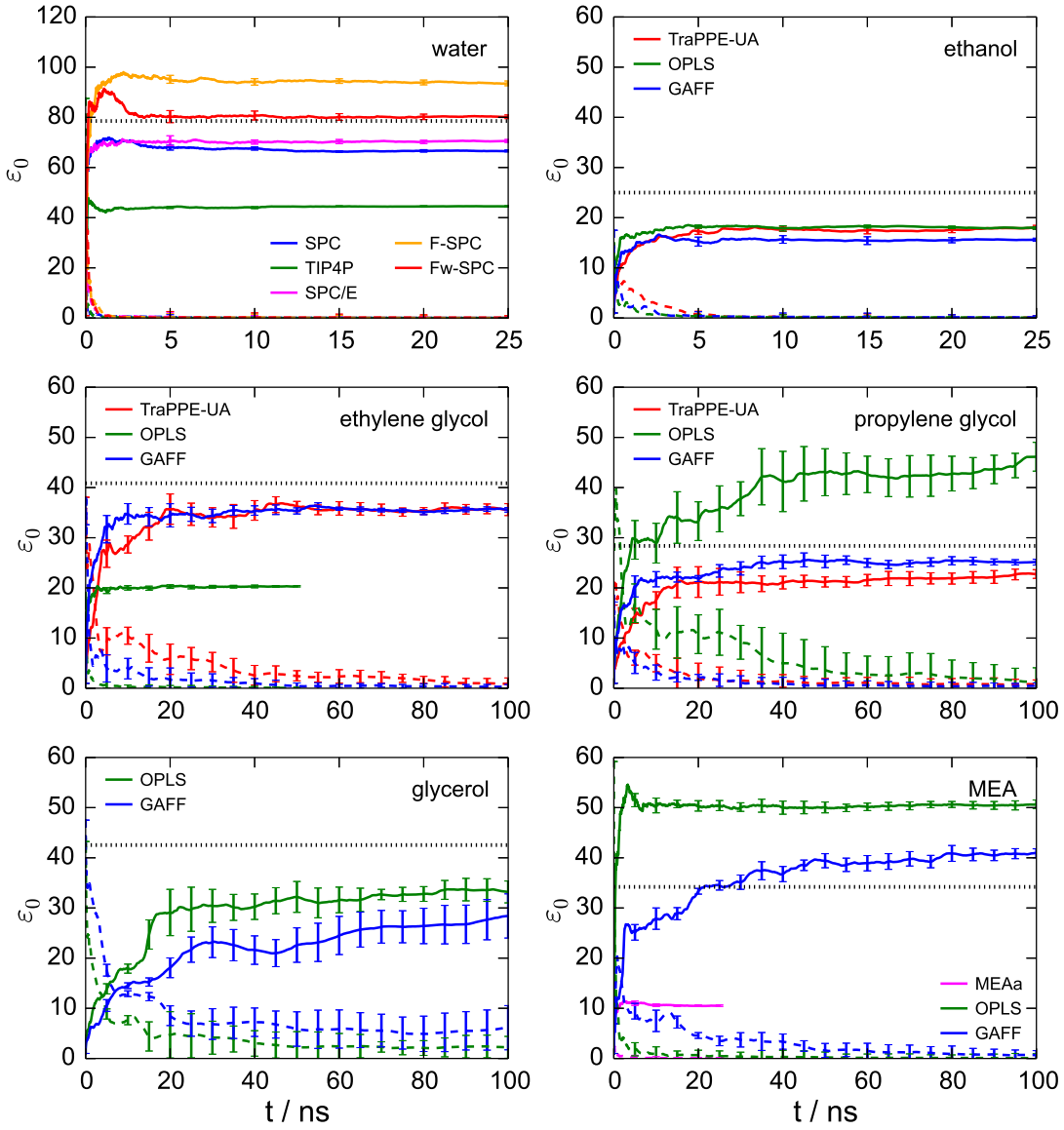

FIGURE 4.5: Effect of the simulation length on the static dielectric constant. Solid lines show running averages of the static dielectric constant for simulations started from energetically equilibrated samples, at 298 K and 1 bar. For MEA, the simulations are performed at 293 K. The results are obtained using Neumann's formula (Eq. (4.18)). Dashed lines correspond to the term containing the square of the average dipole moment $(\langle \mathbf{M} \rangle \cdot \langle \mathbf{M} \rangle)$ in Eq. (4.18), which should vanish at long times to consider the static dielectric constant converged. Dotted horizontal lines represent experimental values obtained from different sources: water [224], ethanol [219], ethylene glycol [226], propylene glycol [228], glycerol [229] and MEA [230].

The importance of employing decorrelated dipole moment data is better illustrated by the results shown in Fig. 4.5 for the compounds studied in this work. To ensure the convergence of the static dielectric constant, the simulations are extended until the term containing the square of the average dipole moment $\left(\langle \mathbf{M} \rangle \cdot \langle \mathbf{M} \rangle\right)$ in Eq. (4.18) converges to zero, with a maximum simulation length of 100 ns. In this manner, we obtain converged values of the static dielectric constant for most models (see Table 4.2). However, this is clearly not possible in the case of glycerol for which longer simulations would be required to obtain the final value predicted by the models.

Nevertheless, even ruling out the effect of the simulation length, most potential models do not seem to provide acceptable results, since none of them gives predictions that statistically agree with the experimental values. It has been reported previously that this property is not well predicted by nonpolarizable force fields, such as the ones used in this work [161]. In the case of water, it would appear flexibility provides an improvement in the prediction of ε_0, particularly in the case of the Fw-SPC model, but this is at the cost of affecting the response at intermediate frequencies, as shown in Sec. 4.3.3.

The consequence of this, through Eq. (3.50), and as shown below in section 4.3.5, is that the loss factor $\varepsilon''(\omega)$ is also poorly estimated, which in turn would lead to inaccurate estimates of dielectric heating rates. Therefore, due to the uncertainty in the prediction of the static dielectric constant, in the following it is decided to use the corresponding experimental value in the determination of dielectric spectra of the different systems under consideration. The effect of this choice on the shape of dielectric spectra is also discussed in section 4.3.5.

4.3.5 Dielectric Spectra

At this point all the parameters that are necessary to obtain dielectric spectra according to the methodology explained in section 3.4.4 have been determined. Figure 4.6 summarises the results obtained in the prediction of the dielectric spectra of several organic compounds, applying the Havriliak-Negami model (Eq. (3.82)). Generally, a fairly good agreement with experimental data is reached, with at least one of the models providing an acceptable result for the prediction of dielectric spectra.

The main absorption peak observed in the low frequency end of the imaginary part of the dielectric spectrum, in Fig. 4.6, is associated with dipole reorientation as a response to a time-dependent electric field [90, 122, 124]. It is typically known as α-relaxation peak, and for relatively small molecules such as the ones studied here, it usually occurs in the microwave or high frequency radio wave region, at ambient conditions. As a description of this process, the Debye model (see Eq. (3.72)) assumes dipoles relax independently from each other, with a common relaxation time. However, in most materials this somehow 'ideal' behaviour does not take place. The fact that for most systems the use of the HN model provides a significant improvement with respect to the Debye model (see Table 4.2), is an indication of a broader distribution of

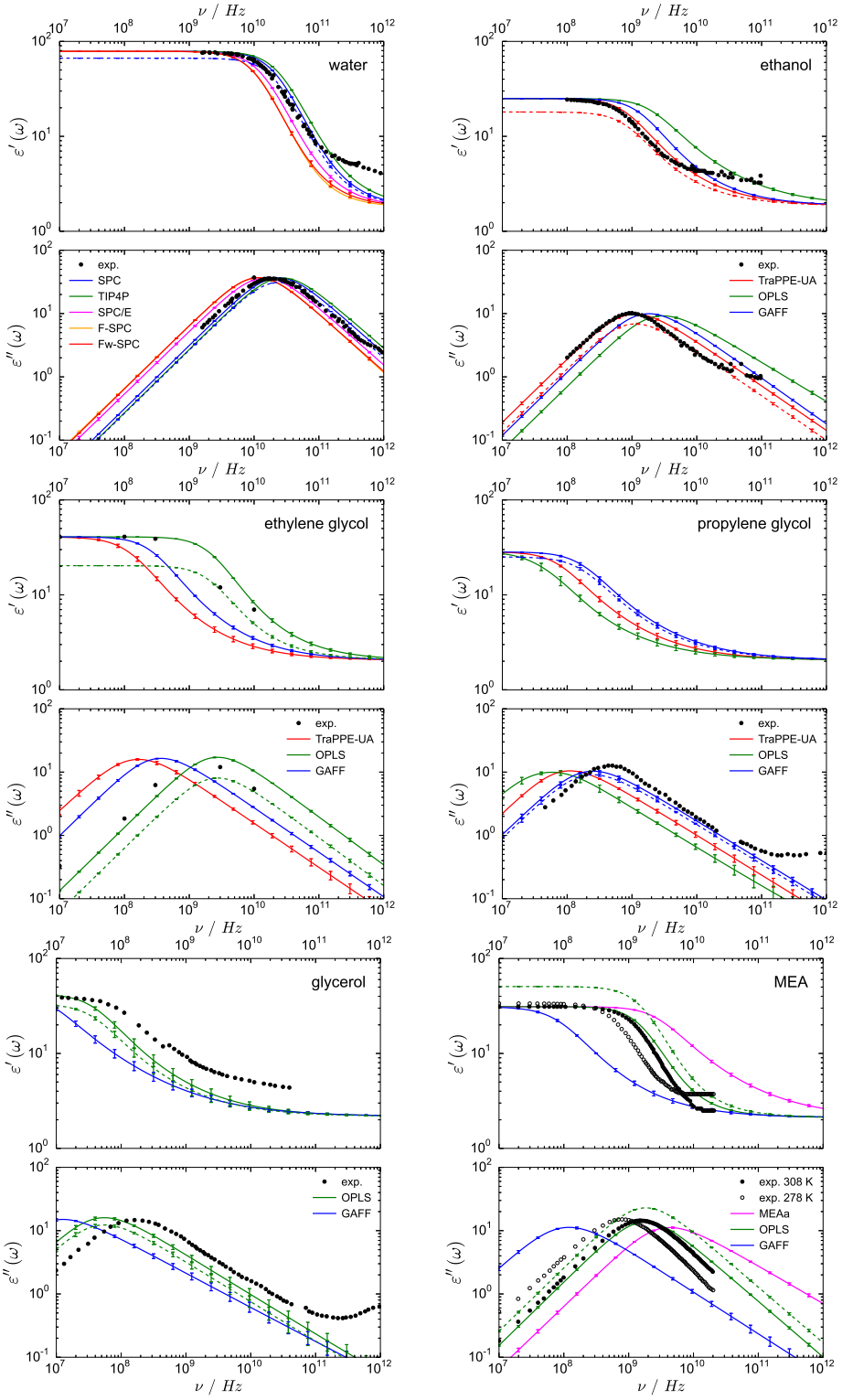

FIGURE 4.6: Dielectric spectra of several organic compounds obtained via molecular dynamics simulations at 298 K and 1 bar. For monoethanolamine (MEA), the simulations are performed at 293 K. Solid lines represent the results obtained in our simulations using the different force fields introduced in the text, and employing the experimental static dielectric constant ε_0 and infinite frequency dielectric constant ε_∞ in the calculations. Dashed lines correspond to results using Neumann's formula (Eq. (4.18)) to calculate the static dielectric constant, for the force fields showing a better performance in the prediction of the dielectric spectrum in every case (water SPC, ethanol TraPPE-UA, ethylene glycol OPLS, propylene glycol GAFF, glycerol OPLS and MEA OPLS). Black circles represent experimental values obtained from different sources for the following systems: water [102–105], ethanol [110–112, 233, 234], ethylene glycol [235], propylene glycol [123], glycerol [122, 124, 236, 237]. For MEA, black open and filled circles are experimental values of the dielectric spectrum at 278 K [238] and 308 K [239], respectively.

relaxation times in those materials. As deduced from the value of the parameters of the Havriliak-Negami model (see Table 4.2), water is the system that conforms most closely to the Debye model. For the remaining materials, the deviation of β from unity results in an asymmetric broadening of the spectrum, also called excess wing [124]. This means that the relaxation time predicted by the HN model will no longer coincide with the relaxation time corresponding to the maximum loss, as estimated by the Debye model. This is clearly the case for ethanol OPLS, where τ_{HN} is definitely larger than τ_D. For other systems, the more β differs from one, the larger is the relaxation time predicted by the Havriliak-Negami model with respect to the Debye relaxation time.

In the high frequency end of the spectra (above 10^{11} Hz), our results seem to systematically underpredict experimental data. This suggests the existence of additional processes in that region which we are not taking into account in our single relaxation model. Adding a second relaxation process in this region will probably provide better results. However, since we are principally interested in commercially available microwave frequencies (0.915, 2.45 and 5.8 GHz), we do not consider necessary to add an additional relaxation process in this study.

Effect of the static dielectric constant

For the different molecules under consideration, dashed lines in Fig. 4.6 represent the best dielectric spectra predictions obtained using Eq. (3.82), when the static dielectric constant ε_0 is calculated from simulation data, using Neumann's approach (Eq. (4.18)). In most cases, the low-frequency end of the real part of the dielectric spectrum and the magnitude of the main absorption peak in the dielectric loss do not match the experimental results. Slight differences can be observed in the cases of water, propylene glycol and glycerol, while the results are clearly underestimated for ethanol and ethylene glycol, and overpredicted for MEA. This is related to the value of the static dielectric constant estimated by the different models (see Table 4.2). This variable acts as a scaling factor for the magnitude of both real and imaginary parts of the dielectric response. However, the dynamics $\big($i.e. the frequency-dependence of $\varepsilon'(\omega)$ and $\varepsilon''(\omega)\big)$ are not clearly affected by this fact and follow the experimental trend, as shown in section 4.3.3.

By using the experimental value of the static dielectric constant in Eq. (3.82), instead of the one obtained from the simulations, the dielectric spectra predictions are clearly improved (solid lines in Figure 4.6). This demonstrates the importance of using a good value for the static dielectric constant. Even though the models may not reproduce the static dielectric constant, they do appear to correctly describe the dipole-dipole autocorrelation function $\phi(t)$. By simply introducing the experimental static dielectric constant in Eq. (3.82), one can obtain good results in the prediction of dielectric spectra. This is clearly the case for the models showing a better performance in the estimation of the dielectric spectra of ethanol (TraPPE-UA), ethylene glycol (OPLS) and MEA (OPLS). In the cases of propylene glycol (GAFF) and glycerol (OPLS), the improvement is also

visible, although not so significant. Finally, the performance of the rigid SPC and TIP4P water models is significantly improved with respect to results obtained by English *et al.* [169, 170]. Therefore, one should not use the static dielectric constant as the only judge of the ability of a molecular model to predict dielectric properties.

Although we recognize the theoretical inconsistency of substituting the calculated ε_0 by the experimental one, we consider this is a useful and practical method to estimate $\varepsilon'(\omega)$ and $\varepsilon''(\omega)$. It avoids the need for extraordinarily long simulations or highly accurate models to determine the static dielectric constant. This becomes particularly important when a good knowledge of the magnitude of the dielectric response is required for the prediction of the heat a molecular system can absorb from a microwave field (see Eq. (2.80)). It seems unlikely that classical force fields of the type used here will ever be satisfactory for production of a wide range of thermodynamic and dynamical phenomena simultaneously, and so methods that can correct for their weaknesses are desirable. In this case, we have shown that prediction of dielectric heating can be systematically improved if the experimental static dielectric constant is known a priori.

Effect of size and polarity

Finally, the dielectric spectra of the different substances under consideration are compared in Fig. 4.7, using the results provided by the best force fields in every case. This clearly shows how as the size of the molecule increases, the relaxation frequency decreases (i.e. the dynamics slow down). This was expected since the rotation of larger molecules is generally more impeded, and therefore the changes in dipole moment will take longer. In addition, it is possible to observe the effect of polarity on the maximum of the dielectric loss. The most polar species (i.e. water, glycerol, ethylene glycol) show a higher peak and, consequently, have the highest potential to transform electromagnetic energy into heat.

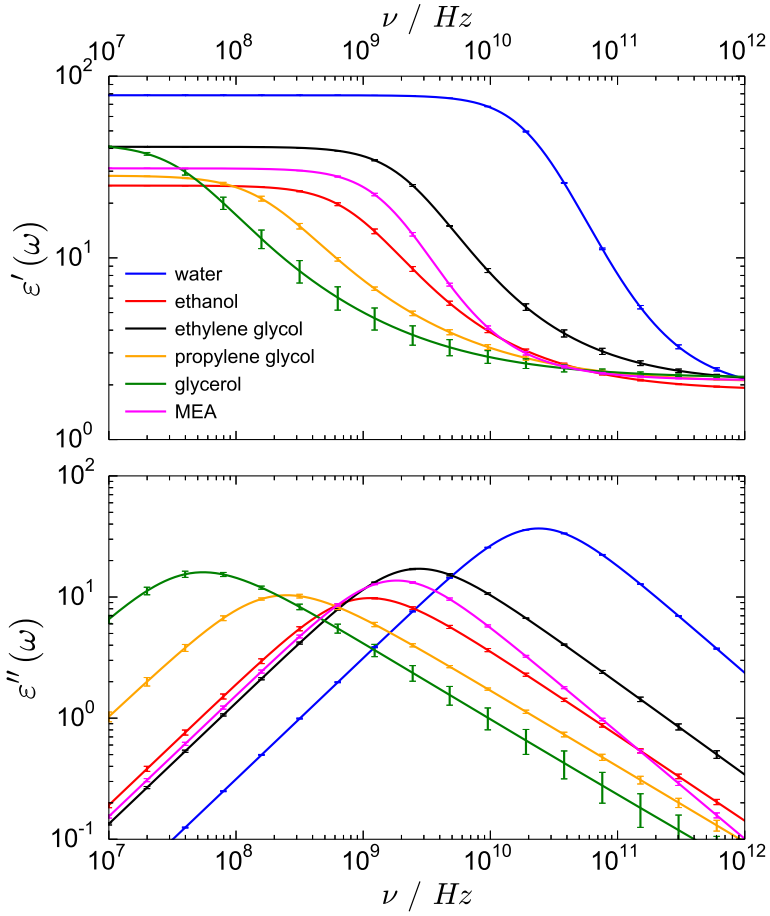

FIGURE 4.7: Comparison of the dielectric spectra of different organic substances. The force fields that show a better performance in the prediction of the dielectric response are used in this representation: water SPC (blue), ethanol TraPPE-UA (red), ethylene glycol OPLS (black), propylene glycol GAFF (orange), glycerol OPLS (green) and MEA OPLS (magenta).

4.4 Conclusions

In this work, we have examined the ability of molecular dynamics simulations to predict the dielectric spectra of small molecules in the microwave region. This is an essential feature if one wants to estimate the heat a dielectric material can absorb from an external microwave field. The methodology used here analyses the time fluctuations of the total dipole moment of a molecular system. All-atom and united-atom force fields, which have mainly been developed to accurately reproduce experimental thermodynamic properties, generally give good predictions for the frequency-dependent dielectric constant of a series of alcohols and glycols, as well as for monoethanolamine, so long as the correct value of the static dielectric constant is used.

Despite the good performance in describing the dynamics of the dielectric response of the systems under consideration, most of the models have difficulties in predicting the static dielectric constant, which is a crucial parameter in the scaling of dielectric

spectra. The use of non-polarizable force fields in our simulations may have an influence on the molecular motion, hence affecting the static dielectric constant. Another limiting factor could be the long time scales required to achieve an accurate value of this property, which corresponds to the magnitude of total dipole moment fluctuations, especially for larger systems.

The solution adopted here is to use the experimental value of this magnitude in conjunction with the dynamics predicted by molecular simulations. This can avoid the need for extraordinarily long simulations for systems for which the static dielectric constant is a well known property or can be easily measured experimentally.

With these considerations in mind, the models evaluated in this work are able to capture the main experimental features. The simulated dielectric spectra of all the systems we analyse exhibit an α-relaxation peak, characteristic of these types of substances. In addition, while water possesses a Debye-like relaxation, alcohols, glycols and monoethanolamine show signs of an excess wing in the high frequency end of the α-relaxation peak, which has been described in the literature [124].

Currently, due to limitations in computational hardware, all-atom molecular dynamics simulations cannot describe interesting features in the dielectric relaxation of a material that occur on times scales greater than or on the order of μs. However, the ability of these simulations to reproduce the characteristics of the dielectric spectra at higher frequencies, as demonstrated here, gives confidence on the possibility of using the force fields studied in this work for the prediction of dielectric spectra of compounds for which experimental data are not available. Together with other recent work in this field, this study opens the possibility to use molecular dynamics simulations as a powerful tool in areas such as the study of glass-forming materials, the analysis of polymer dynamics, or the examination of the dielectric behaviour of mixtures.

Chapter 5

Dielectric Spectra of Ethanol/Water Mixtures

In this chapter we extend the determination of dielectric spectra to two-component systems. Although empirical models have been developed to predict dielectric spectra of mixtures, based on the properties of their pure components, several studies show how the composition dependence of dielectric properties tends to have a complex non-linear behaviour, particularly when polar components are involved. The use of molecular simulations can give a more realistic estimate for these properties, while improving the understanding of the structure and dynamics of the system. We start with a review of some experimental and theoretical studies on dielectric spectroscopy and microwave heating of mixtures, and then proceed to briefly describe the methodology applied for the prediction of dielectric spectra of binary systems in this work. Next, we present our results for the particular case of ethanol/water mixtures, and compare these results with predictions provided by established empirical methods. Finally, we decompose the global dielectric response into contributions at different levels, to provide a deeper insight into the mechanisms leading to this response.

5.1 Introduction

The interest in determining dielectric spectra of mixtures resides on studying the dynamics of these systems and identifying possible deviations from the behaviour of pure components and their ideal mixture. The amount of experimental work in this area is significant and includes systems such as alcohol/water [112, 234, 242–249], glycine/water [250, 251], DMSO/alcohol [252], and mixtures of acetone, DMSO and isopropanol [253]. Other authors have investigated the dielectric response of aqueous solutions of α-D-glucose [254, 255], lysine [256] and nucleotides [257], mixtures of acrylic esters and alcohols [258], ionic liquids in water [259] and ethanol [260], and p-fluorophenyl acetonitile/2-butylphenol and 2-chlor-6-fluoro-benzaldehyde/o-ethylphenol systems [261]. Mixtures of ethanol and benzene have also received some attention in the literature [262–265]. This is an interesting system as it combines polar and non-polar molecules. The microwave heating efficiency in these types of binary systems has been shown to depend significantly on the non-ideality of the mixture,

where higher heating rates are obtained for compositions at which negative deviations from the ideal solution are observed, and intermolecular interactions are weaker [266].

One of the most studied systems is the ethanol/water mixture. Ethanol molecules are among the smallest molecules to have both hydrophobic and hydrophilic groups. This is the reason why aqueous ethanol solutions are considered as a reference for the study of interactions in biological processes, such as protein folding, ligand binding or membrane assembly, where hydrophobic hydration has a significant influence [267]. In addition, ethanol/water mixtures can be found in numerous applications ranging from their use as a solvent, biofuel or alcoholic beverage. Using microwaves as an alternative heating option for these systems (e.g. for distillation or pervaporation) has also been studied in the past [62, 268, 269].

The concentration and temperature dependence of the dielectric spectrum of this binary system has been studied by several authors [112, 234, 242–245, 249, 270, 271], including the interpretation of the physical origin of the different observed relaxation mechanisms. These mixtures are generally characterised by the presence of two relaxation processes, with a third process appearing at high ethanol concentrations. The first and most intense relaxation ($\tau_1 \approx 8 - 200$ ps) has frequently been assigned to the dynamics of the reorganisation of the entire hydrogen bond network and is highly dependent on temperature and concentration. Despite the presence of two different components in the mixture, their individual contributions cannot be clearly discerned, which suggests a collective response appearing as a single peak in the spectrum, generally modelled as a Cole-Cole or Cole-Davidson relaxation. The larger magnitude of this relaxation process is explained by the fact that the majority of the molecules in the mixture form part of an extensive hydrogen bond network, through multiple hydrogen bond interactions [272]. A fact that may appear counter-intuitive is the increase of relaxation time with growing ethanol concentration. Water has a stronger hydrogen bonding structure than ethanol, and one could think that dipole reorientation in highly aqueous systems might be more constrained [249]. In this context, a "wait-and-switch" model [273] has been suggested to describe the dynamics of the liquid phase. According to this mechanism, a "waiting" time (τ_1) is required for the hydrogen bond network to reorganise and find the next available site to "switch" a hydrogen bond (τ_3). It is known that oscillations of free OH groups, related to the formation and breakage of hydrogen bonds, show as fast relaxation processes in the spectrum ($\tau_3 \leq 2$ ps). However, the availability of sites to form new hydrogen bonds is limited. The increase of water concentration in the mixture, results in increasing probability of finding hydrogen bonding sites, which in turn decreases the potential energy barrier between two dipolar orientations. Therefore, the activation energy required to perform a molecular rotation can be more easily overcome in media with high water content, resulting in shorter "waiting" times τ_1 [249]. On another note, in pure ethanol,

hydrogen bonding is known to develop into a chain-like structure [272, 274]. As a consequence, at high ethanol concentrations, an additional intermediate relaxation process is thought to arise from the fluctuations of terminal single hydrogen-bonded ethanol monomers of the chain structure ($\tau_2 \approx 7 - 12$ ps). As water molecules are introduced in the mixture, they tend to infiltrate the ethanol chain structure, giving rise to shorter chains, and therefore increasing the number of terminal ethanol molecules. This results in a more intense intermediate relaxation process with growing fraction of water in the mixture. However, when an approximately equimolar mixture is reached, the speed-up of the main relaxation process (τ_1) results in an overlap with this intermediate mode (τ_2), and its contribution is difficult to observe experimentally. Both the intermediate (τ_2) and fast (τ_3) processes can generally be modelled by means of simple Debye relaxations.

In general, the previous studies have shown how the dielectric response of alcohol/water mixtures is driven by the dynamics of their hydrogen bond network and the hydrophobic effects related to their alkyl groups. In line with the iceberg model suggested by Frank and Evans [275], the first hydration shell around hydrophobic groups has historically been assumed to have the structure of clathrate hydrates, in which water molecules are hydrogen-bonded in a configuration closer to a tetrahedral structure than bulk water itself. The more ordered structure would be characterised by a large entropy decrease and heat capacity rise with respect to bulk water. However, in recent years this assumption has been challenged by several experimental and theoretical studies [271, 276–282], which suggest the enhancement of hydrogen bonding in the first hydration shell of hydrophobic solutes does not actually occur, or at least not to a large enough extent to explain the significant entropy drop [283–285]. In these studies, this more ordered structure is associated to the formation of a cavity in the solvent in which the solute can be introduced [286].

Using molecular dynamics (MD) simulations with polarisable models, Noskov *et al.* [287] have shown how hydrogen bonding is intensified in the first hydration shell in the surroundings of hydrophobic groups, but is more intensely depleted in the vicinity of hydroxyl groups, generating a net depletion of hydrogen bonding in the first hydration shell of ethanol. This phenomenon is however balanced out by a larger enhancement in the second hydration shell, which results in a global strengthening of the hydrogen bond network. At high ethanol concentrations, approximately above the equimolar mixture, a transition from a percolating network of hydrogen-bonded water molecules to a more disperse structure is clearly observed. The lower amount of water molecules in the second hydration shell diminishes its compensation effect, and the depletion of water hydrogen bonds in the first shell becomes dominant. As a consequence, the net outcome is a weakening of the global hydrogen bond structure. Zhong and Patel [288], using a different polarisable model, agree with the net positive

excess in water hydrogen bonding at low ethanol concentrations, although in their case they observed a depletion of hydrogen bonds in the surroundings of hydrophobic groups and an enhancement in the vicinity of hydroxyl groups in the first hydration shell, in contrast with Noskov's results. The contribution of the second hydration shell is also positive but its magnitude is significantly smaller. More recently, Ghoufi *et al.* [289], confirmed Noskov's observations for high ethanol concentrations using non-polarisable force fields. They explain the weakening of the hydrogen bond network as a transition from a percolating network formed by hydrogen-bonded water molecules to a non-percolating network in which water and ethanol form clusters of decreasing size as the concentration of ethanol increases. These clusters may however be in the origin of the difficult separation of water from ethanol at high concentrations. For concentrations higher than the azeotropic composition, water molecules were found to be fully dispersed.

Through experimental studies, Li *et al.* [271] seem to agree with most of the previous conclusions, and suggest a model with three critical alcohol compositions x_1, x_2 and x_3. Below x_1, large hydration shells are formed in the surroundings of the hydrophobic group of alcohol molecules. Above this concentration, extended hydrogen bond networks are generated as water molecules show a preference for the hydroxyl groups of alcohols. The resulting hydrogen bond structure becomes increasingly stronger until a mole fraction x_2 is reached. At this point, a minimum in the diffusivity of alcohol molecules is observed, which corresponds to a situation in which the mixture achieves its most structured configuration. For higher concentrations, alcohol molecules tend to aggregate, reducing the strength of the hydrogen bond network, until reaching a point (x_3) in which water and ethanol diffusivities become independent. Certainly, and although a significant progress has been made in the study of the concentration dependence of the hydrogen bond network of alcohol/water mixtures, the mechanism is not fully understood.

Despite the abundant literature based on experimental studies, computational work on the determination of dielectric properties of mixtures is not very common. Nevertheless, some work has been carried out on this topic, leading to the development of both theoretical and empirical mixing rules for the interpolation of dielectric properties of mixtures from their pure constituents [90, 290–292]. Additionally, Zasetsky *et al.*. determined the dielectric spectrum of methanol/water mixtures in the GHz/THz region using MD simulations [293]. In their study, the authors introduce a method to obtain the distribution of relaxation times from the dipole moment autocorrelation function. Analysing the individual contribution of the two components of the mixture, they conclude that both exhibit two distinct relaxation modes. Additionally, accurate values of the static dielectric constant of ethanol/water mixtures have also been obtained using molecular dynamics simulations with polarisable force fields [287,

TABLE 5.1: Mole fractions and number of molecules employed in the molecular dynamics simulations of ethanol/water mixtures carried out in this work.

x_{EtOH}	$\mathrm{N_{EtOH}}$	$\mathrm{N_{water}}$
0.00	0	1000
0.08	80	920
0.20	200	800
0.50	500	500
0.80	800	200
1.00	1000	0

288]. However, as far as we are aware, no previous attempt has been carried out to obtain dielectric spectra of ethanol/water mixtures through MD simulations.

In this chapter, we show the results we have obtained for the concentration dependence of the dielectric response of ethanol/water mixtures using MD simulations. We compare our predictions with the ones obtained through alternative empirical methods. Additionally, and with the aim of providing further information on the origin of the dielectric response in alcohol/water systems, we decompose the result into different contributions at both the total component and the molecule levels. The results obtained in this work are therefore helpful to reach a better understanding of changes in the dynamics of alcohol/water mixtures with increasing alcohol concentration, and can be useful to model microwave heating profiles of these systems.

5.2 Simulation Details and Analysis

5.2.1 Simulation details

The conditions used to carry out the molecular dynamics simulations which results are presented in this chapter are equivalent to the ones described in section 4.2.2. Ethanol/water mixtures of different concentrations are simulated, as shown in Table 5.1.

Ethanol is modelled by means of the TraPPE-UA force field, which showed the best performance for the prediction of dielectric spectra for pure ethanol, according to the results obtained in Chapter 4. In the case of water, we decide to use a modified version of the Fw-SPC model, in which we suppress bond stretching flexibility. According to the results obtained for pure water (see Table 4.2), flexibility slows down the dielectric response, resulting in longer relaxation times for the Fw-SPC model with respect to the

experimental value. By constraining bond stretching, we intend to speed up the dielectric response of the Fw-SPC model, while hopefully preserving its ability to reproduce the static dielectric constant of water to an acceptable level. In addition, we obtain compatibility between the modified Fw-SPC model and the TraPPE-UA force field, in the sense that both are characterised by rigid bonds and flexible angles. The suppression of bond stretching allows the use of longer time steps (1 fs) and reduces the duration of our simulations, while obtaining reasonable results as shown below.

Previous studies have used polarisable force fields [287, 288]. However, we consider this level of detail is not necessary for the properties we intend to predict. In fact, using non-polarisable force fields, we are able to perform simulations that are 5 to 10 times longer. This is important for the accurate representation of the dielectric response since we assure we are covering enough correlation lengths (see section 3.4.2). In our work, we perform four independent simulations of 25 ns at every concentration, in line with the methodology used in Chapter 4.

5.2.2 Analysis of results: definition of dipole moment correlation functions

As mentioned previously, in this chapter we provide a deeper analysis of the mechanisms leading to the dielectric response of ethanol/water mixtures by decomposing the total dielectric response into different contributions. In Table 5.2 we extend the definition of dipole moment correlation functions (see Section 3.4) to binary systems, and we introduce the separate levels of detail we analyse in this case. This includes the average contribution of individual molecules ($\boldsymbol{\phi_{\mathbf{mol\,1}}}(t)$, $\boldsymbol{\phi_{\mathbf{mol\,2}}}(t)$), the total contribution of each component of the mixture ($\boldsymbol{\phi_{\mathbf{1}}}(t)$, $\boldsymbol{\phi_{\mathbf{2}}}(t)$), and the global response of the entire simulation box ($\boldsymbol{\phi_{\mathbf{box}}}(t)$). Note that for binary systems, the observable global dielectric response is not only generated by the sum within the self-interactions of the individual constituents of the mixture ($\mathbf{C_{11}}(\mathrm{t})$ and $\mathbf{C_{22}}(\mathrm{t})$). Instead, the cross-correlations between species ($\mathbf{C_{12}}(\mathrm{t})$ and $\mathbf{C_{21}}(\mathrm{t})$) also have to be taken into account.

TABLE 5.2: Definition of different levels of dipole moment correlation functions in binary mixtures.

Time series	Correlation function	Normalised correlation function
Molecule		
$\mathbf{M_{mol\,1\,j}}(t) = \sum_{\alpha}^{N_{atom}} [\mathbf{r}_{\alpha j}(t) - \mathbf{r}_{0j}(t)]\ q_{\alpha j}$	$\mathbf{C_{mol\,1\,j}}(t) = \langle \mathbf{M_{mol\,1\,j}}(t) \cdot \mathbf{M_{mol\,1\,j}}(0) \rangle$	$\boldsymbol{\phi}_{\mathbf{mol\,1}}(t) = \frac{1}{N_{mol\,1}} \sum_{j}^{N_{mol\,1}} \frac{\mathbf{C_{mol\,1\,j}}(t)}{\mathbf{C_{mol\,1\,j}}(0)} = \frac{1}{N_{mol\,1}} \sum_{j}^{N_{mol\,1}} \frac{\langle \mathbf{M_{mol\,1\,j}}(t) \cdot \mathbf{M_{mol\,1\,j}}(0) \rangle}{\langle \mathbf{M_{mol\,1\,j}}(0) \cdot \mathbf{M_{mol\,1\,j}}(0) \rangle}$
$\mathbf{M_{mol\,2\,j}}(t) = \sum_{\alpha}^{N_{atom}} [\mathbf{r}_{\alpha j}(t) - \mathbf{r}_{0j}(t)]\ q_{\alpha j}$	$\mathbf{C_{mol\,2\,j}}(t) = \langle \mathbf{M_{mol\,2\,j}}(t) \cdot \mathbf{M_{mol\,2\,j}}(0) \rangle$	$\boldsymbol{\phi}_{\mathbf{mol\,2}}(t) = \frac{1}{N_{mol\,2}} \sum_{j}^{N_{mol\,2}} \frac{\mathbf{C_{mol\,2\,j}}(t)}{\mathbf{C_{mol\,2\,j}}(0)} = \frac{1}{N_{mol\,2}} \sum_{j}^{N_{mol\,2}} \frac{\langle \mathbf{M_{mol\,2\,j}}(t) \cdot \mathbf{M_{mol\,2\,j}}(0) \rangle}{\langle \mathbf{M_{mol\,2\,j}}(0) \cdot \mathbf{M_{mol\,2\,j}}(0) \rangle}$
Component		
$\mathbf{M_1}(t) = \sum_{j}^{N_{mol\,1}} \sum_{\alpha}^{N_{atom}} [\mathbf{r}_{\alpha j}(t) - \mathbf{r}_{0j}(t)]\ q_{\alpha j}$	$\mathbf{C_{11}}(t) = \langle \mathbf{M_1}(t) \cdot \mathbf{M_1}(0) \rangle$	$\boldsymbol{\phi}_{\mathbf{1}}(t) = \frac{\mathbf{C_{11}}(t)}{\mathbf{C_{11}}(0)} = \frac{\langle \mathbf{M_1}(t) \cdot \mathbf{M_1}(0) \rangle}{\langle \mathbf{M_1}(0) \cdot \mathbf{M_1}(0) \rangle}$
$\mathbf{M_2}(t) = \sum_{j}^{N_{mol\,2}} \sum_{\alpha}^{N_{atom}} [\mathbf{r}_{\alpha j}(t) - \mathbf{r}_{0j}(t)]\ q_{\alpha j}$	$\mathbf{C_{22}}(t) = \langle \mathbf{M_2}(t) \cdot \mathbf{M_2}(0) \rangle$	$\boldsymbol{\phi}_{\mathbf{2}}(t) = \frac{\mathbf{C_{22}}(t)}{\mathbf{C_{22}}(0)} = \frac{\langle \mathbf{M_2}(t) \cdot \mathbf{M_2}(0) \rangle}{\langle \mathbf{M_2}(0) \cdot \mathbf{M_2}(0) \rangle}$
	$\mathbf{C_{12}}(t) = \mathbf{C_{21}}(t) = \langle \mathbf{M_1}(t) \cdot \mathbf{M_2}(0) \rangle$	
Box		
$\mathbf{M_{box}}(t) = \sum_{j}^{N_{mol}} \sum_{\alpha}^{N_{atom}} [\mathbf{r}_{\alpha j}(t) - \mathbf{r}_{0j}(t)]\ q_{\alpha j}$	$\mathbf{C_{box}}(t) = \langle \mathbf{M_{box}}(t) \cdot \mathbf{M_{box}}(0) \rangle$	$\boldsymbol{\phi}_{\mathbf{box}}(t) = \frac{\mathbf{C_{box}}(t)}{\mathbf{C_{box}}(0)} = \frac{\langle \mathbf{M_{box}}(t) \cdot \mathbf{M_{box}}(0) \rangle}{\langle \mathbf{M_{box}}(0) \cdot \mathbf{M_{box}}(0) \rangle}$
	$\mathbf{C_{box}}(t) = \mathbf{C_{11}}(t) + \mathbf{C_{12}}(t) + \mathbf{C_{21}}(t) + \mathbf{C_{22}}(t)$	

$\mathbf{r}_{\alpha j}$: position vector of atom α in molecule j (x, y, z coordinates); $q_{\alpha j}$: charge of atom α in molecule j;
$N_{mol\,1}$: number of molecules of component 1; $N_{mol\,2}$: number of molecules of component 2; N_{mol}: total number of molecules;
N_{atom}: number of atoms in molecule;
$\langle \cdots \rangle$ represents an average over all available samples

5.3 Results and Discussion

5.3.1 Thermodynamic properties

In analogy with the work carried out in Chapter 4, we initially validate our simulations by determining a number of thermodynamic properties. Figure 5.1 shows the influence of composition on density ρ, thermal expansion coefficient α_{p}, isothermal compressibility κ_{T} and heat capacity $\mathrm{c_p}$ of ethanol/water mixtures. In general, the main experimental trends are satisfactorily captured by the force fields employed in this work. The evolution of density is particularly well predicted, including a closer estimation of the density of pure water by the modified semi-flexible Fw-SPC model, with respect to the original fully flexible Fw-SPC model (see Table 4.1). For both thermal expansion coefficient and heat capacity, the simulations provide an outstanding prediction of these properties for pure ethanol, however the results for pure water are somehow overestimated. The restriction of bond stretching in the modified Fw-SPC model results in higher thermal expansion coefficient and lower heat capacity (see Table 4.1). The high values obtained for pure water explain the general overprediction of these properties with respect to experimental results at intermediate concentrations. Even though, the evolution with mixture concentration seems to be conserved, especially for heat capacity, where more data are available for comparison. Finally, the isothermal compressibility clearly follows the experimental trend with again a slight overestimation with respect to experimental data. The minimum of isothermal compressibility observed in the experimental results at a mole fraction of ethanol of approximately 0.1 can only be guessed from our predictions. Additional simulations in that concentration region would be required to confirm this feature. In general, the Fw-SPC presents slight deviations in the prediction of absolute values of some thermodynamic properties of water which affect the estimation of these properties of ethanol/water mixtures, particularly at low ethanol concentrations. However, as shown in Chapter 4, this is compensated by a good prediction of dielectric properties which is the main focus of this work.

5.3.2 Dipole moment autocorrelation function in binary systems

In Chapter 4, we limited ourselves to the use of single relaxations in the analysis of the dielectric response of one component systems. However, as mentioned in the introduction of this chapter, ethanol/water mixtures are generally modelled as the superposition of three relaxation processes. Only in the case of pure water, does a two relaxation process suffice to reproduce the response. As an example, in Fig. 5.2 we compare the performance of different models when fitting the dipole moment autocorrelation function (ACF) of an equimolar ethanol/water mixture at 298 K and 1 bar. As expected, the use of a single Havriliak-Negami (HN) relaxation provides a better result than a single Debye process. Nevertheless, it is clearly observed how a

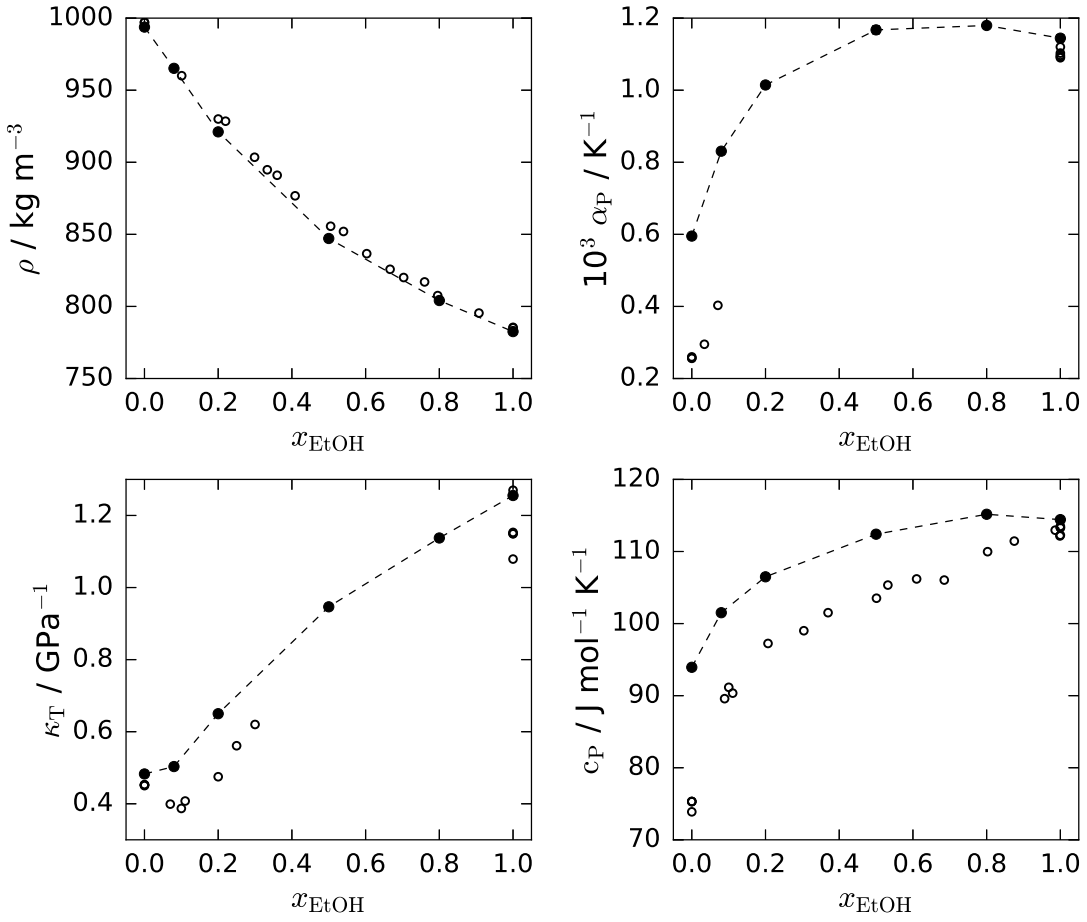

FIGURE 5.1: Influence of composition on thermodynamic properties of ethanol/water mixtures at 298 K and 1 bar. Filled symbols represent results obtained from our simulations. Open symbols correspond to experimental data obtained from different sources: density ρ [243, 294], thermal expansion coefficient α_{p} [203, 207, 295–301], isothermal compressibility κ_{T} [204, 207, 295, 302–309], and heat capacity $\mathrm{c_p}$ [310–317]. Error bars are smaller than symbol sizes. The dashed lines are a guide to the eye.

minimum of two relaxation processes (1 HN + 1 Debye model – Eq. (3.92)) is required to reproduce accurately the result obtained in our simulations. The additional Debye relaxation is included to take into account fast processes occurring at very short correlation times. Moreover, the introduction of an intermediate Debye relaxation process (1 HN + 2 Debye model – Eq. (3.96)) further improves the accuracy of the fit in that region. This result is consistently observed in the wide range of concentrations we have included in our study. Therefore, in the following we will use a combination of one Havriliak-Negami and two Debye relaxation processes to fit dipole moment ACF of ethanol/water mixtures, with the noted exception of pure water, for which adding an intermediate relaxation process does not significantly improve the fit.

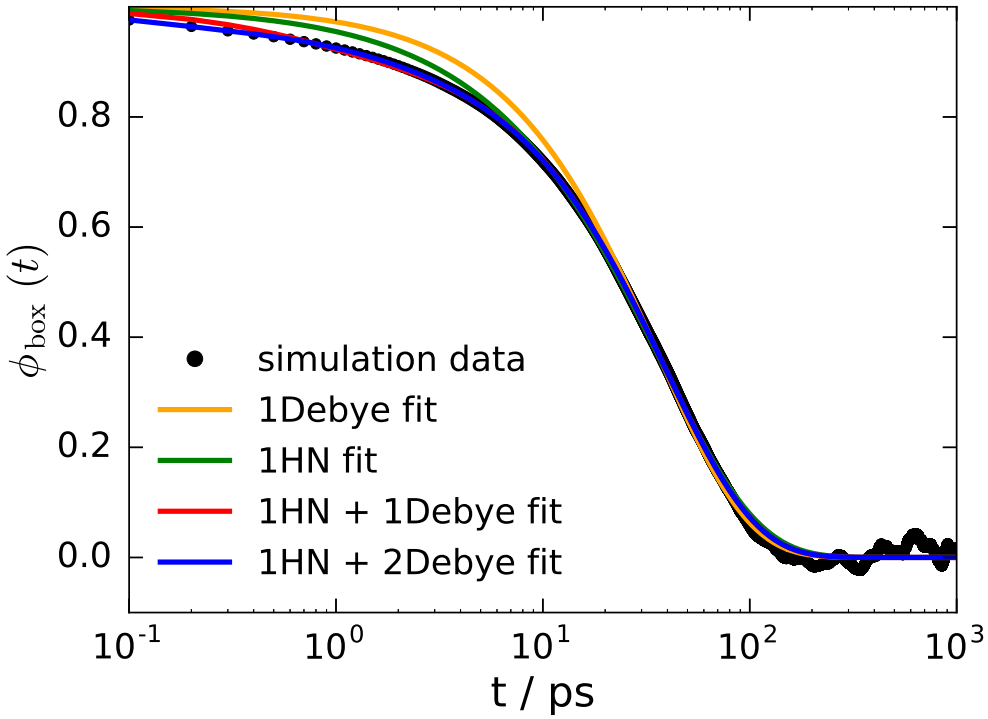

FIGURE 5.2: Comparison of the performance of different models used for the fit of dipole moment ACF of mixtures. Data in the figure correspond to a simulation performed at 298 K and 1 bar for an ethanol/water mixture with an ethanol mole fraction of 0.5. Black circles represent the dipole moment ACF obtained from simulation. Four models are compared: single Debye (orange), single HN (green), 1 HN + 1 Debye (red) and 1 HN + 2 Debye (blue).

5.3.3 Dielectric response of ethanol/water mixtures through MD simulations

The literature survey performed in the introduction of this chapter revealed the significant influence of concentration on the dielectric response of binary systems. In Fig. 5.3 we present the results we obtain for the concentration-dependence of the dipole moment ACF of ethanol/water mixtures. As previously explained in Chapter 4, the results shown in Fig. 5.3 originate from averaging dipole moment ACFs obtained from four independent simulations. The generally small error bars indicate a low variability between the different runs for this particular system. As mentioned above, a 1 HN + 1 Debye model is used for pure water, while a 1 HN + 2 Debye fit is used when ethanol is present in the mixture.

Observing Fig. 5.3, we realise that the initial relaxation at short times is practically independent of composition. However, the influence of concentration becomes clear when we focus on the main relaxation process. The faster decays observed as the mixture approaches pure water are an indication of faster dynamics in the reorganisation of the hydrogen bond structure. As the concentration of water increases, more and

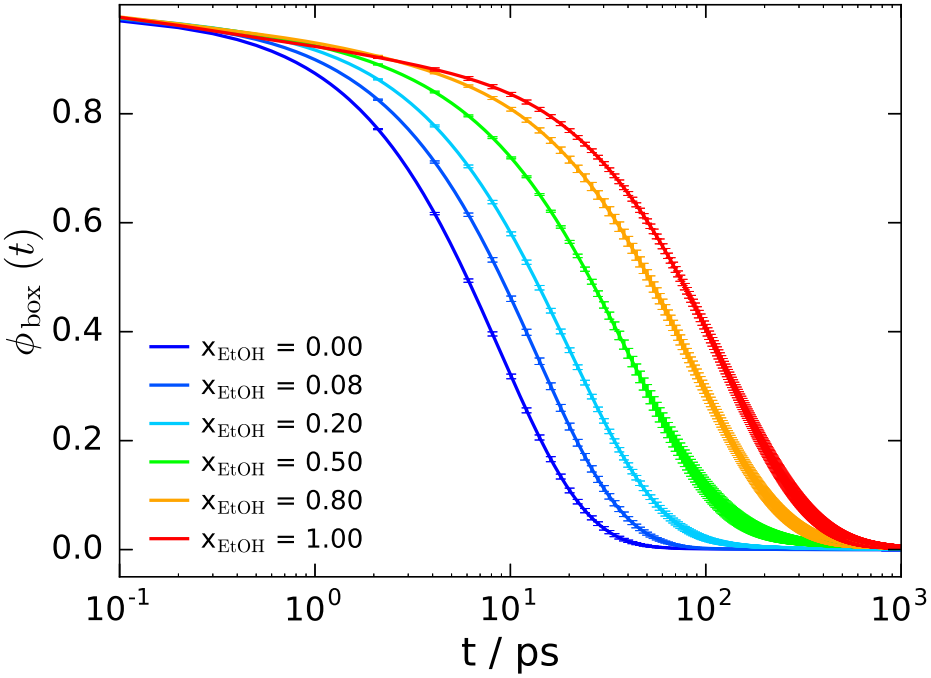

FIGURE 5.3: Evolution of dipole moment autocorrelation function with composition in ethanol/water mixtures at 298 K and 1 bar

more hydrogen bonding sites become available, which results in more frequent modifications of the network. Although it is not easily appreciated, an intermediate and less intense process is also captured by the model. The influence of concentration on the different relaxation parameters given by these models is summarised in Table 5.3 and Fig. 5.4, 5.5 and 5.6.

The first aspect to note observing Fig. 5.4 is the surprisingly good agreement between the main relaxation time (τ_1) obtained from our simulations and the experimental data. A slight underprediction is observed, particularly at intermediate ethanol compositions, but the trend in the data is equivalent. Small differences in the value of τ_1 can be attributed to the fact that most experimental studies have not used a 1 HN + 2 Debye model, and employ simpler expressions instead. Some model the main relaxation by means of three purely Debye processes or use a lower number of relaxations. In any case, this represents a significant achievement in terms of predicting microwave heating rates, since this process is dominated by this relaxation, which corresponds to the reorganisation of the hydrogen bond network according to the literature [234, 242–245, 249, 270, 271]. According to the experimental results, two distinct, nearly linear regions (in logarithmic scale) can be observed and intersect at a mole fraction of approximately 0.2, as previously noted by Bao *et al.* [242]. Despite the reduced number of simulation results, this feature seems to be captured by the force fields used in this work. This mole fraction has previously been reported as a turning point for several processes in ethanol/water mixtures. Below this concentration, ethanol molecules

TABLE 5.3: Dielectric relaxation parameters for ethanol/water mixtures at 298 K and 1 bar.

x_{EtOH}	0.00	0.08	0.20	0.50	0.80	1.00
τ_1/ps	8.93 ± 0.10	13.8 ± 0.3	21.3 ± 0.6	41.3 ± 0.7	85 ± 3	125 ± 3
A_1	0.981 ± 0.004	0.959 ± 0.005	0.95 ± 0.02	0.943 ± 0.008	0.920 ± 0.006	0.910 ± 0.005
α	0.990 ± 0.004	0.992 ± 0.003	0.97 ± 0.02	0.94 ± 0.03	0.97 ± 0.02	0.98 ± 0.02
β	1.00	1.00	0.99 ± 0.02	1.00	1.00	1.00
τ_3/ps	–	1.3 ± 0.4	1.3 ± 1.0	1.0 ± 0.4	1.5 ± 0.4	1.4 ± 0.4
A_3	–	0.018 ± 0.004	0.03 ± 0.02	0.032 ± 0.004	0.046 ± 0.004	0.045 ± 0.001
τ_4/ps	0.03 ± 0.01	0.066 ± 0.005	0.04 ± 0.02	0.09 ± 0.02	0.14 ± 0.02	0.18 ± 0.02
A_4	0.019 ± 0.001	0.023 ± 0.001	0.016 ± 0.004	0.025 ± 0.004	0.034 ± 0.002	0.045 ± 0.004
ε_0	78.4	65.6	55.1	39.2	29.4	24.7
$\varepsilon_{0\,sim}$	76.0 ± 0.7	62.8 ± 0.2	49.9 ± 0.4	29.2 ± 0.3	21.6 ± 0.5	17.7 ± 0.4
ε_∞	3.35	3.24	3.08	2.68	2.27	2.00

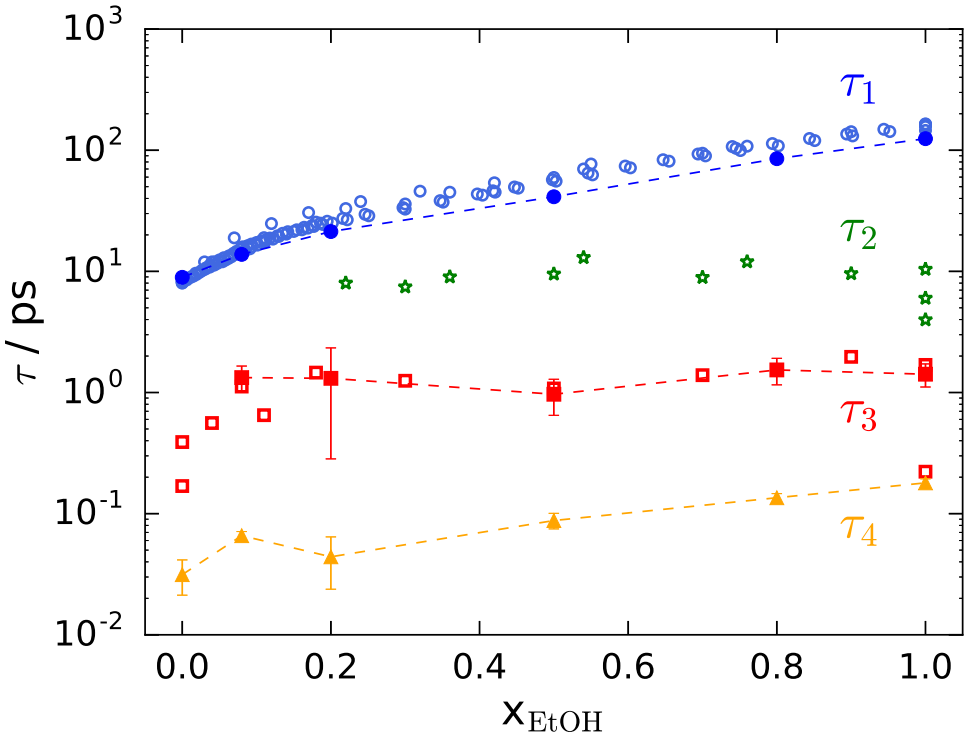

FIGURE 5.4: Variation of relaxation times with concentration in ethanol/water mixtures at 298 K and 1 bar. Circles represent the relaxation times of the dominant HN relaxation (1), while stars, squares and triangles correspond to the intermediate (2), fast (3) and very fast (4) processes, respectively. Filled symbols correspond to the fit of the 1 HN + 2 Debye model to simulation data. In the case of pure water (x_{EtOH} = 0), a 1 HN + 1 Debye model is used. Open symbols correspond to experimental data obtained from different sources: τ_1 [234, 242–244, 249, 271], τ_2 [234, 243, 271] and τ_3 [234, 271]. The dashed lines are a guide to the eye.

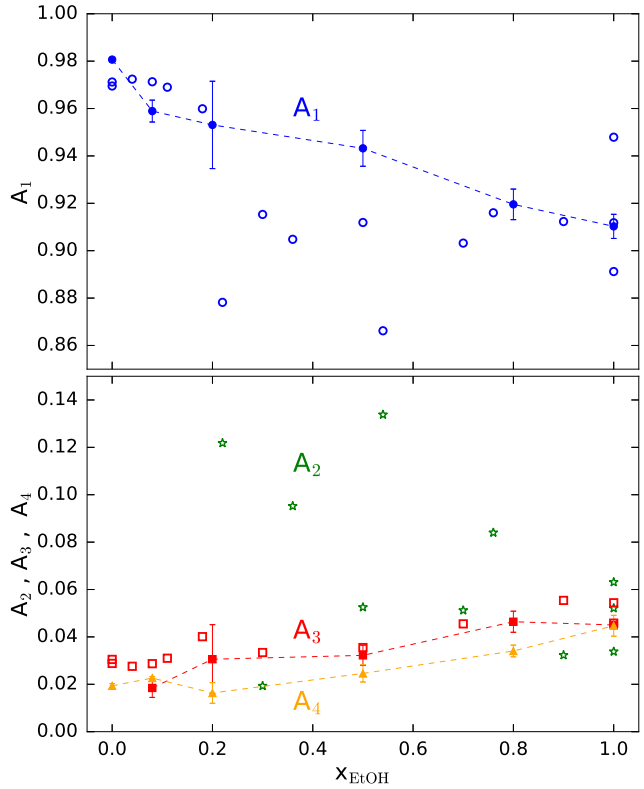

FIGURE 5.5: Variation of relaxation intensities with concentration in ethanol/water mixtures at 298 K and 1 bar. Circles represent the relaxation intensities of the dominant HN relaxation (1), while stars, squares and triangles correspond to the intermediate (2), fast (3) and very fast (4) processes, respectively. Filled symbols correspond to the fit of the 1 HN + 2 Debye model to simulation data. In the case of pure water ($x_{\mathrm{EtOH}} = 0$), a 1 HN + 1 Debye model is used. Open symbols correspond to experimental data obtained from different sources: A_1 [234, 243, 271], A_2 [234, 243, 271] and A_3 [234, 271]. The dashed lines are a guide to the eye.

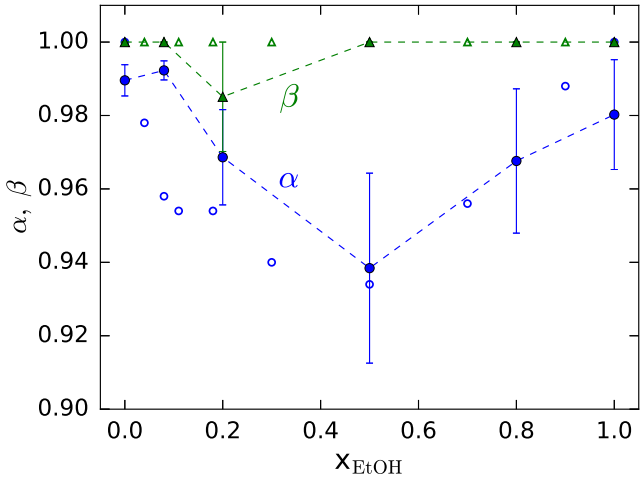

FIGURE 5.6: Variation of Havriliak-Negami's α and β parameters with concentration in ethanol/water mixtures at 298 K and 1 bar. Circles represent values of parameter α, while triangles correspond to parameter β. Filled symbols correspond to the fit of the 1 HN + 2 Debye model to simulation data. In the case of pure water ($x_{\mathrm{EtOH}} = 0$), a 1 HN + 1 Debye model is used. Open symbols correspond to experimental data [234]. The dashed lines are a guide to the eye.

are believed to participate in circular clusters commonly observed in pure water, at the price of slowing down the dielectric response [242]. For higher concentrations, self-interactions between ethanol molecules lead to a different organisation of the hydrogen bond network. In addition, at this concentration both activation enthalpy and activation entropy of the dominant relaxation process reach their maximum value, and the shear viscosity exhibits a relative minimum [243, 244].

Our simulations seem to fully capture the fast relaxations associated to formation and breakage of hydrogen bonds, with relaxation times $\tau_3 \approx 1 - 2$ ps. However, it was not possible to discern an additional intermediate process ($\tau_2 \approx 7 - 12$ ps), as seen in experimental studies, and related to the formation of ethanol chains at higher ethanol concentrations [234, 243, 271, 272, 274]. It is possible that the force fields employed in this work are not able to reproduce this phenomenon. Finally, the accurate fit of dipole moment ACFs generated through simulations requires an even faster process ($\tau_4 \approx 0.02 - 0.2$ ps). Since, these values are greater than the time step used in our simulations (1 fs), but less than the trajectory sampling times (0.1 ps), this process cannot be attributed to any physical mechanism captured by the simulations, and could be the result of the contribution of several high frequency phenomena. Nevertheless, Li *et al.* [271] observed relaxation times τ_4 in this same order of magnitude for pure ethanol. In summary, we can conclude that although our results require the same number of relaxation processes as the most elaborate experimental fits [234, 243, 271], the intermediate relaxation (τ_2) is not captured by our models, and a very fast process (τ_4) appears, whith an uncertain physical mechanism. Even so, the excellent results obtained for the main relaxation process (τ_1) and the fast process (τ_3) allow for further interpretation of the results in terms of the dynamics of the hydrogen bond network.

Analysing the intensity of the different relaxation processes, the relative intensity of the main process (A_1) is significantly larger than that of faster processes. As explained in the introduction of this chapter, this is due to the larger number of molecules implicated in this process, which is believed to correspond to the reorganisation of the entire hydrogen bond network [243]. Although less intense, faster processes seem to gain more importance as the concentration of ethanol in the mixture increases (see Fig. 5.5). In spite of the fact that experimental data are somewhat scattered, the same trend seems to appear for the relaxation processes we are able to reproduce (A_1 and A_3).

The symmetric and asymmetric deviations from the Debye model, given by the Havriliak-Negami parameters α and β, are both relatively weak. In the case of α, a minimum is observed for concentrations close to the equimolar mixture, in correspondence with experimental results [234]. This could have implications on the ideality of the mixture at those concentrations. Another important feature to consider is the nearly Debye behaviour of the main relaxation of pure ethanol (α = 0.98 and β = 1.00, see Table 5.3). This differs significantly from the results obtained in Chapter 4, where we used a single HN relaxation to fit the simulation data (α = 1.00 and β = 0.71, see Table 4.2). This suggests that the asymmetric broadening in the spectra observed for a

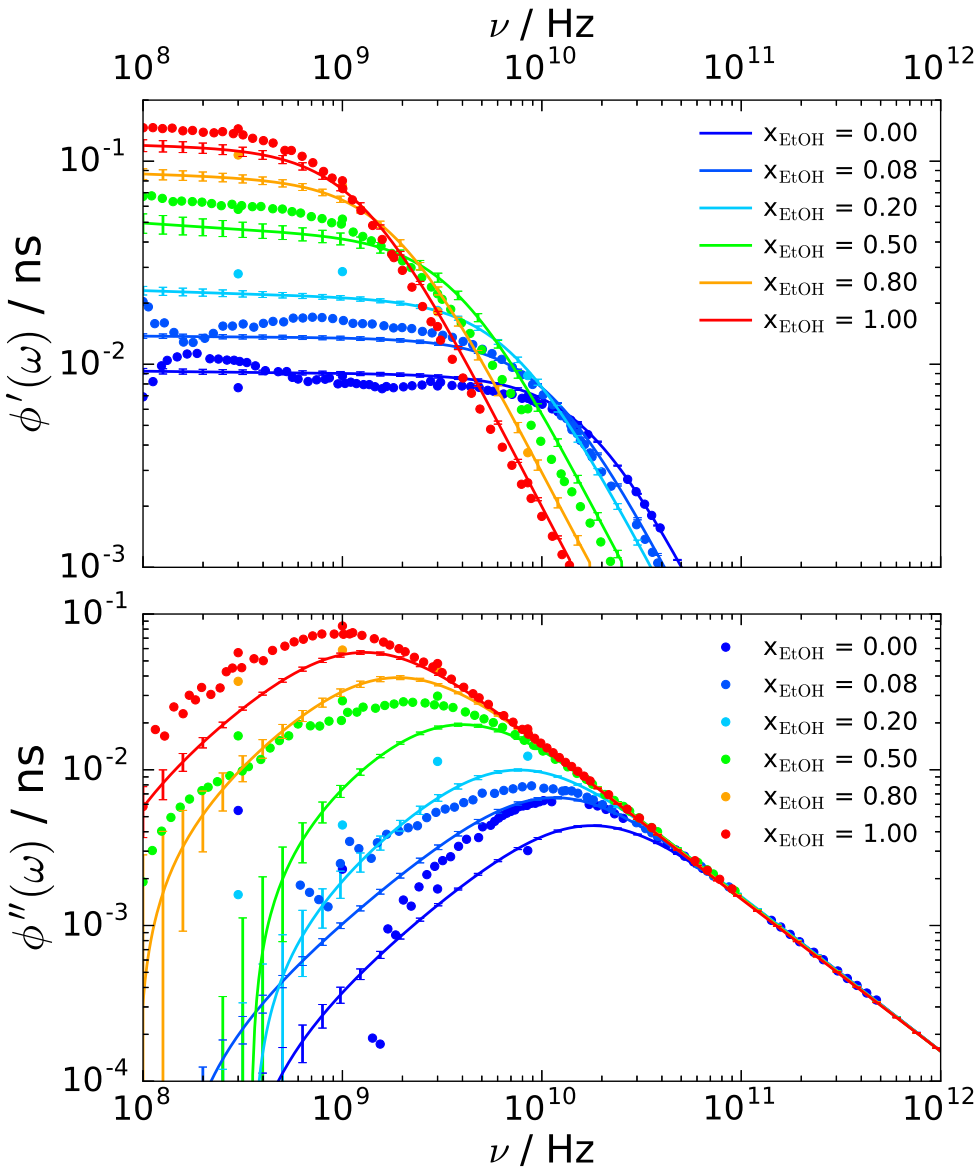

FIGURE 5.7: Dynamic response through the dipole moment ACF in the frequency domain for ethanol/water mixtures at 298 K and 1 bar. Solid lines represent results obtained in our simulations, while circles represent experimental values obtained from Eq. (4.15) using dielectric spectrum data from different sources [112, 234].

single relaxation fit was in fact due to the presence of additional relaxation processes at higher frequencies.

As we did for the analysis of one component systems, next we determine the dielectric response of ethanol/water mixtures in the frequency domain and compare it with available experimental data (using Eq. (4.15)). The results are shown in Fig. 5.7. In general our predictions tend to underestimate the experimental response, although they are always within the same order of magnitude. In addition, the main trends observed in the experimental data, such as the tendency to a more intense but slower response as the concentration of ethanol in the mixture increases, are reproduced adequately

by the models. The most significant deviations appear at intermediate concentrations, particularly for the equimolar mixture.

In order to obtain an accurate representation of the dielectric spectra of ethanol/water mixtures from our simulations, we need a good estimate of the static dielectric constant and the infinite frequency permittivity. In Chapter 4 we showed that the static dielectric constant ε_0 is difficult to determine accurately through MD simulations. In Fig. 5.8a we compare our results with available experimental data [112, 234, 243, 245]. Even though the simulations provide a relatively good prediction, we decide to use the experimental static dielectric constant instead, due to the deviations observed towards higher ethanol concentrations. However, the value of this magnitude for some of the concentrations we have considered in our simulations is unknown. Therefore, we decided to perform a stretched exponential fit through the available data to obtain the missing values:

$$\varepsilon_0 = A \exp\left[-\left(\frac{x_{EtOH}}{\tau_{\varepsilon_0}}\right)^{\gamma}\right] \tag{5.1}$$

with A = 78.4, τ_{ε_0} = 0.821 and γ = 0.740. The fit was forced to pass through the static dielectric constant of pure components, which are the values known with a higher level of certainty. In the case of the infinite frequency permittivity ε_∞, the available data are very scattered, as shown in Fig. 5.8b. Most values provided in the literature originate from fitting experimentally determined dielectric spectra to the Debye (Eq (3.72)) and the HN (Eq (3.74)) models. In this work, we select the results given by Li *et al.* [271] for pure ethanol (ε_∞ = 2.00) and pure water (ε_∞ = 3.35), and use a linear interpolation for intermediate concentrations. These authors use 3 Debye and 2 Debye relaxation models for ethanol and water, respectively, which is a similar strategy to the 1 HN + 2 Debye and 1 HN + 1 Debye models we are employing. The values of ε_0 and ε_∞ obtained according to this procedure, for the concentrations used in this work, are shown in Table 5.3.

With this in mind, and using the relaxation parameters summarised in Table 5.3, we proceed to calculate the dielectric spectra of ethanol/water mixtures. As previously stated, a 1 HN + 1 Debye model (Eq. (3.90)) was used for pure water, while a 1 HN + 2 Debye model (Eq. (3.94)) was employed for the remaining systems. The resulting spectra are shown in Fig. 5.9, and compared with experimental data. We can observe how the prediction of dielectric spectra of ethanol water/mixtures is outstanding, especially at low ethanol concentrations. In particular, the dielectric loss of pure water is extremely well described by the semi-flexible Fw-SPC model used in this work, outperforming the original Fw-SPC model which was shown in Chapter 4. Small deviations appear as the concentration of ethanol in the mixture increases. However, the results are still more than acceptable in those cases. As explained previously, the global dielectric response of the mixture slows down and becomes less intense as ethanol becomes the dominant component.

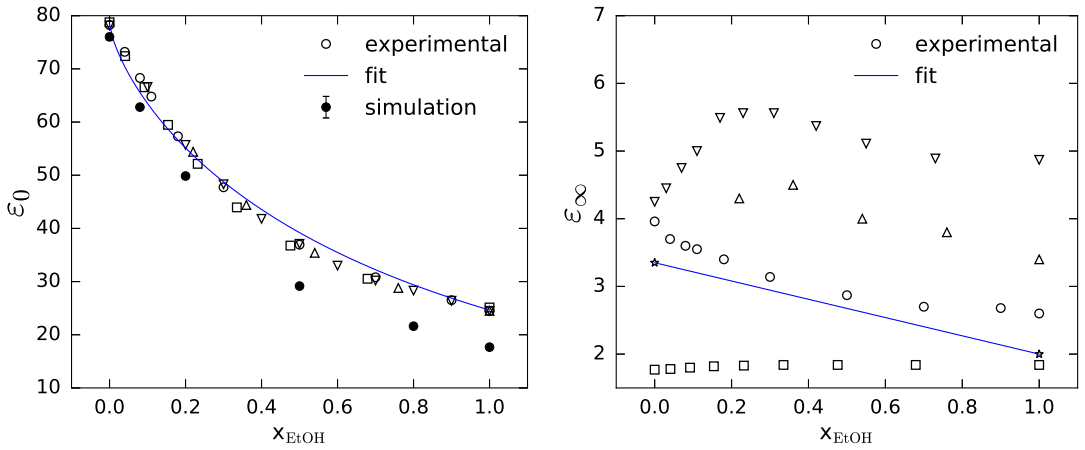

(a) Static dielectric constant

(b) Infinite frequency permittivity

FIGURE 5.8: Influence of concentration on the static dielectric constant and the infinite frequency permittivity of ethanol/water mixtures, at 298 K and 1 bar. Filled circles represent results obtained in our simulations. Open symbols correspond to experimental data obtained from different sources. For static dielectric constant: downward facing triangles [112], circles [234], upward facing triangles [243], squares [245]. For infinite frequency permittivity: circles [234], downward facing triangles [242], upward facing triangles [243], squares [245], stars [271]. Solid lines show fits to experimental data.

5.3.4 Comparison with mixing rules

The use of MD simulations to estimate dielectric spectra of mixtures can be compared to other predictive methods in the literature. In particular, mixing rules are usually employed to estimate properties of mixtures from their corresponding pure constituents. This approach has been used before to interpolate values of the static dielectric constant [318, 319], and the dielectric permittivity and loss at specific frequencies [320]. Although not so common, these techniques have also been extended to the interpolation of entire dielectric spectra of mixtures [321, 322]. The ability of mixing rules to provide reasonable estimates of dielectric spectra at intermediate concentrations have found some interesting applications. As an example, Abeyrathne *et al.* developed a strategy to predict volume fractions of mixtures from dielectric measurements [323].

Several different mixing rules have been developed over time, ranging from a simple linear interpolation to much more complex expressions. In Table 5.4, we compare the results of the application of some of the most common mixing rules with the predictions obtained through MD simulations for the estimation of the dielectric loss of the ethanol/water mixtures considered in this work. In order to assess the performance of the different models, we compute the relative mean-square deviation of their prediction with respect to the experimental value, within the range of frequencies for which the experimental dielectric loss of both pure water and pure ethanol are available. In order to take into account the lower availability of data at certain concentrations (i.e. $x_{\mathrm{EtOH}} = 0.20$ and $x_{\mathrm{EtOH}} = 0.80$), we introduce weights that ensure those concentrations

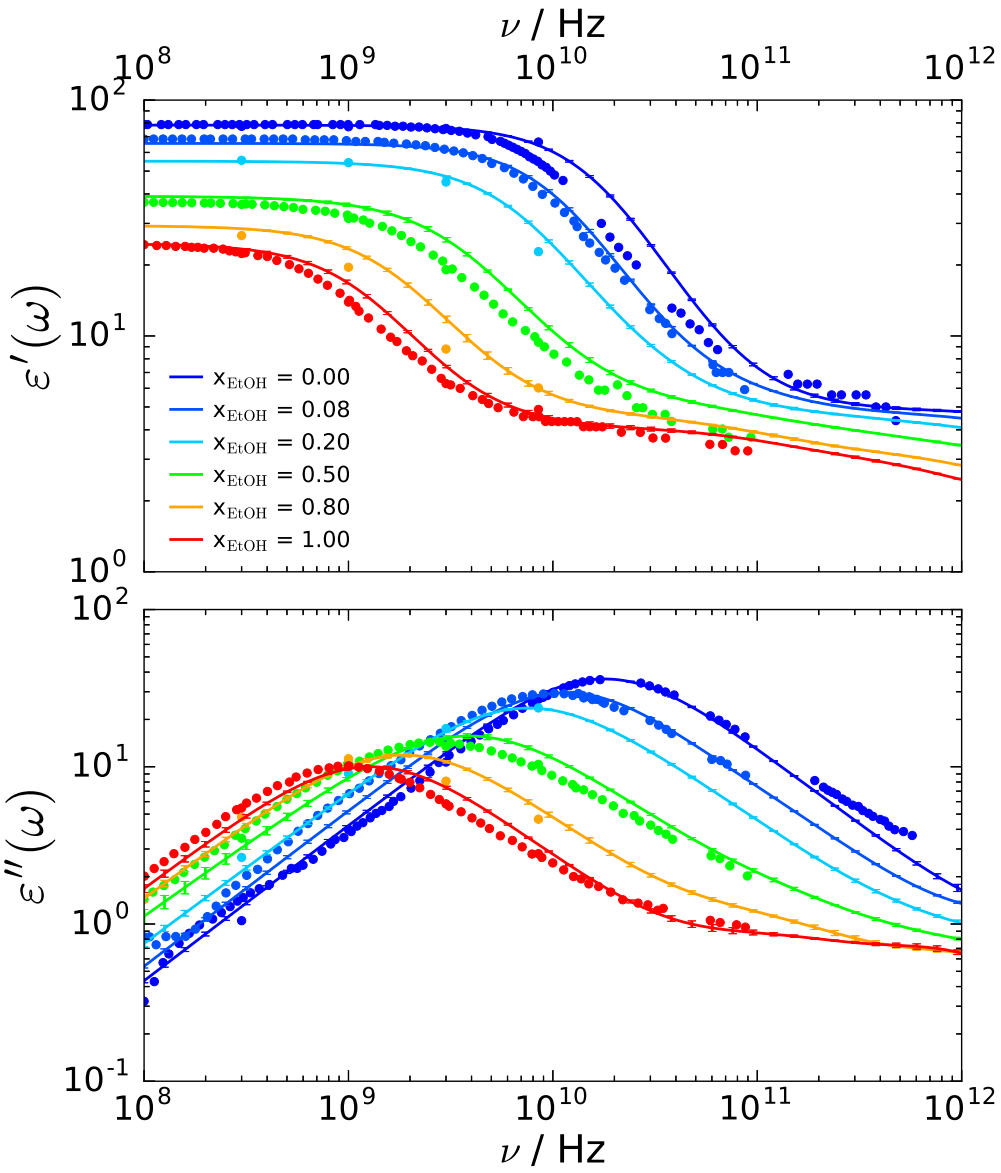

FIGURE 5.9: Dielectric spectra of ethanol/water mixtures at 298 K and 1 bar. Solid lines represent results obtained in our simulations, while circles represent experimental values obtained from different sources [112, 234].

are well represented:

$$\mathrm{MSD} = \sum_{\text{all } x_{\mathrm{EtOH}}} \frac{1}{N} \sum_{j}^{N} \left(\frac{\varepsilon''_{exp\,j} - \varepsilon''_{model\,j}}{\varepsilon''_{exp\,j}} \right)^2 \tag{5.2}$$

where N is the number of available experimental data points at each particular mole fraction.

It had previously been reported that, for this specific mixture, among the mixing rules available in the literature, the one that performs best at a frequency of 2.45 GHz is

TABLE 5.4: Comparison of MD simulation results with mixing rules for the prediction of dielectric loss of ethanol(1)/water(2) mixtures at 298 K and 1 bar.

Method	Equation	MSD
MD simulations	—	0.128 0.163*
Mixing rules		
Ideal mixture	$\varepsilon'' = x_{v1}\,\varepsilon_1'' + x_{v2}\,\varepsilon_2''$	0.472
Kraszewski [324]	$\varepsilon''^{\,1/2} = x_{v1}\,\varepsilon_1''^{\,1/2} + x_{v2}\,\varepsilon_2''^{\,1/2}$	0.344
Looyenga [325]	$\varepsilon''^{\,1/3} = x_{v1}\,\varepsilon_1''^{\,1/3} + x_{v2}\,\varepsilon_2''^{\,1/3}$	0.373
Power law (α = 0.590 - optimum)	$\varepsilon''^{\,\alpha} = x_{v1}\,\varepsilon_1''^{\,\alpha} + x_{v2}\,\varepsilon_2''^{\,\alpha}$	0.339
Lichtenecker-Rother [326, 327]	$\varepsilon'' = \varepsilon_1''^{\,x_{v1}}\,\varepsilon_2''^{\,x_{v2}}$	0.476
Bottcher-Bordewijk [328]	$x_{v1}\,\dfrac{3\varepsilon_1''}{\varepsilon_1'' + 2\varepsilon''} + x_{v2}\,\dfrac{3\varepsilon_2''}{\varepsilon_2'' + 2\varepsilon''} = 1$	0.404
Bruggeman [329]	$x_{v1}\,\dfrac{\varepsilon_1'' - \varepsilon''}{\varepsilon_1'' + 2\varepsilon''} + x_{v2}\,\dfrac{\varepsilon_2'' - \varepsilon''}{\varepsilon_2'' + 2\varepsilon''} = 0$	0.404
Maxwell-Garnett [330]	$\varepsilon'' = \varepsilon_1'' + 3\,x_{v2}\,\varepsilon_1''\,\dfrac{\varepsilon_2'' - \varepsilon_1''}{\varepsilon_2'' + 2\varepsilon_1'' - x_{v2}\,(\varepsilon_2'' - \varepsilon_1'')}$	0.574
Maxwell-Garnett (inverse) [322, 330]	$\varepsilon'' = \varepsilon_2'' + 3\,x_{v1}\,\varepsilon_2''\,\dfrac{\varepsilon_1'' - \varepsilon_2''}{\varepsilon_1'' + 2\varepsilon_2'' - x_{v1}\,(\varepsilon_1'' - \varepsilon_2'')}$	0.357
Peon-Iglesias [331]	$\varepsilon'' = \left(x_{v1}\,\varepsilon_1'' + x_{v2}\,\varepsilon_2''\right)\left[1 - \dfrac{2}{3}\ln\left(\dfrac{1 + x_{v1}\,(\varepsilon_1''/\varepsilon_2'' - 1)}{(\varepsilon_1''/\varepsilon_2'')^{x_{v1}}}\right)\right]$	0.452

* including pure components

the Kraszweski model (power law with exponent 0.5) [332]. The results we obtain (see Table 5.4) suggest that this fact persists when we extend the study to the full dielectric spectrum. The inverse Maxwell-Garnett model and a power law with exponent 1/3 (Looyenga model) provide similar results. However, more complex mixing rules such as Bottcher-Bordewijk, Bruggeman, Lichtenecker-Rother, Maxwell-Garnett and Peon-Iglesias models deviate to a larger extent. Observing that power laws seem to provide the best results, we performed an optimisation of the exponent α using the available data. The result shows how the use of a power law with exponent $\alpha = 0.590$ provides the best fit for the estimation of dielectric spectra of ethanol/water mixtures at 298 K and 1 bar. In Fig. 5.10, we compare the predictions given by this optimum power law model, the ideal mixture, and the results obtained through MD simulations. As shown in this figure, and confirmed by the value of the deviation with respect to experimental data shown in Table 5.4, the use of MD simulations provides a better estimate than any of the mixing rules considered here. Even, including the deviations in the predicted

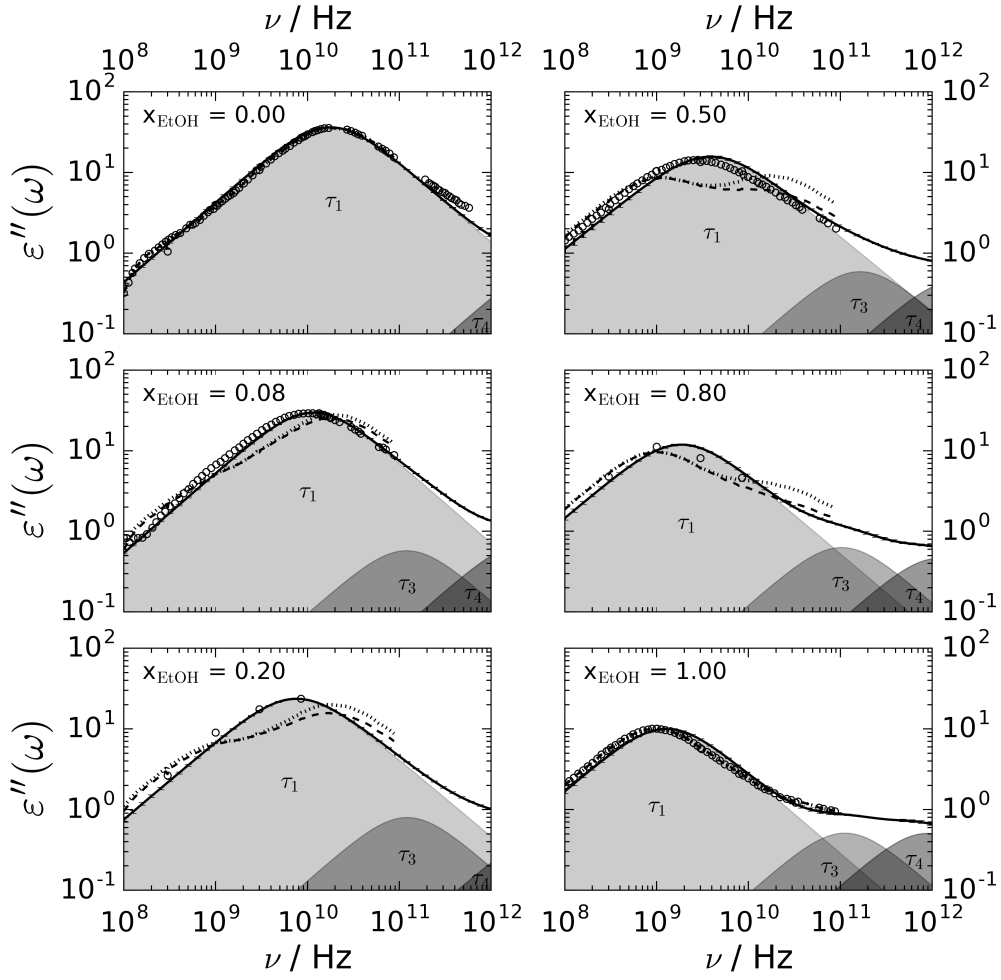

FIGURE 5.10: The dielectric spectra of ethanol/water mixtures at 298 K and 1 bar. Comparison between results obtained by means of MD simulations (solid lines), the best mixing rule (power law with exponent 0.590 – dashed lines) and the ideal mixture (dotted lines). The contribution of different relaxation processes to the dielectric spectra is shown as shaded regions in the figure. Finally, open circles represent experimental values obtained from different sources [112, 234].

dielectric loss of pure components from MD simulations, which is non-existent by definition for mixing rules, our estimate over the entire range of compositions is at least two times more accurate.

In Fig 5.10, we can observe how predictions obtained from mixing rules are very dependent on the contribution of the individual components (ethanol and water), as evidenced by the presence of two distinct peaks in the microwave region. However, this is not observed in the actual experimental results and the results obtained through MD simulations, for the dominant relaxation process. We can consider this as an indication that the main dielectric relaxation in ethanol/water mixtures results from a combined response rather than from individual contributions of the different components [242]. Furthermore, this could partially validate the hypothesis regarding the

significant influence of the dynamics of the global hydrogen bond network on the dielectric response of this system, as described in the introduction of this chapter.

We understand the limitations of MD simulations in terms of time requirements and accuracy of the current force fields. This is particularly true for systems that are not as well studied as the ethanol/water mixture. However, these results suggest that the use of MD simulations to predict dielectric spectra of mixtures clearly outperforms the use of mixing rules and should be considered as an alternative. The foreseeable development of more accurate atomistic force fields and the reduction of computational times in a near future further enhances this possibility. In addition, by using MD simulations, it is possible to provide a reasonable estimate for systems where the dielectric spectra of the pure components are not available - a situation that precludes the use of mixing rules. Finally, and probably most importantly, MD simulations are able to provide a much deeper insight on the physical mechanisms that result in the dielectric response, as we show below.

5.3.5 Contribution of the different relaxation processes

As a first illustration of the ability of our approach to improve the physical understanding of dielectric responses, in this section we study the decomposition of the dielectric spectra into different relaxation processes. Figure 5.10 shows the contribution of these processes to the global response for all the concentrations considered in this work. The parameters defining these processes, and their variation with mole fraction, have been reported previously in Table 5.3 and Figures 5.4, 5.5 and 5.6. In this representation it becomes clear how the different relaxation mechanisms cannot be individually assigned to specific components of the mixture. If we focus on the main relaxation (τ_1), only one dominant peak is observed in the spectra, and it is not formed by separate contributions of processes with the frequencies and amplitudes that correspond to the pure components. This reinforces the hypothesis that the mechanism behind the dominant relaxation originates from the global reorganisation of the entire structure of the fluid. The intensity of this process is significantly greater than that of the remaining faster processes because more molecules are involved in the response [272]. The relaxation mechanism shifts as a whole towards lower frequencies as the concentration of ethanol in the mixture increases, indicating that, as expected, the composition of the mixture is an important factor in the dynamics of the hydrogen bond network. As mentioned before, we do not seem to observe an intermediate relaxation process (τ_2), which had been associated with the presence of chain-like structures formed by ethanol molecules [272, 274]. However, we are able to detect two fast processes (τ_3 and τ_4) that have previously been identified as breaking and formation of individual hydrogen bonds in the literature [249, 273]. The frequency at which these mechanisms occur is not significantly affected by composition, as can be expected in such a local process.

Until this point, we have managed to show how the methodology and the models used in this work lead to an outstanding prediction of the concentration dependence of

TABLE 5.5: Dielectric relaxation parameters for the separate contribution of each component in ethanol/water mixtures at 298 K and 1 bar.

x_{EtOH}	0.00	0.08	0.20	0.50	0.80	1.00
Ethanol						
τ_1/ps	–	9.0 ± 0.8	15 ± 2	48 ± 3	88 ± 5	125 ± 3
A_1	–	0.81 ± 0.05	0.84 ± 0.04	0.76 ± 0.03	0.86 ± 0.02	0.910 ± 0.005
α	–	0.96 ± 0.02	0.90 ± 0.02	1.0	0.99 ± 0.01	0.98 ± 0.02
β	–	0.96 ± 0.03	1.00	0.98 ± 0.03	1.00	1.00
τ_3/ps	–	1.8 ± 0.7	1.9 ± 0.7	5.4 ± 0.8	5 ± 3	1.4 ± 0.4
A_3	–	0.09 ± 0.04	0.07 ± 0.03	0.15 ± 0.02	0.073 ± 0.008	0.045 ± 0.001
τ_4/ps	–	0.103 ± 0.003	0.117 ± 0.005	0.22 ± 0.02	0.25 ± 0.05	0.18 ± 0.02
A_4	–	0.100 ± 0.003	0.091 ± 0.004	0.096 ± 0.004	0.071 ± 0.007	0.045 ± 0.004
Water						
τ_1/ps	8.93 ± 0.1	14.0 ± 0.5	21.0 ± 0.7	34 ± 2	70 ± 20	–
A_1	0.981 ± 0.004	0.973 ± 0.003	0.976 ± 0.002	0.955 ± 0.006	0.95 ± 0.02	–
α	0.990 ± 0.004	0.996 ± 0.002	0.97 ± 0.02	0.93 ± 0.03	0.94 ± 0.04	–
β	1.00	0.96 ± 0.02	0.93 ± 0.02	0.94 ± 0.04	0.76 ± 0.10	–
τ_4/ps	0.03 ± 0.01	0.11 ± 0.04	0.06 ± 0.02	0.15 ± 0.05	0.10 ± 0.04	–
A_4	0.019 ± 0.001	0.027 ± 0.003	0.024 ± 0.002	0.045 ± 0.005	0.06 ± 0.02	–

the dielectric spectrum of ethanol/water mixtures. This is a very important result, since it allows the estimation of the dielectric response, with a good level of confidence, at additional intermediate concentrations that have not been determined experimentally. In addition, it opens the possibility to study the influence on the dielectric response of additional variables, such as temperature as we show in Chapter 6.

However, in terms of the conclusions drawn from these results, most could have been derived from the already existent experimental dielectric spectra. In the following, we demonstrate the potential of MD simulations to obtain results that, as far as we are aware, are not accessible by current experimental techniques. Using the fact that we can track the trajectory of molecules, and therefore the time-evolution of the dipole moment of these individual molecules, we can easily discern the contribution of the two components of the mixture to the dielectric response. We perform this analysis at two different levels: the total contribution of each component, by adding the effect of all the molecules of a particular component, and the contribution of both components at the individual molecule level.

5.3.6 Total dielectric contribution of different components and importance of cross-interactions

The assumption that the main dielectric response of ethanol/water mixtures results from a combined effect of both components is a mere hypothesis when we base it only on the results presented this far. The advantage of MD simulations is that we can examine the role of the individual contributions of each component on its own, as well as the cross-interactions between ethanol and water molecules, which have shown to play a significant role in the dielectric response [234, 243, 244]. In order to do so, first we decompose the global response in terms of the individual contributions of both components and apply the same methodology we used to analyse the dipole moment ACF of the entire simulation box. The results of the fits are summarised in Table 5.5. In this case we also used a 1 HN + 2 Debye model for ethanol and a 1 HN + 1 Debye representation for water.

In Fig. 5.11, we show the evolution with mixture composition of the ACF of the dipole moment of ethanol ($\boldsymbol{\phi_1}(\mathrm{t})$) and water ($\boldsymbol{\phi_2}(\mathrm{t})$) as components (see Table 5.2). If the dynamics of one component of the mixture were not affected by the presence of the other species, the response of these individual constituents would not be affected by the composition of the mixture. This would result in a constant relaxation time of the individual species with composition. The global response would be given by a weighted average of the individual responses, that would lead to the presence of two separate contributions in the dielectric spectrum. However, as we can observe, rather than remaining fixed, the response of each individual component is clearly affected by the composition of the mixture. In fact, we observe how the dielectric response of ethanol becomes faster as the concentration of water in the mixture increases, while the response of water slows down when ethanol content rises. This suggests the existence of a coupling mechanism between the two species, by which the relaxation time of the dominant component seems to govern the relaxation time of the entire mixture, as we can observe in the inset of Fig. 5.11. In this figure, we also observe how, in the case of the main relaxation process (τ_1), the response of ethanol becomes surprisingly faster than that of water at low ethanol concentrations. This could be due to the presence of 'free' ethanol molecules that do not form part of the extended hydrogen bond network at those concentrations and therefore have more freedom to rotate.

As supplementary information, in Appendix D, we include the evolution with concentration of the intensity of the different processes (Fig. D.1), and the parameters α and β of the dominant HN relaxation (Fig. D.2). Additionally, in Fig. D.3 we show the frequency-domain representation of the results presented in Fig. 5.11. One of the most remarkable findings in these results is the fact that additional faster processes are more intense for ethanol than for water, although the distribution of intensities for the entire mixture seems to more closely follow the trend shown by water. Most systems exhibit Debye behaviour for the dominant relaxation ($\alpha > 0.90$ and $\beta > 0.90$). Only at low concentrations of water (x_{EtOH} = 0.8) this trend appears to deviate in the form of an

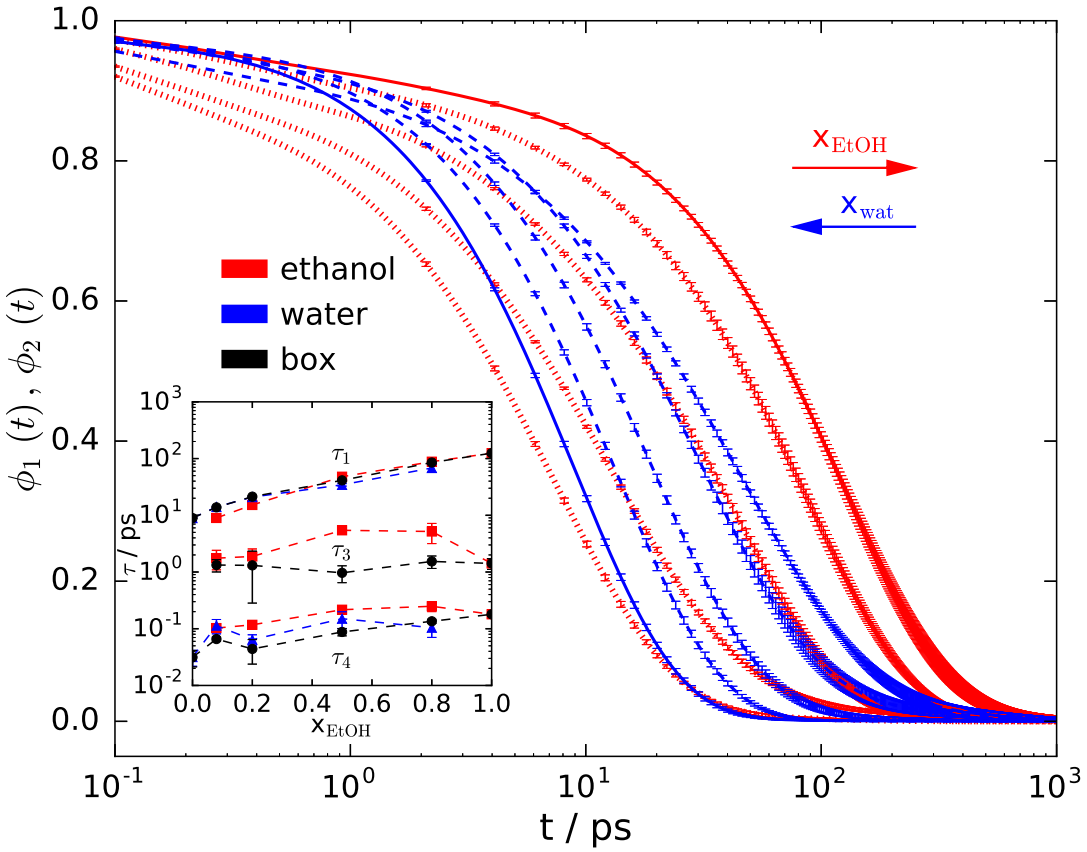

FIGURE 5.11: Contribution of individual species to dynamic response of ethanol/water mixtures at 298 K and 1 bar. Solid lines represent the dipole moment ACF of the pure components: ethanol (red) and water (blue). Dotted (red) lines show the total contribution of ethanol as a component, in mixtures with water of increasing ethanol concentration from left to right. Dashed (blue) lines represent the equivalent results for water as a component. Inset: Relaxation times obtained fitting the 1 HN + 2 Debye model (1 HN + 1 Debye for water) to the dipole moment ACFs of: ethanol as a component (red squares), water as a component (blue triangles) and the entire box (black circles). The dashed lines are a guide to the eye.

asymmetric broadening for this component ($\beta = 0.76 \pm 0.10$).

In Fig 5.12, we show the non-normalised dipole moment correlation functions for the different contributions to the dipole moment ACF of the entire box (see Table 5.2). We decompose the response into the dipole moment ACF of both components ($\mathbf{C_{11}}(t)$ and $\mathbf{C_{22}}(t)$) and the terms corresponding to cross-interactions between components ($\mathbf{C_{12}}(t)$ and $\mathbf{C_{21}}(t)$).

Adding up these four individual terms results in the global response of the entire system. If we analyse the contribution of the dipole moment ACF of the individual constituents of the mixture, we observe how, as expected, the magnitude of this contribution is highly dependent on the mole fraction of every component in the mixture. The larger the concentration of a particular component, the larger its contribution. In the case of the equimolar mixture, the influence of water is significantly stronger

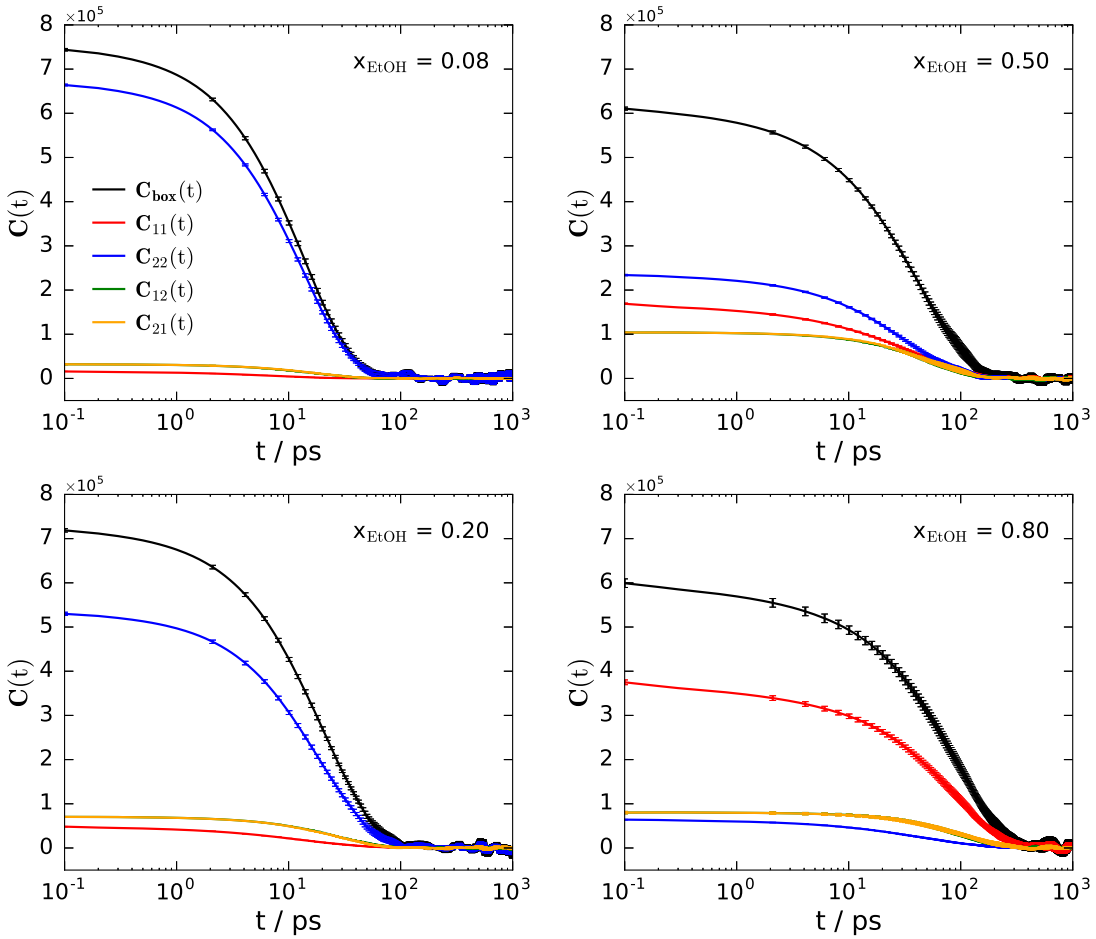

FIGURE 5.12: Contribution of self- and cross-interactions between components to dielectric response of ethanol/water mixtures at 298 K and 1 bar. $\mathbf{C_{box}}(t)$ represents the dipole moment ACF of the entire simulation box, $\mathbf{C_{11}}(t)$ and $\mathbf{C_{22}}(t)$ correspond to the dipole moment ACF of ethanol and water, respectively, and $\mathbf{C_{12}}(t)$ and $\mathbf{C_{21}}(t)$ are dipole moment cross-correlation functions between ethanol and water (see Table 5.2 for definitions of these terms).

than that of ethanol. This means that, the fluctuations of the dipole moment of water molecules are more intense than the ones of ethanol molecules, which could be anticipated from the larger static dielectric constant of the former. Regarding the cross-correlation terms, it is clear that, as expected, the order in which the cross-correlation is performed does not affect the final result, since ethanol-water and water-ethanol correlations show a perfect match (discarding insignificant statistical deviations). But most importantly, we observe how the cross-correlation terms gain strength as the mixture approaches the equimolar state, reaching a maximum at about that concentration, and then decaying for higher ethanol concentrations. This is a consequence of the increase of cross-interactions in the system.

TABLE 5.6: Dielectric relaxation parameters for the separate contribution of each component at the molecule level in ethanol/water mixtures at 298 K and 1 bar.

x_{EtOH}	0.00	0.08	0.20	0.50	0.80	1.00
Ethanol						
τ_1/ps	–	8.2 ± 0.2	12.86 ± 0.08	26.3 ± 0.2	40.1 ± 0.2	49 ± 1
A_1	–	0.898 ± 0.002	0.891 ± 0.001	0.8799 ± 0.0002	0.8549 ± 0.0005	0.837 ± 0.004
α	–	0.979 ± 0.003	0.958 ± 0.001	0.976 ± 0.001	0.976 ± 0.001	0.930 ± 0.003
β	–	0.848 ± 0.009	0.794 ± 0.004	0.679 ± 0.003	0.679 ± 0.002	0.72 ± 0.02
τ_4/ps	–	0.023 ± 0.006	0.016 ± 0.004	0.022 ± 0.007	0.02 ± 0.01	0.110 ± 0.002
A_4	–	0.102 ± 0.002	0.109 ± 0.001	0.1201 ± 0.0002	0.1451 ± 0.0005	0.163 ± 0.004
Water						
τ_1/ps	4.41 ± 0.02	6.630 ± 0.005	9.16 ± 0.04	16.30 ± 0.04	29.3 ± 0.4	–
A_1	0.906 ± 0.001	0.9082 ± 0.0002	0.9071 ± 0.0005	0.9001 ± 0.0005	0.888 ± 0.001	–
α	0.988 ± 0.001	0.9728 ± 0.0003	0.960 ± 0.001	0.951 ± 0.001	0.949 ± 0.003	–
β	0.890 ± 0.003	0.852 ± 0.001	0.825 ± 0.002	0.775 ± 0.002	0.746 ± 0.007	–
τ_4/ps	0.021 ± 0.003	0.018 ± 0.009	0.011 ± 0.004	0.019 ± 0.006	0.021 ± 0.004	–
A_4	0.094 ± 0.001	0.0918 ± 0.0002	0.0929 ± 0.0005	0.0999 ± 0.0005	0.112 ± 0.001	–

5.3.7 Contribution of different components at the individual molecule level

Previously, we have analysed the dielectric response of ethanol and water as separate blocks of molecules ($\boldsymbol{\phi_1}(\mathrm{t})$ and $\boldsymbol{\phi_2}(\mathrm{t})$, respectively). In this section we zoom down to the molecular level to study the response of individual molecules. Figure 5.13 shows the evolution with concentration of the average dipole moment ACF of individual ethanol and water molecules ($\boldsymbol{\phi_{\mathrm{mol\,1}}}(\mathrm{t})$ and $\boldsymbol{\phi_{\mathrm{mol\,2}}}(\mathrm{t})$, see Table 5.2). Due to computational limitations associated with the memory available to calculate these averages, which can comprise up to 1000 ACFs, in this case we only read molecular trajectories every 1 ps instead of the previous 0.1 ps. However, the greater number of samples contributing to the average ACFs shown in Fig. 5.13 has the advantage of providing much better statistics, as can be seen by the reduced size of the error bars in the figure. At the molecular level, a 1 HN + 1 Debye model suffices to accurately describe the dielectric response of both components. However, the relaxation times corresponding to the fast process (τ_4) are significantly lower than the sampling time and cannot be used to extract conclusions on any physical mechanism observed in the simulations. The final results of the parameters involved in the fits are summarised in Table 5.6.

As can be seen in Fig. 5.13, the coupling observed at the total component level is also present at the molecular level, which could suggest that it is actually generated at this scale. As the concentration of ethanol in the mixture decreases, individual ethanol molecules tend to relax faster, approaching the relaxation times of water molecules. The opposite effect is observed for water molecules. Nevertheless, at the molecular level, the trends appear to be neater than at the total component level, and with water

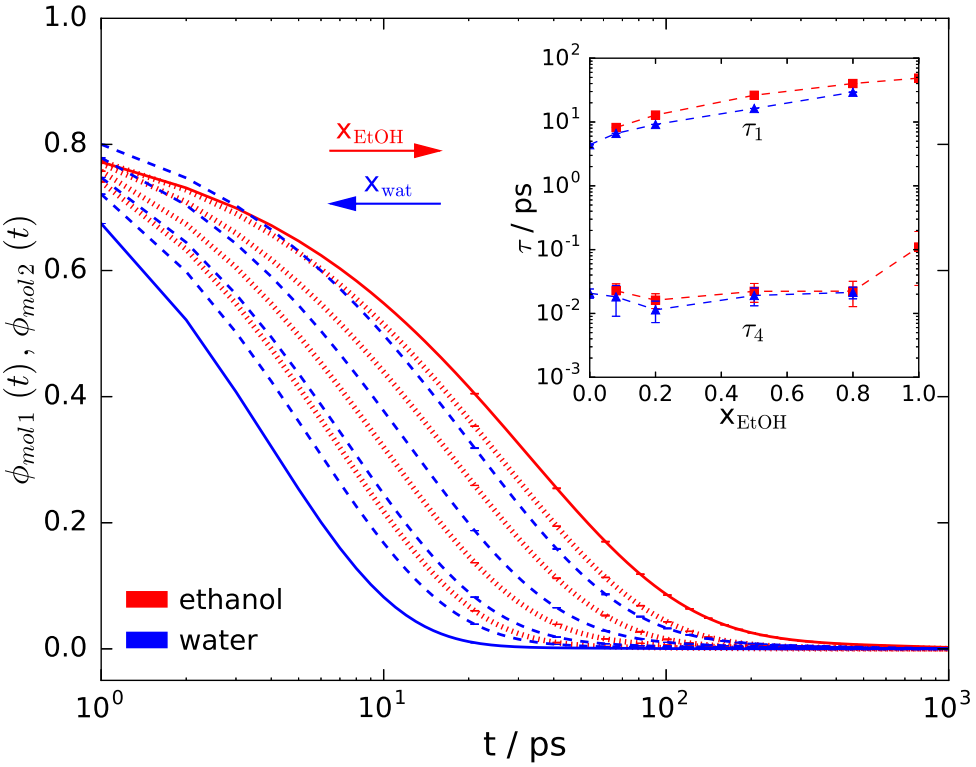

FIGURE 5.13: Contribution of individual molecules to dynamic response of ethanol/water mixtures at 298 K and 1 bar. Solid lines represent the dipole moment ACF at the molecule level for pure components: ethanol (red) and water (blue). Dotted (red) lines show the contribution of individual ethanol molecules, in mixtures with water of increasing ethanol concentration from left to right. Dashed (blue) lines represent the equivalent results for water molecules. Inset: Relaxation times obtained fitting the 1HN + 1Debye model to the dipole moment ACFs of: individual ethanol molecules (red squares), and individual water molecules (blue triangles). Dashed lines are a guide to the eye.

molecules always relaxing faster than ethanol molecules. This is clearly observed in the inset of Fig. 5.13, where we show the concentration-dependence of the relaxation time of the dominant process (τ_1). The fact that an intermediate relaxation (τ_3) is not necessary at the molecule level could be an indication that this additional Debye relaxation observed for groups of molecules might result from phenomena requiring a combined action of those molecules rather than from individual contributions. In general, relaxation times of individual molecules are shorter than the ones corresponding to the component as a block of molecules, or the entire system, which are the ones observed experimentally. This is again an indication that the macroscale dielectric response is a result of the dynamics of structures involving large groups of molecules rather than individual molecules. Even though, the study of the response of at the molecule level can give an insight on the origin of these coupling mechanisms.

In this case we also include additional results in Appendix D. The evolution with concentration of the intensity of the different processes (Fig. D.4), and the parameters α

and β of the dominant HN relaxation (Fig. D.5) are shown here. In addition, in Fig. D.6 we present the frequency-domain representation of the results shown in Fig. 5.13. At the molecular level, the relative importance of dominant and fast relaxation processes is similar for ethanol and water molecules. Even though, fast processes are always slightly more intense in ethanol, particularly at higher ethanol mole fractions. Another interesting effect is the smaller values of the HN parameter β at the molecular level, which can be interpreted as a wider asymmetry in the distribution of relaxation times towards higher frequencies at this level.

5.4 Conclusions

In this chapter, we extend the prediction of dielectric spectra using MD simulations to binary systems. In particular, we focus our attention on ethanol/water mixtures, which is one of the most studied systems due to its simplicity and wide range of applications. MD simulations are performed using the TraPPE-UA force field for ethanol, and a modified version of the Fw-SPC water model. Following the methodology we previously applied to the study of single component systems, we are able to predict the dielectric spectra of ethanol/water mixtures of different concentrations to a high level of accuracy. We show how, when ethanol is present in the mixture, at least three relaxation processes are required to model the dielectric response: a dominant process at microwave frequencies and two additional faster processes. Only in the case of water, two relaxation processes suffice. Although we implemented a Havriliak-Negami model to reproduce the dominant process, the deviations from the Debye model are not very substantial, and a rather ideal response is observed.

We compare our results with predictions provided by several mixing rules used to estimate dielectric properties of mixtures from the characteristics of their pure components. Accepting the limitations of MD simulations in terms of computer time and accuracy of force fields for less studied systems, we demonstrate that, for ethanol/water mixtures, our results clearly outperform all the mixing rules we have tested. Generally, mixing rules seem to give excessive importance to the contribution of individual components.

Previous studies have suggested the dielectric response of ethanol/water mixtures originates from collaborative processes of its extended hydrogen bond network, rather than from individual contributions of the constituents of the mixture. A 'wait-and-switch' mechanism has been proposed, where the dominant and slower relaxation process results from the reorganisation of the entire hydrogen bond network, which simultaneously requires the breaking and formation of individual hydrogen bonds at a faster rate. This fast process involves less molecules and is therefore less intense. In order to provide a deeper insight into this discussion, we use the potential of MD simulations to decompose the dielectric response of the mixture into the contribution of both self- and cross-interactions of the individual components. In this way, we show

how a coupling mechanism between the constituents of the mixture is in place, by which the dominant component tends to dictate the global relaxation time of the entire system. The other component speeds up (ethanol) or slows down (water) accordingly. This is a clear indication that a collaborative process is taking place, since the response of the individual components is being modified. The analysis of the cross-correlation between components reveals how these are most important at concentrations close to the equimolar mixture.

In addition to the decomposition of the dielectric response into the total contribution of the different components of the mixture, we also study the response of individual molecules. The coupling mechanism described above is also present at this scale, which would imply that the interaction between molecules could also be important. However, we find that the relaxation times of individual molecules are generally faster than that of the entire group of molecules forming every component and that of the entire mixture. Since the latter are the ones that coincide with the actual experimental relaxation times, the final dielectric response must be given by a collaborative mechanism involving a large number of molecules, such as the hydrogen bond network.

The next step would precisely be the study of the hydrogen bond network to confirm the hypothesis of a 'wait-and-switch' mechanism, and correlate these fluctuations in the network with the dielectric relaxations times obtained in this work. This is a topic we intend to develop in the future. Instead, at this point we switch to another interesting subject such as the study of the influence of temperature on the dielectric spectra of both single component systems and mixtures.

Chapter 6

Effect of Temperature on Dielectric Spectra

The microwave heating phenomenon originates from intermolecular collisions generated during the coupling of molecular motion to the rapid oscillations of electromagnetic fields. The resulting heat dissipation, and consequent temperature rise, are highly dependent on the dielectric properties of the target material. However, this same temperature increase has the potential to significantly modify the dielectric characteristics of the material. Therefore, it is important to be able to describe these complex trends in order to obtain an accurate prediction of microwave heating profiles. In this chapter, we show how Molecular Dynamics (MD) simulations can be used for this purpose. A brief introduction reviews previous experimental work on the influence of temperature on dielectric properties. Then, we present the predicted effect of temperature on the dielectric spectra of water, ethanol, monoethanolamine (MEA), and ethanol/water mixtures obtained through MD simulations. Finally, in parallel with the analysis performed in Chapter 5, we provide a physical interpretation of the main trends observed through the study of the individual components of the dielectric response. We show how the interaction between molecules to provide a collective dielectric response becomes less significant as temperature increases, and the response tends to that of independent molecules at high temperatures. Additionally, we provide an interpretation of the main relaxation as an activation process and determine its activation enthalpy and entropy.

6.1 Introduction

Despite the large availability of experimental studies on dielectric spectroscopy of several substances, most them are performed at ambient conditions. The influence of temperature on dielectric spectra has generally been less investigated. That said, the dielectric characteristics of water have been extensively determined in the microwave region at different temperatures. The knowledge of this system has evolved over the years, starting from studies that used a single Debye relaxation [102, 103] to the introduction of a second Debye relaxation to improve the description of the high frequency end of

the spectrum [333, 334]. Based on historical data, Ellison *et al.* [101] developed an interpolation function for the real and imaginary parts of the dielectric constant of water for frequencies up to 25 THz and temperatures in the range 273–373 K. The influence of temperature on the dielectric constant of alcohols (C_1 to C_5) at 0.915 and 2.45 GHz has also been established, showing how the real part of the dielectric permittivity ($\varepsilon'(\omega)$) always increases with temperature at those particular frequencies, while the dielectric loss ($\varepsilon''(\omega)$) does not follow a monotonous trend [335]. This is due to the shift in the main absorption peak with temperature. Dielectric spectroscopy has also been performed on a range of organic solvents [233, 336], including water and ethanol, confirming the variability of the dielectric loss and the significant effect of the frequency of the electromagnetic wave on these trends. In addition, the dielectric characteristics of several mixtures of organic solvents have been investigated. The study of the dielectric properties of biodiesel, for which the use of microwave heating technology has shown promising results in the optimisation of the production process, confirms the significant influence of frequency and temperature [337]. The effect of temperature has also been established for mixtures of water with different concentrations of sugars and salts which are frequently used to model solutions that play an important role in the microwave processing of food products [338]. The evolution of relaxation times with temperature can also be used to determine the free energy of activation of dipolar relaxation processes, which can then be employed to establish the deviations of mixtures from an ideal mixing behaviour through the calculation of activity coefficients [339]. Mixtures of MEA with different solvents have shown how it is possible to detect structural modifications or changes of phase following the evolution of dielectric properties with temperature [230, 238, 239]. Finally, one of the most studied systems with regards to the influence of temperature on its dielectric properties is the ethanol/water mixture [112]. The free energy of activation of this mixture was also determined, showing a distinct maximum of both its constituents (activation enthalpy and activation entropy) at mole fractions of ethanol of around 0.22, corresponding to a minimum in the effective dipole moment orientation correlation [243].

Even though we have discussed here some examples of the analysis of the influence of temperature on dielectric properties, the literature on this topic is not abundant. In this chapter, we discuss how MD simulations can be a useful tool to predict the effect of temperature in molecular systems. We apply this reasoning to estimate the dielectric spectrum of water, ethanol, MEA and ethanol/water mixtures at different temperatures. The importance of having a good description of the evolution of dielectric properties with temperature makes these results relevant for modelling microwave heating processes. Additionally, in line with the work developed in Chapter 5, we analyse how temperature affects the individual molecular contributions to the global dielectric response of the entire system.

6.2 Simulation Details

The simulations were performed using the same methodology described in Chapters 4 and 5. As explained before, the temperature stabilisation is handled by means of a Nosé-Hoover thermostat [196, 197] with a time constant of 0.1 ps. The molecular systems included in this study are water, ethanol, MEA and ethanol/water mixtures. As was done in Chapter 5, water and ethanol are simulated with the modified Fw-SPC and the TraPPE-UA force fields, respectively. In the case of MEA, the OPLS force field was used since it showed the best results at ambient conditions (see Chapter 4). Temperatures ranging from 278 K to 343 K were used for all systems. In the case of water, additional simulations were carried out at 353 K and 363 K. In all cases the pressure was set to 1 bar.

6.3 Results and Discussion

In this chapter, we study the influence of temperature on the properties of some of the systems analysed in Chapters 4 and 5. We start by determining the thermodynamic properties of these systems to ensure our simulations are able to capture the main temperature trends observed in experimental results. Then, the focus is shifted to the estimation of the influence of temperature on dielectric properties, with particular interest on the evolution of the decay time of the dominant relaxation process with temperature.

6.3.1 Effect of temperature on thermodynamic properties

In Chapters 4 and 5, we showed how the force fields employed in this work provide satisfactory predictions for thermodynamic properties of water, ethanol, MEA and ethanol/water mixtures at 298 K. In order to evaluate the ability of these force fields to capture the evolution of thermodynamic properties with temperature, we provide the results obtained in the determination of density ρ, thermal expansion coefficient α_{p}, isothermal compressibility κ_{T} and heat capacity $\mathrm{c_p}$.

Figure 6.1 shows the evolution of these properties with temperature for pure water, ethanol and MEA. The experimental trends of density are well captured for both ethanol and MEA using the TraPPE-UA and OPLS force fields, respectively. In the case of water, the modified Fw-SPC provides a good prediction at low temperatures but seems to deviate at higher temperatures. For the remaining properties, the variation with temperature is satisfactorily predicted in most cases, with a general overestimation of the absolute values of these properties from the simulation results. The results provided by the TraPPE-UA model for ethanol are particularly good. The isothermal compressibility of water and the heat capacity of MEA are the only cases for which the variation of these properties with temperature is not properly captured by the simulations.

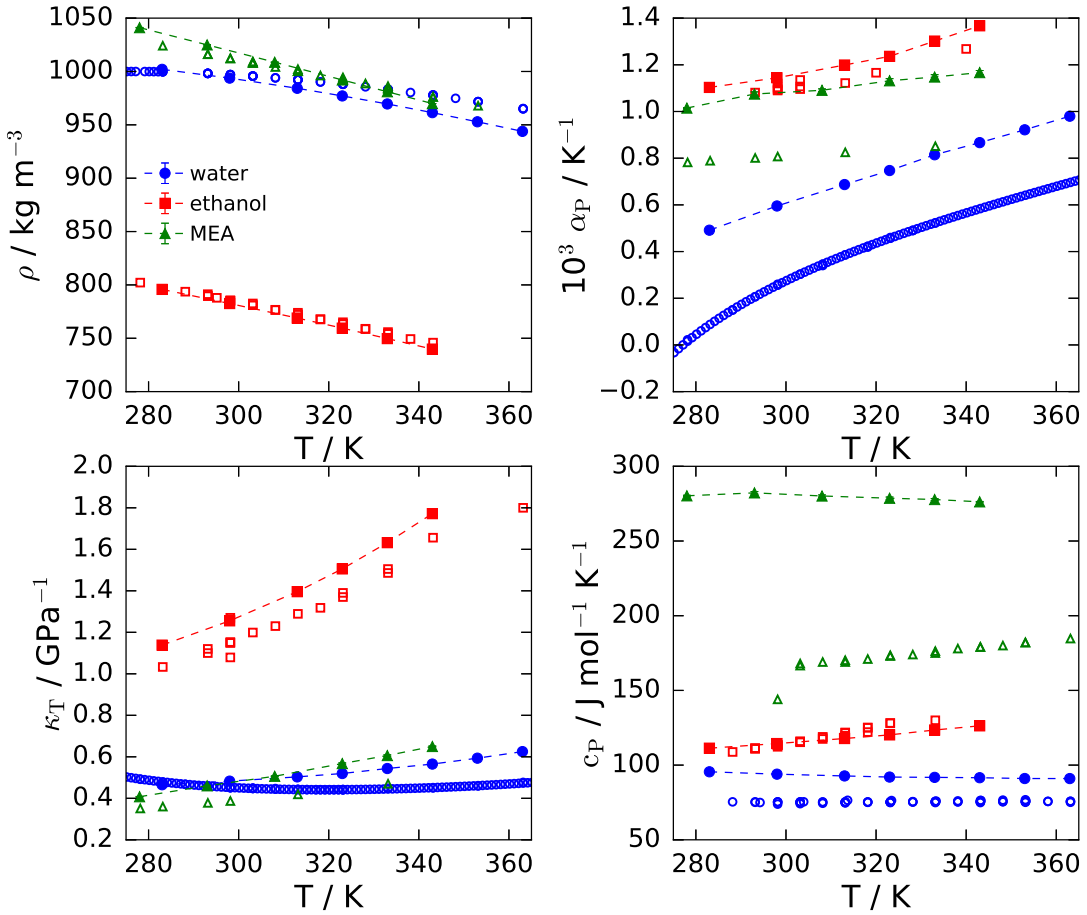

FIGURE 6.1: Influence of temperature on thermodynamic properties of one component systems at 1 bar. Blue circles, red squares and green triangles represent results obtained for water, ethanol and MEA, respectively. Filled symbols represent results obtained from our simulations. Open symbols correspond to experimental data obtained from different sources for water — density ρ [243, 294, 340–345], thermal expansion coefficient α_p [203, 295, 296, 346, 347], isothermal compressibility κ_T [204, 295, 306, 308, 346], and heat capacity c_p [310, 315, 316, 342, 348–350] —, ethanol — density ρ [243, 294, 351–354], thermal expansion coefficient α_p [207, 297, 299–301, 355, 356], isothermal compressibility κ_T [207, 303, 305, 307, 309, 357], and heat capacity c_p [310, 313, 314, 317, 358] —, and MEA — density ρ [359–361], thermal expansion coefficient α_p [220], isothermal compressibility κ_T [220], and heat capacity c_p [221, 362, 363]. Error bars are smaller than symbol sizes. The dashed lines are a guide to the eye.

Figure 6.2 shows the comparison between the predictions provided by our simulations and experimental results for thermodynamic properties of ethanol/water mixtures at different temperatures. The good prediction of the temperature evolution of the density of ethanol/water mixtures is remarkable, with only slight deviations appearing towards higher temperatures. The low availability of experimental data regarding the evolution of the isothermal compressibility does not allow us to draw clear conclusions. However, the increase of this property with ethanol concentration, suggested by the data available at 298 K, seems to be captured by the simulations, with a general

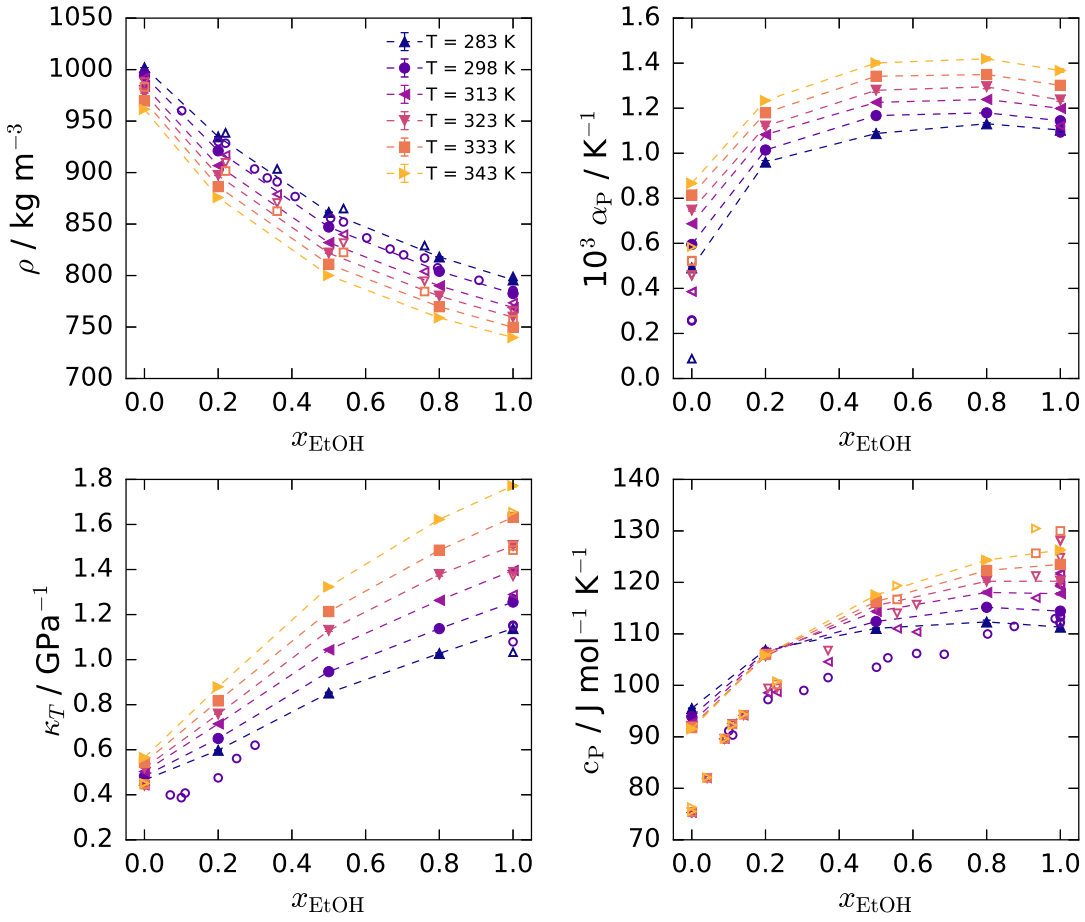

FIGURE 6.2: Influence of temperature on thermodynamic properties of ethanol/water mixtures at 1 bar. Filled symbols represent results obtained from our simulations. Open symbols correspond to experimental data obtained from different sources: density ρ [243, 294], thermal expansion coefficient α_{p} [203, 207, 295–301, 346, 347, 355, 356], isothermal compressibility κ_{T} [204, 207, 295, 302–309, 346, 357], and heat capacity $\mathrm{c_p}$ [310–317, 358, 364]. Error bars are smaller than symbol sizes. The dashed lines are a guide to the eye.

overestimation of the absolute value of this property. In the case of the thermal expansion coefficient and heat capacity, the agreement between the simulations and experimental data is closer at higher ethanol concentrations, with larger deviations observed towards lower concentrations. In line with what was expressed in Chapter 5, the deviations in the prediction of some thermodynamic properties of ethanol/water mixtures at low ethanol concentrations are mainly due to the slightly deficient behaviour of the Fw-SPC model. However, the proven outstanding performance of this model for the prediction of dielectric properties (see Chapters 4 and 5) justifies the choice of this force field in this work.

6.3.2 Influence of temperature on dielectric properties of single component systems

Dipole moment autocorrelation function

We start the discussion on the influence of temperature on dielectric properties by analysing the evolution of the dipole moment autocorrelation function (ACF) entire systems ($\phi_{\mathbf{box}}(\mathrm{t})$ in Table 5.2) of water, ethanol and MEA, as shown in Figure 6.3. It is clear how, in all cases, increasing the temperature results in faster decays of the dipole moment ACF. This is expected since higher temperatures translate into higher kinetic energies, which allow for faster fluctuations in the dipole moment of the system in response to changes in the electric field. As already observed at ambient conditions (see Table 4.2), water presents the faster dynamics followed by MEA and ethanol. This trend is preserved as the temperature increases. The curves presented in Fig. 6.3 correspond to fits to models comprising a Hariliak-Negami (HN) relaxation for the dominant process (τ_1) and a number of Debye relaxations for the additional processes (τ_3, τ_4) — 1 HN + 1 Debye model in the case of water and 1 HN + 2 Debye model for ethanol and MEA. The parameters characterising these fits are summarised in Table 6.1, and a representation of their evolution with temperature is shown in Fig. 6.4, 6.5 and 6.6.

The influence of temperature on the main relaxation time (τ_1) is captured satisfactorily for both water and ethanol (see Fig. 6.4). The comparison with experimental data [103, 243, 337, 365] shows a very close agreement both in terms of absolute values and rate of change of this quantity. In the case of MEA, the OPLS force field underestimates the relaxation time [230, 238, 239], however, the rate of change is very similar. In all three cases, the main relaxation time decreases with temperature, as expected from the faster molecular motion at higher temperatures. As observed in Fig. 6.3, water shows faster relaxation than MEA and ethanol at any given temperature.

In the case of the fastest relaxation (τ_4), no statistically significant variation is observed as temperature increases, except for the shorter relaxation times of water at 353 and 363 K. However, these values of τ_4 ($\approx 2\times10^{-3}$ ps) are well under the sampling time used in our simulations (0.1 ps) and cannot be attributed to any physical mechanism resulting from these simulations. For ethanol and MEA, an intermediate relaxation process is required to describe the dynamic response accurately. In the case of ethanol, relaxation times predicted by the simulations appear to be shorter than the ones determined experimentally [243]. This process seems to become faster as the temperature increases, especially at low temperatures. For MEA, the large statistical variation in the results makes difficult the characterisation of any possible trend with temperature.

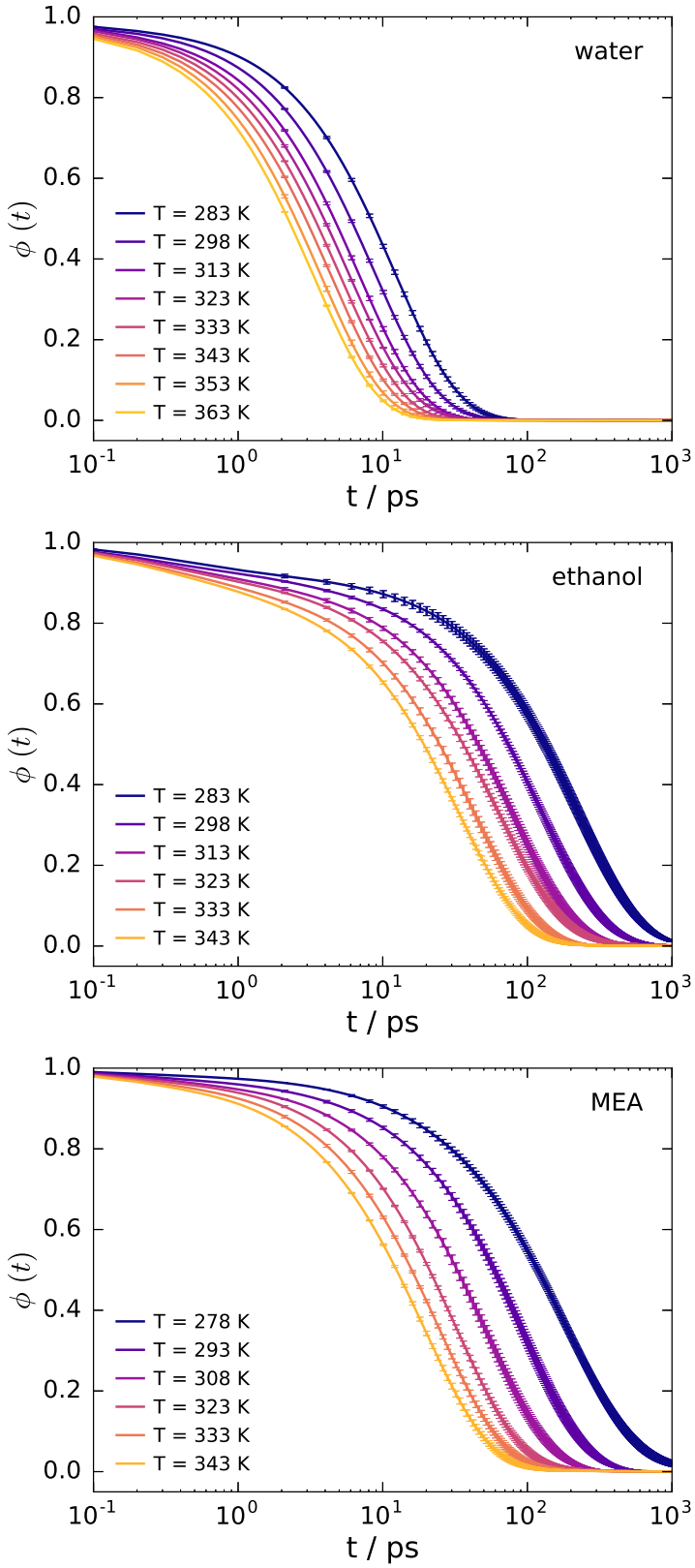

FIGURE 6.3: Influence of temperature on the dipole moment autocorrelation function of one component systems (water, ethanol and MEA) at 1 bar. The lines shown in the figure correspond to the fit of the 1 HN + 1 Debye model (water) and the 1 HN + 2 Debye model (ethanol and MEA) to dipole moment ACF data generated through MD simulations.

TABLE 6.1: Variation of dielectric relaxation parameters with temperature in single component systems at 1 bar. These parameters correspond to the fit of the 1 HN + 1 Debye model (water) and the 1 HN + 2 Debye model (ethanol and MEA) to dipole moment ACF data generated through MD simulations.

T / K	τ_1/ps	A_1	α	β	τ_3/ps	A_3	τ_4/ps	A_4	ε_0	ε_∞
Water										
283	12.3 ± 0.2	0.980 ± 0.002	0.995 ± 0.005	1.000	–	–	0.06 ± 0.02	0.020 ± 0.002	84.07	3.35
298	8.9 ± 0.1	0.981 ± 0.001	0.990 ± 0.004	1.000	–	–	0.03 ± 0.01	0.019 ± 0.001	78.50	3.35
313	6.9 ± 0.1	0.976 ± 0.002	0.996 ± 0.003	1.000	–	–	0.06 ± 0.02	0.024 ± 0.002	73.29	3.35
323	5.90 ± 0.07	0.978 ± 0.003	0.989 ± 0.009	0.996 ± 0.002	–	–	0.05 ± 0.02	0.022 ± 0.003	70.01	3.35
333	5.14 ± 0.06	0.977 ± 0.001	0.996 ± 0.003	0.987 ± 0.004	–	–	0.02 ± 0.01	0.023 ± 0.001	66.87	3.35
343	4.40 ± 0.04	0.975 ± 0.001	0.996 ± 0.004	0.998 ± 0.002	–	–	0.03 ± 0.02	0.025 ± 0.001	63.88	3.35
353	3.75 ± 0.07	0.977 ± 0.001	0.996 ± 0.004	0.997 ± 0.003	–	–	0.002 ± 0.001	0.023 ± 0.001	61.02	3.35
363	3.33 ± 0.01	0.975 ± 0.001	0.996 ± 0.004	0.996 ± 0.004	–	–	0.002 ± 0.001	0.025 ± 0.001	58.29	3.35
Ethanol										
283	224 ± 8	0.90 ± 0.02	0.997 ± 0.003	1.000	7 ± 5	0.039 ± 0.003	0.3 ± 0.2	0.06 ± 0.02	27.13	2.00
298	129 ± 8	0.909 ± 0.005	0.996 ± 0.004	0.97 ± 0.03	1.7 ± 0.4	0.042 ± 0.004	0.20 ± 0.02	0.049 ± 0.005	24.66	2.00
313	79 ± 5	0.896 ± 0.008	0.994 ± 0.006	1.000	1.9 ± 0.9	0.054 ± 0.005	0.20 ± 0.04	0.050 ± 0.009	22.42	2.00
323	66 ± 3	0.898 ± 0.007	0.98 ± 0.02	0.97 ± 0.02	1.9 ± 0.8	0.048 ± 0.006	0.22 ± 0.04	0.05 ± 0.02	21.04	2.00
333	45 ± 4	0.892 ± 0.001	0.997 ± 0.003	0.97 ± 0.03	1.1 ± 0.3	0.057 ± 0.008	0.18 ± 0.03	0.051 ± 0.007	19.74	2.00
343	34.3 ± 0.5	0.884 ± 0.004	0.98 ± 0.02	0.994 ± 0.006	0.9 ± 0.2	0.063 ± 0.004	0.17 ± 0.01	0.052 ± 0.006	18.52	2.00
MEA										
278	210 ± 20	0.97 ± 0.02	0.96 ± 0.02	0.93 ± 0.07	3 ± 3	0.02 ± 0.02	0.05 ± 0.02	0.007 ± 0.003	35.99	2.11
293	94 ± 5	0.940 ± 0.007	1.000	1.000	7 ± 3	0.037 ± 0.006	0.19 ± 0.05	0.023 ± 0.002	33.70	2.11
308	55.1 ± 4	0.92 ± 0.04	0.999 ± 0.001	0.98 ± 0.02	7 ± 4	0.06 ± 0.03	0.14 ± 0.06	0.021 ± 0.006	31.56	2.11
323	32.2 ± 0.7	0.967 ± 0.007	0.98 ± 0.02	1.000	0.7 ± 0.5	0.024 ± 0.001	0.11 ± 0.02	0.010 ± 0.006	29.56	2.11
333	24.9 ± 0.6	0.95 ± 0.02	0.98 ± 0.02	1.000	1 ± 1	0.03 ± 0.02	0.14 ± 0.02	0.024 ± 0.003	28.29	2.11
343	20.0 ± 0.7	0.94 ± 0.02	0.98 ± 0.02	1.000	2 ± 1	0.04 ± 0.02	0.15 ± 0.01	0.029 ± 0.002	27.08	2.11

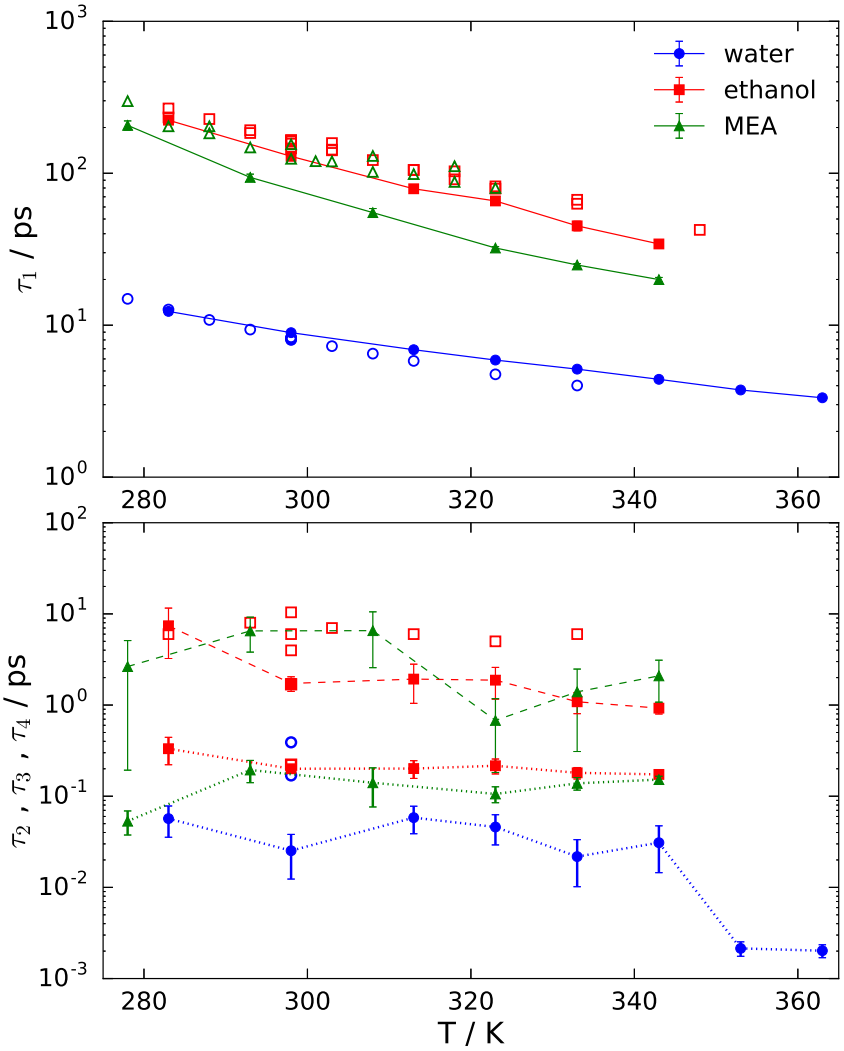

FIGURE 6.4: Variation of relaxation times with temperature in one component systems at 1 bar. Circles, squares and triangles represent results obtained for water, ethanol and MEA, respectively. Filled symbols correspond to the fit of the 1 HN + 1 Debye model (water) and the 1 HN + 2 Debye model (ethanol and MEA) to simulation data. Open symbols correspond to experimental data obtained from different sources: water [103, 234, 242, 244, 249, 271], ethanol [234, 242–244, 249, 271, 337, 365] and MEA [230, 238, 239]. The solid, dashed and dotted lines are a guide to the eye for τ_1, τ_3 and τ_4, respectively.

The intensity of the different relaxation processes is presented in Fig. 6.5. The main relaxation process (A_1) is more dominant for water than for MEA and especially ethanol. The presence of two fast relaxation processes, instead of the single fast process in the case of water, might be the reason behind this difference. A slight decrease of the relative contribution of the main relaxation process is observed for both water and ethanol. In the case of MEA, the trend is not clear due to the previously mentioned statistical variability of the results.

The deviation from the ideal Debye behaviour, given by the parameters α and β of the HN model, is practically non-existent (see Fig. 6.6). All values are above 0.95 for

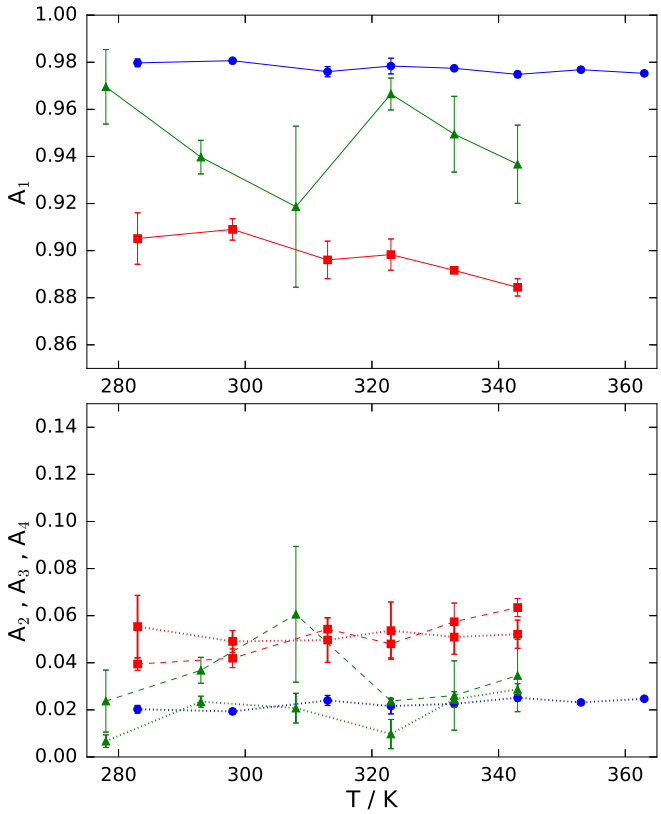

FIGURE 6.5: Variation of relaxation intensities with temperature in one component systems at 1 bar. Circles, squares and triangles represent results obtained for water, ethanol and MEA, respectively. Filled symbols correspond to the fit of the 1 HN + 1 Debye model (water) and the 1 HN + 2 Debye model (ethanol and MEA) to simulation data. The solid, dashed and dotted lines are a guide to the eye for A_1, A_3 and A_4, respectively.

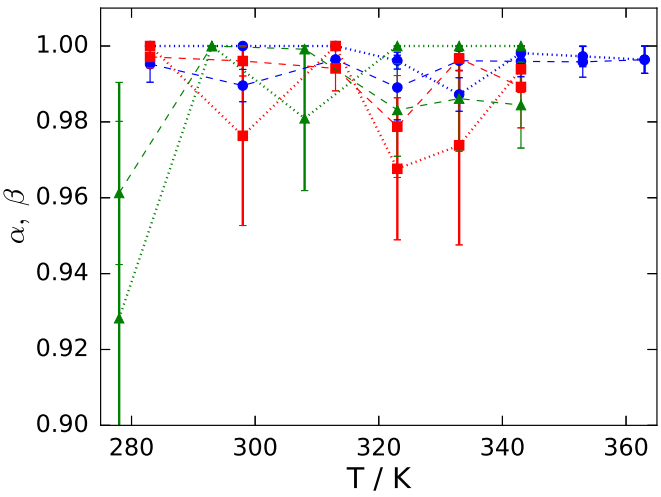

FIGURE 6.6: Variation of Havriliak-Negami's α and β parameters with temperature in one component systems at 1 bar. Circles, squares and triangles represent results obtained for water, ethanol and MEA, respectively. Filled symbols correspond to the fit of the 1 HN + 1 Debye model (water) and the 1 HN + 2 Debye model (ethanol and MEA) to simulation data. The dashed and dotted lines are a guide to the eye for the parameters α and β, respectively.

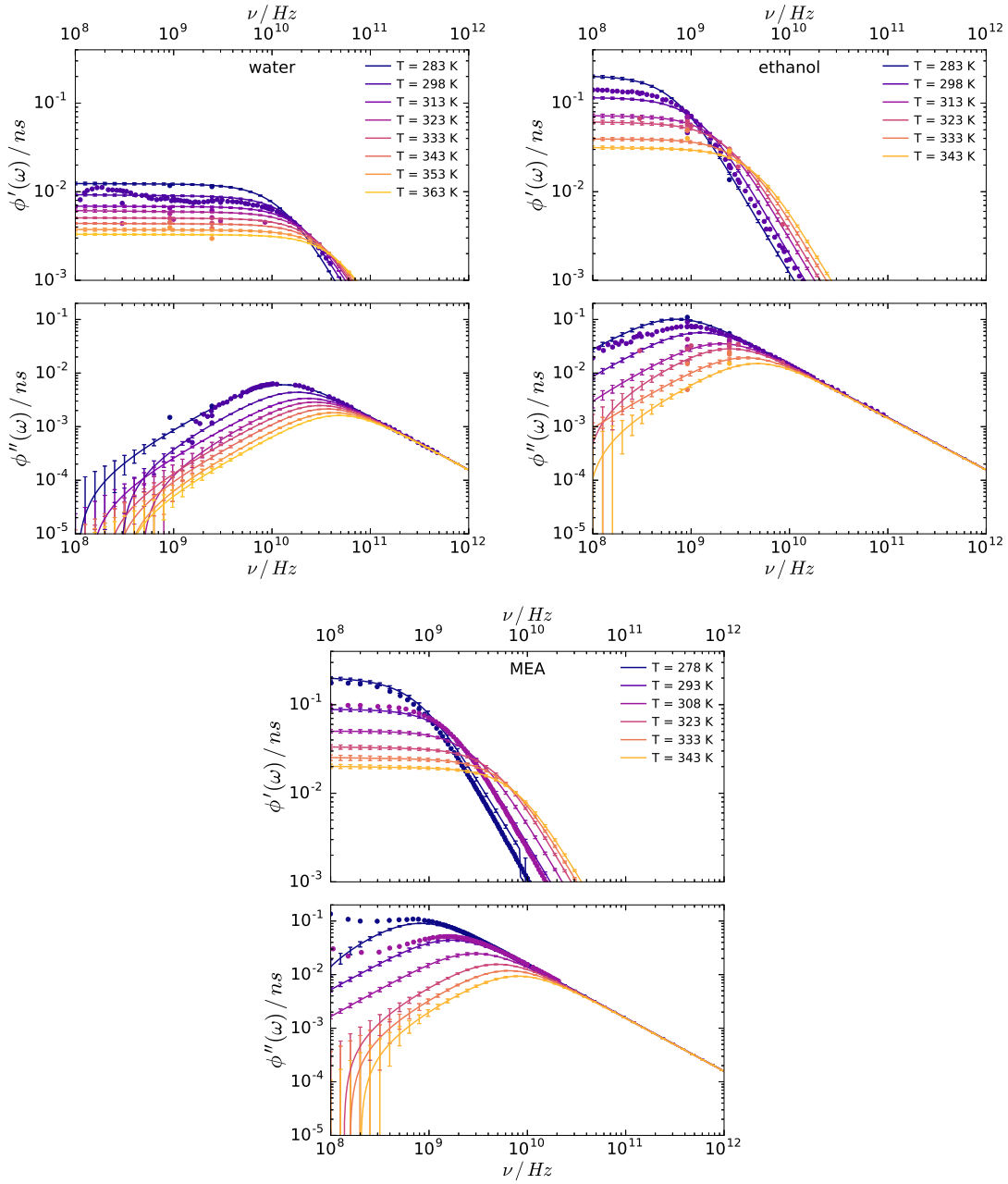

FIGURE 6.7: Influence of temperature on the dielectric response of water, ethanol and MEA through the dipole moment autocorrelation function in the frequency domain at 1 bar. Solid lines represent the results obtained in our simulations. Filled circles represent experimental values obtained from Eq. (4.15) using dielectric spectrum data from different sources: water [103, 104, 112, 234, 338], ethanol [110–112, 233, 234, 335–337, 365], MEA [238, 239].

the whole range of temperatures, with the exception of the results obtained for MEA at 278 K. However, the large error bars observed on these particular values reduce the confidence on these results.

The parameters described above are used to obtain the frequency domain representation of the dipole moment ACF shown in Fig. 6.7. The results are compared with experimental dielectric spectra [103, 104, 110–112, 233, 234, 238, 239, 335–338, 365] transformed into this representation using Eq. (4.15). In general, the results obtained from MD simulations reproduce the experimental trends to a reasonable level of agreement at different temperatures. Some deviations are observed towards the low frequency end of the spectra for all three systems. Even so, the position and intensity of the main features of the spectra are well predicted overall.

Static dielectric constant and infinite frequency permittivity

In previous chapters we stated the importance of using appropriate values of the static dielectric constant ε_0 and the infinite frequency permittivity ε_∞ for the determination of dielectric spectra, in particular to obtain a good estimate of the intensity of the main absorption peak observed in the dielectric loss. In Fig. 6.8 we show the evolution of the static dielectric constant with temperature and we compare the trends obtained in our simulations with available experimental results for water [103, 112, 234, 245, 334, 366] ethanol [112, 234, 243, 245, 365, 367, 368] and MEA [230, 238, 239, 369]. In all three cases ε_0 decreases with temperature. At high temperatures the molecules possess higher thermal energy and more motion is allowed in the system, which implies that the alignment of these molecules with the external electric field will be less probable, which therefore results in lower values of static dielectric constant. The modified version of the Fw-SPC water model shows a particularly good performance, despite the absence of bond stretching. The agreement in the predictions of the TraPPE-UA and the OPLS force fields for ethanol and MEA, respectively, is somehow weaker, although the trends with temperature are maintained to a reasonable level. The larger value of the static dielectric constant of water results from the higher concentration of dipolar groups, with respect to ethanol and MEA [243]. In MEA, both hydroxyl and amino groups have a dipolar nature, which explains the larger value of static dielectric constant when compared with ethanol where only a single hydroxyl group contributes to the response. Due to the importance of this parameter in the prediction of dielectric spectra, we decided to use the experimental value of this quantity to obtain more accurate representations. However, the experimental data do not include some of the temperatures at which the MD simulations were run. For this reason we perform an exponential fit through the available data of the form:

$$\varepsilon_0 = A_T \exp\left(-\frac{T}{\tau_T}\right) \tag{6.1}$$

These fits are shown as solid lines in Fig. 6.8, with the parameters A_T and τ_T for the different systems given by:

- water: $A_T = 307.1$ and $\tau_T = 218.4\ K$
- ethanol: $A_T = 164.1$ and $\tau_T = 157.2\ K$
- MEA: $A_T = 121.5$ and $\tau_T = 228.5\ K$

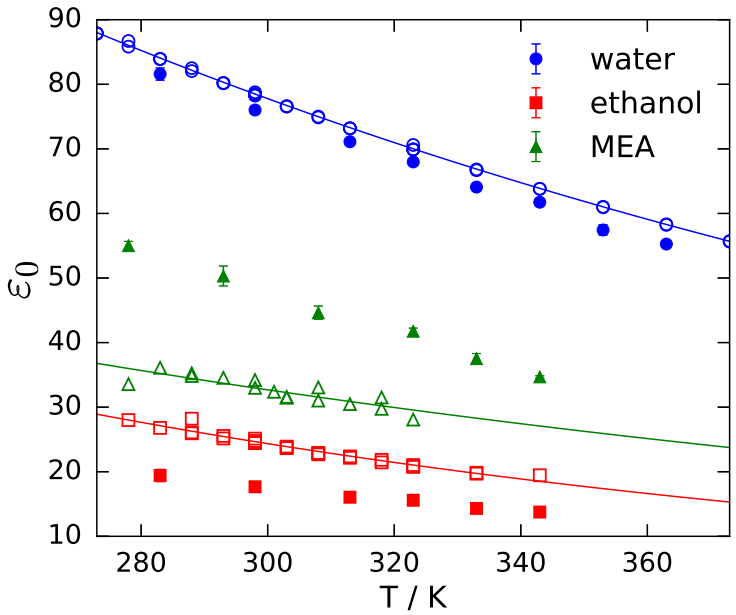

FIGURE 6.8: Influence of temperature on the static dielectric constant of water, ethanol and MEA at 1 bar. Filled symbols represent results obtained in our simulations. Open symbols correspond to experimental results obtained from different sources: water [103, 112, 234, 245, 334, 366] ethanol [112, 234, 243, 245, 365, 367, 368] and MEA [230, 238, 239, 369]. Solid lines correspond to an exponential fit of the experimental data, as shown in the text.

As for the infinite frequency permittivity ε_∞, observing the low variation of this property with temperature in the case of water [370] and the low availability of experimental data for other substances, we assume this variable is independent of temperature, and we use the corresponding ambient temperature values of this quantity for water (ε_∞ = 3.35 [271]), ethanol (ε_∞ = 2.00 [271]) and MEA (ε_∞ = 2.11 [221]).

Dielectric spectra

Once the values of ε_0 and ε_∞ have been established and the parameters of the HN + Debye fits are known (see Table 6.1), the dielectric spectra of water, ethanol and MEA can be determined using Eq. (3.90) and Eq. (3.94). Figure 6.9 shows the influence of temperature on the dielectric spectra of these substances. In all cases, a temperature increase results in a shift of the main relaxation process towards higher frequencies, indicating the expected speed-up of molecular dynamics resulting in a faster reorganisation of the molecular structure at higher temperatures. The comparison with experimental data results in good agreement for both water and ethanol, as expected from the good prediction of the relaxation time of the dominant process (τ_1) in both cases. Similarly, the faster relaxation times obtained for MEA with respect to experimental values explain the shift of the dielectric loss peak towards higher frequencies, especially at 308 K. In general, the inclusion of additional relaxation processes clearly improves the estimation of the high frequency end of the spectra, when compared with the single HN relaxation used in Chapter 4 (see Fig.4.6). As already mentioned in the analysis

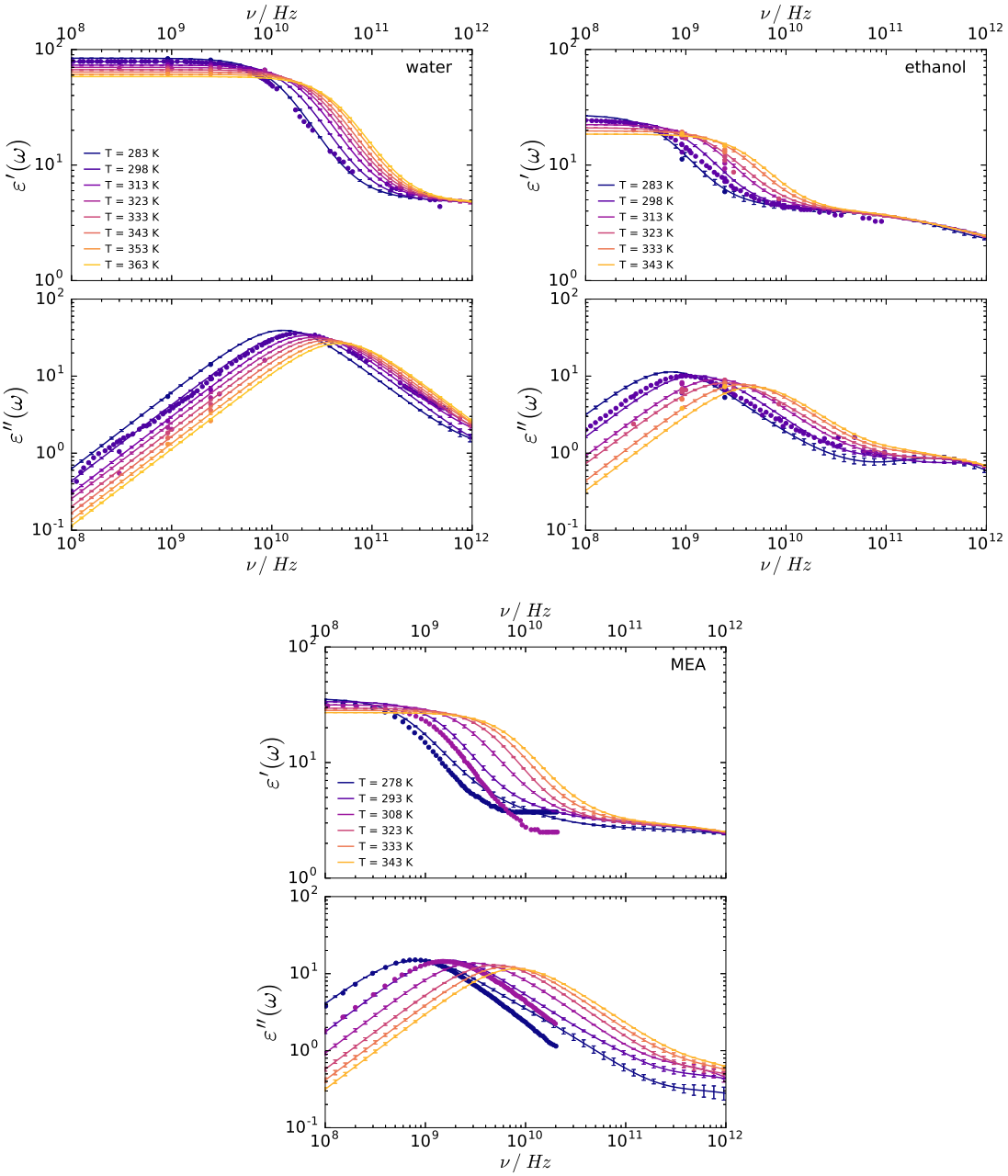

FIGURE 6.9: Influence of temperature on the dielectric spectra of water, ethanol and MEA at 1 bar. Solid lines represent the results obtained in our simulations. Filled circles represent experimental values obtained from different sources: water [103, 104, 112, 234, 338], ethanol [110–112, 233, 234, 335–337, 365], MEA [238, 239].

of dielectric spectra at ambient conditions, the higher polarity of water translates into more intense absorption peaks than ethanol and MEA, which appear to be at a similar level. This means water exhibits larger heating rates in microwave-driven processes. The decrease of the static dielectric constant with temperature observed in Fig. 6.8 decreases the dielectric strength ($\varepsilon_0 - \varepsilon_\infty$) of the substance and results in a lower intensity of the microwave absorption peak at higher temperatures.

TABLE 6.2: Variation of dielectric relaxation parameters with temperature for individual molecules in single component systems at 1 bar.

T / K	τ_1/ps	A_1	α	β	τ_4/ps	A_4
Water						
283	5.91 ± 0.02	0.904 ± 0.001	0.985 ± 0.001	0.903 ± 0.003	0.22 ± 0.01	0.096 ± 0.001
298	4.34 ± 0.03	0.900 ± 0.003	0.986 ± 0.001	0.906 ± 0.008	0.17 ± 0.05	0.100 ± 0.003
313	3.37 ± 0.03	0.902 ± 0.003	0.987 ± 0.001	0.897 ± 0.008	0.09 ± 0.04	0.098 ± 0.003
323	2.87 ± 0.01	0.900 ± 0.002	0.987 ± 0.001	0.900 ± 0.004	0.08 ± 0.04	0.100 ± 0.002
333	2.51 ± 0.03	0.899 ± 0.006	0.989 ± 0.001	0.90 ± 0.02	0.08 ± 0.05	0.101 ± 0.006
343	2.20 ± 0.02	0.899 ± 0.002	0.989 ± 0.001	0.892 ± 0.007	0.002 ± 0.001	0.101 ± 0.002
353	1.93 ± 0.02	0.895 ± 0.005	0.989 ± 0.002	0.90 ± 0.02	0.002 ± 0.001	0.105 ± 0.005
363	1.65 ± 0.01	0.877 ± 0.001	0.984 ± 0.001	0.943 ± 0.003	0.002 ± 0.001	0.123 ± 0.001
Ethanol						
283	66.7 ± 0.7	0.836 ± 0.001	0.894 ± 0.002	0.771 ± 0.005	0.362 ± 0.003	0.164 ± 0.001
298	46.1 ± 0.5	0.825 ± 0.001	0.921 ± 0.001	0.764 ± 0.004	0.359 ± 0.003	0.175 ± 0.001
313	32.7 ± 0.2	0.815 ± 0.001	0.944 ± 0.001	0.756 ± 0.005	0.351 ± 0.003	0.185 ± 0.001
323	26.1 ± 0.3	0.808 ± 0.001	0.955 ± 0.002	0.753 ± 0.005	0.342 ± 0.002	0.192 ± 0.001
333	21.44 ± 0.06	0.804 ± 0.001	0.968 ± 0.001	0.738 ± 0.002	0.328 ± 0.001	0.196 ± 0.001
343	17.36 ± 0.07	0.797 ± 0.001	0.976 ± 0.001	0.739 ± 0.004	0.321 ± 0.002	0.203 ± 0.001
MEA						
278	116.7 ± 0.9	0.923 ± 0.001	0.997 ± 0.001	0.743 ± 0.001	0.415 ± 0.004	0.077 ± 0.001
293	57.9 ± 0.3	0.920 ± 0.001	0.995 ± 0.001	0.760 ± 0.002	0.379 ± 0.001	0.080 ± 0.001
308	33.8 ± 0.2	0.919 ± 0.001	0.996 ± 0.001	0.764 ± 0.002	0.337 ± 0.002	0.081 ± 0.001
323	21.6 ± 0.2	0.918 ± 0.001	0.995 ± 0.002	0.774 ± 0.005	0.31 ± 0.01	0.082 ± 0.001
333	16.9 ± 0.1	0.920 ± 0.001	0.996 ± 0.002	0.770 ± 0.004	0.29 ± 0.01	0.080 ± 0.001
343	13.36 ± 0.04	0.918 ± 0.001	0.996 ± 0.001	0.776 ± 0.003	0.282 ± 0.005	0.082 ± 0.001

Dielectric response at the molecule level

To gain more insight into the mechanisms that lead to the global dielectric response of the different systems, we study next the dielectric relaxation of individual molecules. Figure 6.10 shows the influence of temperature on the dipole moment ACF of individual molecules $\phi_{\mathbf{mol}}(\mathrm{t})$, as defined in Table 5.2. In this case, all the results have been obtained from the fit of the simulation data to the 1 HN + 1 Debye model; the final parameters are shown in Table 6.2 and Figs. E.1, E.2 and E.3 in Appendix E. At the molecule level, the relaxation time of the main relaxation process (τ_1) decreases with temperature in all three cases, as shown in Fig. E.1. This confirms that the dynamics of individual molecules are also faster at higher temperatures. The fast relaxation process (τ_4) seems to be independent of temperature for both ethanol and MEA, while an important decrease of this relaxation time is observed in the case of water at temperatures higher than 343 K. However, and as mentioned when we analysed this relaxation process for the entire simulation box, the relaxation times obtained here are well below the sampling times (1 ps) of our data, and it is not possible to deduce any physical explanation from these results. According to Fig. E.2, the relative intensity of the main and fast relaxation processes seem to be relatively independent of temperature for water and MEA, while in ethanol the fast process gains importance as temperature increases. Regarding the deviations from the ideal Debye behaviour given by the Havriliak-Negami

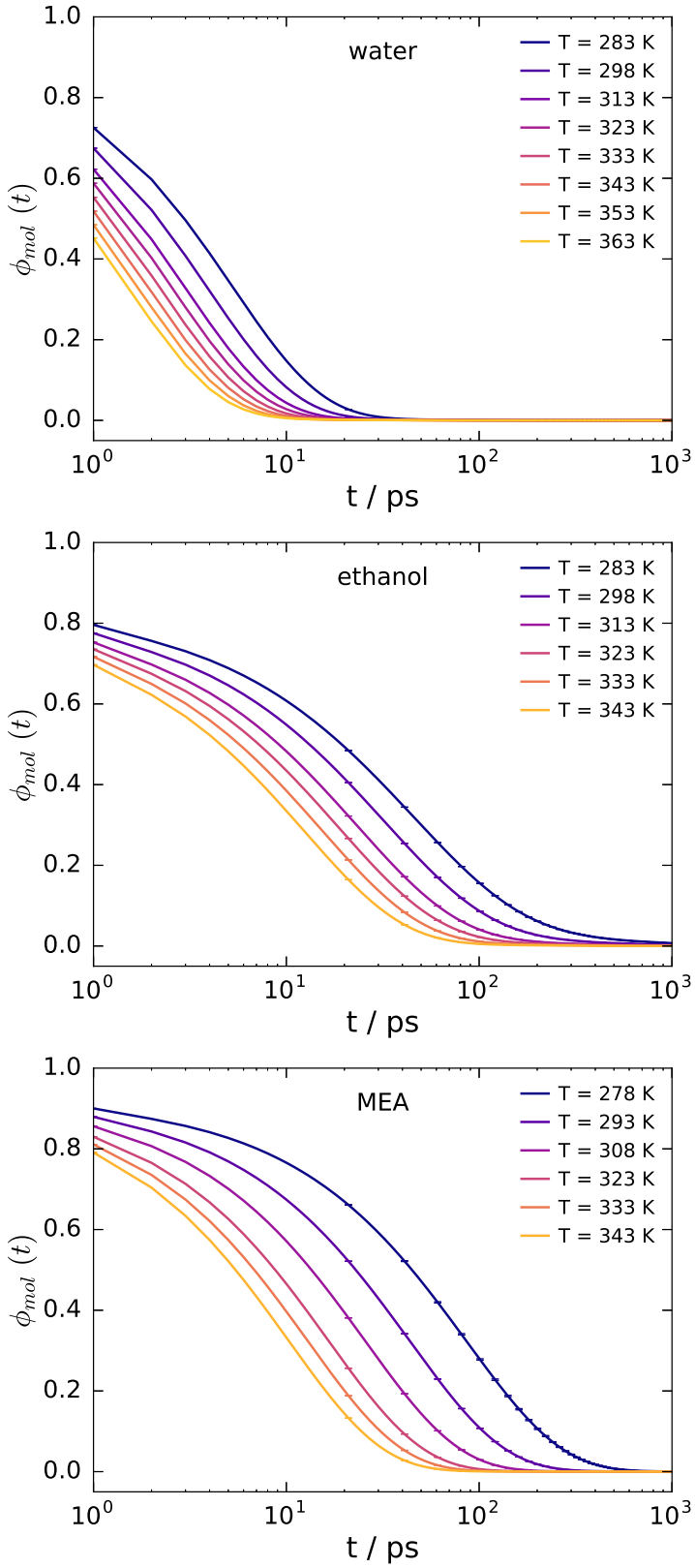

FIGURE 6.10: Influence of temperature on the dipole moment autocorrelation function of one component systems at the individual molecule level at 1 bar.

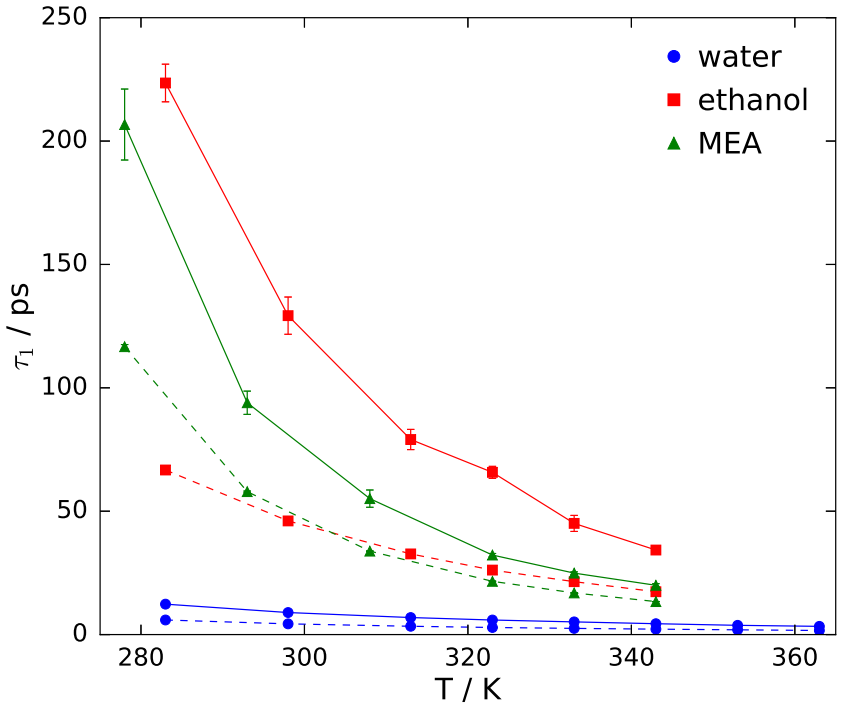

FIGURE 6.11: Influence of temperature on main relaxation process of water, ethanol and MEA at 1 bar. Blue circles, red squares and green triangles represent results obtained for water, ethanol and MEA, respectively. The solid and dashed lines are a guide to the eye for relaxation times of the entire simulation box and individual molecules, respectively.

parameters α and β, these are more intense at the molecule level than when we consider the entire system (see Fig. E.3). In particular, ethanol, shows both a symmetric and asymmetric broadening of the distribution of relaxation times, where the former tends to disappear at high temperatures and the latter tends to become more important. MEA does not show signs of symmetric broadening, however, it presents an important asymmetric effect that is reduced as temperature increases.

Studying in more detail the main relaxation process (τ_1), we observe how in all cases it is faster for individual molecules than for the entire system (see Fig 6.11). This means that, as expected, the global dielectric response of a system is the result of combined and slower mechanisms between its constituent molecules rather than independent contributions of these individual molecules. In general, the relaxation times of entire systems tend to approach the molecular relaxation times as temperature increases, which implies that this combined action becomes less significant (or involves fewer molecules) at higher temperatures. This would be an indication of the weakening of the hydrogen-bond structure of water, ethanol and MEA as the temperature increases.

Interpretation of dielectric relaxation in terms of activation processes

The 'wait-and-switch' mechanism [249, 273] described in Chapter 5 assumes that the main relaxation time represents the period required for a hydrogen-bonding site to

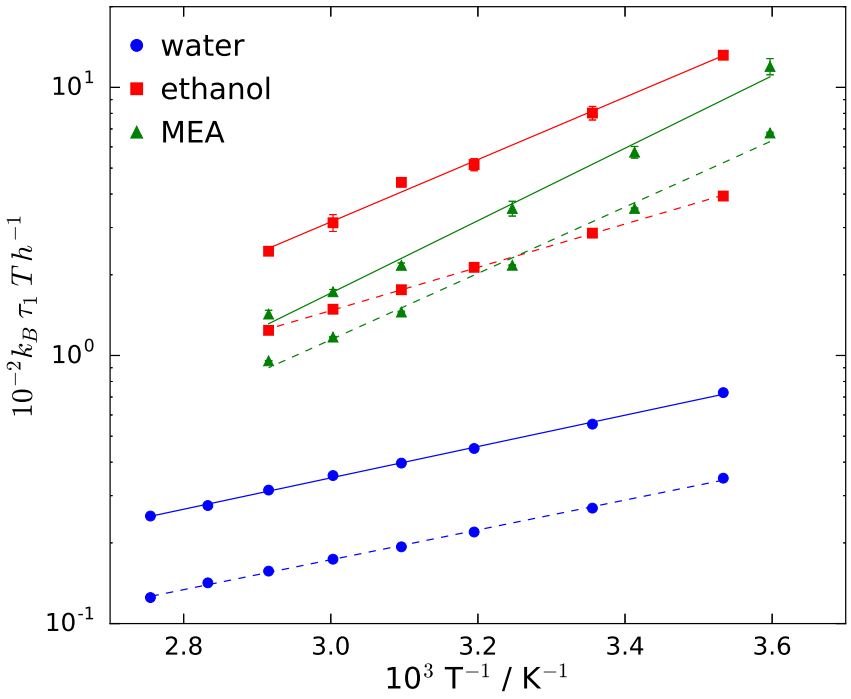

FIGURE 6.12: Eyring plot for the main relaxation process of individual water, ethanol and MEA molecules compared to the main relaxation process of the corresponding entire systems at 1 bar. Blue circles, red squares and green triangles correspond to results obtained for water, ethanol and MEA, respectively. The solid and dashed lines represent the fit of these data to Eyring's equation (Eq (6.3)) for entire systems and individual molecules, respectively.

become available so the dipole reorientation of multiply hydrogen-bonded structures can occur. According to previous studies [243, 249, 273, 339, 371]., this process, which becomes dominant due to the large number of elements participating in this mechanism, can be interpreted as an Eyring-type activation [372, 373]. While the well-known Arrhenius equation [374] is an empirical statement regarding the increase of process rates with temperature, Eyring's equation is fundamentally based on transition state theory [375]. The theory states that, in order to reach its final state, the system needs to jump over an energy barrier corresponding to an intermediate and unstable transition state. In this context, the free energy $\Delta G^{\#}$ of the activated complex is given by:

$$\frac{1}{\tau_1} = \frac{k_B\, T}{h} \exp\left(-\frac{\Delta G^{\#}}{RT}\right) \tag{6.2}$$

where $h = 6.626070040 \times 10^{-34} Js$ is Planck's constant and the activation free energy can be expressed as $\Delta G^{\#} = \Delta H^{\#} - T\Delta S^{\#}$, with $\Delta H^{\#}$ and $\Delta S^{\#}$ being the activation enthalpy and entropy, respectively. Rearranging Eq. (6.2) results in:

$$\ln\left(\frac{k_B\, \tau_1\, T}{h}\right) = \frac{\Delta H^{\#}}{R}\frac{1}{T} - \frac{\Delta S^{\#}}{R} \tag{6.3}$$

TABLE 6.3: Activation enthalpies and entropies of the main relaxation process in water, ethanol and MEA at 1 bar.

	Water		Ethanol		MEA	
	$\Delta H^{\#}$ kJ mol^{-1}	$\Delta S^{\#}$ J mol^{-1} K^{-1}	$\Delta H^{\#}$ kJ mol^{-1}	$\Delta S^{\#}$ J mol^{-1} K^{-1}	$\Delta H^{\#}$ kJ mol^{-1}	$\Delta S^{\#}$ J mol^{-1} K^{-1}
Box	11.0 ± 0.2	3.9 ± 0.5	21.8 ± 0.8	19 ± 3	25 ± 2	34 ± 4
Molecule	10.4 ± 0.2	8.1 ± 0.6	15.1 ± 0.2	4.8 ± 0.5	23 ± 1	31 ± 3

In Fig. 6.12, we show the result of applying this linear representation to the influence of temperature on the decay times of the main relaxation process of both entire systems and individual molecules. Indeed, we observe how water, ethanol and MEA follow the linear trend predicted by Eyring's equation in both cases. The values of activation enthalpy and entropy obtained through this procedure are summarised in Table 6.3. Compared to experimental data reported previously by Petong *et al.* [243, 273], the results obtained here for the entire simulation box tend to underpredict the activation enthalpies and entropies of water ($\Delta H^{\#} = 16.1 \pm 0.5$ kJ mol^{-1} and $\Delta S^{\#} = 20.3 \pm 0.4$ J mol^{-1} K^{-1}), and slightly overestimate these properties for ethanol ($\Delta H^{\#} = 17.6 \pm 0.6$ kJ mol^{-1} and $\Delta S^{\#} = 15.4 \pm 0.5$ J mol^{-1} K^{-1}). However, in all cases the activation enthalpies are in the same order of magnitude as enthalpies corresponding to hydrogen bonds, which generally range from 5 to 25 kJ mol^{-1} in water depending on different assumptions regarding the number of hydrogen bonds formed per water molecule [376–378]. The higher enthalpy of activation of ethanol and MEA with respect to water can be explained by the larger energy penalty for the realignment of these larger and less polar molecules with changes in the electric field [339]. Even though water is characterised by a stronger hydrogen-bond network, and one could think that its molecular motion would be more restricted, the smaller size and larger polarity counteract this effect. It has been shown, however, that methanol manages to break this tendency due to its even smaller size than ethanol and shows lower activation enthalpy than water [249]. Following this same argument, and since the rotation of individual molecules is generally less impeded than that of a group of molecules, the activation enthalpies of individual molecules are always lower than those of the system as a whole. Activation entropies are related to the structural order in the molecular system [379]. As the hydrogen-bond network shifts between two different stable configurations, the system goes through an intermediate activated state with higher entropy. The stronger molecular cohesion in water results in a more ordered structure at the activated state, and therefore in lower activation entropy with respect to ethanol and MEA.

6.3.3 Effect of temperature on dielectric properties of ethanol/water mixtures

Considering the interesting findings observed in the study of one component systems, the analysis of the influence of temperature on dielectric spectra is extended to binary systems, in particular the ethanol/water mixture. Force fields that can capture the effect of both temperature and concentration on dielectric properties would be of great value for modelling processes in which these variables play an important role.

Dipole moment autocorrelation function

Figure 6.13 shows the influence of temperature on the dipole moment ACF of ethanol/water mixtures of different mole fractions. Across all the concentrations studied here, relaxation processes become faster as temperature increases and the molecular dynamics of the system accelerate. In this case, the lines observed in the figure correspond to the fit of dipole moment ACFs obtained through MD simulations to the 1 HN + 2 Debye model, with the exception of pure water for which results are modelled by means of the 1 HN + 1 Debye model. The parameters defining these fits are summarised in Table 6.4, and their variation with temperature is represented graphically in Fig. 6.14 to 6.16.

The relaxation time of the main relaxation process (τ_1) confirms that relaxation processes become faster at higher temperatures (see Fig. 6.14). When compared with experimental data [103, 234, 242–244, 249, 271, 337, 365], the results obtained from simulations tend to slightly underestimate this main relaxation time when ethanol is present in the mixture. Nevertheless, the temperature trends are fully captured by the simulations for all the concentrations. In general, the intermediate relaxation obtained from simulations (τ_3) is faster than the one estimated experimentally (τ_2) [234, 243, 271] in the entire range of temperatures and concentrations. For both intermediate and fast relaxation processes (τ_4), the larger uncertainty in the results makes difficult the characterisation of trends with temperature, although it would appear that these processes are relatively independent of this variable.

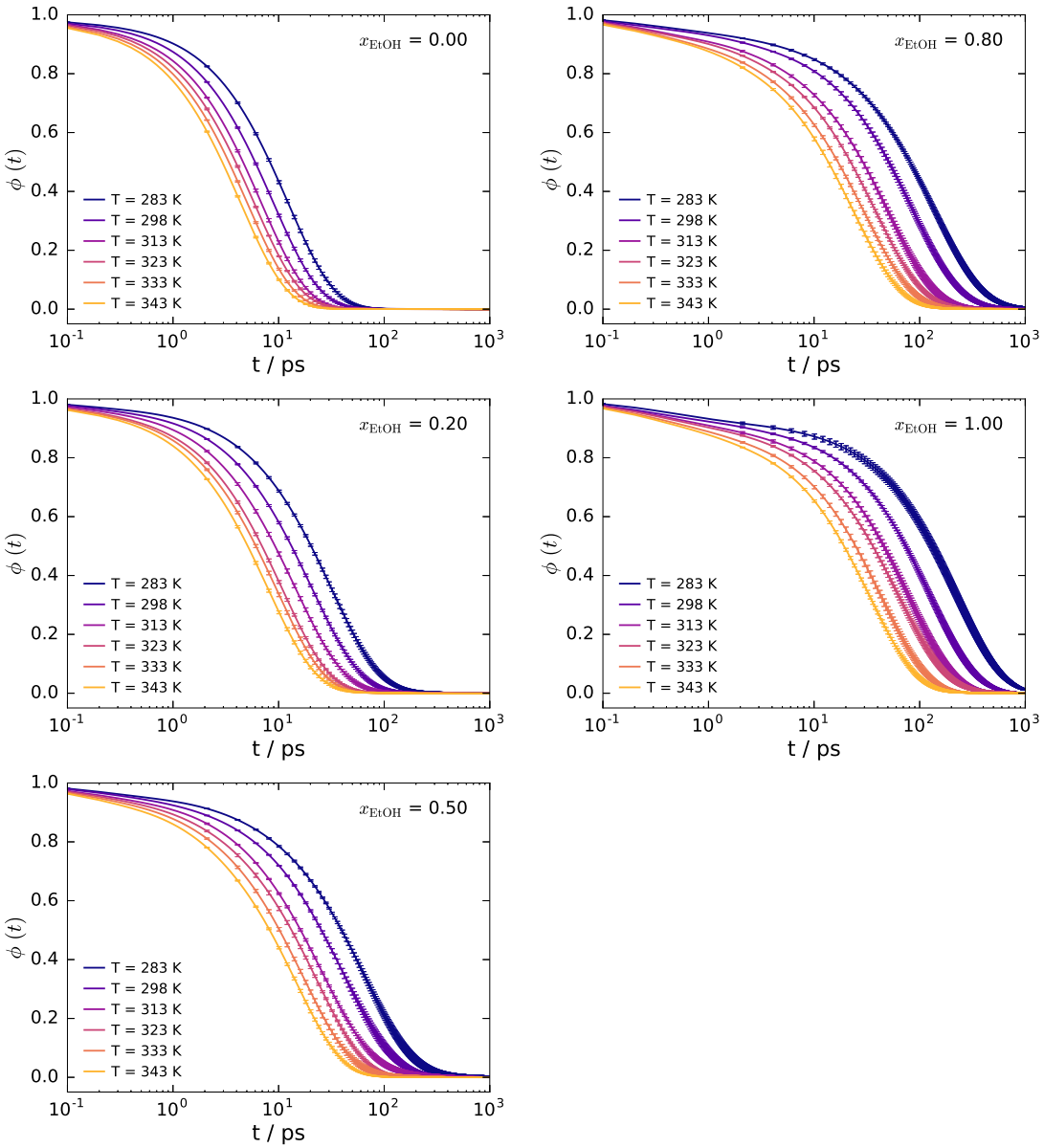

FIGURE 6.13: Influence of temperature on dipole moment autocorrelation function of ethanol/water mixtures at 1 bar. The lines shown in the figure correspond to the fit of the 1 HN + 2 Debye model to dipole moment ACF data generated through MD simulations, except for pure water for which the 1 HN + 1 Debye model is used.

TABLE 6.4: Variation of dielectric relaxation parameters with temperature in ethanol/water mixtures. These parameters correspond to the fit of the 1 HN + 2 Debye model to dipole moment ACF data generated through simulations, except for pure water for which the 1 HN + 1 Debye model is used.

T / K	τ_1/ps	A_1	α	β	τ_3/ps	A_3	τ_4/ps	A_4	ε_0	ε_∞
$x_{EtOH} = 0.00$										
283	12.3 ± 0.2	0.980 ± 0.002	0.995 ± 0.005	1.000	–	–	0.04 ± 0.03	0.020 ± 0.002	84.07	3.35
298	8.9 ± 0.1	0.981 ± 0.001	0.990 ± 0.004	1.000	–	–	0.03 ± 0.01	0.019 ± 0.001	78.50	3.35
313	6.9 ± 0.1	0.976 ± 0.002	0.996 ± 0.003	1.000	–	–	0.06 ± 0.02	0.024 ± 0.002	73.29	3.35
323	5.89 ± 0.07	0.979 ± 0.003	0.989 ± 0.008	0.996 ± 0.002	–	–	0.03 ± 0.02	0.021 ± 0.003	70.01	3.35
333	5.14 ± 0.06	0.977 ± 0.001	0.996 ± 0.003	0.988 ± 0.004	–	–	0.04 ± 0.01	0.023 ± 0.001	66.87	3.35
343	4.40 ± 0.04	0.975 ± 0.001	0.996 ± 0.004	0.998 ± 0.002	–	–	0.04 ± 0.01	0.025 ± 0.001	63.88	3.35
$x_{EtOH} = 0.20$										
283	33 ± 2	0.94 ± 0.02	0.98 ± 0.02	1.000	3 ± 2	0.04 ± 0.02	0.10 ± 0.02	0.024 ± 0.002	60.82	3.08
298	22.7 ± 0.8	0.88 ± 0.05	0.99 ± 0.01	1.000	5 ± 2	0.10 ± 0.04	0.11 ± 0.02	0.027 ± 0.003	55.66	3.08
313	15.9 ± 0.9	0.91 ± 0.05	0.98 ± 0.02	0.97 ± 0.03	2 ± 2	0.07 ± 0.04	0.06 ± 0.03	0.020 ± 0.007	50.95	3.08
323	11.4 ± 0.5	0.95 ± 0.03	0.990 ± 0.008	0.97 ± 0.03	1.0 ± 0.8	0.03 ± 0.02	0.04 ± 0.03	0.020 ± 0.006	48.02	3.08
333	10.3 ± 0.3	0.94 ± 0.02	0.998 ± 0.002	0.96 ± 0.03	1.9 ± 0.8	0.038 ± 0.009	0.07 ± 0.02	0.027 ± 0.004	45.27	3.08
343	8.7 ± 0.7	0.89 ± 0.06	0.99 ± 0.01	0.98 ± 0.02	2 ± 1	0.08 ± 0.06	0.05 ± 0.02	0.022 ± 0.006	42.68	3.08
$x_{EtOH} = 0.50$										
283	67 ± 2	0.91 ± 0.02	0.97 ± 0.02	1.000	4 ± 2	0.05 ± 0.01	0.17 ± 0.03	0.036 ± 0.003	40.80	2.68
298	47 ± 6	0.87 ± 0.07	0.98 ± 0.02	1.000	5 ± 4	0.10 ± 0.06	0.19 ± 0.07	0.039 ± 0.006	37.12	2.68
313	27 ± 2	0.93 ± 0.03	0.95 ± 0.03	1.000	2 ± 2	0.06 ± 0.02	0.09 ± 0.05	0.02 ± 0.02	33.78	2.68
323	24.9 ± 0.9	0.92 ± 0.03	0.996 ± 0.004	0.93 ± 0.05	1.5 ± 0.6	0.05 ± 0.02	0.11 ± 0.02	0.034 ± 0.006	31.72	2.68
333	18 ± 1	0.92 ± 0.02	0.98 ± 0.03	0.97 ± 0.03	1.0 ± 0.4	0.050 ± 0.009	0.08 ± 0.03	0.029 ± 0.008	29.78	2.68
343	14.7 ± 0.4	0.88 ± 0.01	0.996 ± 0.004	1.000	1.7 ± 0.2	0.077 ± 0.008	0.12 ± 0.01	0.046 ± 0.002	27.97	2.68
$x_{EtOH} = 0.80$										
283	142 ± 6	0.90 ± 0.02	0.98 ± 0.03	0.98 ± 0.02	6 ± 4	0.06 ± 0.02	0.23 ± 0.07	0.041 ± 0.007	31.33	2.27
298	89 ± 6	0.921 ± 0.007	0.98 ± 0.02	0.97 ± 0.03	1.6 ± 0.4	0.044 ± 0.006	0.14 ± 0.01	0.035 ± 0.002	28.32	2.27
313	51 ± 2	0.889 ± 0.007	0.99 ± 0.01	0.994 ± 0.006	2.9 ± 0.6	0.055 ± 0.003	0.21 ± 0.02	0.056 ± 0.005	25.61	2.27
323	38.5 ± 0.7	0.897 ± 0.005	0.980 ± 0.009	1.000	1.6 ± 0.2	0.053 ± 0.005	0.170 ± 0.005	0.050 ± 0.002	23.94	2.27
333	31 ± 1	0.87 ± 0.03	0.98 ± 0.02	1.000	3 ± 2	0.07 ± 0.02	0.21 ± 0.04	0.063 ± 0.009	22.38	2.27
343	25 ± 2	0.894 ± 0.005	0.991 ± 0.009	0.97 ± 0.04	1.13 ± 0.05	0.056 ± 0.006	0.15 ± 0.01	0.050 ± 0.002	20.93	2.27
$x_{EtOH} = 1.00$										
283	224 ± 8	0.91 ± 0.02	0.997 ± 0.003	1.000	7 ± 5	0.039 ± 0.003	0.3 ± 0.2	0.05 ± 0.02	27.57	2.00
298	129 ± 8	0.909 ± 0.005	0.996 ± 0.004	0.98 ± 0.03	1.7 ± 0.4	0.042 ± 0.004	0.20 ± 0.02	0.049 ± 0.005	24.93	2.00
313	79 ± 5	0.896 ± 0.008	0.994 ± 0.006	1.000	1.9 ± 0.9	0.054 ± 0.005	0.20 ± 0.04	0.050 ± 0.009	22.55	2.00
323	66 ± 3	0.898 ± 0.007	0.98 ± 0.02	0.97 ± 0.02	1.9 ± 0.8	0.048 ± 0.006	0.22 ± 0.04	0.05 ± 0.02	21.09	2.00
333	45 ± 3	0.892 ± 0.001	0.997 ± 0.003	0.97 ± 0.03	1.1 ± 0.3	0.057 ± 0.008	0.18 ± 0.03	0.051 ± 0.007	19.72	2.00
343	34 ± 0.5	0.884 ± 0.004	0.99 ± 0.01	0.994 ± 0.006	0.9 ± 0.2	0.063 ± 0.004	0.17 ± 0.01	0.052 ± 0.006	18.44	2.00

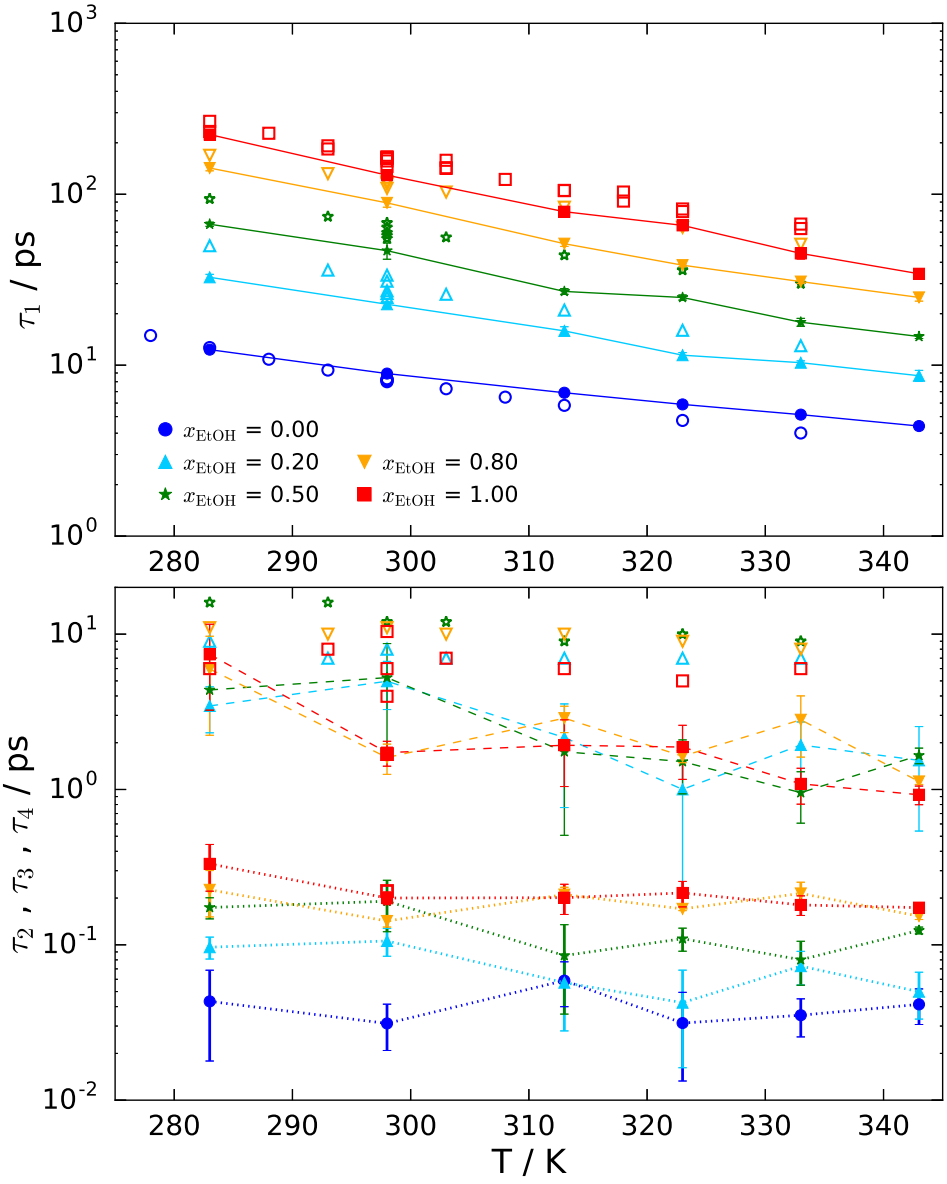

FIGURE 6.14: Influence of temperature on relaxation times of ethanol/water mixtures at 1 bar. Blue circles, cyan upward facing triangles, green stars, orange downward facing triangles and red squares represent the relaxation times of mixtures of ethanol mole fractions 0.00, 0.20, 0.50, 0.80, and 1.00, respectively. Filled symbols correspond to the fit of the 1 HN + 2 Debye model to simulation data. In the case of pure water (x_{EtOH} = 0.00), a 1 HN + 1 Debye model is used. Open symbols correspond to experimental data obtained from different sources: τ_1 [103, 234, 242–244, 249, 271, 337, 365], τ_2 [234, 243, 271] and τ_3 [234, 271]. The solid, dashed and dotted lines are a guide to the eye for τ_1, τ_3 and τ_4, respectively.

According to Fig. 6.15, the relative importance of the main relaxation process (A_1) is greater in the case of pure water than in systems containing ethanol, for which a larger variability appears, particularly at intermediate concentrations. Once more, the presence of two additional relaxation processes, instead of the single additional process observed for water, can explain this difference. Even though, the contribution of the

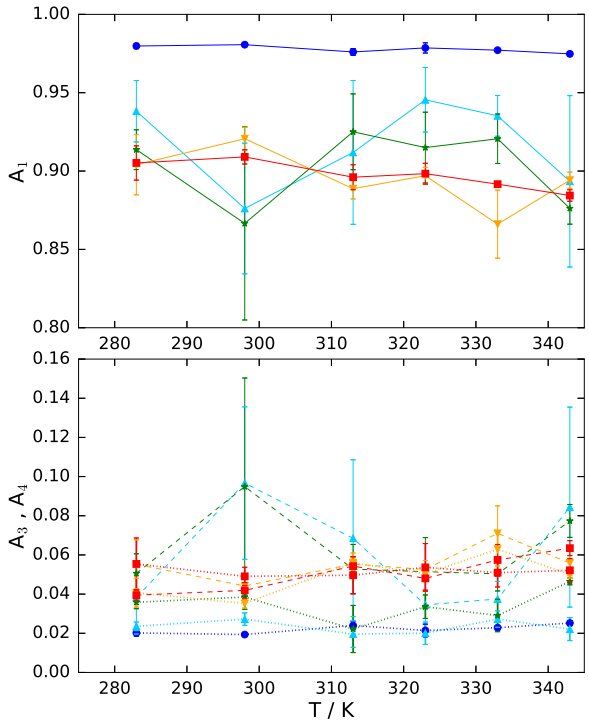

FIGURE 6.15: Influence of temperature on relaxation intensities of ethanol/water mixtures at 1 bar. Blue circles, cyan upward facing triangles, green stars, orange downward facing triangles and red squares represent the relaxation times of mixtures of ethanol mole fractions 0.00, 0.20, 0.50, 0.80, and 1.00, respectively. Filled symbols correspond to the fit of the 1 HN + 2 Debye model to simulation data. In the case of pure water (x_{EtOH} = 0.00), a 1 HN + 1 Debye model is used. The solid, dashed and dotted lines are a guide to the eye for A_1, A_3 and A_4, respectively.

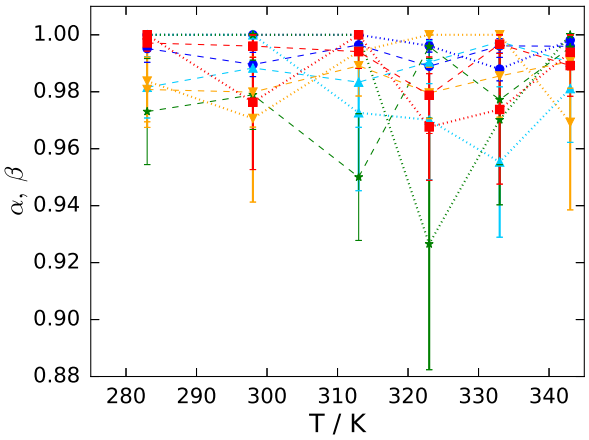

FIGURE 6.16: Influence of temperature on Havriliak-Negami's α and β parameters in ethanol/water mixtures at 1 bar. Blue circles, cyan upward facing triangles, green stars, orange downward facing triangles and red squares represent the relaxation times of mixtures of ethanol mole fractions 0.00, 0.20, 0.50, 0.80, and 1.00, respectively. The dashed and dotted lines are a guide to the eye for the parameters α and β, respectively.

main relaxation process is always greater than 80%. Temperature does not seem to have a significant influence on the intensity of the different relaxation processes, although a slight decrease can be observed in the case of pure ethanol towards high temperatures.

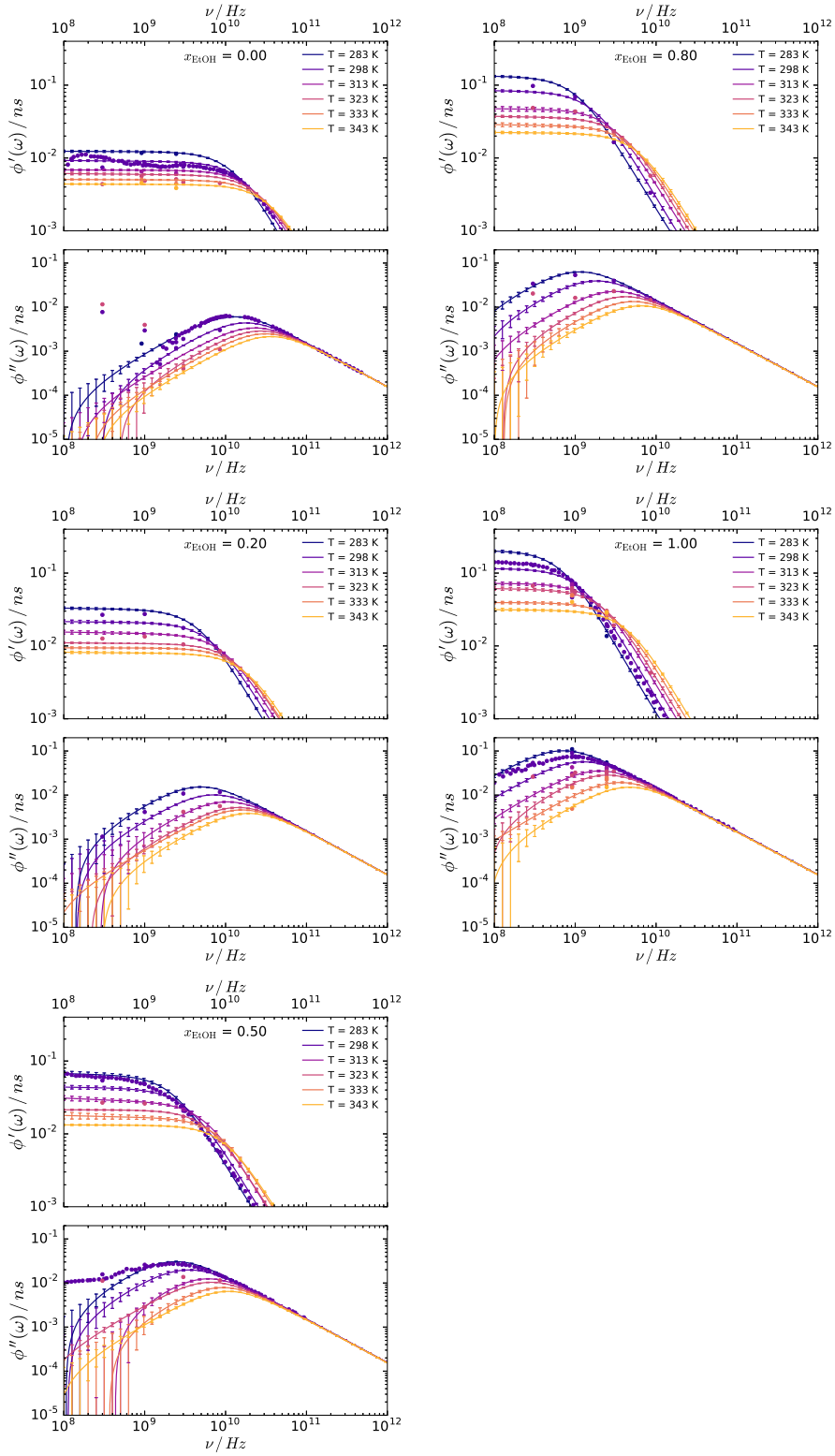

FIGURE 6.17: Influence of temperature on the dielectric response of ethanol/water mixtures through the dipole moment autocorrelation function in the frequency domain at 1 bar. Solid lines represent the results obtained in our simulations. Filled circles represent experimental values obtained from Eq. (4.15) using dielectric spectrum data from different sources [103, 104, 110–112, 233, 234, 335–338, 365]

TABLE 6.5: Parameters for the exponential fit of the evolution of the static dielectric constant with temperature in ethanol/water mixtures at 1 bar.

x_{EtOH}	0.00	0.20	0.50	0.80	1.00
A_T	307.1	323.4	242.1	210.1	164.1
τ_T	218.4	169.4	158.9	148.7	157.2

The influence of temperature on the deviations of the main relaxation process from an ideal Debye process are presented in Fig. 6.16 in the form of the parameters α and β of the HN model. As observed previously at ambient temperature in Chapter 5, these deviations are minor since α and β are always greater than 0.9. Temperature does not have a significant influence on these parameters.

The frequency domain representation of the dipole moment ACF of ethanol/water mixtures at different temperatures is presented in Fig. 6.17. Although the low availability of experimental data [103, 104, 110–112, 233, 234, 335–338, 365] at intermediate concentrations and temperatures other than 298 K makes the comparison difficult, the results obtained from simulations are reasonable. Even though some deviations are observed, the main features observed experimentally, such as the shift of the frequency and intensity of the main relaxation process with temperature, seem to be captured satisfactorily by the models used in this work.

Static dielectric constant and infinite frequency permittivity

As stated previously, the static dielectric constant has a significant effect on the magnitude of the dielectric response. Figure 6.18 shows the influence of temperature on this magnitude for ethanol/water mixtures of different compositions. In Chapter 5 (Fig. 5.8a) we showed how, despite the good prediction of the static dielectric constant of pure water, small deviations of the simulation results with respect to experimental data appear when the concentration of ethanol increases in the mixture. The trend is the same here when we study the influence of temperature on this quantity, although these deviations are slightly reduced at higher temperatures. In line with the decisions made in previous chapters, we decide to use experimental static dielectric constants in the following calculations. As we did in the case of one component systems, we characterise the temperature dependence of the experimental dielectric constant using an exponential decay such as the one given by Eq. (6.1). These fits for ethanol/water mixtures of different compositions are shown as solid lines in Fig. 6.18, and the parameters defining the exponential decay are presented in Table 6.5. Regarding the infinite frequency permittivity ε_∞, here we also assume this variable is independent of temperature and we use the corresponding values at 298 K we presented in Chapter 5 (see Table 5.3).

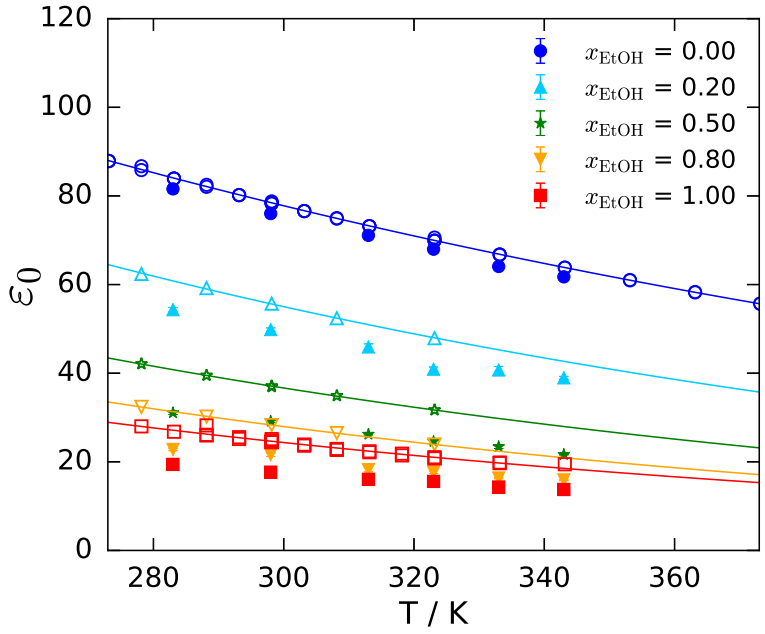

FIGURE 6.18: Influence of temperature on the static dielectric constant of ethanol/water mixtures at 1 bar. Blue circles, cyan upward facing triangles, green stars, orange downward facing triangles and red squares represent results for ethanol mole fractions of 0.00, 0.20, 0.50, 0.80, and 1.00, respectively. Filled symbols represent results obtained in our simulations. Experimental values are shown as open symbols and obtained from different sources [103, 112, 234, 243, 245, 334, 365–368] . Solid lines correspond to an exponential fit of the experimental data, as shown in the text.

Dielectric spectra

Having determined all the parameters required to obtain the dielectric spectra through Eq. (3.90) and (3.94), in Fig 6.19 we show the influence of temperature on this property of ethanol/water mixtures. The results for pure water and pure ethanol have already been analysed above (see Fig 6.9) showing the good predictions that can be achieved through this methodology. The availability of experimental data at intermediate concentrations is again limited but in accordance with the results shown for the frequency-dependent dipole moment ACF in Fig. 6.17, it would appear that the main features of the dielectric spectra are also captured by the simulations. As expected, at any given concentration the main relaxation process is shifted to higher frequencies as the temperature of the system increases. The analysis of the relaxation times of intermediate and fast processes (τ_3 and τ_4) revealed their apparent independence from temperature. This is confirmed here since the high frequency phenomena in the spectra tend to be identical at different temperatures at a particular concentration.

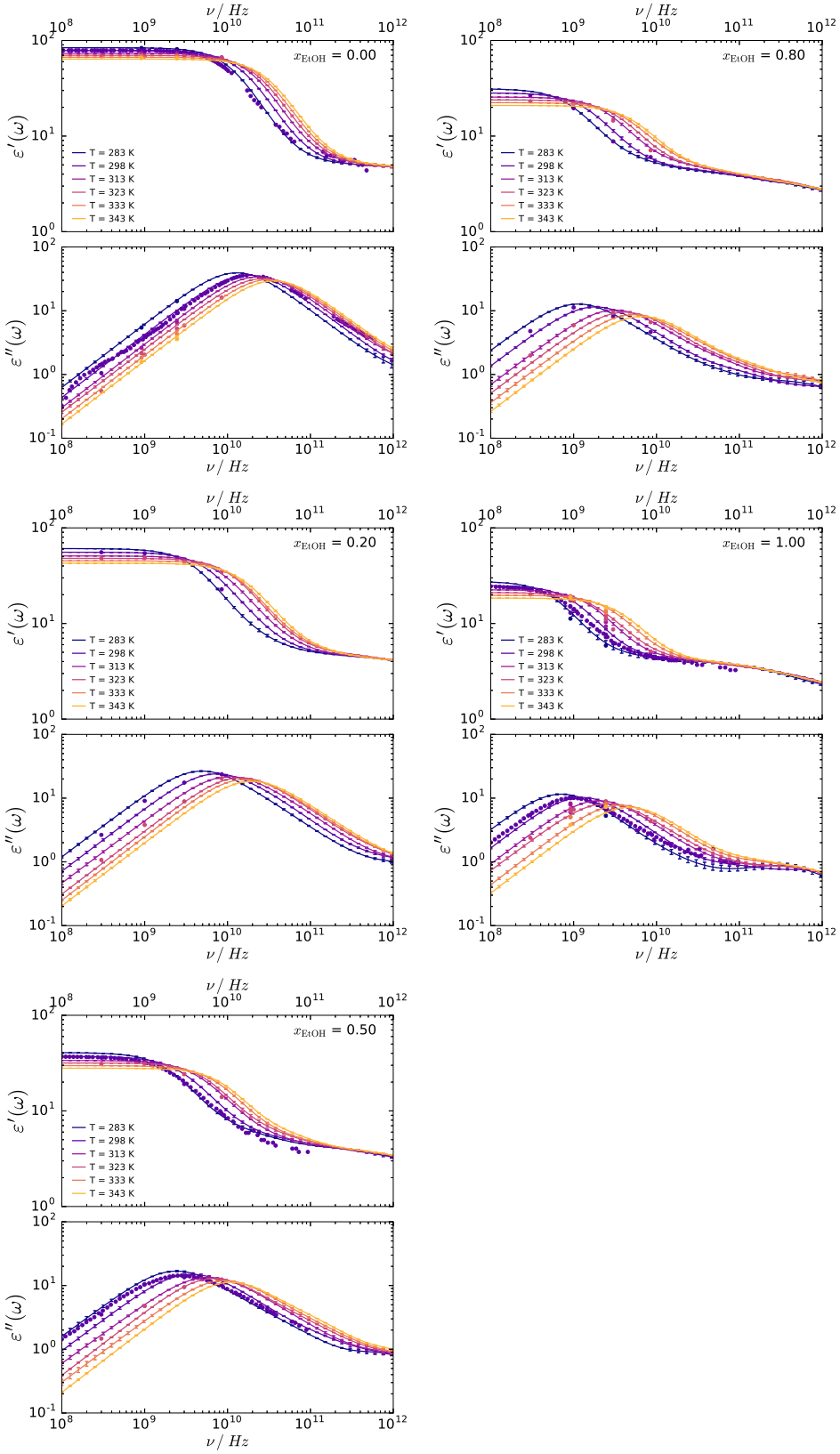

FIGURE 6.19: Influence of temperature on the dielectric spectra of ethanol/water mixtures at 1 bar. Solid lines represent the results obtained in our simulations. Filled circles represent experimental values obtained from different sources [103, 104, 110–112, 233, 234, 335–338, 365]

Contribution of individual species

Following the example of the previous analysis of one component systems, next we decompose the dielectric response into its different constituents in an attempt to provide a deeper insight on the influence of temperature on dielectric relaxation mechanisms. For mixtures, in addition to the analysis of the dielectric relaxation of individual molecules,

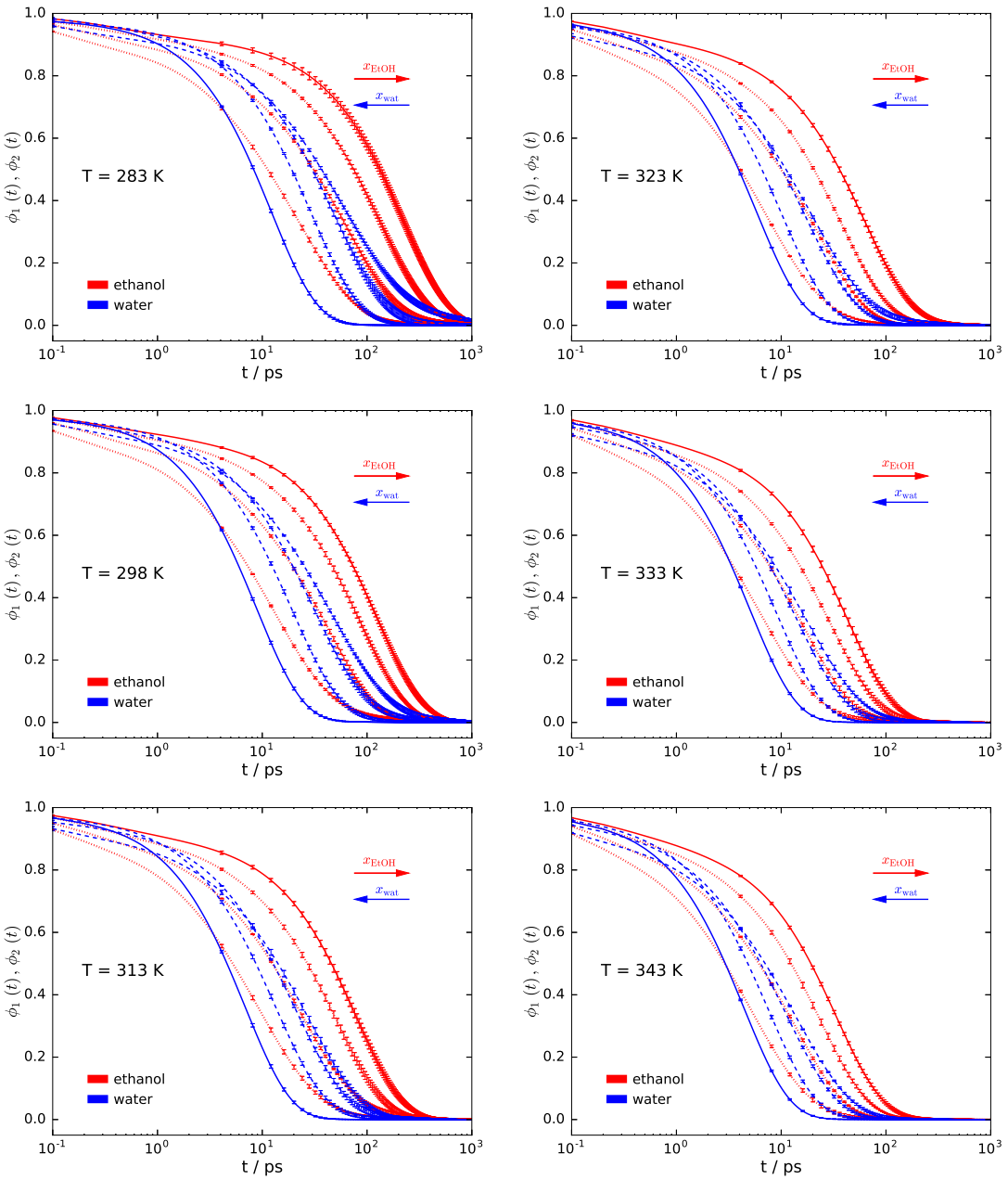

FIGURE 6.20: Influence of temperature on the contribution of individual species to the dielectric response of ethanol/water mixtures. Solid lines represent the dipole moment autocorrelation function of the pure components: ethanol (red) and water (blue). Dotted (red) lines show the total contribution of ethanol as a component, in mixtures with water of increasing ethanol concentration from left to right. Dashed (blue) lines represent the equivalent results for water as a component.

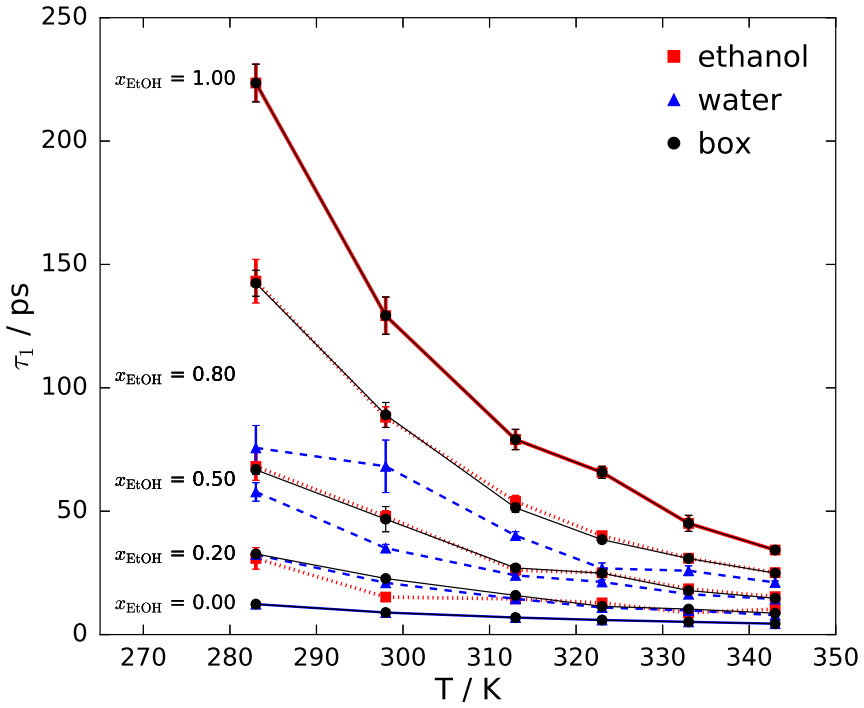

FIGURE 6.21: Influence of temperature on main relaxation times of individual species compared to entire system in ethanol/water mixtures at 1 bar. The results are obtained fitting the 1 HN + 2 Debye model (1 HN + 1 Debye for water) to dipole moment ACFs from MD simulations. Black circles, red squares and blue triangles correspond to results obtained for the entire mixture, ethanol and water, respectively. The solid, dotted and dashed lines are a guide to the eye for the entire mixture, ethanol and water, respectively.

we also study the total contribution of each component, as was done in Chapter 5. Figure 6.20 shows the evolution with mixture composition of the dipole moment ACF of each species (defined as $\phi_1(t)$ for ethanol and $\phi_2(t)$ for water in Table 5.2) at different temperatures. The results presented here correspond to 1 HN + 2 Debye fits for ethanol and 1 HN + 1 Debye fits for water, which parameters at different mixture compositions and temperatures are summarised in Table E.1 in Appendix E. The general shift to shorter relaxation times as temperature increases, which was already observed for the mixture as a whole, is also present here. Moreover, the coupling mechanism detected at 298 K in Chapter 5, by which the dielectric response of ethanol accelerates as water becomes the dominant component of the mixture, and water dynamics slow down as the concentration of ethanol increases, appears to be conserved at different temperatures.

The main temperature trends of the parameters defining the fits are shown in Appendix E. Figure E.4 confirms that for both ethanol and water the main relaxation process becomes faster as temperature increases. However, the influence of temperature on the fast relaxation processes (τ_3 and τ_4) is not easy to identify due to the larger statistical uncertainty in the results. The relative intensity of the main relaxation process (A_1) is generally independent from temperature, particularly in the case of water (see

Fig. E.5). For ethanol, fast processes seem to gain importance as temperature increases, especially when the amount of ethanol in the mixture is low. The deviations of the main relaxation process from an ideal Debye behaviour are generally minor (see Fig. E.6). However, these deviations tend to become more significant for the component that is in defect in the mixture.

If we analyse in more detail the influence of temperature on the relaxation time of the main process (τ_1), we observe how, as noted at 298 K, this relaxation process tends to be governed by the dynamics of the dominant component of the mixture at any given temperature (see Fig. 6.21). At high ethanol concentrations ($x_{\mathrm{EtOH}} = 0.80$), the response of the entire simulation box is almost identical to the response of the ethanol component. A similar behaviour is observed at high water content ($x_{\mathrm{EtOH}} = 0.20$), where the dynamics of the system reproduce that of component water. In the case of the equimolar mixture, the global dielectric response seems to rather approach that of ethanol, although this preference tends to disappear as temperature increases.

Until this point, we have only analysed self-interactions within each component. In Fig. 6.22 we show the influence of temperature on the cross-correlation between the two components of the mixture, as defined in Table 5.2. In general, the magnitude of the dipole moment cross-correlations between ethanol and water decreases with temperature, which indicates a weaker interaction between components at higher temperatures. As expected the equimolar mixture shows the most intense cross-interactions due to the larger availability of pairs of distinct molecules. Interestingly, a gap seems to be opening between 298 K and 313 K at high ethanol concentrations. In order to investigate if this phenomenon is related to the structure of the hydrogen bond network, we determine radial distribution functions for all the O–H pairs participating in hydrogen bonds. The results are included and Appendix F, and the evolution of the intensity of the peaks corresponding to hydrogen-bonded $\mathrm{O_{Water}}$–$\mathrm{H_{EtOH}}$ and $\mathrm{O_{EtOH}}$–$\mathrm{H_{Water}}$ pairs is shown in the insets of Fig. 6.22. The decrease of the intensity of those peaks with temperature is a clear indication of the progressive weakening of the hydrogen bond network towards high temperatures. A slight shift from this approximately linear trend is observed at ethanol mole fractions of 0.50 and 0.80, between 298 K and 313 K. This could partially explain the gap formed in the cross-correlation functions at those conditions.

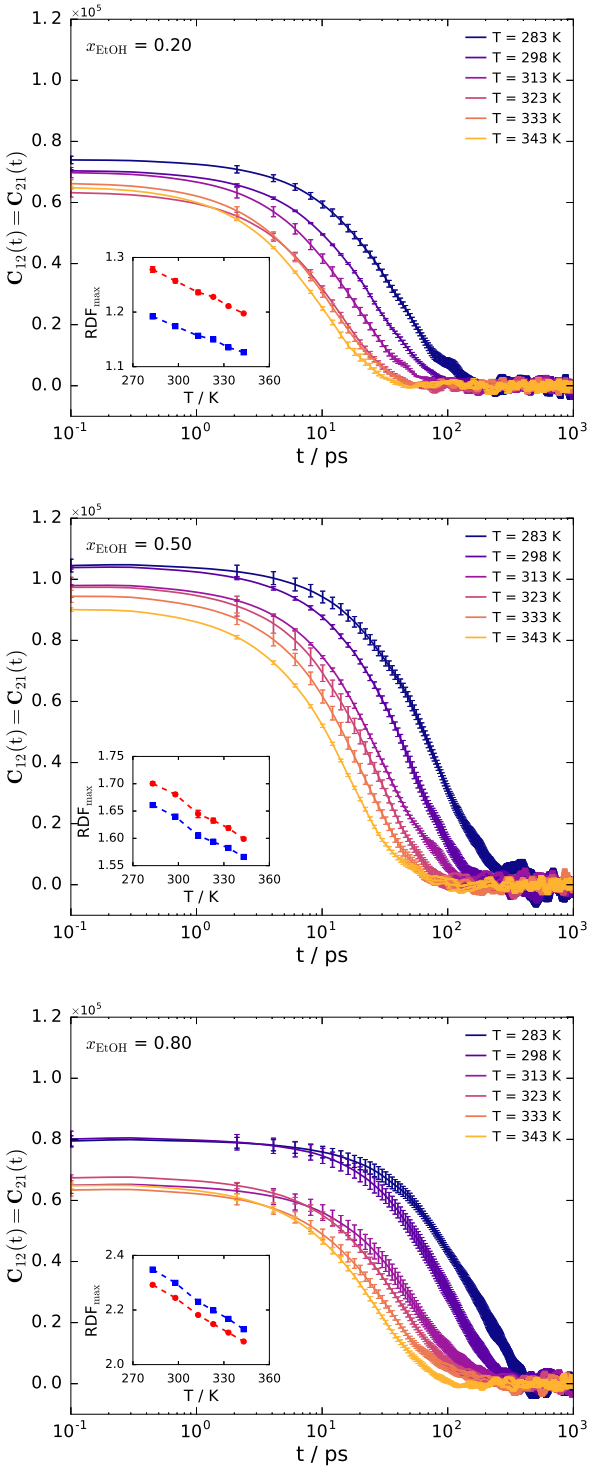

FIGURE 6.22: Influence of temperature on non-normalised cross-correlations between components in ethanol/water mixtures.Inset: Influence of temperature on the height of the RDF peak corresponding to hydrogen-bond for O_{Water}–H_{EtOH} (red) and O_{EtOH}–H_{Water} (blue) (see Appendix F).

Dielectric response at the molecule level

The average contribution of individual ethanol and water molecules to the global dielectric response at different temperatures is presented in Fig. 6.23. We use the dipole

moment ACF at the molecule level defined as $\phi_{\mathbf{mol\,1}}(\mathrm{t})$ for ethanol and $\phi_{\mathbf{mol\,2}}(\mathrm{t})$ for water in Table 5.2. In this case, the 1 HN + 1 Debye model is used for both ethanol and water dipole moment ACFs, with the resulting parameters summarised in Table E.2 in Appendix E. Once again, the temperature increase results in faster molecular relaxations at any concentration. Additionally, the coupling mechanism between ethanol and water dynamics mentioned above is preserved at the individual molecule level.

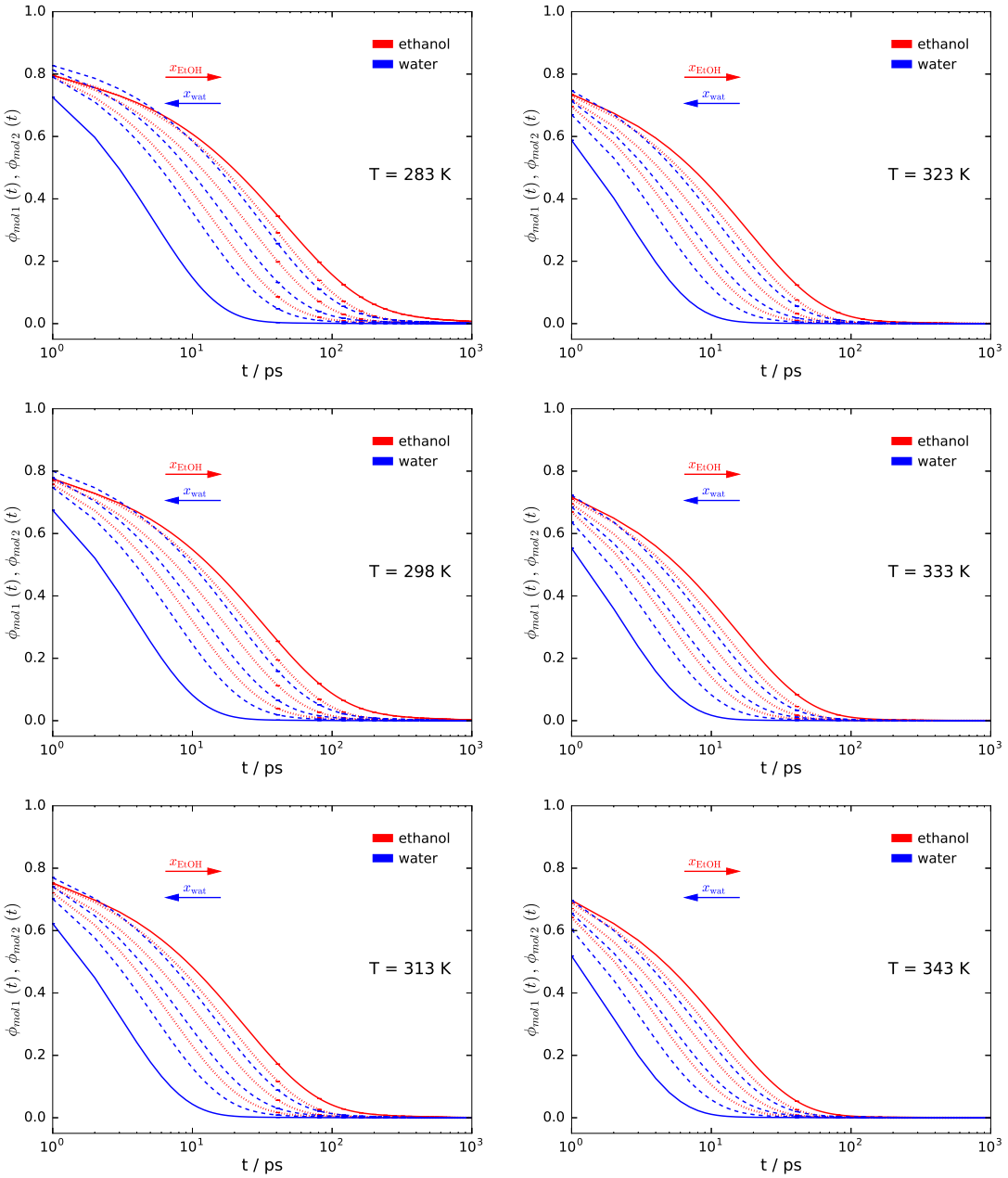

FIGURE 6.23: Influence of temperature on the average contribution of individual ethanol and water molecules to the dielectric response of ethanol/water mixtures at 1 bar. Solid lines represent the dipole moment autocorrelation function at the molecule level for the pure components: ethanol (red) and water (blue). Dotted (red) lines show the contribution of individual ethanol molecules, in mixtures with water of increasing ethanol concentration from left to right. Dashed (blue) lines represent the equivalent results for water molecules.

The influence of temperature on the different parameters of the 1 HN + 1 Debye model is represented graphically in Appendix E. The trends observed at the individual molecule level are similar to the ones observed previously for the entire mixture and the total contribution of each species. The characteristic time of the principal relaxation process (τ_1) becomes shorter as temperature increases (see Fig E.7). The faster molecular process (τ_4) is independent from temperature for pure ethanol, while it shows an apparent speed-up for pure water. At intermediate concentrations, the statistical uncertainty does not allow to infer any valid conclusion. Figure E.8 shows how the fast process has a larger influence for ethanol molecules than for water molecules. This becomes more obvious at higher ethanol concentrations, for which a temperature increase has the effect of further accentuating this trend. The parameters α and β of the HN model used to represent the main relaxation process seem to follow opposite trends with temperature at the molecule level. While the symmetric broadening (α) with respect to the Debye model seems to disappear at high temperatures, the asymmetric broadening (β) becomes slightly more important.

In Fig. 6.24, we compare the evolution of the main relaxation time (τ_1) for the entire mixture and individual ethanol and water molecules at differnt concentrations. As we saw for one component systems (Fig 6.11), the molecular relaxation times are clearly lower than the relaxation time of the entire system, especially at low temperatures. As temperature increases, those differences are vastly reduced and mixture and individual molecules appear to share similar dynamics. This can be explained as the weakening of the hydrogen-bond network in the mixture as temperature increases, which reduces the number of molecules participating in collective processes. The dynamics of the mixture tend then to that of a system formed by non-interacting molecules, governed by the relaxation time of these independent processes.

Interpretation of dielectric relaxation in terms of activation processes

As we mentioned for one components systems, the temperature evolution of the principal relaxation time (τ_1) can be interpreted in terms of an activation process governed by Eyring's equation (see Eq (6.3)). Here we apply this analysis to mixtures of various compositions at the different levels studied above: the entire simulation box, each species as a whole and individual molecules of each component. Figures 6.25 and 6.26 show Eyring plots at these different levels, where the linear trend is preserved in most cases. Only when the number of molecules of one of the components of the mixture is low (ethanol at $x_{\mathrm{EtOH}} = 0.20$ and water at $x_{\mathrm{EtOH}} = 0.80$), the trend is more uncertain due to poorer statistics. The activation enthalpies and entropies corresponding to these linear fits are summarised in Table 6.6. The results are within the same order of magnitude of the ones obtained by Petong *et al.* [243] for ethanol/water mixtures, particularly at high ethanol concentrations. However, we do not observe the maxima of both activation enthalpy and entropy at mole fractions around 0.22 noted by the authors. Instead, we obtain a monotonous increase of the activation enthalpy from

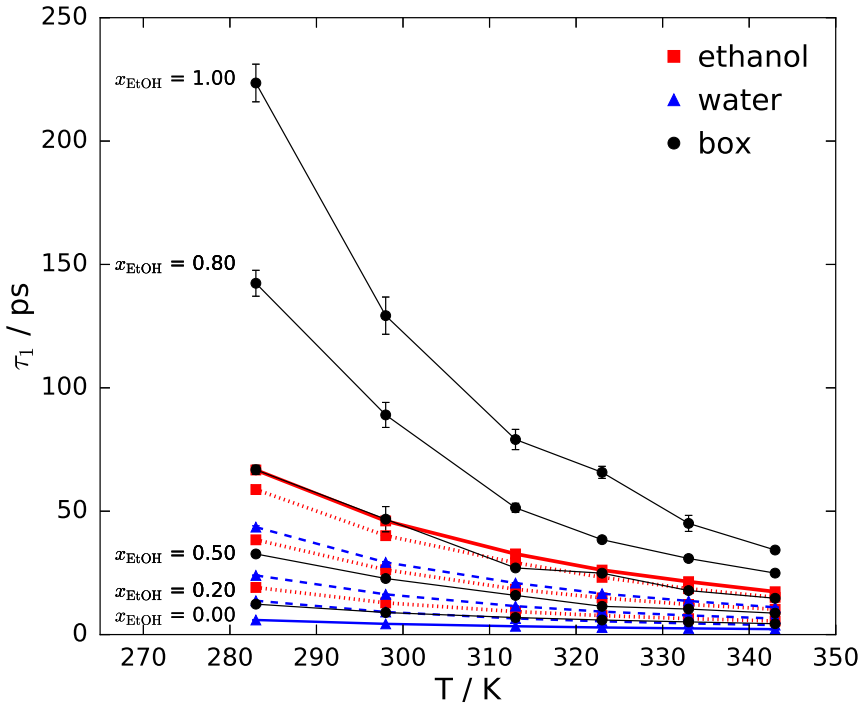

FIGURE 6.24: Influence of temperature on main relaxation times of individual ethanol and water molecules compared to entire system in ethanol/water mixtures at 1 bar.The results are obtained fitting the 1 HN + 1 Debye to the dipole moment ACFs from MD simulations. Black circles, red squares and blue triangles correspond to results obtained for the entire mixture, ethanol and water, respectively. The solid, dotted and dashed lines are a guide to the eye for the entire mixture, ethanol and water, respectively.

pure water to pure ethanol, similar to the one observed for ethanol/n-hexanol [273] and nitrobenzene/toluene mixtures [339]. The increasing energy jump required for the reorganisation of the entire molecular structure as the concentration of ethanol raises is due to the bigger energy penalty associated to the rotation of a larger and less polar molecule such as ethanol when compared to water. Studying the total contribution of each species, both activation enthalpy and entropy of the predominant component in the mixture tend to be very similar to those of the mixture itself, indicating that the same relaxation mechanisms are involved at those levels. As mentioned in the case of one component systems, activation enthalpies of individual molecules tend to be smaller due to the lower energy barrier required for the rotation of these individual molecules when compared with the reorientation of entire molecular systems. As mentioned before, the stronger hydrogen-bond network in pure water results in a more ordered fluid structure at the activated state and, therefore, in lower activation entropy than ethanol. The disruption of the hydrogen-bond network of water when ethanol molecules are added to the mixture translates into a continuous raise of the activation entropy of the relaxation process as the concentration of ethanol increases.

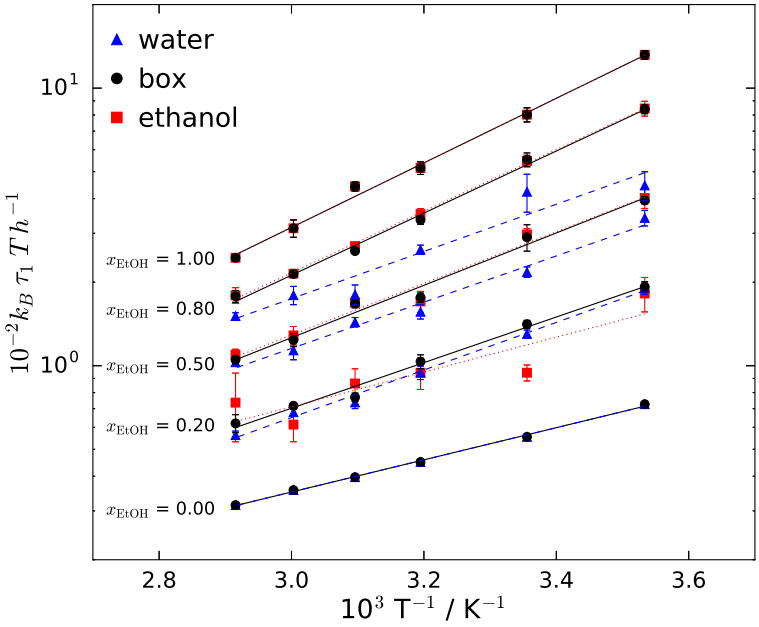

FIGURE 6.25: Eyring plot for the main relaxation process of entire species (ethanol and water) compared to the main relaxation process of the mixture at 1 bar. Black circles, red squares and blue triangles correspond to results obtained for the entire mixture, ethanol and water, respectively. In the same order, the solid, dotted and dashed lines represent the fit of these data to Eyring's equation (Eq (6.3)).

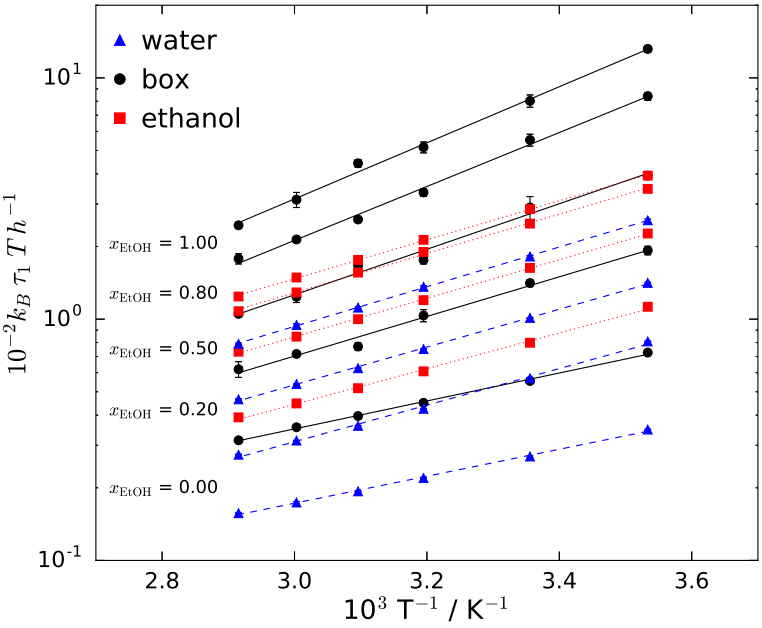

FIGURE 6.26: Eyring plot for the main relaxation process of individual ethanol and water molecules compared to the main relaxation process of the mixture at 1 bar. Black circles, red squares and blue triangles correspond to results obtained for the entire mixture, ethanol and water, respectively. In the same order, the solid, dotted and dashed lines represent the fit of these data to Eyring's equation (Eq. (6.3)).

TABLE 6.6: Activation enthalpies and entropies of the main relaxation process in ethanol/water mixtures at 1 bar.

	Activation enthalpy $\Delta H^{\#}$ / kJ mol^{-1}				
	$x_{\mathrm{EtOH}} = 0.00$	$x_{\mathrm{EtOH}} = 0.20$	$x_{\mathrm{EtOH}} = 0.50$	$x_{\mathrm{EtOH}} = 0.80$	$x_{\mathrm{EtOH}} = 1.00$
Box	10.9 ± 0.3	15.4 ± 0.9	18 ± 2	20.9 ± 0.8	21.8 ± 0.8
Ethanol total	–	12 ± 3	17 ± 2	20.8 ± 0.4	21.8 ± 0.8
Water total	10.8 ± 0.3	16.1 ± 0.7	16 ± 1	16 ± 3	–
Ethanol molecule	–	13.8 ± 0.4	15.0 ± 0.2	15.2 ± 0.3	15.1 ± 0.2
Water molecule	10.5 ± 0.3	14.2 ± 0.4	14.7 ± 0.2	15.4 ± 0.2	–

	Activation entropy $\Delta S^{\#}$ / J mol^{-1} K^{-1}				
	$x_{\mathrm{EtOH}} = 0.00$	$x_{\mathrm{EtOH}} = 0.20$	$x_{\mathrm{EtOH}} = 0.50$	$x_{\mathrm{EtOH}} = 0.80$	$x_{\mathrm{EtOH}} = 1.00$
Box	3.6 ± 0.8	12 ± 3	14 ± 4	19 ± 3	19 ± 3
Ethanol total	—	1 ± 9	13 ± 5	19 ± 2	19 ± 3
Water total	3.6 ± 0.8	14 ± 3	8 ± 4	6 ± 7	—
Ethanol molecule	—	11 ± 2	8.8 ± 0.5	6.3 ± 0.9	4.8 ± 0.5
Water molecule	8.3 ± 0.8	15 ± 2	11.7 ± 0.7	9.3 ± 0.4	—

6.4 Conclusions

In this chapter, we analyse the effect of temperature on the dielectric properties of one component systems and mixtures. This is relevant for the study of microwave heating processes since these properties, which are highly dependent on temperature, dictate the heating rates that can be achieved within the system.

The use of molecular simulations to estimate dielectric spectra at different temperatures provides satisfactory results for water, ethanol, MEA and ethanol/water mixtures when compared with available experimental data. In addition, it allows the prediction of this property at temperatures for which data is not available in the literature. In general, the dielectric response of these systems becomes faster as temperature increases, as expected from the faster molecular motions envisioned at high temperatures. This translates into shorter relaxation times as temperature increases for the main relaxation process (τ_1). From the results obtained in our simulations, the influence of this variable on the relaxation times of faster processes (τ_3 and τ_4) does not appear to be very significant. In general, the contribution of the main relaxation process tends to decrease at high temperatures with the faster processes becoming more significant, particularly for ethanol. The deviations of the main relaxation process from the ideal Debye behaviour are minor for entire systems. However, they become more important at the molecule level with different response to temperature variations depending on the system.

The study of the dielectric response at the individual molecule level reveals an interesting finding: the dynamics of entire systems get closer to that of a system of independent molecules at high temperatures. This demonstrates that the hydrogen-bond

network, characteristic of the systems studied here, tends to weaken as temperature increases. The complex collaborative processes between molecules that give shape to the dielectric response of the system at low temperatures disappear at higher temperatures where the response is governed by the contribution of independent molecules.

Additionally, we provide an interpretation of the main relaxation process as a rate process described as an Eyring-type activation. The characteristic activation enthalpy and entropy of the process are determined for entire systems, entire species and individual molecules. For one component systems, water shows lower activation energies than both ethanol and MEA due to its smaller size and higher polarity which causes less restrictions for the reorientation of the molecular system in the direction of the external electric field. For ethanol/water mixtures, a monotonous increase of the activation enthalpy is observed from pure water to pure ethanol. Analysing the contribution of each species, we note that activation enthalpy and entropy of the mixture coincide with that of the predominant component. Finally, the energy penalty of reorienting a single molecule in the direction of the electric field is always lower than that of entire systems of molecules, which translates in smaller activation energies at the molecule level.

At this point, we have shown how we are able to predict the evolution of the dielectric spectra of one component systems and mixtures with temperature and concentration by means of MD simulations. In Chapter 7, we use this information to estimate heating rates in microwave heating processes, and to analyse the influence of temperature on the penetration depth of electromagnetic waves in dielectric materials.

Chapter 7

Prediction of Microwave Heating Rates

The results obtained in previous chapters have shown how molecular dynamics simulations can be a useful tool to accurately estimate the dielectric properties of a variety of systems. This includes the prediction of the evolution of these properties with temperature and concentration. In this chapter, we use this information to provide estimates of observable macroscopic quantities. In particular, we focus on quantities that are relevant to microwave heating processes at the most common commercial microwave frequency: 2.45 GHz. We are able to obtain accurate predictions of the penetration depth of electromagnetic waves in dielectric materials at that frequency. In addition, we propose a simple model to describe the temperature profiles within a material subject to microwave radiation. We apply this model for water and monoethanolamine (MEA) systems and compare our estimates with available experimental data. Although the predictions are generally within one order of magnitude of the expected results, it becomes evident that a detailed description of the electric field distribution, both inside and outside the dielectric material, is necessary to obtain accurate heating profiles.

7.1 Introduction

Microwave heating processes have proven to be more efficient than other conventional heating technologies for a wide range of applications [2]. The volumetric effect of electromagnetic heating implies a more uniform distribution of heat within the workload and leads to faster heating rates for materials that couple appropriately with the microwave field. In addition, a series of non-thermal effects, whose origin is not fully understood, have the ability to modify phase equilibrium and enhance chemical reaction rates, thus promoting the advantages of microwave heating. In Chapter 2 we provide a review of some of the main applications of microwave heating in fields such as food processing, separation technologies or the enhancement of chemical reaction rates in organic chemistry [4].

The transmission of microwaves to a target workload can be performed in various ways. The most common equipment are multimode and monomode ovens [2, 4]. The former have been implemented in both domestic and larger industrial applications,

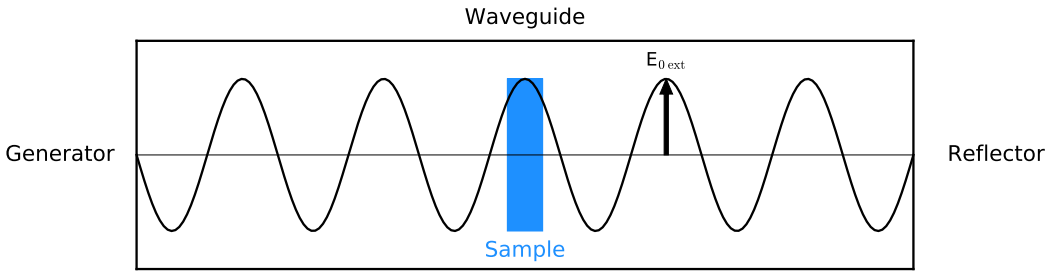

FIGURE 7.1: Microwave heating: rectangular waveguide set-up.

and generally consist of metallic boxes with at least two dimensions larger than the wavelength of the incoming radiation, and where the wave suffers multiple reflections on the oven walls. Mono or single-mode ovens are more suitable for smaller scales. They are formed by a generator and a waveguide that transmits the electromagnetic radiation to the sample in a single direction (see Fig. 7.1). The reflection of the wave at the opposite end of the waveguide allows for the establishment of standing waves. In this set-up the electric field distribution is more defined, and it is the one we consider for the remainder of this chapter.

The presence of a dielectric workload in the oven cavity can significantly modify the characteristics of the established field in the surroundings of the material. The electric field inside the workload is determined by the continuity of displacement current at the boundary with the surrounding air, which can result in significantly lower internal electric field intensities depending on the geometry and the dielectric properties of the material. Having a good description of the electric field distribution inside the sample is essential since this is one of the main factors determining microwave heating rates. In this context, another important aspect to consider is the attenuation of the electromagnetic field as it interacts with the sample. The conversion of electromagnetic energy into heat as the radiation penetrates the material limits the depth of this interaction. The concept of penetration depth is defined as the distance at which the electric field intensity is reduced to $1/e$ of its original value. This is an important design parameter determined from the frequency-dependent dielectric characteristics of the material. Generally, it is more beneficial to reach larger penetration depths, even if it is at the expense of obtaining lower absorption rates. In fact, this is the main reason why domestic microwave ovens operate at frequencies lower than the one corresponding to the maximum energy absorption of water.

Computational electromagnetics can be a powerful tool to describe the electromagnetic field distribution within the workload. Different numerical techniques, such as finite-difference time-domain (FDTD) [97] or finite element (FE) [98, 99] methods, are available to solve Maxwell's equations under predefined constitutive relations and boundary conditions. These simulations can provide very accurate representations

of electromagnetic field distributions. However, since this is not the main focus of this thesis, here we only consider simple approximate models to determine microwave heating rates.

7.2 Microwave heating profiles

The evolution of temperature in a microwave heating process is the result of the conservation of energy within the system. In this chapter, we assume that the microwave heating process takes place in a closed cylindrical tube such as the one depicted in Fig. 7.1. A generator produces microwaves, which are transmitted to the sample through a rectangular waveguide. In such system, the energy balance is dictated by the contribution of different terms including the absorption of heat from the electromagnetic wave, the accumulation of energy within the system and the heat losses to the surroundings due to convection and conduction processes.

7.2.1 Energy balance

In general, the conservation of energy in the system can be expressed as:

$$\text{Accumulation} = \text{In} - \text{Out} + \text{Generation} - \text{Consumption} \tag{7.1}$$

However, for the systems we are studying both generation and consumption can be discarded since no chemical reaction occurs. This restricts the energy balance to:

$$\text{Accumulation} = \text{In} - \text{Out}, \tag{7.2}$$

where the heat entering the system results from the absorption of energy from the electromagnetic wave ($\dot{Q}_{abs}$), and the energy leaving the system is due to convective ($\dot{Q}_{conv}$) and conductive ($\dot{Q}_{cond}$) losses to the surroundings:

$$\boxed{\dot{Q}_{acc} = \dot{Q}_{abs} - \left(\dot{Q}_{conv} + \dot{Q}_{cond}\right)} \tag{7.3}$$

The different terms contributing to this balance can be defined as follows:

- Energy accumulation rate within the system:

$$\dot{Q}_{acc} = m c_p(T) \frac{dT}{dt} \tag{7.4}$$

  where m and c_p are the mass and specific heat capacity of the material, respectively, T is the temperature and t the time.

- Energy absorbed by the system from the microwaves (as defined in Chapter 2):

$$\dot{Q}_{abs} = \omega\ \varepsilon_{vac}\ \varepsilon''(\omega, T)\ |\mathbf{E}(\omega)|^2\ V \tag{2.80}$$

where ω is the angular frequency, ε_{vac} is the vacuum permittivity, $\varepsilon''(\omega)$ is the imaginary part of the frequency-dependent dielectric constant, $|\mathbf{E}(\omega)|$ is the strength of the electric field inside the material and V is the volume of the system.

- Heat losses due to convection and conduction to the surroundings:

$$\dot{Q}_{conv} + \dot{Q}_{cond} = UA\ (T - T_{amb}) \tag{7.5}$$

where U represents the overall heat transfer coefficient, A is the external surface area of the cylinder and T_{amb} is the ambient temperature.

Therefore, for a microwave heating process in a closed system where no chemical reaction occurs, the conservation of energy is given by:

$$\boxed{mc_p(T)\frac{dT}{dt} = \omega\ \varepsilon_{vac}\ \varepsilon''(\omega, T)\ |\mathbf{E}(\omega)|^2\ V - UA\ (T - T_{amb})} \tag{7.6}$$

This first order differential equation can be solved using numerical methods to obtain microwave heating profiles.

7.2.2 Considerations regarding the intensity of the electric field within the dielectric material

In the energy balance presented in Eq (7.6), most variables can be easily obtained provided a minimum knowledge of the conditions at which the microwave heating process occurs. However, the determination of the intensity of the electric field within the sample requires special attention. In a first instance, the electric field propagation in free space within the waveguide has to be specified. Then, we assume the sample is placed in the optimum position for maximum energy absorption from the electromagnetic wave. Finally, it is necessary to consider the attenuation of the intensity of the electric field at the boundary between the air, where the wave propagates initially, and the dielectric material. Due to the small size of the samples analysed in this work, the influence of the penetration depth will not be considered here. Even so, an estimate of this parameter is provided in our results.

Standing waves in Rectangular Waveguides

As mentioned above we consider that the transmission of microwaves to the sample takes place in a rectangular waveguide. The wave, originated in the generator (or magnetron) at one end of the waveguide, is reflected at the other end, producing a standing wave [380, 381]. Standing waves result from the interference between incident and reflected waves, and are characterised by having a constant amplitude at each point of the waveguide, as shown in Fig. 7.1. If the process operates under ideal conditions, the wave does not lose power while propagating within the waveguide.

Electric Field Distribution in Rectangular Waveguides

In order to maximise the absorption of electromagnetic energy, the sample is positioned at the point of maximum intensity of the electric field. According to Metaxas and Meredith [2, 382], for rectangular waveguides the maximum electric field intensity is given by:

$$E_{0\,\mathrm{ext}} = \sqrt{\frac{4P}{ab}\frac{\lambda_g}{\lambda_0}\left(\frac{\mu_{vac}}{\varepsilon_{vac}}\right)^{0.5}} \tag{7.7}$$

where P is the power transmitted through the waveguide, a and b are the width and height of the waveguide, respectively, and λ_0 and λ_g, are the free space and waveguide wavelengths, respectively.

Continuity of displacement current at the boundary between two different dielectric materials

As shown in Fig. 7.1, the electromagnetic wave propagates through free space until it makes contact with the cylindrical tube containing the sample. If we consider that the glass tube is transparent to microwaves and does not have an influence on the intensity of the field, the electromagnetic radiation reaches the sample at its maximum intensity. As we mentioned in Chapter 2 (Eq. (2.36)), at the boundary between two different materials, there must exist continuity of displacement current. For cylindrical geometries, such as the ones considered here, the relationship between the electric field on the outside ($E_{0\,\mathrm{ext}}$) and within ($E_{0\,\mathrm{int}}$) a dielectric material is given by [383, 384]:

$$E_{0\,\mathrm{int}} = \frac{2}{1+\hat{\varepsilon}'(\omega)}\,E_{0\,\mathrm{ext}} \tag{7.8}$$

Penetration depth

Once the electromagnetic field reaches the dielectric material, the interaction of the radiation with dynamic processes within the material will cause an attenuation of the intensity of the field (see Fig. 7.2). According to Beer-Lambert law [385–387], the intensity of the electromagnetic signal decays exponentially with the distance to the external boundary of the material:

$$E_{\mathrm{int}}(z,\omega) = E_{0\,\mathrm{int}}\exp\left(-\frac{z}{\delta_p(\omega)}\right) \tag{7.9}$$

where $\delta_p(\omega)$ is defined as penetration depth, and corresponds to the distance where the intensity of the field is reduced to $1/e$ (approximately 37%) of its value at the boundary $E_{0\,\mathrm{int}}$. It can be shown that the penetration depth of an electromagnetic signal within a

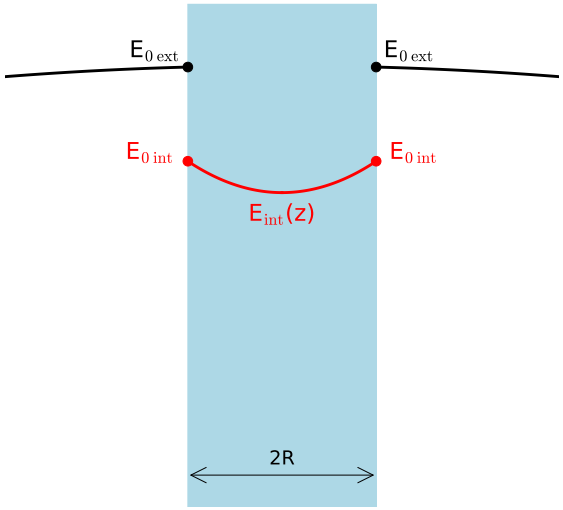

FIGURE 7.2: Electric field distribution in the sample.

dielectric material is given by [2, 382]:

$$\delta_p(\omega) = \frac{\lambda_0}{2\pi\sqrt{2\varepsilon'(\omega)\left[\sqrt{1+\left(\frac{\varepsilon''(\omega)}{\varepsilon'(\omega)}\right)^2}-1\right]}} \tag{7.10}$$

Empirical estimation of the electric field within the workload

An alternative to the calculation of the electric field inside the sample from Eqs. (7.7) and (7.8) is the use of empirical formulas. The electric field inside the workload can be estimated from the input power of the microwaves and the characteristics of the sample as [388, 389]:

$$|\mathbf{E}(\omega)| = E_{0\,\mathrm{int}} = \sqrt{\frac{2P}{1-|S_{11}|^2}} \tag{7.11}$$

where S_{11} is the reflection coefficient, associated with the fraction of power reflected by the dielectric material.

7.3 Results and Discussion

Temperature profiles in microwave heating processes can be obtained from the integration of Eq. (7.6). The main aim of this section is to implement the results obtained in previous chapters for dielectric properties of different materials to obtain their corresponding heating profiles for microwave heating processes at 2.45 GHz. We start by showing the good prediction of the evolution of real and imaginary parts of the dielectric constant with temperature at this particular frequency. Then, we determine the

influence of temperature on the penetration depth. To conclude, we present the estimated microwave heating profiles of water and MEA at 2.45 GHz and different input powers, and we compare our results with experimental heating profiles obtained at the University of Edinburgh.

7.3.1 Temperature dependence of the dielectric constant at 2.45 GHz

In Chapter 6 we predict the influence of temperature on the dielectric spectra of water, ethanol, MEA and ethanol/water mixtures. Here we focus on the results obtained at the most common frequency operated commercially, 2.45 GHz.

Pure components

Figure 7.3 shows the effect of temperature on the real and imaginary parts of the dielectric constant of water, ethanol and MEA. The comparison with experimental data confirms the particularly good agreement obtained for water [103, 104, 112, 234, 338] in the entire range of temperatures. In the case of ethanol, the results agree with experimental data determined by most authors [336, 337, 365] but differ slightly from results obtained by Liao et al. [335] for the real dielectric permittivity, particularly at high temperatures. Finally, for MEA better results seem to be obtained for the imaginary part than for the real part, although a very limited number of experimental data [238] are available in this case.

Solid lines in Fig. 7.3 represent quadratic fits

$$\varepsilon'(T) = a'T^2 + b'T + c'$$
$$\varepsilon''(T) = a''T^2 + b''T + c''$$

to the data obtained from molecular simulation, which fitting parameters are summarised in Table 7.1. The objective of these fits is to create a function for the temperature-dependence of these dielectric properties that can be invoked later during the determination of microwave heating profiles.

Different trends are observed in the data for the systems we have considered in this study. While the real permittivity of water tends to decrease with temperature at 2.45 GHz, the opposite trend is observed for ethanol and MEA. In the case of the dielectric loss, while water shows a continuous decrease, for both ethanol and MEA the imaginary part of the dielectric constant initially increases with temperature and then decreases at higher temperatures. This is related to the shift of the position of the characteristic frequency of the main relaxation process with temperature (see Fig. 6.9). For water, the main relaxation process occurs at frequencies higher than 2.45 GHz for the entire range of temperatures. However, for both ethanol and MEA, the main relaxation process takes place at frequencies lower than 2.45 GHz at low temperatures but shifts to frequencies higher than this value at high temperatures.

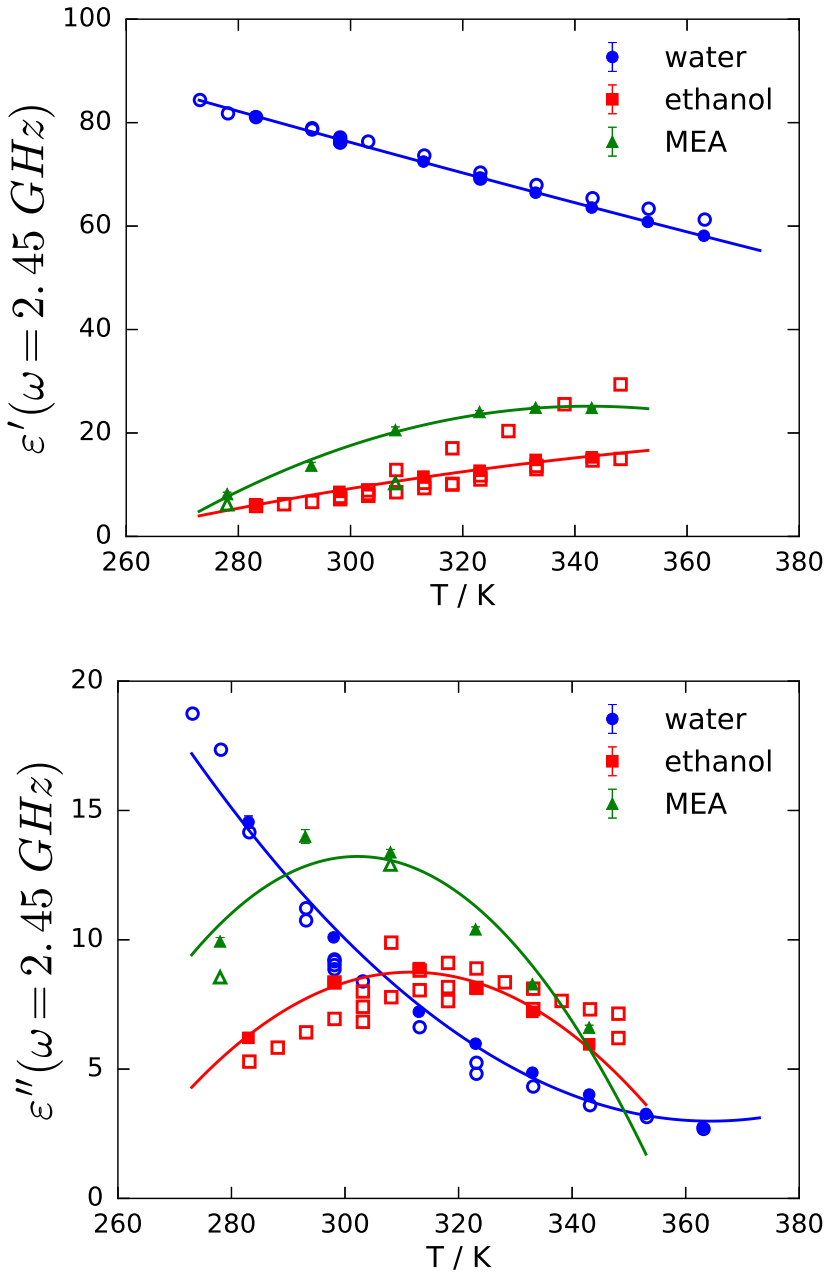

FIGURE 7.3: Temperature dependence of real and imaginary parts of the dielectric constant of water (blue circles), ethanol (red squares) and MEA (green triangles) at 2.45 GHz. Filled symbols represent results obtained from our simulations. Solid lines are quadratic fits to these results. Open symbols correspond to experimental data gathered from different sources for water [103, 104, 112, 234, 338] , ethanol [335–337, 365] and MEA [238].

TABLE 7.1: Parameters for the quadratic fits of the influence of temperature on dielectric properties of water, ethanol and MEA at 2.45 GHz.

Molecule	$10^3 a$ / K^{-2}	b / K^{-1}	c
Real part ε'			
Water	1.56	−0.391	180
Ethanol	−0.707	0.601	−107
MEA	−4.22	2.89	−469
Imaginary part ε''			
Water	1.70	−1.24	229
Ethanol	−2.99	1.86	−281
MEA	−4.46	2.70	−394

Mixtures

Figure 7.4 shows the results obtained for ethanol/water mixtures. Once again, the predictions from our simulations are in good agreement with experimental data [103, 104, 112, 234, 335–338, 365] . The parameters defining the quadratic fits to the simulation data are presented in Table 7.2. We observe a progressive shift from decreasing real permittivities with temperature at low ethanol concentrations to an increasing trend at higher ethanol concentrations. The shift of characteristic frequency of the main relaxation process with temperature and concentration (see Fig. 6.19) is also visible on the distinct temperature trends of the dielectric loss.

7.3.2 Temperature dependence of the penetration depth at 2.45 GHz

An important parameter in the design of microwave heating equipment is the penetration depth given by Eq. (7.10). Here we present estimations of this parameter at 2.45 GHz, using real dielectric permittivities and imaginary dielectric losses obtained through MD simulations and shown above.

Pure components

Figure 7.5 shows the evolution of the penetration depth of the water, ethanol and MEA with temperature. Available experimental results [335] for water and ethanol confirm the good prediction of this important quantity from our simulations. As we mentioned previously, the penetration depth is an indicator of the rate of conversion of electromagnetic energy into heat as radiation penetrates the target material. Since it is the imaginary part of the dielectric constant ε'' the one that dictates the heat losses within the material, one would expect these two quantities to be strongly correlated. Indeed, the decrease in dielectric loss of water, ethanol and MEA at high temperatures (see

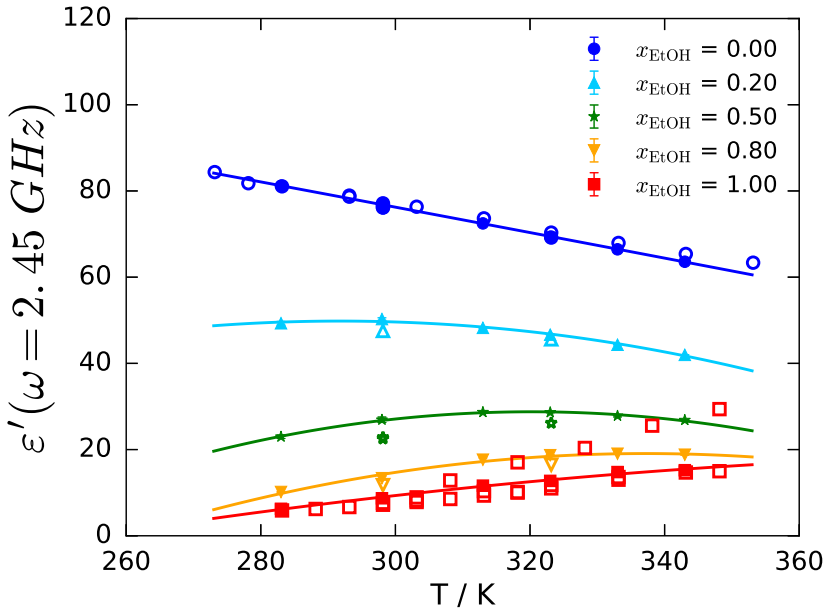

(a) Real part

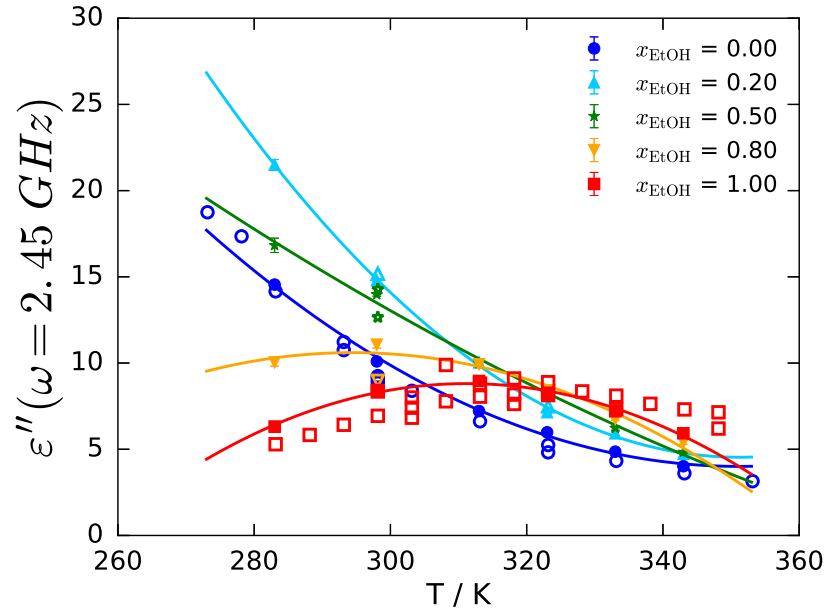

(b) Imaginary part

FIGURE 7.4: Temperature dependence of real and imaginary parts of the dielectric constant of ethanol/water mixtures at 2.45 GHz. Blue circles, cyan upward facing triangles, green stars, orange downward facing triangles and red squares correspond to mixtures of ethanol mole fractions 0.00, 0.20, 0.50, 0.80, and 1.00, respectively. Filled symbols represent results obtained from our simulations. Solid lines are quadratic fits to these results. Open symbols correspond to experimental data gathered from different sources [103, 104, 112, 234, 335–338, 365]

TABLE 7.2: Parameters for the quadratic fits of the influence of temperature on dielectric properties of ethanol/water mixtures at 2.45 GHz.

x_{EtOH}	$10^3 a$ / K^{-2}	b / K^{-1}	c
Real part ε'			
0.0	-0.0422	-0.269	161
0.2	-3.07	1.79	-212
0.5	-4.10	2.63	-392
0.8	-3.16	2.13	-340
1.0	-0.707	0.601	-107
Imaginary part ε''			
0.0	2.24	-1.57	280
0.2	3.65	-2.56	454
0.5	0.668	-0.624	140
0.8	-2.35	1.38	-193
1.0	-2.99	1.86	-281

Fig. 7.3) translates into larger penetration depths, as would be expected from the lower microwave absorption rates.

Mixtures

The influence of temperature on the penetration depth of ethanol/water mixtures is presented in Fig. 7.6. A general increase of the penetration depth with temperature is observed at any given concentration. Additionally, it is clear how the larger the concentration of ethanol in the mixture, the shorter the penetration of the electromagnetic wave in the sample at 2.45 GHz.

7.3.3 Heating profiles at 2.45 GHz

Experimental datasets

As part of the *Wetting Layer Absorption (WLA)* project (EPSRC Grant EP/J019704/1), and in collaboration with the Institute of Materials and Processes at the University of Edinburgh (Dr Claudia Martin, Dr Stephen McGurk, Dr Xianfeng Fan and Dr Martin Sweatman), experiments were carried out to determine microwave heating profiles of water and MEA at a frequency of 2.45 GHz and different input powers (see Table 7.3).

A waveguide with rectangular cross-section of dimensions 86.36 mm $\times$ 43.18 mm was used to transmit the power generated in a magnetron to the sample of dielectric material. The wavelength of the generated microwave in free space is λ_0 = 12.24 cm, while the waveguide wavelength is λ_g = 17.35 cm [2]. For all the experiments performed, a volume of 5 ml of sample was contained in a cylindrical tube with an inner

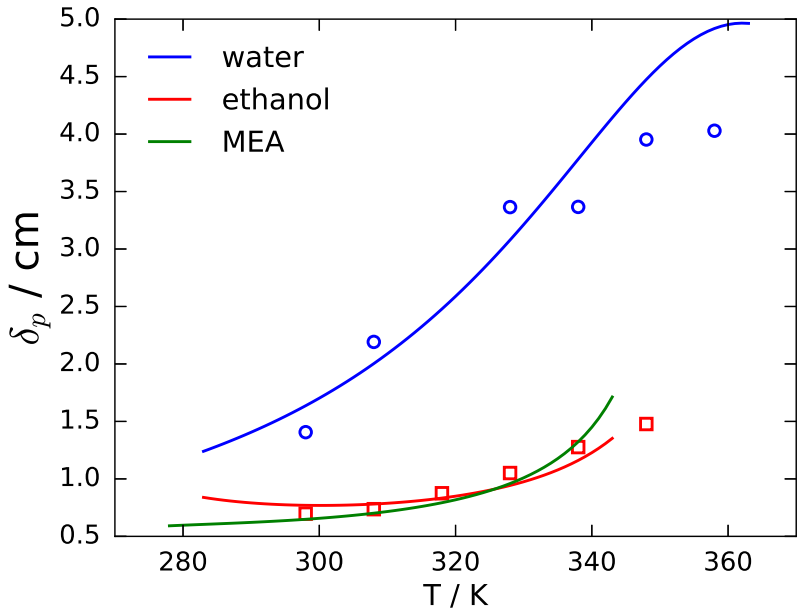

FIGURE 7.5: Temperature dependence of penetration depth of water ethanol and MEA at 2.45 GHz. Solid lines represent predictions obtained from our simulations for water (blue), ethanol (red) and MEA (green). Open symbols correspond to experimental data for water (circles) and ethanol (squares) [335].

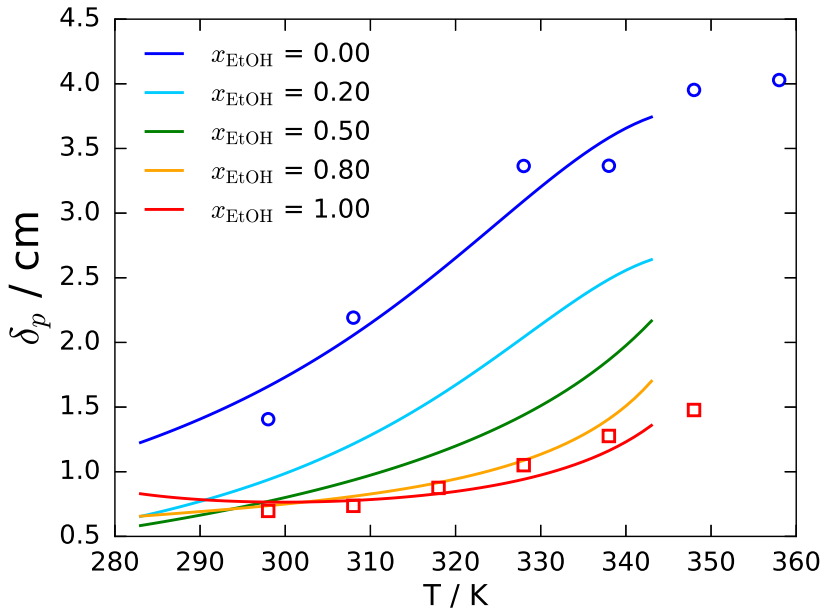

FIGURE 7.6: Temperature dependence of penetration depth of ethanol/water mixtures at 2.45 GHz. Solid lines represent predictions obtained from our simulations. Open symbols correspond to experimental data for water (circles) and ethanol (squares) [335].

diameter of 1.5 cm. During the experiments, microwave heating was turned on until a cutoff temperature was reached (100°C for water and 70°C for MEA). Then, the microwave power was switched off and the system was left to naturally reach thermal equilibrium.

Determination of heat transfer coefficient

The cooling profiles obtained once the microwaves are switched off can be used to determine the heat transfer coefficient term UA, which can then be implemented to model heat losses to the surroundings during the heating step. Discarding the heating term in Eq. (7.6) results in a model for the cooling profiles:

$$mc_p(T)\frac{dT}{dt} = -\,UA\;(T - T_{amb}) \tag{7.12}$$

Figure 7.7 shows the experimental cooling profiles for water and MEA after irradiation with microwaves at different input powers, together with the fits to the model defined in Eq. (7.12). In this representation the initial time corresponds to the instant where microwaves are switched off. The influence of temperature on the heat capacity of water and MEA is captured through a linear fit of the experimental data presented in Fig. 6.1 that results in:

$$c_{p\,water} = 0.0115\;T + 71.7$$
$$c_{p\,MEA} = 0.291\;T + 79.1$$

where T is in K and c_p in J mol^{-1} K^{-1}. The ambient temperature changes, not only between different experiments, but also within a same experiment. For this reason this magnitude was recorded at the start ($T_{amb\,h}$) and the end ($T_{amb\,c}$) of each experiment. The corresponding values are shown in Table 7.3. In order to obtain the cooling profiles presented in Fig. 7.7, the least squares method is employed to minimise the differences

TABLE 7.3: Parameters of microwave heating profiles.

P / W	$T_{amb\,h}$ / °C	$T_{amb\,c}$ / °C	UA / W K^{-1}	$E_{0\,\mathrm{ext}}$ / V m^{-1}	S_{11}
Water					
84	22.37	23.05	0.0500	6868	0.856
120	22.98	23.96	0.0723	8209	0.881
200	22.51	23.80	0.0413	10598	0.848
MEA					
60	25.11	23.66	0 0303	5805	0.439
84	23.22	25.45	0.0326	6868	0.601
120	25.29	25.54	0.0339	8209	0.676

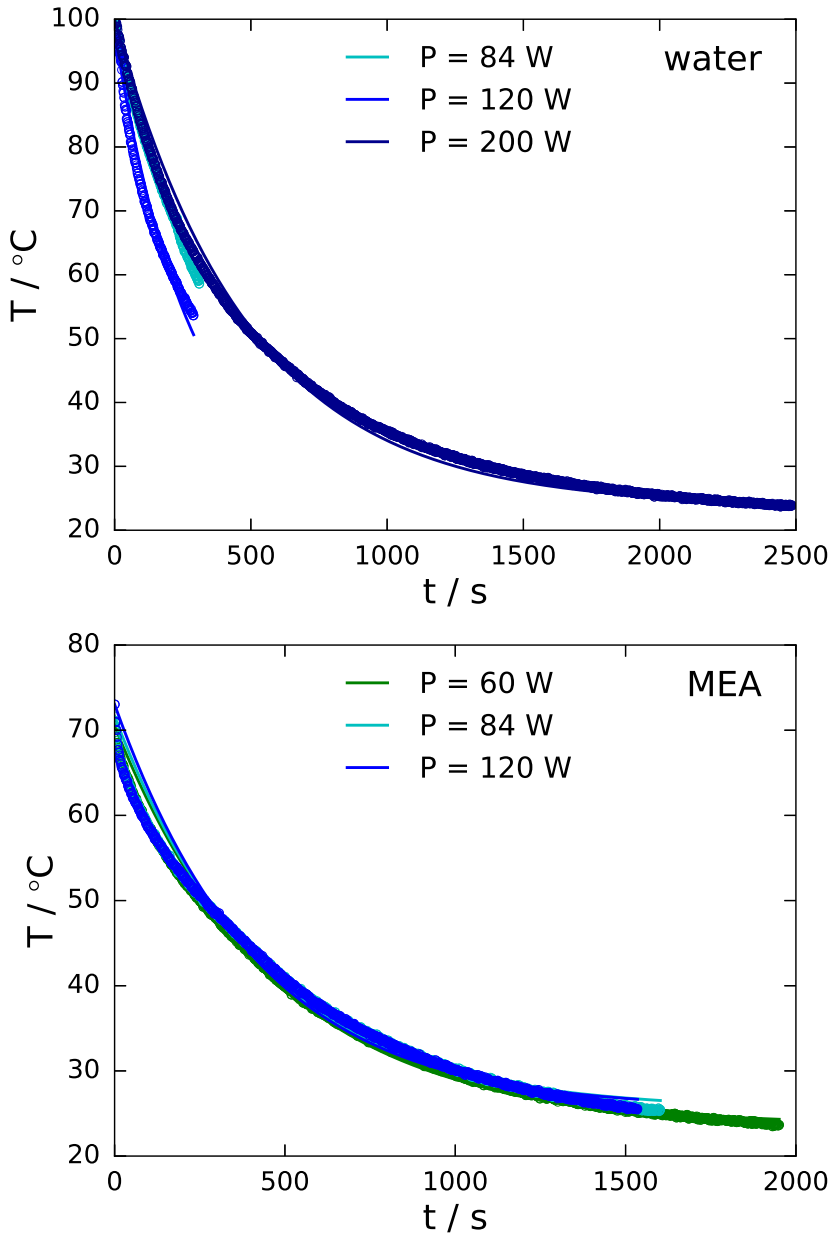

FIGURE 7.7: Cooling profiles of water and MEA after microwave irradiation. Open symbols correspond to different sets of experimental data, while solid lines represent the fit of these data to the cooling model described by Eq. (7.12).

between model and experimental results using UA as the single model parameter. The resulting values of this parameter are shown in Table 7.3. In all cases the cooling model provides reasonable results.

Heating profiles

Once all the terms in the energy balance given by Eq. (7.6) are known, we proceed to determine the heating profiles corresponding to the different experiments that have been carried out. Figure 7.8 shows microwave heating profiles of water and MEA at a frequency of 2.45 GHz and different input powers. The predictions obtained through this procedure clearly underestimate the experimental heating rates for all the different power inputs. Particularly pronounced is the effect on water profiles, although the results obtained for MEA are also far from the expected. Since we have proven the good estimation of dielectric properties at this particular frequency, the deviation must originate from either the electric field distribution defined by Eqs. (7.7) and (7.8) or other effects not considered in the energy balance given by Eq. (7.6).

The values of penetration depth shown in Fig. 7.5, which are close or, in some cases, even shorter than the width of the sample (1.5 cm), suggest that some attenuation of the electric field intensity can occur within the dielectric material. However, including this effect would lead to even lower heating rates.

As we stated at the start of the chapter, the model used to describe the electric field distribution within the equipment is a simple approximation. The results obtained here confirm the need for a more careful treatment of this issue. However, this work is out of the scope covered by this thesis. Instead, we finish this chapter by obtaining the best fit of the microwave heating model given by Eq. (7.6) to the experimental results. In this process, we use the empirical expression given by Eq.(7.11) to determine the electric field inside the sample, employing the reflection coefficient S_{11} as fitting parameter. Although there appears to be an excessive influence of the term corresponding to heat losses to the surroundings, which results in excessive bending of the temperature profile, the fits are generally satisfactory (see dashed lines in Fig. 7.8). The values of the reflection coefficient resulting from the fit are summarised in Table 7.3. This parameter is relatively stable with input power for water, while for MEA it increases as more power is introduced into the system. The larger reflection coefficients obtained for water with respect to MEA indicate a more intense reflection of microwave power for this system, which is consistent with the larger value of the real dielectric permittivity of water at 2.45 GHz. However, observing the experimental heating profiles in Fig.7.8, similar heating rates are obtained for both systems at the same input power. This result can be explained by the deeper penetration of electromagnetic radiation in water as shown in Fig. 7.5.

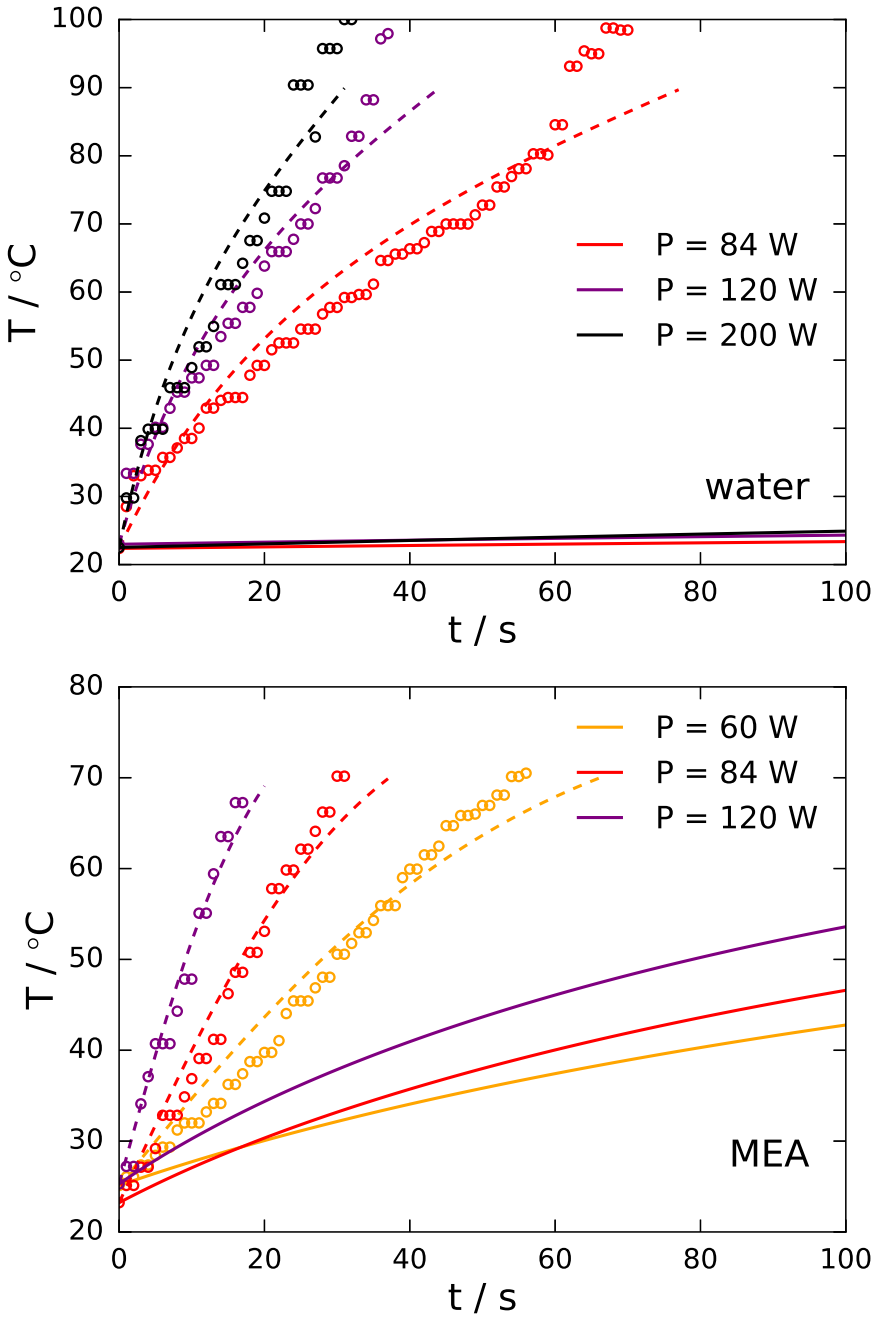

FIGURE 7.8: Microwave heating profiles of water and MEA at 2.45 GHz and different input powers. Open symbols correspond to experimental data. Solid lines represent predictions obtained through the heating model described by Eq. (7.6), using electric field distributions given by Eqs. (7.7) and (7.8). Dashed lines correspond to the fit of this same model to the corresponding experimental data, using the empirical Eq. (7.11) to determine the electric field inside the workload.

7.4 Conclusions

The idea behind this chapter is to apply the knowledge generated in previous chapters for the estimation of macroscopic quantities. With this aim in mind, we define the conservation of energy in a dielectric material irradiated by a microwave field taking into account the heat absorbed from the electromagnetic field, the heat accumulated within the sample and possible energy losses to the surroundings. This heat balance offers the possibility to determine temperature profiles for microwave heating processes. These are mostly dominated by the electric field distribution within the sample and the dielectric properties of the material.

We demonstrate good predictions of both real dielectric permittivity and imaginary dielectric loss for water, ethanol, MEA and ethanol/water mixtures at the most common microwave frequency for commercial applications (2.45 GHz). Additionally, we determine an important magnitude such as the penetration length. This quantity gives valuable information on the depth of propagation of the radiation inside the dielectric material and on the rate of conversion of electromagnetic energy into heat. We show how it can be predicted accurately from the results of MD simulations.

With regard to microwave heating profiles, we compare the predictions provided by the previously mentioned heating model with experimental results generated by collaborators at the University of Edinburgh for water and MEA at 2.45 GHz and different input powers. In all cases the results clearly underpredict the expected microwave heating rates. Since we have proven the good performance of our simulations for the prediction of dielectric properties, we believe the discrepancies reside in the simple models used for the determination of the electric field distribution outside and inside the target dielectric material. More detailed approaches on this topic have to be undertaken in order to obtain accurate heating profiles. Once some confidence is built on the estimation provided by these models, it will be possible to move forward and use this tool in the search for the conditions that provide the most efficient microwave heating process.

Chapter 8

Conclusions and Future Work

The aim of this thesis is to shed some light on the physical mechanisms that define the interaction of microwaves with fluids using molecular simulations, testing the ability of currently available force fields to predict dielectric response. This chapter summarises the main conclusions extracted from this work and suggests possible directions for further research based on these conclusions.

8.1 Conclusions

The interaction of electromagnetic waves with matter is governed by the characteristics of the wave and the dielectric properties of the irradiated material. At microwave frequencies, the effects of this interaction can be observed macroscopically in the form of heat dissipation for materials able to absorb radiation at these particular wavelengths. The main advantage of this type of heating with respect to conventional heating technologies is its volumetric nature. It avoids the slow heat transfer by thermal diffusivity from the external surface of the workload and, therefore, provides faster heating rates. This fact has been exploited for the development of microwave heating processes in several fields including food processing, various separation technologies or the enhancement of chemical reaction rates. A review of these and other applications is presented in Chapter 2. Although microwave heating processes have been used in a relatively large number of scenarios, the widespread industrial implementation of this technology is only starting recently.

From a macroscopic point of view, the propagation of electromagnetic waves in dielectric media is dictated by Maxwell's equations. The specific interaction between the material and the electric and magnetic components of the field are defined through constitutive relations that are governed by the dielectric and magnetic properties of the workload. In Chapter 2 we develop the theoretical framework behind these relations which leads to the determination of an expression for the microwave heating rate in dielectric materials. This expression shows the importance of the accurate determination of the frequency-dependent dielectric properties of the workload and the electric field distribution within the material for an adequate prediction of microwave heating rates.

This level of knowledge allows the simulation of microwave heating processes through numerical approximations to Maxwell's equations combined with predefined

constitutive relations. However, a more detailed understanding of the origin of this phenomenon has to be sought at the molecular level. The presence of an electromagnetic field interferes with the natural motion of molecular systems causing the polarisation of molecular dipoles as they tend to align with the direction of the field. Within the framework of the fluctuation-dissipation theorem and linear response theory, the response of the system to weak perturbation fields is interpreted as identical to the relaxation of internal equilibrium fluctuations within the system. This means that key properties, such as the dielectric properties of a material, can be inferred from the natural dynamic fluctuations of unperturbed systems. In Chapter 3 we exploit this result to develop a methodology for the determination of frequency-dependent dielectric properties from dipole moment fluctuations using equilibrium molecular dynamics simulations (see Eq. (3.50) and Fig. 3.3).

This methodology is applied for the estimation of the dielectric spectra of one component systems (water, ethanol, ethylene glycol, propylene glycol, glycerol and monoethanolamine) in Chapter 4, ethanol/water mixtures in Chapter 5 and the influence of temperature on these properties for some of these systems in Chapter 6. In general the results obtained in these studies show good agreement with experimental data.

In Chapter 4, the ability of different force fields to predict dielectric spectra is tested for each substance taking part in the study. The results presented in Fig. 4.6 show that at least one of the force fields provides a good estimate of this dynamic property. In particular, the SPC model shows the best results for water, the TraPPE-UA force field beats other force fields for ethanol, the GAFF force field is the best option for propylene glycol, and the dielectric spectra of ethylene glycol, glycerol and monoethanolamine is best predicted by the OPLS force field. However, despite the good performance of these models describing the dynamics of the dielectric response of the different systems, in most cases the static dielectric constant, related to the magnitude of this dielectric response, is not well predicted (see Fig. 4.5). In order to obtain appropriate estimations of dielectric spectra, it was decided to use the experimental value of this quantity in the calculations. The fit of the results to established dielectric relaxation models reveals that water follows an ideal Debye relaxation mechanism while larger systems show deviations from this ideal behaviour that can be captured by the Havriliak-Negami model. This strand of work also confirms that smaller molecules tend to be characterised by shorter relaxation times and that the more polar a molecule is the more intense is its dielectric response (see Fig. 4.7).

The estimation of dielectric spectra is extended to binary systems, in particular the ethanol/water mixture, in Chapter 5. In this case we adopt a multirelaxation approach that shows how the dielectric response of water is well described by the combination of a dominant relaxation process at microwave frequencies and a faster and less intense process. However, when ethanol is present in the mixture, an additional fast process is required to model the dielectric response adequately. This approach leads to accurate representations of the concentration-dependence of the dielectric spectra

of ethanol/water mixtures when compared with experimental results, as shown in Fig. 5.9. In fact, the performance of these predictions is evaluated against widely used mixing rules that consist on empirical estimations of properties of mixtures based on the properties of its individual constituents. The better performance of the results obtained through MD simulations for ethanol/water mixtures confirms established hypotheses that identify the origin of the dielectric response of these systems as collaborative processes of its hydrogen bond network rather than individual contributions of its components (see Fig. 5.10). Additionally, the study of the relaxation process of entire species and individual molecules within those species confirms the need for collaborative processes between groups of molecules in order to explain the global dielectric response.

The influence of temperature on the dielectric spectra of water, ethanol, MEA and ethanol/water mixtures is studied in Chapter 6. Once again, the main trends of the evolution of dielectric properties with temperature are captured appropriately by MD simulations (see Figs .6.9 and 6.19). In all cases, the dielectric response becomes increasingly faster as temperature increases, as expected from the faster molecular motions at high temperatures. The results confirm that the dielectric spectrum of water can be modelled through two relaxation processes for the entire range of temperatures. The remaining systems require an additional fast relaxation. For all the systems, the introduction of fast relaxations reduces the deviations of the dominant relaxation process from an ideal Debye behaviour. The study of the influence of temperature on the relaxation times of entire molecular systems and individual molecules reveals that the dynamics of molecular systems approach that of independent molecules as temperature increases. This is an indication of the weakening of hydrogen bond networks at high temperatures. In addition, it is shown how the main relaxation process can be interpreted as an activation process in which an energy barrier has to be overcome in order to proceed to the reorganisation of the hydrogen bond network. The results conclude that the activation enthalpy of water is lower than that of ethanol and MEA due to its smaller size and higher polarity that cause less restrictions to the reorientation of the molecular structure in the direction of the alternating electric field.

Finally, the results obtained in previous chapters are implemented in Chapter 7 for the estimation of macroscopic quantities relevant to microwave heating processes operating at the most common commercial frequency, 2.45 GHz. The results show accurate predictions of penetration depths, which are a good indicator of the depth of propagation of electromagnetic radiation within a dielectric material. However, microwave heating profiles obtained as a result of the conservation of energy in the dielectric workload provide unexpected results. Since the estimation of dielectric properties has been proven to be accurate, it is believed that the main reason for the underestimation of microwave heating rates is the crude calculation of the electric field distribution within the sample. More detailed treatment of this issue is required in order to obtain accurate representations of microwave heating profiles.

8.2 Future Work

The work presented in this thesis opens the door for further research in related topics. The methodology implemented here can be used to predict the performance of new materials and processes. An example of this application is research that will be carried out at the University of Edinburgh to investigate the microwave regeneration of amine solutions used in carbon capture processes. The formation of free ions in solution makes of this system a particularly interesting one since the transport of charge can play a significant role on microwave heating rates.

Additionally, the method described in this thesis for the prediction of dielectric properties from MD simulations could be applied to more complex systems. Similar methods have been used for the study of the dynamics of systems such as 1,4-polybutadiene [390, 391], polyethylene [392, 393], polypropylene [394], polystyrene [125, 393, 395–399], poly(methyl-methacrylate) [393], and model polymers [400]. Initial work has been performed within our group on the estimation of the influence of temperature on the dielectric spectrum of polystyrene, with particular interest on glass transition processes observed in this system. However, limitations have been encountered due to the low characteristic frequencies of these processes below the glass transition temperature, which require extremely long simulations (in the order of ms) to obtain reliable results. The evolution of computational resources will allow some time to perform atomistic molecular simulations of such lengths. Currently, coarse-grained molecular dynamics simulations offer the possibility to reach longer timescales and can be considered as an alternative.

In this work we have shown how the influence of temperature on dielectric properties can be accurately described using molecular dynamics simulations. This study could be extended to the prediction of the effect of another important process variable such as pressure, for which some experimental research has already been performed [90, 401, 402].

Another interesting topic that could be covered in the future is the analysis of the effect of fluid confinement on the dielectric response. In such systems, the response will no longer be homogeneous since the confinement restricts the molecular motion in specific directions. The dielectric constant becomes a tensor with directional dependency. Examples of these systems are carbon nanotubes or porous materials for absorption [133, 403].

Following the apparent relationship between dielectric response and dynamics of hydrogen bond networks, a deeper analysis of the molecular mechanisms leading to this connection could be carried out. This would involve a more detailed study of the evolution of the structure of the fluid with temperature and concentration, including the implementation of cluster size analysis to determine the shape of the hydrogen bond network.

An alternative to the estimation of properties from equilibrium molecular dynamics simulations is the direct implementation of an external time-dependent electric field within the simulation box [141, 171, 172, 180, 181, 183, 404]. This type of simulation can also be applied to study the effect of external electric fields on a range of thermodynamic properties, even for electric field intensities falling in the non-linear regime.

Finally, since the determination of the electric field distribution within the workload has proven to be very important for the accurate prediction of microwave heating rates, robust electromagnetic simulations, that make use of dielectric properties estimated through molecular dynamics simulations, would be an interesting option to consider for the optimisation of microwave heating processes.

Bibliography

[1] A. A. Penzias and R. W. Wilson, "A Measurement of Excess Antenna Temperature at 4080 Mc/s", *The Astrophysical Journal*, 142 (July 1965), 419–421, DOI: 10.1086/148307.

[2] R. Meredith, *Engineers' Handbook of Industrial Microwave Heating*, Energy Engineering, Institution of Engineering and Technology, 1998.

[3] E. Altman, "Microwave Enhanced Reactive Distillation", PhD thesis, TU Delft, 2011.

[4] G. D. Stefanidis et al., "A helicopter view of microwave application to chemical processes: reactions, separations, and equipment concepts", *Reviews in Chemical Engineering*, 30, 3 (2014), 233–259.

[5] J. C. Gallawa, *The Complete Microwave Oven Service Handbook: Operation, Maintenance, Troubleshooting, and Repair*, Prentice Hall, 1988.

[6] C. o. E. Committee on Microwave Processing of Materials: An Emerging Industrial Technology and N. R. C. Technical Systems, *Microwave Processing of Materials*, The National Academy Press, 1994.

[7] E. Thostenson and T.-W. Chou, "Microwave processing: fundamentals and applications", *Composites Part A: Applied Science and Manufacturing*, 30, 9 (1999), 1055 –1071, DOI: 10.1016/S1359-835X(99)00020-2.

[8] S. Chandrasekaran, S. Ramanathan, and T. Basak, "Microwave food processing - A review", *Food Research International*, 52, 1 (2013), 243 –261, DOI: 10.1016/j.foodres.2013.02.033.

[9] C. Salazar-Gonzalez et al., "Recent Studies Related to Microwave Processing of Fluid Foods", English, *Food and Bioprocess Technology*, 5, 1 (2012), 31–46, DOI: 10.1007/s11947-011-0639-y.

[10] R. Vadivambal and D. Jayas, "Non-uniform Temperature Distribution During Microwave Heating of Food Materials - A Review", English, *Food and Bioprocess Technology*, 3, 2 (2010), 161–171, DOI: 10.1007/s11947-008-0136-0.

[11] M. Zhang et al., "Trends in microwave-related drying of fruits and vegetables", *Trends in Food Science & Technology*, 17, 10 (2006), 524 –534, DOI: 10.1016/j.tifs.2006.04.011.

[12] E. Dominguez-Tortajada et al., "Optimisation of electric field uniformity in microwave heating systems by means of multi-feeding and genetic algorithms", *Int. J. of Materials and Product Technology*, 29, 1-4 (2007), 149–162, DOI: 10.1504/IJMPT.2007.013134.

[13] S. Geedipalli, V. Rakesh, and A. Datta, "Modeling the heating uniformity contributed by a rotating turntable in microwave ovens", *Journal of Food Engineering*, 82, 3 (2007), 359 –368, DOI: 10.1016/j.jfoodeng.2007.02.050.

[14] X. Hu, X. Yang, and G. Jia, "Effective Optimization of Temperature Uniformity and Power Efficiency in Two-ports Microwave Ovens", *Journal of Microwave Power and Electromagnetic Energy*, 48, 4 (2014), 261–268.

[15] D. K. Agrawal, "Microwave processing of ceramics", *Current Opinion in Solid State and Materials Science*, 3, 5 (1998), 480 –485, DOI: 10.1016/S1359-0286(98)80011-9.

[16] J. Osepchuk, "Microwave power applications", *Microwave Theory and Techniques, IEEE Transactions on*, 50, 3 (2002), 975–985, DOI: 10.1109/TMTT.2002.989981.

[17] D. Agrawal et al., *Microwave Solutions for Ceramic Engineers - Microwave Processing of Ceramics, Composites and Metallic Materials*, ed. by D. Clark et al., Wiley, 2005.

[18] M. Oghbaei and O. Mirzaee, "Microwave versus conventional sintering: A review of fundamentals, advantages and applications", *Journal of Alloys and Compounds*, 494, 1-2 (2010), 175 –189, DOI: 10.1016/j.jallcom.2010.01.068.

[19] J. Cheng, "Study of microwave sintering technique of ceramic materials", PhD thesis, China Wuhan University of Technology, 1991.

[20] J. P. Cheng et al., "Microwave processing of WC-Co composities and ferroic titanates", English, *Material Research Innovations*, 1, 1 (1997), 44–52, DOI: 10.1007/s100190050017.

[21] C. Ebner et al., "One Decade of Microwave-Assisted Polymerizations: Quo vadis?", *Macromolecular Rapid Communications*, 32, 3 (2011), 254–288, DOI: 10.1002/marc.201000539.

[22] D. Bogdal et al., "Microwave Assisted Synthesis, Crosslinking, and Processing of Polymeric Materials", English, *Liquid Chromatography / FTIR Microspectroscopy / Microwave Assisted Synthesis*, vol. 163, Advances in Polymer Science, Springer Berlin Heidelberg, 2003, 194–263, DOI: 10.1007/b11051.

[23] C. Zhang, L. Liao, and S. S. Gong, "Recent developments in microwave-assisted polymerization with a focus on ring-opening polymerization", *Green Chem.* 9 (4 2007), 303–314, DOI: 10.1039/B608891K.

[24] R. Hoogenboom and U. S. Schubert, "Microwave-Assisted Polymer Synthesis: Recent Developments in a Rapidly Expanding Field of Research", *Macromolecular Rapid Communications*, 28, 4 (2007), 368–386, DOI: 10.1002/marc.200600749.

[25] F. Wiesbrock, R. Hoogenboom, and U. S. Schubert, "Microwave-Assisted Polymer Synthesis: State-of-the-Art and Future Perspectives", *Macromolecular Rapid Communications*, 25, 20 (2004), 1739–1764, DOI: 10.1002/marc.200400313.

[26] D. Jones et al., "Microwave heating applications in environmental engineering - a review", *Resources, Conservation and Recycling*, 34, 2 (2002), 75 –90, DOI: 10.1016/S0921-3449(01)00088-X.

[27] T. Appleton et al., "Microwave technology for energy-efficient processing of waste", *Applied Energy*, 81, 1 (2005), 85 –113, DOI: 10.1016/j.apenergy.2004.07.002.

[28] R. A. Abramovitch et al., "In situ remediation of soils contaminated with toxic metal ions using microwave energy", *Chemosphere*, 53, 9 (2003), 1077 –1085, DOI: 10.1016/S0045-6535(03)00572-1.

[29] X. Liu and G. Yu, "Combined effect of microwave and activated carbon on the remediation of polychlorinated biphenyl-contaminated soil", *Chemosphere*, 63, 2 (2006), 228 –235, DOI: 10.1016/j.chemosphere.2005.08.030.

[30] Y.-C. Chien, "Field study of in situ remediation of petroleum hydrocarbon contaminated soil on site using microwave energy", *Journal of Hazardous Materials*, 199-200 (2012), 457 –461, DOI: 10.1016/j.jhazmat.2011.11.012.

[31] C. Ania et al., "Microwave-induced regeneration of activated carbons polluted with phenol. A comparison with conventional thermal regeneration", *Carbon*, 42, 7 (2004), Carbon '03 Conference, 1383 –1387, DOI: 10.1016/j.carbon.2004.01.010.

[32] C. Ania et al., "Microwave-assisted regeneration of activated carbons loaded with pharmaceuticals", *Water Research*, 41, 15 (2007), 3299 –3306, DOI: 10.1016/j.watres.2007.05.006.

[33] F. K. Yuen and B. Hameed, "Recent developments in the preparation and regeneration of activated carbons by microwaves", *Advances in Colloid and Interface Science*, 149, 1-2 (2009), 19 –27, DOI: 10.1016/j.cis.2008.12.005.

[34] M. Fayaz et al., "Using Microwave Heating To Improve the Desorption Efficiency of High Molecular Weight VOC from Beaded Activated Carbon", *Environmental Science & Technology*, 49, 7 (2015), PMID: 25751588, 4536–4542, DOI: 10.1021/es505953c.

[35] N. Remya and J.-G. Lin, "Current status of microwave application in wastewater treatment - A review", *Chemical Engineering Journal*, 166, 3 (2011), 797 –813, DOI: 10.1016/j.cej.2010.11.100.

[36] D. Martin et al., "Application of accelerated electron beam and microwave irradiation to biological waste treatment", *Vacuum*, 77, 4 (2005), 7th International Conference on Electron Beam Technologies, 501 –506, DOI: 10.1016/j.vacuum.2004.09.019.

[37] Y. Yang et al., "Microwave enhanced Fenton-like process for the treatment of high concentration pharmaceutical wastewater", *Journal of Hazardous Materials*, 168, 1 (2009), 238 –245, DOI: 10.1016/j.jhazmat.2009.02.038.

[38] M. Saha, C. Eskicioglu, and J. Marin, "Microwave, ultrasonic and chemomechanical pretreatments for enhancing methane potential of pulp mill wastewater treatment sludge", *Bioresource Technology*, 102, 17 (2011), 7815 –7826, DOI: 10.1016/j.biortech.2011.06.053.

[39] R. S. Varma, "Solvent-free organic syntheses . using supported reagents and microwave irradiation", *Green Chem.* 1 (1 1999), 43–55, DOI: 10.1039/A808223E.

[40] P. Lidstrom et al., "Microwave assisted organic synthesis - a review", *Tetrahedron*, 57, 45 (2001), 9225 –9283, DOI: 10.1016/S0040-4020(01)00906-1.

[41] S. Caddick and R. Fitzmaurice, "Microwave enhanced synthesis", *Tetrahedron*, 65, 17 (2009), 3325 –3355, DOI: 10.1016/j.tet.2009.01.105.

[42] P. He, S. J. Haswell, and P. D. I. Fletcher, "Microwave heating of heterogeneously catalysed Suzuki reactions in a micro reactor", *Lab Chip*, 4 (1 2004), 38–41, DOI: 10.1039/B313057F.

[43] E. Comer, and M. G. Organ, "A Microreactor for Microwave-Assisted Capillary (Continuous Flow) Organic Synthesis", *Journal of the American Chemical Society*, 127, 22 (2005), PMID: 15926844, 8160–8167, DOI: 10.1021/ja0512069.

[44] R. J. J. Jachuck, D. K. Selvaraj, and R. S. Varma, "Process intensification: oxidation of benzyl alcohol using a continuous isothermal reactor under microwave irradiation", *Green Chem.* 8 (1 2006), 29–33, DOI: 10.1039/B512732G.

[45] R. S. Varma and V. V. Namboodiri, "An expeditious solvent-free route to ionic liquids using microwaves", *Chem. Commun.* 7 (7 2001), 643–644, DOI: 10.1039/B101375K.

[46] F. Langa et al., "Microwave irradiation: more than just a method for accelerating reactions", *Contemp. Org. Synth.* 4 (5 1997), 373–386, DOI: 10.1039/CO9970400373.

[47] T. N. Glasnov and C. O. Kappe, "The Microwave-to-Flow Paradigm: Translating High-Temperature Batch Microwave Chemistry to Scalable Continuous-Flow Processes", *Chemistry - A European Journal*, 17, 43 (2011), 11956–11968, DOI: 10.1002/chem.201102065.

[48] R. Mato et al., "Solvent-Free Microwave Extraction of Essential Oil from Lavandin Super", *Proceedings of the AiChE Annual Meeting*, 2008.

[49] X. Pan, G. Niu, and H. Liu, "Microwave-assisted extraction of tea polyphenols and tea caffeine from green tea leaves", *Chemical Engineering and Processing: Process Intensification*, 42, 2 (2003), 129 –133, DOI: 10.1016/S0255-2701(02)00037-5.

[50] W. Ma et al., "Application of ionic liquids based microwave-assisted extraction of three alkaloids N-nornuciferine, O-nornuciferine, and nuciferine from lotus leaf", *Talanta*, 80, 3 (2010), 1292 –1297, DOI: 10.1016/j.talanta.2009.09.027.

[51] V. Sridhar, J.-H. Jeon, and I.-K. Oh, "Microwave extraction of graphene from carbon fibers", *Carbon*, 49, 1 (2011), 222 –226, DOI: 10.1016/j.carbon.2010.09.007.

[52] R. Cherbanski and E. Molga, "Intensification of desorption processes by use of microwaves - An overview of possible applications and industrial perspectives", *Chemical Engineering and Processing: Process Intensification*, 48, 1 (2009), 48 –58, DOI: 10.1016/j.cep.2008.01.004.

[53] M. Meier et al., "Microwave regeneration of zeolites in a 1 meter column", *AIChE Journal*, 55, 7 (2009), 1906–1913, DOI: 10.1002/aic.11793.

[54] Z. Hashisho, M. Rood, and L. Botich, "Microwave-Swing Adsorption To Capture and Recover Vapors from Air Streams with Activated Carbon Fiber Cloth", *Environmental Science & Technology*, 39, 17 (2005), PMID: 16190249, 6851–6859, DOI: 10.1021/es050338z.

[55] K. Foo and B. Hameed, "A cost effective method for regeneration of durian shell and jackfruit peel activated carbons by microwave irradiation", *Chemical Engineering Journal*, 193-194 (2012), 404 –409, DOI: 10.1016/j.cej.2012.04.055.

[56] T. Chowdhury et al., "Regeneration of Na-ETS-10 using microwave and conductive heating", *Chemical Engineering Science*, 75 (2012), 282 –288, DOI: 10.1016/j.ces.2012.03.039.

[57] X. Gao et al., "Influence of a microwave irradiation field on vapor-liquid equilibrium", *Chemical Engineering Science*, 90, 0 (2013), 213 –220, DOI: 10.1016/j.ces.2012.12.037.

[58] E. Altman et al., "Process Intensification of Reactive Distillation for the Synthesis of n-Propyl Propionate: The Effects of Microwave Radiation on Molecular Separation and Esterification Reaction", *Industrial & Engineering Chemistry Research*, 49, 21 (2010), 10287–10296, DOI: 10.1021/ie100555h.

[59] D. R. Baghurst and D. M. P. Mingos, "Superheating effects associated with microwave dielectric heating", *J. Chem. Soc., Chem. Commun.* 9 (9 1992), 674–677, DOI: 10.1039/C39920000674.

[60] F. Chemat and E. Esveld, "Microwave Super-Heated Boiling of Organic Liquids: Origin, Effect and Application", *Chemical Engineering & Technology*, 24, 7 (2001), 735–744, DOI: 10.1002/1521-4125(200107)24:7<735::AID-CEAT735>3.0.CO;2-H.

[61] Y. Nakai, H. Yoshimizu, and Y. Tsujita, "Enhancement of Gas Permeability in HPC, CTA and PMMA under Microwave Irradiation", *Polymer Journal*, 38 (2006), 376–380, DOI: 10.1295/polymj.38.376.

[62] M. Komorowska-Durka, R. van Houten, and G. D. Stefanidis, "Application of microwave heating to pervaporation: A case study for separation of ethanol-water mixtures", *Chemical Engineering and Processing: Process Intensification*, 81, 0 (2014), 35 –40, DOI: 10.1016/j.cep.2014.04.009.

[63] D. Adam, "Microwave chemistry: Out of the kitchen", *Nature*, 421, 6923 (2003), 571–572.

[64] A. de la Hoz, A. Diaz-Ortiz, and A. Moreno, "Microwaves in organic synthesis. Thermal and non-thermal microwave effects", *Chem. Soc. Rev.* 34 (2 2005), 164–178, DOI: 10.1039/B411438H.

[65] A. de la Hoz, D.-O. A., and A. Moreno, "Review on non-thermal effects of microwave irradiation in organic synthesis", *J Microw Power Electromagn Energy*, 41, 1 (2007), 45–66.

[66] C. O. Kappe, B. Pieber, and D. Dallinger, "Microwave Effects in Organic Synthesis: Myth or Reality?", *Angewandte Chemie International Edition*, 52, 4 (2013), 1088–1094, DOI: 10.1002/anie.201204103.

[67] K. D. Raner et al., "A comparison of reaction kinetics observed under microwave irradiation and conventional heating", *The Journal of Organic Chemistry*, 58, 4 (1993), 950–953, DOI: 10.1021/jo00056a031.

[68] E. G. E. Jahngen et al., "Hydrolysis of adenosine triphosphate by conventional or microwave heating", *The Journal of Organic Chemistry*, 55, 10 (1990), 3406–3409, DOI: 10.1021/jo00297a083.

[69] M. A. Herrero, J. M. Kremsner, and C. O. Kappe, "Nonthermal Microwave Effects Revisited: On the Importance of Internal Temperature Monitoring and Agitation in Microwave Chemistry", *The Journal of Organic Chemistry*, 73, 1 (2008), PMID: 18062704, 36–47, DOI: 10.1021/jo7022697.

[70] G. B. Dudley, R. Richert, and A. E. Stiegman, "On the existence of and mechanism for microwave-specific reaction rate enhancement", *Chem. Sci.* 6 (4 2015), 2144–2152, DOI: 10.1039/C4SC03372H.

[71] W. Huang and R. Richert, "The Physics of Heating by Time-Dependent Fields: Microwaves and Water Revisited", *The Journal of Physical Chemistry B*, 112, 32 (2008), PMID: 18646805, 9909–9913, DOI: 10.1021/jp8038187.

[72] H. Jobic et al., "Experimental Evidence of Selective Heating of Molecules Adsorbed in Nanopores under Microwave Radiation", *Phys. Rev. Lett.* 106 (15 2011), 157401, DOI: 10.1103/PhysRevLett.106.157401.

[73] M. R. Rosana et al., "Microwave-Specific Acceleration of a Friedel-Crafts Reaction: Evidence for Selective Heating in Homogeneous Solution", *The Journal of Organic Chemistry*, 79, 16 (2014), PMID: 25050855, 7437–7450, DOI: 10.1021/jo501153r.

[74] D. Dallinger et al., "Scale-Up of Microwave-Assisted Reactions in a Multimode Bench-Top Reactor", *Organic Process Research & Development*, 15, 4 (2011), 841–854, DOI: 10.1021/op200090k.

[75] G. S. Sturm et al., "Exploration of rectangular waveguides as a basis for microwave enhanced continuous flow chemistries", *Chemical Engineering Science*, 89 (2013), 196 –205, DOI: 10.1016/j.ces.2012.11.039.

[76] G. S. Sturm et al., "Microwaves and microreactors: Design challenges and remedies", *Chemical Engineering Journal*, 243, 0 (2014), 147 –158, DOI: 10.1016/j.cej.2013.12.088.

[77] P. Rattanadecho, "The simulation of microwave heating of wood using a rectangular wave guide: Influence of frequency and sample size", *Chemical Engineering Science*, 61, 14 (2006), 4798 –4811, DOI: 10.1016/j.ces.2006.03.001.

[78] G. S. Sturm et al., "On the effect of resonant microwave fields on temperature distribution in time and space", *International Journal of Heat and Mass Transfer*, 55, 13-14 (2012), 3800 –3811, DOI: 10.1016/j.ijheatmasstransfer.2012.02.065.

[79] A. Navarrete, R. Mato, and M. Cocero, "A predictive approach in modeling and simulation of heat and mass transfer during microwave heating. Application to {SFME} of essential oil of Lavandin Super", *Chemical Engineering Science*, 68, 1 (2012), 192 –201, DOI: 10.1016/j.ces.2011.09.026.

[80] R. H. Vaz et al., "Simulation and uncertainty quantification in high temperature microwave heating", *Applied Thermal Engineering*, 70, 1 (2014), 1025 –1039, DOI: 10.1016/j.applthermaleng.2014.06.005.

[81] A. F. Oskooi et al., "Meep: A flexible free-software package for electromagnetic simulations by the {FDTD} method", *Computer Physics Communications*, 181, 3 (2010), 687 –702, DOI: 10.1016/j.cpc.2009.11.008.

[82] D. Sullivan, *Electromagnetic Simulation Using the FDTD Method*, Wiley, 2013.

[83] K. Solyom et al., "Dielectric properties of grape marc: Effect of temperature, moisture content and sample preparation method", *Journal of Food Engineering*, 119, 1 (2013), 33 –39, DOI: 10.1016/j.jfoodeng.2013.05.005.

[84] *Electromagnetic fields & public health: Microwave ovens*, World Health Organization, 2005, URL: http://www.who.int/peh-emf/publications/facts/info_microwaves/en/.

[85] J. Goldsmith, "Epidemiologic evidence relevant to radar (microwave) effects", *Environ Health Perspect.* 105, Suppl 6 (1997), 1579–1587, DOI: 10.2307/3433674.

[86] M. Kundi, "The Controversy about a Possible Relationship between Mobile Phone Use and Cancer", *Environ Health Perspect.* 117, 3 (2009), 316.324, DOI: 10.1289/ehp.11902.

[87] R. Baan et al., "Carcinogenicity of radiofrequency electromagnetic fields", *The Lancet Oncology*, 12, 7 (2011), 624 –626, DOI: 10.1016/S1470-2045(11)70147-4.

[88] NRPB, *Advice on Limiting Exposure to Electromagnetic Fields (0-300 GHz)*, NRPB (National Radiological Protection Board), 2004, URL: http://grouper.ieee.org/groups/scc28/sc4/.

[89] A. von Starck, A. Muhlbauer, and C. Kramer, *Handbook of Thermoprocessing Technologies: Fundamentals, Processes, Components, Safety*, Vulkan-Verlag, 2005.

[90] F. Kremer and A. Schonhals, eds., *Broadband Dielectric Spectroscopy*, Springer, 2003.

[91] R. d. L. Kronig, "On the Theory of Dispersion of X-Rays", *J. Opt. Soc. Am.* 12, 6 (1926), 547–557, DOI: 10.1364/JOSA.12.000547.

[92] J. C. Maxwell, "A Dynamical Theory of the Electromagnetic Field", *Philosophical Transactions of the Royal Society of London*, 155 (1865), 459–512, DOI: 10.1098/rstl.1865.0008.

[93] R. P. Feynman, R. B. Leighton, and S. Matthew, *The Feynman Lectures on Physics*, ed. by R. P. Feynman, vol. 2, Addison-Wesley, 1964.

[94] J. Jackson, *Classical Electrodynamics*, ed. by J. Jackson, 2nd, John Wiley And Sons, Inc., 1975.

[95] D. Halliday, R. Resnick, and K. S. Krane, *Physics*, ed. by D. Halliday, R. Resnick, and K. S. Krane, 5th, vol. 2, Wiley, 2002.

[96] D. Fleisch, *A Student's Guide to Maxwell's Equations*, ed. by D. Fleisch, Cambridge University Press, 2008.

[97] A. Taflove and S. Hagness, *Computational Electrodynamics: The Finite-difference Time-domain Method*, Artech House antennas and propagation library, Artech House, 2005.

[98] P. Monk, *Finite Element Methods for Maxwell's Equations*, Numerical Mathematics and Scientific Computation, Clarendon Press, 2003.

[99] J. L. Volakis, A. Chatterjee, and L. C. Kempel, *Finite Element Method Electromagnetics: Antennas, Microwave Circuits, and Scattering Applications*, Wiley-IEEE Press, 1998.

[100] B. Lambert and K. A. Mauritz, *Dielectric spectroscopy*, The University of Southern Mississippi, 2008, URL: https://commons.wikimedia.org/wiki/File:Dielectric_responses.svg.

[101] W. J. Ellison, "Permittivity of Pure Water, at Standard Atmospheric Pressure, over the Frequency Range 0-25THz and the Temperature Range 0-100C", *Journal of Physical and Chemical Reference Data*, 36, 1 (2007), 1–18, DOI: 10.1063/1.2360986.

[102] U. Kaatze and V. Uhlendorf, "The Dielectric Properties of Water at Microwave Frequencies", *Zeitschrift fur Physikalische Chemie*, 126 (1981), 151–165.

[103] U. Kaatze, "Complex permittivity of water as a function of frequency and temperature", *Journal of Chemical & Engineering Data*, 34, 4 (1989), 371–374, DOI: 10.1021/je00058a001.

[104] J. Barthel et al., "Dielectric spectra of some common solvents in the microwave region. Water and lower alcohols", *Chemical Physics Letters*, 165, 4 (1990), 369 – 373, DOI: 10.1016/0009-2614(90)87204-5.

[105] J. B. Hasted and S. H. M. El Sabeh, "The dielectric properties of water in solutions", *Trans. Faraday Soc.* 49 (0 1953), 1003–1011, DOI: 10.1039/TF9534901003.

[106] A. de la Hoz and A. Loupy, eds., *Microwave in Organic Synthesis*, 3rd ed., Wiley-VCH, 2012.

[107] D. W. Davidson and R. H. Cole, "Dielectric Relaxation in Glycerol, Propylene Glycol, and n-Propanol", *J. Chem. Phys.* 19, 12 (1951), 1484–1490, DOI: 10.1063/1.1748105.

[108] R. H. Cole and D. W. Davidson, "High Frequency Dispersion in n-Propanol", *J. Chem. Phys.* 20, 9 (1952), 1389–1391, DOI: 10.1063/1.1700767.

[109] J. Poley, "Microwave dispersion of some polar liquids", PhD thesis, Technische Hogeschool te Delft, 1955.

[110] R. W. Rampolla, R. C. Miller, and C. P. Smyth, "Microwave Absorption and Molecular Structure in Liquids. XXV. Measurements of Dielectric Constant and Loss at 3.1-mm Wavelength by an Interferometric Method", *J. Chem. Phys.* 30, 2 (1959), 566–573, DOI: 10.1063/1.1729988.

[111] J. A. Saxton et al., "Dispersion at Millimeter Wavelengths in Methyl and Ethyl Alcohols", *J. Chem. Phys.* 37, 9 (1962), 2132–2138, DOI: 10.1063/1.1733434.

[112] D. E. Buck, "The dielectric spectra of ethanol-water mixtures in the microwave region", PhD thesis, Massachusetts Institute of Technology. Dept. of Chemistry., 1965.

[113] N. Hirose and A. R. West, "Impedance Spectroscopy of Undoped BaTiO3 Ceramics", *Journal of the American Ceramic Society*, 79, 6 (1996), 1633–1641, DOI: 10.1111/j.1151-2916.1996.tb08775.x.

[114] P. S. Dobal et al., "Micro-Raman scattering and dielectric investigations of phase transition behavior in the BaTiO3-BaZrO3 system", *Journal of Applied Physics*, 89, 12 (2001), 8085–8091, DOI: 10.1063/1.1369399.

[115] D. Grischkowsky et al., "Far-infrared time-domain spectroscopy with terahertz beams of dielectrics and semiconductors", *J. Opt. Soc. Am. B*, 7, 10 (1990), 2006–2015, DOI: 10.1364/JOSAB.7.002006.

[116] U. Kaatze and K. Giese, "Dielectric spectroscopy on some aqueous solutions of 3:2 valent electrolytes. A combined frequency and time domain study.", *Journal of Molecular Liquids*, 36 (1987), 15 –35, DOI: 10.1016/0167-7322(87)80028-4.

[117] K. Asami, "Characterization of heterogeneous systems by dielectric spectroscopy", *Progress in Polymer Science*, 27, 8 (2002), 1617 –1659, DOI: 10.1016/S0079-6700(02)00015-1.

[118] P. G. Bruce and C. A. Vincent, "Polymer electrolytes", *J. Chem. Soc., Faraday Trans.* 89 (17 1993), 3187–3203, DOI: 10.1039/FT9938903187.

[119] B. Natesan et al., "Segmental relaxation and ion transport in polymer electrolyte films by dielectric spectroscopy", *Journal of Non-Crystalline Solids*, 352, 42-49 (2006), Proceedings of the 5th International Discussion Meeting on Relaxations in Complex Systems5th International Discussion Meeting on Relaxations in Complex Systems, 5205 –5209, DOI: 10.1016/j.jnoncrysol.2006.01.138.

[120] S. Ramesh, T. F. Yuen, and C. J. Shen, "Conductivity and {FTIR} studies on PEO-LiX [X: CF3SO3-, SO42-] polymer electrolytes", *Spectrochimica Acta Part A: Molecular and Biomolecular Spectroscopy*, 69, 2 (2008), 670 –675, DOI: 10.1016/j.saa.2007.05.029.

[121] A. Karmakar and A. Ghosh, "Dielectric permittivity and electric modulus of polyethylene oxide (PEO)-LiClO4 composite electrolytes", *Current Applied Physics*, 12, 2 (2012), 539 –543, DOI: 10.1016/j.cap.2011.08.017.

[122] U. Schneider et al., "Dielectric and far-infrared spectroscopy of glycerol", *Journal of Non-Crystalline Solids*, 235-237, 0 (1998), 173 –179, DOI: 10.1016/S0022-3093(98)00561-4.

[123] J. Bartos et al., "Positron annihilation and broadband dielectric spectroscopy: A series of propylene glycols", *Journal of Non-Crystalline Solids*, 357, 2 (2011), <ce:title>6th International Discussion Meeting on Relaxation in Complex Systems</ce:title>, 376 –384, DOI: 10.1016/j.jnoncrysol.2010.07.030.

[124] P. Lunkenheimer et al., "Glassy dynamics", *Contemporary Physics*, 41, 1 (2000), 15–36, DOI: 10.1080/001075100181259.

[125] Y. He et al., "NMR Experiments and Molecular Dynamics Simulations of the Segmental Dynamics of Polystyrene", *Macromolecules*, 37, 13 (2004), 5032–5039, DOI: 10.1021/ma049843r.

[126] G. A. Schwartz, J. Colmenero, and A. Alegria, "Dielectric study of the segmental relaxation of low and high molecular weight polystyrenes under hydrostatic pressure", *Journal of Non-Crystalline Solids*, 353, 47-51 (2007), Dielectric Relaxation and Related Phenomena Proceedings of the 4th Conference of the International Dielectric Society and the 9th International Conference on Dielectric and Related Phenomena 4th Conference of the International Dielectric Society and the 9th International Conference on Dielectric and Related Phenomena, 4298 – 4302, DOI: 10.1016/j.jnoncrysol.2007.02.070.

[127] G. A. Schwartz, J. Colmenero, and A. Alegria, "Pressure-Temperature Dependence of Polymer Segmental Dynamics. Comparison between the Adam-Gibbs Approach and Density Scalings", *Macromolecules*, 39, 11 (2006), 3931–3938, DOI: 10.1021/ma052464t.

[128] K. Kaminski et al., "Comparative Study on the Molecular Dynamics of a Series of Polypropylene Glycols", *Macromolecules*, 46, 5 (2013), 1973–1980, DOI: 10.1021/ma302611x.

[129] C. Gerstl et al., "Segmental and Normal Mode Relaxation of Poly(alkylene oxide)s Studied by Dielectric Spectroscopy and Rheology", *Macromolecules*, 43, 11 (2010), 4968–4977, DOI: 10.1021/ma100384j.

[130] A. Abou Elfadl et al., "From Rouse to Fully Established Entanglement Dynamics: A Study of Polyisoprene by Dielectric Spectroscopy", *Macromolecules*, 43, 7 (2010), 3340–3351, DOI: 10.1021/ma902564b.

[131] C. Riedel et al., "Rouse-Model-Based Description of the Dielectric Relaxation of Nonentangled Linear 1,4-cis-Polyisoprene", *Macromolecules*, 42, 21 (2009), 8492–8499, DOI: 10.1021/ma901102q.

[132] M. Doxastakis et al., "Chain and local dynamics of polyisoprene as probed by experiments and computer simulations", *The Journal of Chemical Physics*, 119, 13 (2003), 6883–6894, DOI: 10.1063/1.1603720.

[133] F. Kremer, ed., *Dynamics in Geometrical Confinement*, 1st ed., Advances in Dielectrics, Springer International Publishing, 2014, DOI: 10.1007/978-3-319-06100-9.

[134] P. Debye, "The collected papers of Peter J. W. Debye", *Interscience, New York*, 15 (1913), 777, DOI: 10.1002/pol.1954.120137203.

[135] R. Kubo, "Statistical-Mechanical Theory of Irreversible Processes. I. General Theory and Simple Applications to Magnetic and Conduction Problems", *Journal of the Physical Society of Japan*, 12, 6 (1957), 570–586, DOI: 10.1143/JPSJ.12.570.

[136] S. H. Glarum, "Dielectric Relaxation of Polar Liquids", *The Journal of Chemical Physics*, 33, 5 (1960), 1371–1375, DOI: 10.1063/1.1731414.

[137] R. H. Cole, "Correlation Function Theory of Dielectric Relaxation", *The Journal of Chemical Physics*, 42, 2 (1965), 637–643, DOI: 10.1063/1.1695984.

[138] M. Neumann and O. Steinhauser, "On the calculation of the frequency-dependent dielectric constant in computer simulations", *Chemical Physics Letters*, 102, 6 (1983), 508 –513, DOI: 10.1016/0009-2614(83)87455-7.

[139] M. Neumann and O. Steinhauser, "Computer simulation and the dielectric constant of polarizable polar systems", *Chemical Physics Letters*, 106, 6 (1984), 563 –569, DOI: 10.1016/0009-2614(84)85384-1.

[140] J.-P. Hansen and I. R. McDonald, "Chapter 7 - Time-dependent Correlation and Response Functions", *Theory of Simple Liquids*, ed. by J.-P. Hansen and I. R. McDonald, Third Edition, Burlington: Academic Press, 2006, 178 –218, DOI: 10.1016/B978-012370535-8/50009-4.

[141] N. J. English and C. J. Waldron, "Perspectives on external electric fields in molecular simulation: progress, prospects and challenges", *Phys. Chem. Chem. Phys.* 17 (19 2015), 12407–12440, DOI: 10.1039/C5CP00629E.

[142] H. Nyquist, "Thermal Agitation of Electric Charge in Conductors", *Phys. Rev.* 32 (1 1928), 110–113, DOI: 10.1103/PhysRev.32.110.

[143] H. B. Callen and T. A. Welton, "Irreversibility and Generalized Noise", *Phys. Rev.* 83 (1 1951), 34–40, DOI: 10.1103/PhysRev.83.34.

[144] R Kubo, "The fluctuation-dissipation theorem", *Reports on Progress in Physics*, 29, 1 (1966), 255.

[145] I. Newton, *Philosophae naturalis principia mathematica*, Jussu Societatis Regiae ac Typis Iosephi Streater, 1687.

[146] D. Frenkel and B. Smit, *Understanding Molecular Simulation*, 2nd, Orlando, FL, USA: Academic Press, Inc., 2001.

[147] B. Hess et al., "GROMACS 4: Algorithms for Highly Efficient, Load-Balanced, and Scalable Molecular Simulation", *Journal of Chemical Theory and Computation*, 4, 3 (2008), 435–447, DOI: 10.1021/ct700301q.

[148] J. E. Jones, "On the Determination of Molecular Fields. II. From the Equation of State of a Gas", *Proceedings of the Royal Society of London. Series A*, 106, 738 (1924), 463–477, DOI: 10.1098/rspa.1924.0082, eprint: http://rspa.royalsocietypublishing.org/content/106/738/463.full.pdf+html.

[149] H. A. Lorentz, "Ueber die Anwendung des Satzes vom Virial in der kinetischen Theorie der Gase", *Annalen der Physik*, 248, 1 (1881), 127–136, DOI: 10.1002/andp.18812480110.

[150] D. Berthelot, "Sur le melange des gaz", *Comptes rendus hebdomadaires des seances de l'Academie des Sciences*, 126 (1898), 1703–1855.

[151] B. Smit, "Phase diagrams of Lennard-Jones fluids", *The Journal of Chemical Physics*, 96, 11 (1992), 8639–8640, DOI: 10.1063/1.462271.

[152] C. Coulomb, *Histoire de l'Academie Royale des Sciences. Premier et second memoire sur l'electricite et le magnetisme*, ed. by A. R. des Sciences, Paris, France: L'Imprimerie Royale, 1785, 569–611.

[153] M. P. Allen and D. J. Tildesley, *Computer simulation of liquids*, New York, NY, USA: Clarendon Press, 1989.

[154] P. Ewald, "The calculation of optical and electrostatic grid potential", German, *ANNALEN DER PHYSIK*, 64, 3 (1921), 253–287.

[155] J. Eastwood and R. Hockney, "Shaping the force law in two-dimensional particle-mesh models", *Journal of Computational Physics*, 16, 4 (1974), 342 –359, DOI: 10.1016/0021-9991(74)90044-8.

[156] T. Darden, D. York, and L. Pedersen, "Particle mesh Ewald: An N [center-dot] log(N) method for Ewald sums in large systems", *The Journal of Chemical Physics*, 98, 12 (1993), 10089–10092, DOI: 10.1063/1.464397.

[157] J. Lekner, "Summation of Coulomb fields in computer-simulated disordered systems", *Physica A: Statistical Mechanics and its Applications*, 176, 3 (1991), 485 –498, DOI: 10.1016/0378-4371(91)90226-3.

[158] H. J. C. Berendsen et al., *Intermolecular Forces*, ed. by B. Pullman, D. Reidel Publishing Company, 1981, 331–342.

[159] D. T. Gillespie, "Exact numerical simulation of the Ornstein-Uhlenbeck process and its integral", *Phys. Rev. E*, 54 (2 1996), 2084–2091, DOI: 10.1103/PhysRevE.54.2084.

[160] W. L. Jorgensen and J. Tirado-Rives, "Potential energy functions for atomic-level simulations of water and organic and biomolecular systems", *Proceedings of the National Academy of Sciences of the United States of America*, 102, 19 (2005), 6665–6670, DOI: 10.1073/pnas.0408037102.

[161] C. Caleman et al., "Force Field Benchmark of Organic Liquids: Density, Enthalpy of Vaporization, Heat Capacities, Surface Tension, Isothermal Compressibility, Volumetric Expansion Coefficient, and Dielectric Constant", *Journal of Chemical Theory and Computation*, 8, 1 (2012), 61–74, DOI: 10.1021/ct200731v.

[162] A. M. Holtzer, "The collected papers of Peter J. W. Debye", *J. Polym. Sci.* 13, 72 (1954), 548–548, DOI: 10.1002/pol.1954.120137203.

[163] K. S. Cole and R. H. Cole, "Dispersion and Absorption in Dielectrics I. Alternating Current Characteristics", *The Journal of Chemical Physics*, 9, 4 (1941), 341–351, DOI: 10.1063/1.1750906.

[164] D. W. Davidson and R. H. Cole, "Dielectric Relaxation in Glycerine", *The Journal of Chemical Physics*, 18, 10 (1950), 1417–1417, DOI: 10.1063/1.1747496.

[165] S. Havriliak and S. Negami, "A complex plane representation of dielectric and mechanical relaxation processes in some polymers", *Polymer*, 8, 0 (1967), 161 – 210, DOI: 10.1016/0032-3861(67)90021-3.

[166] M. Powell, *The BOBYQA algorithm for bound constrained optimization without derivatives*, Department of Applied Mathematics and Theoretical Physics, Cambridge University, 2009, URL: http://www.damtp.cam.ac.uk/user/na/NA_papers/NA2009_06.pdf.

[167] C. Shannon, "Communication In The Presence Of Noise", *Proceedings of the IEEE*, 86, 2 (1998), 447–457, DOI: 10.1109/JPROC.1998.659497.

[168] S. W. Rick, S. J. Stuart, and B. J. Berne, "Dynamical fluctuating charge force fields: Application to liquid water", *The Journal of Chemical Physics*, 101, 7 (1994), 6141–6156, DOI: 10.1063/1.468398.

[169] N. J. English and J. M. D. MacElroy, "Atomistic simulations of liquid water using Lekner electrostatics", *Molecular Physics*, 100, 23 (2002), 3753–3769, DOI: 10.1080/0026897021000028438.

[170] N. J. English, "Molecular dynamics simulations of liquid water using various long-range electrostatics techniques", *Molecular Physics*, 103, 14 (2005), 1945–1960, DOI: 10.1080/00268970500105003.

[171] N. J. English and J. M. D. MacElroy, "Molecular dynamics simulations of microwave heating of water", *The Journal of Chemical Physics*, 118, 4 (2003), 1589–1592, DOI: 10.1063/1.1538595.

[172] N. J. English and J. M. D. MacElroy, "Hydrogen bonding and molecular mobility in liquid water in external electromagnetic fields", *The Journal of Chemical Physics*, 119, 22 (2003), 11806–11813, DOI: 10.1063/1.1624363.

[173] N. J. English, "Molecular dynamics simulations of microwave effects on water using different long-range electrostatics methodologies", *Molecular Physics*, 104, 2 (2006), 243–253, DOI: 10.1080/14733140500352322.

[174] N. J. English and J. M. D. MacElroy, "Theoretical studies of the kinetics of methane hydrate crystallization in external electromagnetic fields", *The Journal of Chemical Physics*, 120, 21 (2004), 10247–10256, DOI: 10.1063/1.1730092.

[175] N. J. English, J. K. Johnson, and C. E. Taylor, "Molecular-dynamics simulations of methane hydrate dissociation", *The Journal of Chemical Physics*, 123, 24, 244503 (2005), –, DOI: 10.1063/1.2138697.

[176] N. J. English and G. M. Phelan, "Molecular dynamics study of thermal-driven methane hydrate dissociation", *J. Chem. Phys.* 131, 7, 074704 (2009), 074704, DOI: 10.1063/1.3211089.

[177] J. Petravic and J. Delhommelle, "Conductivity of molten sodium chloride in an alternating electric field", *The Journal of Chemical Physics*, 119, 16 (2003), 8511–8518, DOI: 10.1063/1.1613256.

[178] N. J. English, D. C. Sorescu, and J. K. Johnson, "Effects of an external electromagnetic field on rutile Tio2: A molecular dynamics study", *Journal of Physics and Chemistry of Solids*, 67, 7 (2006), 1399 –1409, DOI: 10.1016/j.jpcs.2006.01.101.

[179] C. Desgranges and J. Delhommelle, "Estimating the conductivity of a nanoconfined liquid subjected to an experimentally accessible external field", *Molecular Simulation*, 34, 2 (2008), 177–181, DOI: 10.1080/08927020801930604.

[180] N. J. English and D. A. Mooney, "Very Different Responses to Electromagnetic Fields in Binary Ionic Liquid-Water Solutions", *The Journal of Physical Chemistry B*, 113, 30 (2009), PMID: 19719281, 10128–10134, DOI: 10.1021/jp902500m.

[181] N. J. English and D. A. Mooney, "Electromagnetic field effects on binary dimethylimidazolium-based ionic liquid/water solutions", *Phys. Chem. Chem. Phys.* 11 (41 2009), 9370–9374, DOI: 10.1039/B910462C.

[182] N. J. English, D. A. Mooney, and S. W. O'Brien, "Electrical conductivity and dipolar relaxation of binary dimethylimidazolium chloride-water solutions: A molecular dynamics study", *Journal of Molecular Liquids*, 157, 2-3 (2010), 163 – 167, DOI: 10.1016/j.molliq.2010.10.001.

[183] N. J. English, D. A. Mooney, and S. O'Brien, "Ionic liquids in external electric and electromagnetic fields: a molecular dynamics study", *Molecular Physics*, 109, 4 (2011), 625–638, DOI: 10.1080/00268976.2010.544263.

[184] D. V. Matyushov, "On the theory of dielectric spectroscopy of protein solutions", *Journal of Physics: Condensed Matter*, 24, 32 (2012), 325105.

[185] M. Heyden, D. J. Tobias, and D. V. Matyushov, "Terahertz absorption of dilute aqueous solutions", *The Journal of Chemical Physics*, 137, 23, 235103 (2012), –, DOI: 10.1063/1.4772000.

[186] D. R. Martin and D. V. Matyushov, "Hydration shells of proteins probed by depolarized light scattering and dielectric spectroscopy: Orientational structure is significant, positional structure is not", *The Journal of Chemical Physics*, 141, 22, 22D501 (2014), –, DOI: 10.1063/1.4895544.

[187] W. L. Jorgensen et al., "Comparison of simple potential functions for simulating liquid water", *J. Chem. Phys.* 79, 2 (1983), 926–935, DOI: 10.1063/1.445869.

[188] H. J. C. Berendsen, J. R. Grigera, and T. P. Straatsma, "The missing term in effective pair potentials", *The Journal of Physical Chemistry*, 91, 24 (1987), 6269–6271, DOI: 10.1021/j100308a038.

[189] D. M. Ferguson, "Parameterization and evaluation of a flexible water model", *Journal of Computational Chemistry*, 16, 4 (1995), 501–511, DOI: 10.1002/jcc.540160413.

[190] Y. Wu, H. L. Tepper, and G. A. Voth, "Flexible simple point-charge water model with improved liquid-state properties", *J. Chem. Phys.* 124, 2, 024503 (2006), 024503, DOI: 10.1063/1.2136877.

[191] B. Chen, J. J. Potoff, and J. I. Siepmann, "Monte Carlo Calculations for Alcohols and Their Mixtures with Alkanes. Transferable Potentials for Phase Equilibria. 5. United-Atom Description of Primary, Secondary, and Tertiary Alcohols", *The Journal of Physical Chemistry B*, 105, 15 (2001), 3093–3104, DOI: 10.1021/jp003882x.

[192] J. M. Stubbs, J. J. Potoff, and J. I. Siepmann, "Transferable Potentials for Phase Equilibria. 6. United-Atom Description for Ethers, Glycols, Ketones, and Aldehydes", *The Journal of Physical Chemistry B*, 108, 45 (2004), 17596–17605, DOI: 10.1021/jp049459w.

[193] J. Wang et al., "Development and testing of a general amber force field", *Journal of Computational Chemistry*, 25, 9 (2004), 1157–1174, DOI: 10.1002/jcc.20035.

[194] E. F. da Silva et al., "Molecular Dynamics Study of Ethanolamine as a Pure Liquid and in Aqueous Solution", *The Journal of Physical Chemistry B*, 111, 14 (2007), 3695–3703, DOI: 10.1021/jp068227p.

[195] R. Hockney, S. Goel, and J. Eastwood, "Quiet high-resolution computer models of a plasma", *Journal of Computational Physics*, 14, 2 (1974), 148 –158, DOI: 10.1016/0021-9991(74)90010-2.

[196] S. Nose, "A molecular dynamics method for simulations in the canonical ensemble", *Molecular Physics*, 52, 2 (1984), 255–268, DOI: 10.1080/00268978400101201.

[197] W. G. Hoover, "Canonical dynamics: Equilibrium phase-space distributions", *Phys. Rev. A*, 31 (3 1985), 1695–1697, DOI: 10.1103/PhysRevA.31.1695.

[198] M. Parrinello and A. Rahman, "Polymorphic transitions in single crystals: A new molecular dynamics method", *Journal of Applied Physics*, 52, 12 (1981), 7182–7190, DOI: 10.1063/1.328693.

[199] S. Nose and M. Klein, "Constant pressure molecular dynamics for molecular systems", *Molecular Physics*, 50, 5 (1983), 1055–1076, DOI: 10.1080/00268978300102851.

[200] B. Hess et al., "LINCS: A linear constraint solver for molecular simulations", *Journal of Computational Chemistry*, 18, 12 (1997), 1463–1472, DOI: 10.1002/(SICI)1096-987X(199709)18:12<1463::AID-JCC4>3.0.CO;2-H.

[201] S. W. de Leeuw, J. W. Perram, and E. R. Smith, "Simulation of Electrostatic Systems in Periodic Boundary Conditions. I. Lattice Sums and Dielectric Constants", *Proceedings of the Royal Society of London A: Mathematical, Physical and Engineering Sciences*, 373, 1752 (1980), 27–56, DOI: 10.1098/rspa.1980.0135.

[202] X. Zhang and C. Jian, "Liquid-Liquid Equilibrium for the Ternary System Methanol + Acrylonitrile + Water", *Journal of Chemical & Engineering Data*, 57, 1 (2012), 142–147, DOI: 10.1021/je2009208.

[203] Z. Orekhova et al., "Electrical Conductance and Volumetric Studies in Aqueous Solutions of Nicotinic Acid", English, *Journal of Solution Chemistry*, 34, 6 (2005), 687–700, DOI: 10.1007/s10953-005-4493-2.

[204] H. Doi, K. Tamura, and S. Murakami, "Thermodynamic properties of aqueous solution of 2-isobutoxyethanol at T = (293.15, 298.15, and 303.15) K, below and above LCST", *The Journal of Chemical Thermodynamics*, 32, 6 (2000), 729 –741, DOI: 10.1006/jcht.1999.0645.

[205] A. M. Kolker and L. P. Safonova, "Molar heat capacities of the (water + acetonitrile) mixtures at T = (283.15, 298.15, 313.15, and 328.15) K", *The Journal of Chemical Thermodynamics*, 42, 10 (2010), 1209 –1212, DOI: 10.1016/j.jct.2010.04.019.

[206] M. Antosik, M. Galka, and S. K. Malanowski, "Vapor-Liquid Equilibrium in a Ternary System Cyclohexane + Ethanol + Water", *Journal of Chemical & Engineering Data*, 49, 1 (2004), 7–10, DOI: 10.1021/je025621h.

[207] Y. Marcus, *The Properties of Solvents*, Wiley, 1998, 254.

[208] S. K. Begum et al., "Densities, Viscosities, and Surface Tensions of the System Water + Diethylene Glycol", *Journal of Chemical & Engineering Data*, 56, 2 (2011), 303–306, DOI: 10.1021/je1009976.

[209] G. Egorov and D. Makarov, "The bulk properties of ethylene glycol-dimethylsulfoxide mixtures over the temperature range 278-323 K at p = 0.1 MPa", English, *Russian Journal of Physical Chemistry A, Focus on Chemistry*, 82, 10 (2008), 1778–1784, DOI: 10.1134/S003602440810021X.

[210] M. G. Technische Hochschule Carl Schorlemmer Leuna-Merseburg, "Unpublished data", Unpublished data, 1989.

[211] C. Yang et al., "Excess Molar Volumes, Viscosities, and Heat Capacities for the Mixtures of Ethylene Glycol + Water from 273.15 K to 353.15 K", *Journal of Chemical & Engineering Data*, 48, 4 (2003), 836–840, DOI: 10.1021/je020140j.

[212] S. P. Verevkin, "Determination of vapor pressures and enthalpies of vaporization of 1,2-alkanediols", *Fluid Phase Equilibria*, 224, 1 (2004), 23 –29, DOI: 10.1016/j.fluid.2004.05.010.

[213] M. Rodrigues and A. Francesconi, "Experimental Study of the Excess Molar Volumes of Binary and Ternary Mixtures Containing Water + (1,2-Ethanediol, or 1,2-Propanediol, or 1,3-Propanediol, or 1,2-Butanediol) + (1-n-Butyl-3-methylimidazolium Bromide) at 298.15 K and Atmospheric Pressure", English, *Journal of Solution Chemistry*, 40, 11 (2011), 1863–1873, DOI: 10.1007/s10953-011-9756-5.

[214] H. A. Zarei, S. Asadi, and H. Iloukhani, "Temperature dependence of the volumetric properties of binary mixtures of (1-propanol, 2-propanol and 1,2-propanediol) at ambient pressure (81.5 kPa)", *Journal of Molecular Liquids*, 141, 1-2 (2008), 25 –30, DOI: 10.1016/j.molliq.2008.02.006.

[215] C. Yang, P. Ma, and S. Xia, "Heat capacity of glycol determined by differential scanning calorimeter", *Tianjin Daxue Xuebao*, 36, 2 (2003), 192–196.

[216] R. Belda Maximino, "Viscosity and density of binary mixtures of alcohols and polyols with three carbon atoms and water: equation for the correlation of viscosities of binary mixtures", *Physics and Chemistry of Liquids*, 47, 5 (2009), 515–529, DOI: 10.1080/00319100802372114.

[217] C. L. Yaws, *Yaws' Handbook of Thermodynamic and Physical Properties of Chemical Compounds*, McGraw-Hill, 2003.

[218] M. Bastos et al., "Thermodynamic properties of glycerol enthalpies of combustion and vaporization and the heat capacity at 298.15 K. Enthalpies of solution in water at 288.15, 298.15, and 308.15 K", *The Journal of Chemical Thermodynamics*, 20, 11 (1988), 1353 –1359, DOI: 10.1016/0021-9614(88)90173-5.

[219] D. R. Lide, *CRC Handbook of Chemistry and Physics*, ed. by D. R. Lide, 90th, CRC Press, 2009.

[220] V. Kartsev et al., "Piezometry and Densitometry of Aqueous Solutions of Diamines, Aminoalcohols, and Diols. II. Solutions of Monoethanolamine and Diols", *Russ. J. Phys. Chem.* 62, 8 (1988), 1152–1153.

[221] G. Liessmann, W. Schmidt, and S. Reiffarth, *Recommended Thermophysical Data*, Data compilation of the Saechsische Olefinwerke Boehlen Germany, 1995.

[222] DIPPR, *DIPPR Project 801*, Design Institute for Physical Properties Research, AIChE, 2010.

[223] Y. S. Badyal et al., "Electron distribution in water", *The Journal of Chemical Physics*, 112, 21 (2000), 9206–9208, DOI: 10.1063/1.481541.

[224] G. Gente and C. La Mesa, "Water-Trifluoroethanol Mixtures: Some Physicochemical Properties", English, *Journal of Solution Chemistry*, 29, 11 (2000), 1159–1172, DOI: 10.1023/A:1005147318013.

[225] T. Hanai, N. Koizumi, and R. Gotoh, "Temperature Dependence of Dielectric Constants and Dipole Moments in Polar Liquids", *Bull. Inst. Chem. Res, Kyoto Univ.* 39, 3 (1961), 195–201.

[226] C. M. Kinart and M. Klimczak, "Thermodynamic and structural properties of binary mixtures of some glycols with 2-butoxyethanol at T=293.15, 298.15 and 303.15 K", *Journal of Molecular Liquids*, 148, 2-3 (2009), 132 –139, DOI: 10.1016/j.molliq.2009.07.009.

[227] J. Gmehling et al., *Pure compound data from DDB*, The Dortmund Data Bank, 1983-2012, URL: http://www.ddbst.com/ddb-pure.html.

[228] N. V. Sastry and M. C. Patel, "Densities, Excess Molar Volumes, Viscosities, Speeds of Sound, Excess Isentropic Compressibilities, and Relative Permittivities for Alkyl (Methyl, Ethyl, Butyl, and Isoamyl) Acetates + Glycols at Different Temperatures", *Journal of Chemical & Engineering Data*, 48, 4 (2003), 1019–1027, DOI: 10.1021/je0340248.

[229] C. M. Kinart and W. J. Kinart, "Physicochemical Properties of Glycerol-Formamide Liquid Mixtures and Their Assumed Internal Structures", *Physics and Chemistry of Liquids*, 33, 3 (1996), 159–170, DOI: 10.1080/00319109608039817.

[230] P. Undre et al., "Study of solute-solvent interaction through dielectrics properties of N,N-dimethylacetamide in ethanolamine", *Journal of Molecular Liquids*, 137, 1-3 (2008), 147 –151, DOI: 10.1016/j.molliq.2007.06.004.

[231] A. A. Chialvo et al., "Vapor-Liquid Equilibrium and Polarization Behavior of the GCP Water Model: Gaussian Charge-on-Spring versus Dipole Self-Consistent Field Approaches to Induced Polarization", *The Journal of Physical Chemistry B*, 119, 15 (2015), PMID: 25803267, 5010–5019, DOI: 10.1021/acs.jpcb.5b00595.

[232] F. Wooten, "Chapter 2 - Maxwell's equations and the dielectric function", *Optical Properties of Solids*, ed. by F. Wooten, Academic Press, 1972, 15 –41, DOI: http://dx.doi.org/10.1016/B978-0-12-763450-0.50007-6.

[233] S. Horikoshi et al., "Microwave frequency effects on dielectric properties of some common solvents and on microwave-assisted syntheses: 2-Allylphenol and the C12-C2-C12 Gemini surfactant", *Radiation Physics and Chemistry*, 81, 12 (2012), 1885 –1895, DOI: 10.1016/j.radphyschem.2012.07.011.

[234] T. Sato and R. Buchner, "Dielectric Relaxation Processes in Ethanol/Water Mixtures", *The Journal of Physical Chemistry A*, 108, 23 (2004), 5007–5015, DOI: 10.1021/jp035255o.

[235] M. Zahn et al., "Dielectric properties of water and water/ethylene glycol mixtures for use in pulsed power system design", *Proceedings of the IEEE*, 74, 9 (1986), 1182–1221, DOI: 10.1109/PROC.1986.13611.

[236] P. Lunkenheimer et al., "High-frequency dielectric spectroscopy on glycerol", *EPL (Europhysics Letters)*, 33, 8 (1996), 611.

[237] P. Lunkenheimer et al., "Fast Dynamics of Glass-Forming Glycerol Studied by Dielectric Spectroscopy", *Phys. Rev. Lett.* 77 (2 1996), 318–321, DOI: 10.1103/PhysRevLett.77.318.

[238] A. Patil and V. Pawar, "Microwave dielectric spectra and molecular interaction in a binary mixture of ethanolamine with diethanolamine", *Journal of Molecular Liquids*, 188, 0 (2013), 1 –4, DOI: 10.1016/j.molliq.2013.09.007.

[239] A. Patil, G. Shinde, and V. Pawar, "Dielectric relaxation study of hydrogen bonded structures in ethanolamine with diethanolamine using {TDR} technique", *Journal of Molecular Liquids*, 168, 0 (2012), 42 –46, DOI: 10.1016/j.molliq.2012.01.017.

[240] O. Gereben and L. Pusztai, "On the accurate calculation of the dielectric constant from molecular dynamics simulations: The case of SPC/E and SWM4-DP water", *Chemical Physics Letters*, 507, 1-3 (2011), 80 –83, DOI: 10.1016/j.cplett.2011.02.064.

[241] G. Raabe and R. J. Sadus, "Molecular dynamics simulation of the dielectric constant of water: The effect of bond flexibility", *The Journal of Chemical Physics*, 134, 23, 234501 (2011), –, DOI: 10.1063/1.3600337.

[242] J.-Z. Bao, M. L. Swicord, and C. C. Davis, "Microwave dielectric characterization of binary mixtures of water, methanol, and ethanol", *The Journal of Chemical Physics*, 104, 12 (1996), 4441–4450, DOI: 10.1063/1.471197.

[243] P. Petong, R. Pottel, and U. Kaatze, "Water-Ethanol Mixtures at Different Compositions and Temperatures. A Dieletric Relaxation Study", *The Journal of Physical Chemistry A*, 104, 32 (2000), 7420–7428, DOI: 10.1021/jp001393r.

[244] T. Sato and R. Buchner, "Cooperative and molecular dynamics of alcohol/water mixtures: the view of dielectric spectroscopy", *Journal of Molecular Liquids*, 117, 1-3 (2005), Routes from Local Order to Large Scale Cooperativity EuroConference, 23 –31, DOI: 10.1016/j.molliq.2004.08.015.

[245] R. Sengwa et al., "Characterization of Heterogeneous Interaction Behavior in Ternary Mixtures by a Dielectric Analysis: Equi-Molar H-bonded Binary Polar Mixtures in Aqueous Solutions", English, *Journal of Solution Chemistry*, 35, 8 (2006), 1037–1055, DOI: 10.1007/s10953-006-9053-x.

[246] A. Megriche, A. Belhadj, and A. Mgaidi, "Microwave dielectric properties of binary solvent wateralcohol, alcohol-alcohol mixtures at temperatures between -35C and +35C and dielectric relaxation studies", *Mediterranean Journal of Chemistry*, 1, 4 (2012), 200–209.

[247] A. Singh et al., "Effect of Dielectric Properties of a Solvent-Water Mixture Used in Microwave-Assisted Extraction of Antioxidants from Potato Peels", *Antioxidants*, 3, 1 (2014), 99, DOI: 10.3390/antiox3010099.

[248] W.-N. Liu and J.-H. Wei, "Effective permittivity of alcohol + water mixtures as influenced by concentration", *Journal of Chemical & Pharmaceutical Research*, 6, 7 (2014), 1432.

[249] M. Dzida and U. Kaatze, "Compressibility and Dielectric Relaxation of Mixtures of Water with Monohydroxy Alcohols", *The Journal of Physical Chemistry B*, 119, 38 (2015), PMID: 26335254, 12480–12489, DOI: 10.1021/acs.jpcb.5b07093.

[250] T. Sato et al., "Dielectric relaxation spectroscopy of aqueous amino acid solutions: dynamics and interactions in aqueous glycine", *Journal of Molecular Liquids*, 117, 1-3 (2005), Routes from Local Order to Large Scale Cooperativity EuroConference, 93 –98.

[251] R. Talware et al., "Dielectric relaxation study of glycine-water mixtures using time domain reflectometry technique", *Physics and Chemistry of Liquids*, 50, 1 (2012), 102–112, DOI: 10.1080/00319104.2010.551345.

[252] J. Guo-Zhu and Q. Jie, "Dielectric constant of dimethyl sulfoxide-monohydric alcohol mixture solution at the microwave frequency", *Fluid Phase Equilibria*, 365 (2014), 5 –10, DOI: 10.1016/j.fluid.2013.12.014.

[253] U. Kaatze and V. Lonnecke-Gabel, "Dielectric spectroscopy on binary mixtures of organic solvents", *Journal of Molecular Liquids*, 48, 1 (1991), 45 –60, DOI: 10.1016/0167-7322(91)80025-Y.

[254] X. Liao, G. Raghavan, and V. Yaylayan, "Dielectric properties of aqueous solutions of alpha-d-glucose at 915 {MHz}", *Journal of Molecular Liquids*, 100, 3 (2002), 199 –205, DOI: 10.1016/S0167-7322(02)00041-7.

[255] X. Liao et al., "Dielectric properties of alpha-d-glucose aqueous solutions at 2450 {MHz}", *Food Research International*, 36, 5 (2003), 485 –490, DOI: 10.1016/S0963-9969(02)00196-5.

[256] X. Liao et al., "Dielectric properties of lysine aqueous solutions at 2450 {MHz}", *Journal of Molecular Liquids*, 107, 1-3 (2003), 15 –19, DOI: 10.1016/S0167-7322(03)00136-3.

[257] P. Glancy and W. P. Beyermann, "Dielectric properties of fully hydrated nucleotides in the terahertz frequency range", *The Journal of Chemical Physics*, 132, 24, 245102 (2010), –, DOI: 10.1063/1.3457941.

[258] K. Dharmalingam et al., "Dielectric relaxation of binary mixtures of alcohols with acrylic esters", *Journal of Applied Polymer Science*, 107, 4 (2008), 2312–2316, DOI: 10.1002/app.27384.

[259] M. Koeberg et al., "{THz} dielectric relaxation of ionic liquid:water mixtures", *Chemical Physics Letters*, 439, 1-3 (2007), 60 –64, DOI: 10.1016/j.cplett.2007.03.075.

[260] L. Ma and K. Zhao, "Dielectric relaxation spectroscopy for the binary system of 1-butyl-3-methylimidazolium hexafluorophosphate and ethanol: interactions and micro phase behavior", *RSC Adv.* 2 (26 2012), 10007–10014, DOI: 10.1039/C2RA20732J.

[261] S. Vasan et al., "Dielectric relaxation in relation to viscosity of some organic molecules and some of their binary mixtures", *Journal of Molecular Liquids*, 135, 1-3 (2007), 115 –119, DOI: 10.1016/j.molliq.2006.11.010.

[262] J. F. King and W. A. Patrick, "The measurement of dielectric constants", *J. Am. Chem. Soc.* 43, 8 (1921), 1835–1843, DOI: 10.1021/ja01441a010.

[263] F. R. Goss, "173. The magnitude of the solvent effect in dipole-moment measurements. Part III. Polarisation and association of alcohols in the liquid phase", *J. Chem. Soc.* 0 (0 1940), 888–894, DOI: 10.1039/JR9400000888.

[264] M. T. Ratzsch, C. Wohlfarth, and M. Claudius, "Kirkwoodsche Korrelationsfaktoren von binaren Systemen mit Alkoholen und Diethylether", *J. Prakt. Chem.* 319, 3 (1977), 353–361, DOI: 10.1002/prac.19773190302.

[265] V. Sharma et al., "Dielectric Relaxation Study of Ethanol in Benzene from Microwave Absorption Data", *Zeitschrift fur Naturforschung A*, 62, 7-8 (2007), 406–408, DOI: 10.1515/zna-2007-7-809.

[266] T. Sumi, R. Dillert, and S. Horikoshi, "Novel Microwave Thermodynamic Model for Alcohol with Clustering Structure in Nonpolar Solution", *The Journal of Physical Chemistry B*, 119, 45 (2015), PMID: 26468761, 14479–14485, DOI: 10.1021/acs.jpcb.5b06168.

[267] P. Ball, "Water as an Active Constituent in Cell Biology", *Chemical Reviews*, 108, 1 (2008), PMID: 18095715, 74–108, DOI: 10.1021/cr068037a.

[268] A. Paoli and A. Schiraldi, "Microwave heating of water-ethanol mixtures", *Food Flavors: Generation, Analysis and Process Influence Proceedings of the 8th International Flavor Conference*, ed. by G. Charalambous, vol. 37, Developments in Food Science, Elsevier, 1995, 1065 –1072, DOI: 10.1016/S0167-4501(06)80219-0.

[269] Q. L. Feng et al., "Study on Microwave Desorption Azeotropic Distillation of Ethanol-Loaded Activated Carbon under Vacuum Condition", *Progress in Environmental Protection and Processing of Resource*, vol. 295, Applied Mechanics and Materials, Trans Tech Publications, Apr. 2013, 1240–1244, DOI: 10.4028/www.scientific.net/AMM.295-298.1240.

[270] R. Olmi et al., "Monitoring alcoholic fermentation by microwave dielectric spectroscopy", *Journal of Microwave Power and Electromagnetic Energy*, 41, 3 (2007), 38–49.

[271] R. Li et al., "Mesoscopic Structuring and Dynamics of Alcohol/Water Solutions Probed by Terahertz Time-Domain Spectroscopy and Pulsed Field Gradient Nuclear Magnetic Resonance", *The Journal of Physical Chemistry B*, 118, 34 (2014), PMID: 25117060, 10156–10166, DOI: 10.1021/jp502799x.

[272] W. L. Jorgensen, "Optimized intermolecular potential functions for liquid alcohols", *The Journal of Physical Chemistry*, 90, 7 (1986), 1276–1284, DOI: 10.1021/j100398a015.

[273] P. Petong et al., "Dielectric Relaxation of H-Bonded Liquids. Mixtures of Ethanol and n-Hexanol at Different Compositions and Temperatures", *The Journal of Physical Chemistry A*, 103, 31 (1999), 6114–6121, DOI: 10.1021/jp9910461.

[274] L. Saiz et al., "Structure and Dynamics of Liquid Ethanol", *The Journal of Physical Chemistry B*, 101, 1 (1997), 78–86, DOI: 10.1021/jp961786j.

[275] H. S. Frank and M. W. Evans, "Free Volume and Entropy in Condensed Systems III. Entropy in Binary Liquid Mixtures; Partial Molal Entropy in Dilute Solutions; Structure and Thermodynamics in Aqueous Electrolytes", *The Journal of Chemical Physics*, 13, 11 (1945), 507–532, DOI: 10.1063/1.1723985.

[276] S. Dixit et al., "Water structure and solute association in dilute aqueous methanol", *EPL (Europhysics Letters)*, 59, 3 (2002), 377.

[277] T. M. Raschke and M. Levitt, "Nonpolar solutes enhance water structure within hydration shells while reducing interactions between them", *Proceedings of the National Academy of Sciences of the United States of America*, 102, 19 (2005), 6777–6782, DOI: 10.1073/pnas.0500225102.

[278] D. Laage, G. Stirnemann, and J. T. Hynes, "Why Water Reorientation Slows without Iceberg Formation around Hydrophobic Solutes", *The Journal of Physical Chemistry B*, 113, 8 (2009), PMID: 19193030, 2428–2435, DOI: 10.1021/jp809521t.

[279] C. Petersen, K. Tielrooij, and H. J. Bakker, "Strong temperature dependence of water reorientation in hydrophobic hydration shells", *The Journal of Chemical Physics*, 130, 21, 214511 (2009), 214511, DOI: 10.1063/1.3142861.

[280] S. Garde and A. J. Patel, "Unraveling the hydrophobic effect, one molecule at a time", *Proceedings of the National Academy of Sciences*, 108, 40 (2011), 16491–16492, DOI: 10.1073/pnas.1113256108.

[281] G. Guevara-Carrion, J. Vrabec, and H. Hasse, "Prediction of self-diffusion coefficient and shear viscosity of water and its binary mixtures with methanol and ethanol by molecular simulation", *The Journal of Chemical Physics*, 134, 7, 074508 (2011), 074508, DOI: 10.1063/1.3515262.

[282] O. Gereben and L. Pusztai, "Investigation of the Structure of Ethanol-Water Mixtures by Molecular Dynamics Simulation I: Analyses Concerning the Hydrogen-Bonded Pairs", *The Journal of Physical Chemistry B*, 119, 7 (2015), PMID: 25635651, 3070–3084, DOI: 10.1021/jp510490y.

[283] N. Galamba, "Water's Structure around Hydrophobic Solutes and the Iceberg Model", *The Journal of Physical Chemistry B*, 117, 7 (2013), PMID: 23360515, 2153–2159, DOI: 10.1021/jp310649n.

[284] G. Graziano, "Comment on 'Water's Structure around Hydrophobic Solutes and the Iceberg Model'", *The Journal of Physical Chemistry B*, 118, 9 (2014), PMID: 24524630, 2598–2599, DOI: 10.1021/jp5008895.

[285] N. Galamba, "Reply to 'Comment on 'Water's Structure around Hydrophobic Solutes and the Iceberg Model'", *The Journal of Physical Chemistry B*, 118, 9 (2014), PMID: 24524595, 2600–2603, DOI: 10.1021/jp501450n.

[286] J. G. Davis et al., "Water structural transformation at molecular hydrophobic interfaces", *Nature*, 491, 1 (2012), 582–585, DOI: 10.1038/nature11570.

[287] S. Y. Noskov et al., "Molecular Dynamics Study of Hydration in Ethanol-Water Mixtures Using a Polarizable Force Field", *The Journal of Physical Chemistry B*, 109, 14 (2005), PMID: 16851754, 6705–6713, DOI: 10.1021/jp045438q.

[288] Y. Zhong and S. Patel, "Electrostatic Polarization Effects and Hydrophobic Hydration in Ethanol-Water Solutions from Molecular Dynamics Simulations", *The Journal of Physical Chemistry B*, 113, 3 (2009), 767–778, DOI: 10.1021/jp807053p.

[289] A. Ghoufi, F. Artzner, and P. Malfreyt, "Physical Properties and Hydrogen-Bonding Network of Water-Ethanol Mixtures from Molecular Dynamics Simulations", *The Journal of Physical Chemistry B*, 0, 0 (2016), PMID: 26743948, null, DOI: 10.1021/acs.jpcb.5b11776.

[290] J. Lou, T. A. Hatton, and P. E. Laibinis, "Effective Dielectric Properties of Solvent Mixtures at Microwave Frequencies", *The Journal of Physical Chemistry A*, 101, 29 (1997), 5262–5268, DOI: 10.1021/jp970731u.

[291] A. Sihvola, "Mixing Rules with Complex Dielectric Coefficients", *Subsurface Sensing Technologies and Applications*, 1, 4 (2000), 393–415, DOI: 10.1023/A:1026511515005.

[292] F. Carpi et al., *Dielectric Elastomers as Electromechanical Transducers: Fundamentals, Materials, Devices, Models and Applications of an Emerging Electroactive Polymer Technology*, Elsevier Science, 2011.

[293] A. Y. Zasetsky, A. S. Lileev, and A. K. Lyashchenko, "Molecular dynamic simulations of terahertz spectra for water-methanol mixtures", *Molecular Physics*, 108, 5 (2010), 649–656, DOI: 10.1080/00268971003657086.

[294] J. Herraez and R. Belda, "Refractive Indices, Densities and Excess Molar Volumes of Monoalcohols + Water", English, *Journal of Solution Chemistry*, 35, 9 (2006), 1315–1328, DOI: 10.1007/s10953-006-9059-4.

[295] G. S. Kell, "Precise representation of volume properties of water at one atmosphere", *Journal of Chemical & Engineering Data*, 12, 1 (1967), 66–69, DOI: 10.1021/je60032a018.

[296] D. F. Grant-Taylor and D. D. Macdonald, "Thermal pressure and energy-volume coefficients for the acetonitrile + water system", *Canadian Journal of Chemistry*, 54, 17 (1976), 2813–2819, DOI: 10.1139/v76-398.

[297] J. Hales and J. Ellender, "Liquid densities from 293 to 490 K of nine aliphatic alcohols", *The Journal of Chemical Thermodynamics*, 8, 12 (1976), 1177 –1184, DOI: 10.1016/0021-9614(76)90126-9.

[298] E. Dickinson, L. J. Thrift, and L. Wilson, "Thermal expansion and shear viscosity coefficients of water + ethanol + sucrose mixtures", *Journal of Chemical & Engineering Data*, 25, 3 (1980), 234–236, DOI: 10.1021/je60086a029.

[299] M. Costas, M. C. Alonso, and A. Heintz, "Experimental and theoretical study of the apparent molar volumes of 1-alcohols in linear hydrocarbons", *Berichte der Bunsengesellschaft fur physikalische Chemie*, 91, 3 (1987), 184–190, DOI: 10.1002/bbpc.19870910306.

[300] W. Mier et al., "Excess Enthalpy HE of Binary Mixtures Containing Alkanes, Ethanol and Ethyl-Tert. Butyl Ether (ETBE)", *Berichte der Bunsengesellschaft fur physikalische Chemie*, 99, 9 (1995), 1123–1130, DOI: 10.1002/bbpc.199500043.

[301] Y. Uosaki et al., "Excess molar volumes of binary mixtures of 1,3-dimethylimidazolidin-2-one with an alkan-1-ol at the temperatures 283.15 K, 298.15 K, and 313.15 K", *The Journal of Chemical Thermodynamics*, 39, 5 (2007), 810 –816, DOI: 10.1016/j.jct.2006.09.017.

[302] K. Jung, "MSc thesis", MA thesis, University of Calgary, 1969.

[303] B. P. Sahli, H. Gager, and A. J. Richard, "Ultracentrifugal studies of the isothermal compressibilities of organic alcohols and alkanes. Correlation with surface tension", *The Journal of Chemical Thermodynamics*, 8, 2 (1976), 179 –188, DOI: 10.1016/0021-9614(76)90091-4.

[304] T. Moriyoshi and H. Inubushi, "Compressions of some alcohols and their aqueous binary mixtures at 298.15 K and at pressures up to 1400 atm", *The Journal of Chemical Thermodynamics*, 9, 6 (1977), 587 –592, DOI: 10.1016/0021-9614(77)90163-X.

[305] M. D. Pena and G Tardajos, "Isothermal compressibilities of n-1-alcohols from methanol to 1-dodecanol at 298.15, 308.15, 318.15, and 333.15 K", *The Journal of Chemical Thermodynamics*, 11, 5 (1979), 441 –445, DOI: 10.1016/0021-9614(79)90121-6.

[306] W. Brostow, T. Grindley, and M. Macip, "Volumetric properties of organic liquids as a function of temperature and pressure: Experimental data and prediction of compressibility", *Materials Chemistry and Physics*, 12, 1 (1985), 37 –97, DOI: 10.1016/0254-0584(85)90035-5.

[307] E. Hamad et al., "Relations Among Concentration Fluctuation Integrals in Mixtures (Theory and Experiments)", *International journal of research in physical chemistry and chemical physics*, 162, 1 (1989), 27–45, DOI: 10.1524/zpch.1989.162.Part_1.027.

[308] M. Vedamuthu, S. Singh, and G. W. Robinson, "Properties of Liquid Water. 4. The Isothermal Compressibility Minimum near 50 .degree.C", *The Journal of Physical Chemistry*, 99, 22 (1995), 9263–9267, DOI: 10.1021/j100022a047.

[309] D. Papaioannou and C. Panayiotou, "Viscosity of Binary Mixtures of Propylamine with Alkanols at Moderately High Pressures", *Journal of Chemical & Engineering Data*, 40, 1 (1995), 202–209, DOI: 10.1021/je00017a042.

[310] S. Rivkin and A. Winnikova, "The specific heat of aqueous solutions of ethyl alcohol", *Chem. Ing. Tech.* 37, 5 (1965), 556–560.

[311] V. Vasilev et al., "Physico-chemical properties of copper chloride solutions in mixed ethanol - water solutions", *Izv. Vyssh. Uchebn. Zaved. Khim. Khim. Tekhnol.* 21, 8 (1978), 1131–1138.

[312] V. Vasilev et al., "Heat Capacity and Density of the CoCl2; - Ethanol - Water System at 298.15 K", *Izv. Vyssh. Uchebn. Zaved. Khim. Khim. Tekhnol.* 28, 5 (1985), 52–55.

[313] G. Garcia-Miaja, J. Troncoso, and L. Romani, "Density and Heat Capacity as a Function of Temperature for Binary Mixtures of 1-Butyl-3-methylpyridinium Tetrafluoroborate + Water, + Ethanol, and + Nitromethane", *Journal of Chemical & Engineering Data*, 52, 6 (2007), 2261–2265, DOI: 10.1021/je7002836.

[314] K. Rubini et al., "Excess molar enthalpies and heat capacities of dimethyl sulfoxide + seven normal alkanols at 303.15 K and atmospheric pressure", *Thermochimica Acta*, 452, 2 (2007), 124 –127, DOI: 10.1016/j.tca.2006.10.025.

[315] M. Anouti et al., "Liquid densities, heat capacities, refractive index and excess quantities for protic ionic liquids + water binary system", *The Journal of Chemical Thermodynamics*, 41, 6 (2009), 799 –808, DOI: 10.1016/j.jct.2009.01.011.

[316] N. Nie et al., "Thermodynamic Properties of the Water + 1-(2-Hydroxylethyl)-3-methylimidazolium Chloride System", *Journal of Chemical & Engineering Data*, 57, 12 (2012), 3598–3603, DOI: 10.1021/je3007953.

[317] Y. Hou, Z. Sha, and Y. Wang, "Determination of Specific Heat Capacity of Butylated Hydroxytoluene - Ethanol Binary System by DSC Method", *Shiyou Huagong*, 41, 2 (2012), 215–218.

[318] R. D. Mountain and A. H. Harvey, "Molecular Dynamics Evaluation of Dielectric Constant Mixing Rules for H2O–CO2 at Geologic Conditions", *Journal of Solution Chemistry*, 44, 11 (2015), 2179–2193, DOI: 10.1007/s10953-015-0401-6.

[319] Y. Wu et al., "Evaluation of Mixing Rules for Dielectric Constants of Composite Dielectrics by MC-FEM Calculation on 3D Cubic Lattice", *Journal of Electroceramics*, 11, 3 (2003), 227–239, DOI: 10.1023/B:JECR.0000026377.48598.4d.

[320] J. Sheen et al., "Studies of dielectric constant measurements at microwave frequency using mixing equations:The analyses on five rules", *Microwave and Optical Technology Letters*, 53, 11 (2011), 2481–2485, DOI: 10.1002/mop.26357.

[321] Y. Liu, J. Tang, and Z. Mao, "Analysis of bread dielectric properties using mixture equations", *Journal of Food Engineering*, 93, 1 (2009), 72 –79, DOI: 10.1016/j.jfoodeng.2008.12.032.

[322] A. Sihvola, "Homogenization principles and effect of mixing on dielectric behavior", *Photonics and Nanostructures - Fundamentals and Applications*, 11, 4 (2013), 364 –373, DOI: 10.1016/j.photonics.2013.01.004.

[323] C. D. Abeyrathne et al., "On the Utility of Dielectric Spectroscopy Techniques to Identify Compounds and Estimate Concentrations of Binary Mixtures", *IEEE Sensors Journal*, 14, 2 (2014), 538–546, DOI: 10.1109/JSEN.2013.2285279.

[324] A. Kraszewski, S. Kulinski, and M. Matuszewski, "Dielectric properties and a model of biphase water suspension at 9.4 GHz", *Journal of Applied Physics*, 47, 4 (1976), 1275–1277, DOI: 10.1063/1.322825.

[325] H. Looyenga, "Dielectric constants of heterogeneous mixtures", *Physica*, 31, 3 (1965), 401–406, DOI: 10.1016/0031-8914(65)90045-5.

[326] K. Lichtenecker and K. Rother, "Die Herleitung des logarithmischen Mischungs-gesetzes aus allegemeinen Prinzipien der stationaren Stromung", *Phys. Z.* 32 (1931), 255–260.

[327] R. Simpkin, "Derivation of Lichtenecker's Logarithmic Mixture Formula From Maxwell's Equations", *IEEE Transactions on Microwave Theory and Techniques*, 58, 3 (2010), 545–550, DOI: 10.1109/TMTT.2010.2040406.

[328] C. Bottcher, *Theory of Electric Polarization*, ed. by C. Bottcher, 2nd, Theory of Electric Polarization, Amsterdam: Elsevier, 1973.

[329] D. Bruggeman, "Berechnung verschiedener physikalischer Konstanten von heterogenen Substanzen. I. Dielektrizitatskonstanten und Leitfahigkeiten der Mischkorper aus isotropen Substanzen", *Annalen der Physik*, 24, 7-8 (1935), 636–679.

[330] J. C. M. Garnett, "Colours in Metal Glasses and in Metallic Films", *Philosophical Transactions of the Royal Society of London A: Mathematical, Physical and Engineering Sciences*, 203, 359-371 (1904), 385–420, DOI: 10.1098/rsta.1904.0024, eprint: http://rsta.royalsocietypublishing.org/content/203/359-371/385.full.pdf.

[331] J. Peon-Fernandez and T. Iglesias, "On the permittivity of mixtures: a low-fluctuation approach", *Journal of Electrostatics*, 32, 2 (1994), 113 –122, DOI: 10.1016/0304-3886(94)90002-7.

[332] A. Alvarez et al., "Measurement and correlation of dielectric properties of a grapepomace extraction media. Effect of temperature and composition.", Work in progress, 2016.

[333] H. J. Liebe, G. A. Hufford, and T. Manabe, "A model for the complex permittivity of water at frequencies below 1 THz", *International Journal of Infrared and Millimeter Waves*, 12, 7 (1991), 659–675, DOI: 10.1007/BF01008897.

[334] W. Ellison, K. Lamkaouchi, and J.-M. Moreau, "Water: a dielectric reference", *Journal of Molecular Liquids*, 68, 2 (1996), 171 –279, DOI: 10.1016/0167-7322(96)00926-9.

[335] X. Liao, G. Raghavan, and V. Yaylayan, "Dielectric properties of alcohols (C1-C5) at 2450 {MHz} and 915 {MHz}", *Journal of Molecular Liquids*, 94, 1 (2001), 51 –60, DOI: 10.1016/S0167-7322(01)00241-0.

[336] D. C. Campos et al., "Investigation of dielectric properties of the reaction mixture during the acid-catalyzed transesterification of Brazil nut oil for biodiesel production", *Fuel*, 117, Part B (2014), 957 –965, DOI: 10.1016/j.fuel.2013.10.037.

[337] P. D. Muley and D. Boldor, "Investigation of microwave dielectric properties of biodiesel components", *Bioresource Technology*, 127 (2013), 165 –174, DOI: 10.1016/j.biortech.2012.10.008.

[338] A. P. Franco et al., "Dielectric properties of green coconut water relevant to microwave processing: Effect of temperature and field frequency", *Journal of Food Engineering*, 155 (2015), 69 –78, DOI: 10.1016/j.jfoodeng.2015.01.011.

[339] J. Lou et al., "Effect of Temperature on the Dielectric Relaxation in Solvent Mixtures at Microwave Frequencies", *The Journal of Physical Chemistry A*, 101, 51 (1997), 9892–9899, DOI: 10.1021/jp972785+.

[340] X. Wang et al., "Volumetric Properties of Binary Mixtures of 3-(Methylamino)propylamine with Water, N-Methyldiethanolamine, N,N-Dimethylethanolamine, and N,N-Diethylethanolamine from (283.15 to 363.15) K", *Journal of Chemical & Engineering Data*, 58, 12 (2013), 3430–3439, DOI: 10.1021/je400679k.

[341] G. I. Egorov, D. M. Makarov, and A. M. Kolker, "Volume properties of liquid mixture of water + glycerol over the temperature range from 278.15 to 348.15 K at atmospheric pressure", *Thermochimica Acta*, 570 (2013), 16 –26, DOI: 10.1016/j.tca.2013.07.012.

[342] M. Krolikowska, M. Zawadzki, and M. Krolikowski, "Physicochemical and thermodynamic study on aqueous solutions of dicyanamide-based ionic liquids", *The Journal of Chemical Thermodynamics*, 70 (2014), 127 –137, DOI: 10.1016/j.jct.2013.10.034.

[343] A. Yadav and S. Pandey, "Densities and Viscosities of (Choline Chloride + Urea) Deep Eutectic Solvent and Its Aqueous Mixtures in the Temperature Range 293.15 K to 363.15 K", *Journal of Chemical & Engineering Data*, 59, 7 (2014), 2221–2229, DOI: 10.1021/je5001796.

[344] A. Yadav et al., "Densities and dynamic viscosities of (choline chloride + glycerol) deep eutectic solvent and its aqueous mixtures in the temperature range (283.15-363.15) K", *Fluid Phase Equilibria*, 367 (2014), 135 –142, DOI: 10.1016/j.fluid.2014.01.028.

[345] D. Keshapolla et al., "Apparent molar properties of benzyldimethylammonium based protic ionic liquids in water and ethanol at different temperatures", *Fluid Phase Equilibria*, 385 (2015), 92 –104, DOI: 10.1016/j.fluid.2014.11.005.

[346] G. Egorov, E. Gruznov, and A. Kolker, "The P-V-T-X properties of water - acetone mixtures at 298-323 K and 1-1000 bar. Isothermal compressibility and volume expansion coefficients and inner pressure", *Zh. Fiz. Khim.* 70, 2 (1996), 216–223.

[347] G. I. Egorov and D. M. Makarov, "The bulk properties of the water-dimethylsulfoxide system at 278–323.15 K and atmospheric pressure", *Russian Journal of Physical Chemistry A*, 83, 5 (2009), 693–698, DOI: 10.1134/S003602440905001X.

[348] M. Shokouhi et al., "Heat capacity, thermal conductivity and thermal diffusivity of aqueous sulfolane solutions", *Thermochimica Acta*, 560 (2013), 63 –70, DOI: 10.1016/j.tca.2013.03.017.

[349] Y. Zheng et al., "Isobaric heat capacity measurements of liquid HFE-7200 and HFE-7500 from 245 to 353 K at pressures up to 15 {MPa}", *Fluid Phase Equilibria*, 372 (2014), 56 –62, DOI: 10.1016/j.fluid.2014.03.017.

[350] N. C. Merkel et al., "Thermophysical Properties of the Binary Mixture of Water + Diethylmethylammonium Trifluoromethanesulfonate and the Ternary Mixture of Water + Diethylmethylammonium Trifluoromethanesulfonate + Diethylmethylammonium Methanesulfonate", *Journal of Chemical & Engineering Data*, 59, 3 (2014), 560–570, DOI: 10.1021/je400097b.

[351] C. Zhu et al., "Densities and Viscosities of Diaminotoluene with Water, Ethanol, Propan-1-ol, and Butan-1-ol from (293.15 to 333.15) K", *Journal of Chemical & Engineering Data*, 59, 3 (2014), 880–889, DOI: 10.1021/je400968v.

[352] M. C. Castro et al., "Mixtures of Ethanol and the Ionic Liquid 1-Ethyl-3-methylimidazolium Acetate for the Fractionated Solubility of Biopolymers of Lignocellulosic Biomass", *Industrial & Engineering Chemistry Research*, 53, 29 (2014), 11850–11861, DOI: 10.1021/ie501956x.

[353] M. Silveira et al., "Ab-diesel: Liquid-liquid equilibrium and volumetric transport properties", *Fuel*, 119 (2014), 292 –300, DOI: 10.1016/j.fuel.2013.11.022.

[354] M. Massel et al., "Phase Equilibrium, Excess Enthalpies, and Densities of Binary Mixtures of Trimethylbutylammonium Bis(trifluoromethylsulfonyl)imide with Ethanol, 1-Propanol, and Dimethylformamide", *Journal of Chemical & Engineering Data*, 60, 1 (2015), 65–73, DOI: 10.1021/je500696p.

[355] S. K. Mehta, R. K. Chauhan, and R. K. Dewan, "Excess volumes and isentropic compressibilities of pyrrolidin-2-one-alkanol (C1-C5) binary mixtures", *J. Chem. Soc., Faraday Trans.* 92 (7 1996), 1167–1173, DOI: 10.1039/FT9969201167.

[356] S. L. Oswal, and K. D. Prajapati, "Speeds of Sound, Isentropic Compressibilities, and Excess Molar Volumes of an Alkanol + Cycloalkane at 303.15 K. 1. Results for Alkan-1-ols + Cyclohexane", *Journal of Chemical & Engineering Data*, 43, 3 (1998), 367–372, DOI: 10.1021/je970235z.

[357] V. Kartsev and V. Zabelin, "Isothermal compressibilities of liquid straight-chain alcohols", *Russ. J. Phys. Chem.* 52, 8 (1978), 1221–1222.

[358] D. Vega-Maza et al., "Thermodynamic properties of biofuels: Heat capacities of binary mixtures containing ethanol and hydrocarbons up to 20 {MPa} and the pure compounds using a new flow calorimeter", *The Journal of Chemical Thermodynamics*, 43, 12 (2011), 1893 –1896, DOI: 10.1016/j.jct.2011.06.019.

[359] X.-X. Li et al., "Density and Viscosity for Binary Mixtures of Diethylene Glycol Monobutyl Ether with Monoethanolamine, Diethanolamine, and Triethanolamine from (293.15 to 333.15) K", *Journal of Chemical & Engineering Data*, 58, 5 (2013), 1229–1235, DOI: 10.1021/je4000372.

[360] X. Wang et al., "Volumetric properties of binary mixtures of dimethyl sulfoxide with amines from (293.15 to 363.15) K", *The Journal of Chemical Thermodynamics*, 57 (2013), 145 –151, DOI: 10.1016/j.jct.2012.08.021.

[361] M. S. Shaikh et al., "Physicochemical Properties of Aqueous Solutions of Sodium l-Prolinate as an Absorbent for CO2 Removal", *Journal of Chemical & Engineering Data*, 59, 2 (2014), 362–368, DOI: 10.1021/je400830w.

[362] M. Mundhwa and A. Henni, "Molar Heat Capacity of Various Aqueous Alkanolamine Solutions from 303.15 K to 353.15 K", *Journal of Chemical & Engineering Data*, 52, 2 (2007), 491–498, DOI: 10.1021/je0604232.

[363] A. V. Rayer, A. Henni, and P. Tontiwachwuthikul, "Molar heat capacities of solvents used in CO2 capture: A group additivity and molecular connectivity analysis", *The Canadian Journal of Chemical Engineering*, 90, 2 (2012), 367–376, DOI: 10.1002/cjce.20646.

[364] A. Shul'gin and L. Puchkov, "Heat capacity of water - ethanol solutions", *Zh. Obshch. Khim.* 53, 10 (1983), 2181–2184.

[365] A. Gregory and R. N. Clarke, *Tables of the complex permittivity of dielectric reference liquids at frequencies up to 5 GHz.* NPL Report MAT 23, National Physical Laboratory, 2012.

[366] H. Kienitz and K. N. Marsh, "Recommended reference materials for realization of physicochemical properties. Section: Permittivity", *Pure and Applied Chemistry.* 53, 10 (1981), 1847–1862, DOI: 10.1351/pac198153101847.

[367] W. Dannhauser and L. W. Bahe, "Dielectric Constant of Hydrogen Bonded Liquids. III. Superheated Alcohols", *The Journal of Chemical Physics*, 40, 10 (1964), 3058–3066, DOI: 10.1063/1.1724948.

[368] M. Khimenko, V. Aleksandrov, and N. Gritsenko, "An Experimental Study of the Dielectric Constant of the Ethanol - Benzene Binary System along the Saturation Line from 20 to 240 C", *Russ. J. Phys. Chem.* 47, 11 (1973), 2914–2915.

[369] R. Sengwa, S. Choudhary, and A. Bald, "Dielectric Dispersion and Electric Relaxation Processes Induced by Ionic Conduction in Formamide, 2-Aminoethanol and Their Binary Mixtures", English, *Journal of Solution Chemistry*, 42, 10 (2013), 1960–1975, DOI: 10.1007/s10953-013-0087-6.

[370] T. Meissner and F. J. Wentz, "The complex dielectric constant of pure and sea water from microwave satellite observations", *IEEE Transactions on Geoscience and Remote Sensing*, 42, 9 (2004), 1836–1849, DOI: 10.1109/TGRS.2004.831888.

[371] J. Chao et al., "Eyring activation barriers for the anomalous dielectric relaxations of diphenyl ether-type molecules", *The Journal of Physical Chemistry*, 88, 4 (1984), 711–716, DOI: 10.1021/j150648a019.

[372] H. Eyring, "The Activated Complex in Chemical Reactions", *The Journal of Chemical Physics*, 3, 2 (1935), 107–115, DOI: 10.1063/1.1749604.

[373] S. Glasstone, K. J. Laidle, and H Eyring, "The Theory of Rate Processes", PhD thesis, Massachusetts Institute of Technology, 1941.

[374] S. Arrhenius, "Uber die Dissociationswarme und den Einflusb der Temperatur auf den Dissociationsgrad der Elektrolyte", *Z. Phys. Chem*, 1, 4 (1889), 96–116.

[375] K. J. Laidler and M. C. King, "Development of transition-state theory", *The Journal of Physical Chemistry*, 87, 15 (1983), 2657–2664, DOI: 10.1021/j100238a002.

[376] K. A. T. Silverstein, A. D. J. Haymet, and K. A. Dill, "The Strength of Hydrogen Bonds in Liquid Water and Around Nonpolar Solutes", *Journal of the American Chemical Society*, 122, 33 (2000), 8037–8041, DOI: 10.1021/ja000459t.

[377] S. J. Suresh and V. M. Naik, "Hydrogen bond thermodynamic properties of water from dielectric constant data", *The Journal of Chemical Physics*, 113, 21 (2000), 9727–9732, DOI: 10.1063/1.1320822.

[378] I. F. Hakem et al., "Temperature, pressure, and isotope effects on the structure and properties of liquid water: A lattice approach", *The Journal of Chemical Physics*, 127, 22 (2007), 224106, DOI: 10.1063/1.2804418.

[379] P. Atkins, *Atkins' Physical Chemistry*, ed. by P. Atkins, Oxford University Press, 1986.

[380] F. Melde, *Ueber einige krumme Flachen, welche von Ebenen, parallel einer bestimmten Ebene, durchschnitten, als Durchschnittsfigur einen Kegelschnitt liefern*, Marburg Koch, 1859.

[381] F. Melde, "Ueber die Erregung stehender Wellen eines fadenformigen Korpers", *Annalen der Physik*, 187, 12 (1860), 513–537, DOI: 10.1002/andp.18601871202.

[382] A. C. Metaxas and R. J. Meredith, *Industrial Microwave Heating*, IEE power engineering series, London : Peter Peregrinus, 1993.

[383] D. J. Griffiths, *Introduction to Electrodynamics*, ed. by A. Reeves, 3rd, Prentice Hall, 1999.

[384] *Dielectric cylinder in uniform electric field*, 2012, URL: http://www.physicspages.com/2012/10/20/dielectric-cylinder-in-uniform-electric-field/.

[385] P. Bouguer, *Essai d'optique sur la gradation de la lumiere*, ed. by C. Jombert, C. Jombert, 1729.

[386] J. Lambert and E. Andig, *Photometria sive de mensura et gradibus luminis, colorum et umbrae*, Leipzig : W. Engelmann, 1760.

[387] A. Beer, "Bestimmung der Absorption des rothen Lichts in farbigen Flussigkeiten", *Annalen der Physik und Chemie*, ed. by J. C. Poggendorff, vol. 86, Johann Christian Poggendorff, 1852, chap. III, 78–88.

[388] M. Soltysiak, U. Erle, and M. Celuch, "Load curve estimation for microwave ovens: Experiments and electromagnetic modelling", *Microwaves, Radar and Wireless Communications, 2008. MIKON 2008. 17th International Conference on*, IEEE, 2008, 1–4.

[389] K. Pitchai, "Electromagnetic and Heat Transfer Modeling of Microwave Heating in Domestic Ovens", MA thesis, University of Nebraska at Lincoln, 2011.

[390] M. Solar et al., "The dielectric alpha -relaxation in polymer films: A comparison between experiments and atomistic simulations", *EPL (Europhysics Letters)*, 104, 6 (2013), 66004.

[391] M. Solar et al., "Polymer Dynamics in a Polymer-Solid Interphase: Molecular Dynamics Simulations of 1,4-Polybutadiene At a Graphite Surface", *Soft Materials*, 12, sup1 (2014), S80–S89, DOI: 10.1080/1539445X.2014.937495.

[392] J. Ramos et al., "Entanglement Relaxation Time in Polyethylene: Simulation versus Experimental Data", *Macromolecules*, 41, 8 (2008), 2959–2962, DOI: 10.1021/ma702445e.

[393] A. N. Rissanou and V. Harmandaris, "Dynamics of various polymer-graphene interfacial systems through atomistic molecular dynamics simulations", *Soft Matter*, 10 (16 2014), 2876–2888, DOI: 10.1039/C3SM52688G.

[394] G. E. Logotheti and D. N. Theodorou, "Segmental and Chain Dynamics of Isotactic Polypropylene Melts", *Macromolecules*, 40, 6 (2007), 2235–2245, DOI: 10.1021/ma062234u.

[395] A. V. Lyulin et al., "Strain softening and hardening of amorphous polymers: Atomistic simulation of bulk mechanics and local dynamics", *EPL (Europhysics Letters)*, 71, 4 (2005), 618.

[396] A. V. Lyulin and M. Michels, "Simulation of polymer glasses: From segmental dynamics to bulk mechanics", *Journal of Non-Crystalline Solids*, 352, 42-49 (2006), Proceedings of the 5th International Discussion Meeting on Relaxations in Complex Systems 5th International Discussion Meeting on Relaxations in Complex Systems, 5008 –5012, DOI: 10.1016/j.jnoncrysol.2006.02.156.

[397] V. A. Harmandaris and K. Kremer, "Predicting polymer dynamics at multiple length and time scales", *Soft Matter*, 5 (20 2009), 3920–3926, DOI: 10.1039/B905361A.

[398] A. R. C. Baljon et al., "Simulated glass transition in free-standing thin polystyrene films", *Journal of Polymer Science Part B: Polymer Physics*, 48, 11 (2010), 1160–1167, DOI: 10.1002/polb.22005.

[399] V. A. Harmandaris, G. Floudas, and K. Kremer, "Temperature and Pressure Dependence of Polystyrene Dynamics through Molecular Dynamics Simulations and Experiments", *Macromolecules*, 44, 2 (2011), 393–402, DOI: 10.1021/ma102179b.

[400] S. Peter et al., "Modeling Dielectric Relaxation in Polymer Glass Simulations: Dynamics in the Bulk and in Supported Polymer Films", *Macromolecules*, 41, 20 (2008), 7729–7743, DOI: 10.1021/ma800694v.

[401] M. Paluch, A. Patkowski, and E. W. Fischer, "Temperature and Pressure Scaling of the α Relaxation Process in Fragile Glass Formers: A Dynamic Light Scattering Study", *Phys. Rev. Lett.* 85 (10 2000), 2140–2143, DOI: 10.1103/PhysRevLett.85.2140.

[402] G. Floudas et al., "Effect of pressure on the segmental and chain dynamics of polyisoprene. Molecular weight dependence", *The Journal of Chemical Physics*, 111, 21 (1999), 9847–9852, DOI: 10.1063/1.480327.

[403] Y. Lin et al., "Dielectric relaxation of water inside a single-walled carbon nanotube", *Phys. Rev. B*, 80 (4 2009), 045419, DOI: 10.1103/PhysRevB.80.045419.

[404] D. Li and G. Jia, "Dielectric properties of SPC/E and TIP4P under the static electric field and microwave field", *Physica A: Statistical Mechanics and its Applications*, 449 (2016), 348 –356, DOI: 10.1016/j.physa.2016.01.007.

Appendix A

Dielectric relaxation expressions according to the Debye and the Havriliak-Negami models

In this appendix we derive the real and imaginary parts of the complex dielectric permittivity for the Debye and the Havriliak-Negami models in the frequency domain. In addition we develop the time domain expressions of the dipole moment autocorrelation function for both models.

A.1 Real and imaginary parts

A.1.1 The Debye model

In the frequency domain, the single Debye relaxation is given by the expression:

$$\frac{\hat{\varepsilon}(\omega)-\varepsilon_\infty}{\varepsilon_0-\varepsilon_\infty}=\frac{1}{1-i\,\omega\tau_{\mathrm{D}}} \tag{(3.72)}$$

$$\hat{\varepsilon}(\omega)=\varepsilon_\infty+(\varepsilon_0-\varepsilon_\infty)\,\frac{1}{1-i\,\omega\tau_{\mathrm{D}}} \tag{A.1}$$

$$\hat{\varepsilon}(\omega)=\varepsilon_\infty+(\varepsilon_0-\varepsilon_\infty)\,\frac{1+i\,\omega\tau_{\mathrm{D}}}{1+\omega^2\tau_{\mathrm{D}}^2} \tag{A.2}$$

Therefore, defining the complex dielectric permittivity as $\hat{\varepsilon}(\omega)=\hat{\varepsilon}'(\omega)+i\;\hat{\varepsilon}''(\omega)$, the real and imaginary parts result in:

$$\boxed{\begin{aligned}\hat{\varepsilon}'(\omega)&=\varepsilon_\infty+\frac{\varepsilon_0-\varepsilon_\infty}{1+\omega^2\tau_{\mathrm{D}}^2}\\ \hat{\varepsilon}''(\omega)&=\frac{(\varepsilon_0-\varepsilon_\infty)\,\omega\tau_{\mathrm{D}}}{1+\omega^2\tau_{\mathrm{D}}^2}\end{aligned}} \tag{A.3}$$

A.1.2 The Havriliak-Negami model

In the frequency domain, the single Havrilak-Negami relaxation is given by the expression:

$$\frac{\hat{\varepsilon}(\omega)-\varepsilon_\infty}{\varepsilon_0-\varepsilon_\infty}=\frac{1}{\left[1+(-i\omega\tau_{\text{HN}})^\alpha\right]^\beta} \tag{(3.74)}$$

$$\hat{\varepsilon}(\omega)=\varepsilon_\infty+(\varepsilon_0-\varepsilon_\infty)\left[1+(-i\omega\tau_{\text{HN}})^\alpha\right]^{-\beta} \tag{A.4}$$

where, taking into account that $i=e^{i\frac{\pi}{2}}$, we obtain:

$$\left[1+(-i\omega\tau_{\text{HN}})^\alpha\right]^{-\beta}=\left[1+\left(-e^{i\frac{\pi}{2}}\ \omega\tau_{\text{HN}}\right)^\alpha\right]^{-\beta} \tag{A.5}$$

$$\left[1+(-i\omega\tau_{\text{HN}})^\alpha\right]^{-\beta}=\left[1+\left(-e^{i\frac{\pi}{2}\alpha}\right)(\omega\tau_{\text{HN}})^\alpha\right]^{-\beta} \tag{A.6}$$

$$\left[1+(-i\omega\tau_{\text{HN}})^\alpha\right]^{-\beta}=\left[1-e^{i\frac{\pi}{2}\alpha}(\omega\tau_{\text{HN}})^\alpha\right]^{-\beta} \tag{A.7}$$

$$\left[1+(-i\omega\tau_{\text{HN}})^\alpha\right]^{-\beta}=\left\{1-\left[\cos\left(\frac{\pi\alpha}{2}\right)+i\sin\left(\frac{\pi\alpha}{2}\right)\right](\omega\tau_{\text{HN}})^\alpha\right\}^{-\beta} \tag{A.8}$$

$$\left[1+(-i\omega\tau_{\text{HN}})^\alpha\right]^{-\beta}=\left[1-(\omega\tau_{\text{HN}})^\alpha\cos\left(\frac{\pi\alpha}{2}\right)-i\,(\omega\tau_{\text{HN}})^\alpha\sin\left(\frac{\pi\alpha}{2}\right)\right]^{-\beta} \tag{A.9}$$

Converting into polar form:

$$\left[1+(-i\omega\tau_{\text{HN}})^\alpha\right]^{-\beta}=\left\{\sqrt{\left[1-(\omega\tau_{\text{HN}})^\alpha\cos\left(\frac{\pi\alpha}{2}\right)\right]^2+\left[-(\omega\tau_{\text{HN}})^\alpha\sin\left(\frac{\pi\alpha}{2}\right)\right]^2}e^{i\varphi_{\text{HN}}}\right\}^{-\beta} \tag{A.10}$$

with:

$$\varphi_{\text{HN}}=\arctan\left[-\frac{(\omega\,\tau_{\text{HN}})^\alpha\sin(\pi\alpha/2)}{1-(\omega\,\tau_{\text{HN}})^\alpha\cos(\pi\alpha/2)}\right] \tag{A.11}$$

$$\left[1+(-i\omega\tau_{\text{HN}})^\alpha\right]^{-\beta}=\left[1-2\,(\omega\tau_{\text{HN}})^\alpha\cos\left(\frac{\pi\alpha}{2}\right)+(\omega\tau_{\text{HN}})^{2\alpha}\cos^2\left(\frac{\pi\alpha}{2}\right)+(\omega\tau_{\text{HN}})^{2\alpha}\sin^2\left(\frac{\pi\alpha}{2}\right)\right]^{-\beta/2}e^{-i\beta\varphi_{\text{HN}}} \tag{A.12}$$

$$\left[1+(-i\omega\tau_{\text{HN}})^\alpha\right]^{-\beta}=\left[1-2\,(\omega\tau_{\text{HN}})^\alpha\cos\left(\frac{\pi\alpha}{2}\right)+(\omega\tau_{\text{HN}})^{2\alpha}\right]^{-\beta/2}e^{-i\beta\varphi_{\text{HN}}} \tag{A.13}$$

$$\left[1+(-i\omega\tau_{\text{HN}})^\alpha\right]^{-\beta}=\left[1-2\,(\omega\tau_{\text{HN}})^\alpha\cos\left(\frac{\pi\alpha}{2}\right)+(\omega\tau_{\text{HN}})^{2\alpha}\right]^{-\beta/2}\left[\cos\left(-\beta\varphi_{\text{HN}}\right)+i\sin\left(-\beta\varphi_{\text{HN}}\right)\right] \tag{A.14}$$

Therefore, according to Eq. (A.4), the real and imaginary parts of the Havriliak-Negami model are finally given by:

$$\boxed{\begin{aligned}\hat{\varepsilon}'(\omega) &= \varepsilon_\infty + (\varepsilon_0 - \varepsilon_\infty)\left[1 - 2(\omega\,\tau_{\text{HN}})^\alpha \cos(\pi\alpha/2) + (\omega\,\tau_{\text{HN}})^{2\alpha}\right]^{-\beta/2} \cos(-\beta\varphi_{\text{HN}}) \\ \hat{\varepsilon}''(\omega) &= (\varepsilon_0 - \varepsilon_\infty)\left[1 - 2(\omega\,\tau_{\text{HN}})^\alpha \cos(\pi\alpha/2) + (\omega\,\tau_{\text{HN}})^{2\alpha}\right]^{-\beta/2} \sin(-\beta\varphi_{\text{HN}})\end{aligned}} \tag{A.15}$$

with:

$$\varphi_{\text{HN}} = \arctan\left[-\frac{(\omega\,\tau_{\text{HN}})^\alpha \sin(\pi\alpha/2)}{1 - (\omega\,\tau_{\text{HN}})^\alpha \cos(\pi\alpha/2)}\right] \tag{A.16}$$

A.2 Frequency domain dipole moment autocorrelation function

A.2.1 The Debye model

Combining Eq. (3.50) and Eq. (3.72), we obtain:

$$1 + i\omega\hat{\phi}(\omega) = \frac{1}{1 - i\,\omega\tau_{\text{D}}} \tag{A.17}$$

$$\hat{\phi}(\omega) = \frac{1}{i\omega}\left(\frac{1}{1 - i\,\omega\tau_{\text{D}}} - 1\right) \tag{A.18}$$

$$\hat{\phi}(\omega) = \frac{1}{i\omega}\left(\frac{1 + i\,\omega\tau_{\text{D}}}{1 + \omega^2\tau_{\text{D}}^2} - 1\right) \tag{A.19}$$

$$\hat{\phi}(\omega) = \frac{1}{i\omega}\left(\frac{i\,\omega\tau_{\text{D}} - \omega^2\tau_{\text{D}}^2}{1 + \omega^2\tau_{\text{D}}^2}\right) \tag{A.20}$$

$$\hat{\phi}(\omega) = \frac{\tau_{\text{D}} + \omega\tau_{\text{D}}^2}{1 + \omega^2\tau_{\text{D}}^2} \tag{A.21}$$

Therefore:

$$\boxed{\begin{aligned}\hat{\phi}'(\omega) &= \frac{\tau_{\text{D}}}{1 + \omega^2\tau_{\text{D}}^2} \\ \hat{\phi}''(\omega) &= \frac{\omega\tau_{\text{D}}^2}{1 + \omega^2\tau_{\text{D}}^2}\end{aligned}} \tag{A.22}$$

A.2.2 The Havriliak-Negami model

Combining Eq. (3.50) and Eq. (3.74), we obtain:

$$1 + i\omega\hat{\phi}(\omega) = \left[1 + (-i\omega\tau_{\text{HN}})^\alpha\right]^{-\beta} \tag{A.23}$$

$$\hat{\phi}(\omega) = \frac{1}{-i\omega} - \frac{1}{-i\omega}\left[1 + (-i\omega\tau_{\text{HN}})^\alpha\right]^{-\beta}, \tag{A.24}$$

where according to Eq. (A.14):

$$[1+(-i\omega\tau_{\text{HN}})^{\alpha}]^{-\beta}=\left[1-2\left(\omega\tau_{\text{HN}}\right)^{\alpha}\cos\left(\frac{\pi\alpha}{2}\right)+\left(\omega\tau_{\text{HN}}\right)^{2\alpha}\right]^{-\beta/2}\left[\cos\left(-\beta\varphi_{\text{HN}}\right)+i\sin\left(-\beta\varphi_{\text{HN}}\right)\right] \tag{(A.14)}$$

Then:

$$\hat{\phi}(\omega)=\frac{1}{-i\omega}-\frac{1}{-i\omega}\left[1-2\left(\omega\tau_{\text{HN}}\right)^{\alpha}\cos\left(\frac{\pi\alpha}{2}\right)+\left(\omega\tau_{\text{HN}}\right)^{2\alpha}\right]^{-\beta/2}\left[\cos\left(-\beta\varphi_{\text{HN}}\right)+i\sin\left(-\beta\varphi_{\text{HN}}\right)\right] \tag{A.25}$$

$$\hat{\phi}(\omega)=\frac{1}{\omega}\,i+\frac{1}{\omega}\left[1-2\left(\omega\tau_{\text{HN}}\right)^{\alpha}\cos\left(\frac{\pi\alpha}{2}\right)+\left(\omega\tau_{\text{HN}}\right)^{2\alpha}\right]^{-\beta/2}\left[\sin\left(-\beta\varphi_{\text{HN}}\right)-i\cos\left(-\beta\varphi_{\text{HN}}\right)\right] \tag{A.26}$$

Therefore:

$$\boxed{\begin{aligned}\hat{\phi}'(\omega)&=\frac{1}{\omega}\left[1-2\left(\omega\tau_{\text{HN}}\right)^{\alpha}\cos\left(\frac{\pi\alpha}{2}\right)+\left(\omega\tau_{\text{HN}}\right)^{2\alpha}\right]^{-\beta/2}\sin\left(-\beta\varphi_{\text{HN}}\right)\\ \hat{\phi}\prime(\omega)&=\frac{1}{\omega}-\frac{1}{\omega}\left[1-2\left(\omega\tau_{\text{HN}}\right)^{\alpha}\cos\left(\frac{\pi\alpha}{2}\right)+\left(\omega\tau_{\text{HN}}\right)^{2\alpha}\right]^{-\beta/2}\cos\left(-\beta\varphi_{\text{HN}}\right)\end{aligned}} \tag{A.27}$$

with:

$$\varphi_{\text{HN}}=\arctan\left[-\frac{(\omega\,\tau_{\text{HN}})^{\alpha}\sin(\pi\alpha/2)}{1-(\omega\,\tau_{\text{HN}})^{\alpha}\cos(\pi\alpha/2)}\right] \tag{A.28}$$

A.3 Time domain dipole moment autocorrelation function

Since the Debye model represents a particular case of the HN model, we start by deriving a general expression for the latter, and next we apply this expression for the specific case in which α = 1 and β = 1.

A.3.1 The Havriliak-Negami model

$$\frac{\hat{\varepsilon}(\omega)-\varepsilon_{\infty}}{\varepsilon_{0}-\varepsilon_{\infty}}=\frac{1}{[1+(-i\omega\tau_{\text{HN}})^{\alpha}]^{\beta}} \tag{(3.74)}$$

The combination of the frequency domain representation of the Havriliak-Negami model (Eq. (3.74)) with Eq. (3.50) results in:

$$1+i\omega\hat{\phi}(\omega)=[1+(-i\omega\tau_{\text{HN}})^{\alpha}]^{-\beta} \tag{A.29}$$

$$-i\omega\hat{\phi}(\omega)=1-[1+(-i\omega\tau_{\text{HN}})^{\alpha}]^{-\beta} \tag{A.30}$$

In this expression:

$$[1+(-i\omega\tau_{\text{HN}})^{\alpha}]^{-\beta}=\left[(-i\omega\tau_{\text{HN}})^{\alpha}\left[1+(-i\omega\tau_{\text{HN}})^{-\alpha}\right]\right]^{-\beta} \tag{A.31}$$

$$[1+(-i\omega\tau_{\text{HN}})^{\alpha}]^{-\beta} = (-i\omega\tau_{\text{HN}})^{-\alpha\beta}\left[1+(-i\omega\tau_{\text{HN}})^{-\alpha}\right]^{-\beta} \tag{A.32}$$

If we introduce the gamma function defined as:

$$\Gamma(x) = \int_0^{\infty} dt\; t^{x-1}e^{-t} \tag{A.33}$$

And a change of variable such as $t \equiv at$, $dt \equiv adt$:

$$\Gamma(x) = \int_0^{\infty} a\; dt\,(at)^{x-1}\,e^{-at} = a^x \int_0^{\infty} dt\; t^{x-1}e^{-at} \tag{A.34}$$

$$a^{-x} = \frac{1}{\Gamma(x)}\int_0^{\infty} dt\; t^{x-1}e^{-at} \tag{A.35}$$

Let $a = 1+(-i\omega\tau_{\text{HN}})^{-\alpha}$ and $x = \beta$:

$$\left[1+(-i\omega\tau_{\text{HN}})^{-\alpha}\right]^{-\beta} = \frac{1}{\Gamma(\beta)}\int_0^{\infty} dt\; t^{\beta-1}\; e^{-\left[1+(-i\omega\tau_{\text{HN}})^{-\alpha}\right]t} \tag{A.36}$$

Therefore, according to Eq. (A.32):

$$[1+(-i\omega\tau_{\text{HN}})^{\alpha}]^{-\beta} = (-i\omega\tau_{\text{HN}})^{-\alpha\beta}\,\frac{1}{\Gamma(\beta)}\int_0^{\infty} dt\; t^{\beta-1}\; e^{-\left[1+(-i\omega\tau_{\text{HN}})^{-\alpha}\right]t} \tag{A.37}$$

$$[1+(-i\omega\tau_{\text{HN}})^{\alpha}]^{-\beta} = (-i\omega\tau_{\text{HN}})^{-\alpha\beta}\,\frac{1}{\Gamma(\beta)}\int_0^{\infty} dt\; t^{\beta-1}\; e^{-t}\; e^{-t(-i\omega\tau_{\text{HN}})^{-\alpha}} \tag{A.38}$$

where:

$$e^{-t(-i\omega\tau_{\text{HN}})^{-\alpha}} = \sum_{k=0}^{\infty}\frac{(-1)^k}{k!}\;\left[t\,(-i\omega\tau_{\text{HN}})^{-\alpha}\right]^k = \sum_{k=0}^{\infty}\frac{(-1)^k}{k!}\;t^k\,(-i\omega\tau_{\text{HN}})^{-\alpha k} \tag{A.39}$$

Therefore:

$$[1+(-i\omega\tau_{\text{HN}})^{\alpha}]^{-\beta} = (-i\omega\tau_{\text{HN}})^{-\alpha\beta}\,\frac{1}{\Gamma(\beta)}\int_0^{\infty} dt\; t^{\beta-1}\; e^{-t}\;\sum_{k=0}^{\infty}\frac{(-1)^k}{k!}\;t^k\,(-i\omega\tau_{\text{HN}})^{-\alpha k} \tag{A.40}$$

$$[1+(-i\omega\tau_{\text{HN}})^{\alpha}]^{-\beta} = (-i\omega\tau_{\text{HN}})^{-\alpha\beta}\,\frac{1}{\Gamma(\beta)}\sum_{k=0}^{\infty}\frac{(-1)^k}{k!}\;(-i\omega\tau_{\text{HN}})^{-\alpha k}\int_0^{\infty} dt\; t^{\beta-1+k}\; e^{-t} \tag{A.41}$$

$$[1+(-i\omega\tau_{\text{HN}})^{\alpha}]^{-\beta} = \frac{1}{\Gamma(\beta)}\sum_{k=0}^{\infty}\frac{(-1)^k}{k!}\;(-i\omega\tau_{\text{HN}})^{-\alpha(\beta+k)}\,\Gamma(\beta+k) \tag{A.42}$$

where $k! = \Gamma(1+k)$, so:

$$[1+(-i\omega\tau_{\text{HN}})^{\alpha}]^{-\beta} = \frac{1}{\Gamma(\beta)}\sum_{k=0}^{\infty}(-1)^k\,\frac{\Gamma(\beta+k)}{\Gamma(1+k)}\,(-i\omega\tau_{\text{HN}})^{-\alpha(\beta+k)} \tag{A.43}$$

Replacing this expression in Eq. (A.30), we obtain:

$$-i\omega\hat{\phi}(\omega) = 1 - \frac{1}{\Gamma(\beta)}\sum_{k=0}^{\infty}(-1)^k\,\frac{\Gamma(\beta+k)}{\Gamma(1+k)}\,(-i\omega\tau_{\text{HN}})^{-\alpha(\beta+k)} \tag{A.44}$$

$$\hat{\phi}(\omega) = \frac{1}{-i\omega} - \frac{1}{\Gamma(\beta)}\sum_{k=0}^{\infty}(-1)^k\,\frac{\Gamma(\beta+k)}{\Gamma(1+k)}\,(-i\omega)^{-\alpha(\beta+k)-1}\;\tau_{\text{HN}}^{-\alpha(\beta+k)} \tag{A.45}$$

where, from Eq. (A.35), we can deduce that:

$$(-i\omega)^{-\alpha(\beta+k)-1} = \frac{1}{\Gamma\left[\alpha(\beta+k)+1\right]}\int_0^{\infty} dt\; t^{\alpha(\beta+k)}\; e^{i\omega t} \tag{A.46}$$

Therefore:

$$\hat{\phi}(\omega) = \frac{1}{-i\omega} - \frac{1}{\Gamma(\beta)}\sum_{k=0}^{\infty}(-1)^k\,\frac{\Gamma(\beta+k)}{\Gamma(1+k)}\frac{1}{\Gamma\left[\alpha(\beta+k)+1\right]}\int_0^{\infty} dt\;\frac{t^{\alpha(\beta+k)}}{\tau_{\text{HN}}^{\alpha(\beta+k)}}\,e^{i\omega t} \tag{A.47}$$

$$\hat{\phi}(\omega) = \frac{1}{-i\omega} - \frac{1}{\Gamma(\beta)}\sum_{k=0}^{\infty}(-1)^k\,\frac{\Gamma(\beta+k)}{\Gamma(1+k)}\frac{1}{\Gamma\left[\alpha(\beta+k)+1\right]}\int_0^{\infty} dt\;\left(\frac{t}{\tau_{\text{HN}}}\right)^{\alpha(\beta+k)}\,e^{i\omega t} \tag{A.48}$$

$$\hat{\phi}(\omega) = \frac{1}{-i\omega} - \frac{1}{\Gamma(\beta)}\sum_{k=0}^{\infty}(-1)^k\,\frac{\Gamma(\beta+k)}{\Gamma(1+k)}\frac{1}{\Gamma\left[\alpha(\beta+k)+1\right]}\,\mathcal{F}\left[\left(\frac{t}{\tau_{\text{HN}}}\right)^{\alpha(\beta+k)}\right] \tag{A.49}$$

Performing the inverse Fourier transform of this expression, we finally obtain:

$$\phi(t) = \mathcal{F}^{-1}\left[\frac{1}{-i\omega}\right] - \frac{1}{\Gamma(\beta)}\sum_{k=0}^{\infty}(-1)^k\,\frac{\Gamma(\beta+k)}{\Gamma(1+k)}\frac{1}{\Gamma\left[\alpha(\beta+k)+1\right]}\,\mathcal{F}^{-1}\left\{\mathcal{F}\left[\left(\frac{t}{\tau_{\text{HN}}}\right)^{\alpha(\beta+k)}\right]\right\} \tag{A.50}$$

$$\boxed{\phi(t) = 1 - \sum_{k=0}^{\infty}(-1)^k\,\frac{\Gamma(\beta+k)}{\Gamma(1+k)}\;\frac{(t/\tau_{\text{HN}})^{\alpha(\beta+k)}}{\Gamma(\beta)\,\Gamma\left[\alpha(\beta+k)+1\right]}} \tag{A.51}$$

A.3.2 The Debye model

Even though the Debye model has more theoretical implications than the empirical Havriliak-Negami model, it can also be seen as a particular case of the HN model when α = 1 and β = 1. As a consequence, substituting these conditions into Eq. (A.51), gives

the time domain expressions of the dipole moment autocorrelation function according to the Debye model.

$$\phi(t) = 1 - \sum_{k=0}^{\infty} (-1)^k \frac{1}{\Gamma(2+k)} \left(\frac{t}{\tau_{\mathrm{D}}}\right)^{1+k} \tag{A.52}$$

Let $k' = 1 + k$:

$$\phi(t) = 1 - \sum_{k'=1}^{\infty} (-1)^{k'-1} \frac{1}{\Gamma(1+k')} \left(\frac{t}{\tau_{\mathrm{D}}}\right)^{k'} \tag{A.53}$$

$$\phi(t) = 1 - (-1)^{-1} \sum_{k'=1}^{\infty} (-1)^{k'} \frac{1}{\Gamma(1+k')} \left(\frac{t}{\tau_{\mathrm{D}}}\right)^{k'} \tag{A.54}$$

$$\phi(t) = 1 + \sum_{k'=1}^{\infty} \frac{1}{\Gamma(1+k')} \left(-\frac{t}{\tau_{\mathrm{D}}}\right)^{k'} \tag{A.55}$$

The term that would correspond to k' = 0, would result in:

$$\frac{1}{\Gamma(1+k')} \left(-\frac{t}{\tau_{\mathrm{D}}}\right)^{k'} = 1$$

Therefore, the sum becomes:

$$\phi(t) = \sum_{k'=0}^{\infty} \frac{1}{\Gamma(1+k')} \left(-\frac{t}{\tau_{\mathrm{D}}}\right)^{k'} \tag{A.56}$$

$$\phi(t) = \sum_{k'=0}^{\infty} \frac{1}{k'!} \left(-\frac{t}{\tau_{\mathrm{D}}}\right)^{k'} \tag{A.57}$$

However:

$$\exp(x) = \sum_{n'=0}^{\infty} \frac{x^n}{n!}$$

Therefore:

$$\boxed{\phi(t) = \exp\left(-\frac{t}{\tau_{\mathrm{D}}}\right)} \tag{A.58}$$

Appendix B

REPRINT: Molecular Dynamics Simulations for the Prediction of the Dielectric Spectra of Alcohols, Glycols and Monoethanolamine

Molecular Simulation, 2016
Vol. 42, No. 5, 370–390, http://dx.doi.org/10.1080/08927022.2015.1055741

Taylor & Francis
Taylor & Francis Group

Molecular dynamics simulations for the prediction of the dielectric spectra of alcohols, glycols and monoethanolamine

Javier Cardona[a]*, Rui Fartaria[b], Martin B. Sweatman[b] and Leo Lue[a]

[a]*Department of Chemical and Process Engineering, University of Strathclyde, James Weir Building, 75 Montrose Street, Glasgow G1 1XJ, UK;* [b]*School of Engineering, The University of Edinburgh, The King's Buildings, Sanderson Building, Mayfield Road, Edinburgh EH9 3JL, UK*

(*Received 2 February 2015; final version received 21 May 2015*)

The response of molecular systems to electromagnetic radiation in the microwave region (0.3–300 GHz) has been principally studied experimentally, using broadband dielectric spectroscopy. However, relaxation times corresponding to reorganisation of molecular dipoles due to their interaction with electromagnetic radiation at microwave frequencies are within the scope of modern molecular simulations. In this work, fluctuations of the total dipole moment of a molecular system, obtained through molecular dynamics simulations, are used to determine the dielectric spectra of water, a series of alcohols and glycols, and monoethanolamine. Although the force fields employed in this study have principally been developed to describe thermodynamic properties, most them give fairly good predictions of this dynamical property for these systems. However, the inaccuracy of some models and the long simulation times required for the accurate estimation of the static dielectric constant can sometimes be problematic. We show that the use of the experimental value for the static dielectric constant in the calculations, instead of the one predicted by the different models, yields satisfactory results for the dielectric spectra, and hence the heat absorbed from microwaves, avoiding the need for extraordinarily long simulations or re-calibration of molecular models.

Keywords: dielectric spectra; microwaves; molecular dynamics; alcohols; monoethanolamine

1. Introduction

Microwave heating arises from the coupling of charges in dielectric media to an electromagnetic field. In molecular systems, molecular dipoles reorganise in an attempt to align themselves with the oscillating electric field. However, the resulting motions are often impeded by collisions between molecules, and, consequently, the charges are not always able to keep up with the rate at which the field oscillates in the microwave region (0.3–300 GHz) and a lag is observed. This delay or relaxation in the molecular response with respect to the application of the electric field provides the origin of the conversion of electromagnetic energy into thermal energy in microwave heating. At lower frequencies, the dipoles are able to remain in phase with the electric field, and no major variation is observed in the temperature of the irradiated material. At higher frequencies, the dipoles are not fast enough to follow the rapid oscillations of the electric field.[1] In this case, absorption takes place through electronic degrees of freedom.

The dielectric properties of a material dictate its tendency to convert electromagnetic energy into thermal energy. This is reflected in the definition of the dielectric permittivity $\hat{\varepsilon}(\omega)$ as a complex frequency-dependent quantity given by

$$\hat{\varepsilon}(\omega) = \varepsilon'(\omega) + i\varepsilon''(\omega), \tag{1}$$

where $\varepsilon'(\omega)$ is the real part of the complex dielectric permittivity and represents the ability of a material to store potential energy due to polarisation by an electric field, while $\varepsilon''(\omega)$ is the imaginary part of the complex dielectric permittivity or dielectric loss, and represents its ability to transform the absorbed energy into heat.

One of the simplest models used to describe dielectric relaxation was suggested by Debye [2]. According to the Debye model, the different dipoles forming a dielectric medium interact with each other only through random collisions, captured through a relaxation time, and the resulting complex dielectric permittivity is given by

$$\hat{\varepsilon}(\omega) = \varepsilon_\infty + \frac{\varepsilon_0 - \varepsilon_\infty}{1 + i\,\omega\tau_D}, \tag{2}$$

where ε_∞ is the infinite frequency dielectric constant, ε_0 is the static or zero-frequency dielectric constant and τ_D is the dielectric relaxation time. This expression is generally valid for gases and liquids formed by small molecules. More complicated representations (e.g. Cole-Cole [3], Cole–Davidson [4], or Havriliak–Negami [5] models) are

*Corresponding author. Email: j.cardona-amengual@strath.ac.uk

typically necessary to describe the dielectric behaviour of higher molecular weight systems, such as polymers.

The study of microwave heating processes at a larger scale requires the resolution of an energy balance in which the heat absorbed by a dielectric material in a microwave field has to be considered. This term mainly depends on the dielectric properties of the material and the characteristics of the field [1]:

$$\dot{Q}_{\text{abs}} = \frac{\omega}{4\pi}\varepsilon''(\omega)|\mathbf{E}|^2 V, \tag{3}$$

where ω is the angular frequency of the electromagnetic field, $\mathbf{E}$ represents the electric field strength and V is the volume of the system.

Applications of microwave heating are rapidly growing, as its volumetric effect can lead to faster heat transfer in comparison with conventional conductive heating methods. One of the fields in which microwave heating is having a high impact is organic synthesis. Some of the most recent applications in this area have been summarised by de la Hoz and Loupy [6]. Another interesting aspect is the development of techniques based on dielectric properties to study the conformation and dynamics of molecular systems. Kremer and Schönhals [7] provide a review on recent advances in broadband dielectric spectroscopy, including applications in the analysis of the molecular dynamics (MD) of glasses, supercooled fluids and polymers.

The dielectric characteristics of pure water and aqueous solutions are, for obvious reasons, among the most studied. Using dielectric spectroscopy, it has been shown that, in liquid water, dipole rotation translates into a so called α-relaxation process which clearly exhibits simple Debye behaviour in the microwave region over a wide range of temperatures,[8–11] despite the presence of hydrogen bonding. The effect of adding different solutes on the strength of this hydrogen bonding network has also been analysed for various aqueous solutions.[12] Short alcohols start to show small deviations from the ideal Debye behaviour at high frequencies, while the deviation in larger alcohols is more significant. The hydroxyl groups in alcohols can relax freely in the gas phase, but the presence of hydrogen bonding in the liquid phase limits the rotation of these groups.[6] This is signalled by the appearance of multiple absorption regions [13–17] in the dielectric absorption spectra. A similar effect has been observed in water/ethanol mixtures, which show a distribution of relaxation times, as opposed to the single peaks observed for the pure components.[18]

Despite the relatively large literature on microwave heating and dielectric spectroscopy, the majority of the work in this area has been experimental, while there is relatively little computational work. Nevertheless, Rick, Stuart, and Berne [19] and later English and MacElroy [20,21] determined the dielectric spectrum of water via equilibrium MD simulations using the relationship between dipole moment fluctuations and the frequency-dependent dielectric constant initially developed by Neumann and Steinhauser [22,23]. Non-equilibrium MD simulations have also been performed in order to model the microwave heating of water,[24–26] and the effects of an external electromagnetic field on the conductivity of molten sodium chloride,[27] rutile TiO_2,[28] nanoconfined fluids [29] and binary dimethylimidazolium-based ionic liquid/water solutions.[30–33] In addition, recent work has been carried out on dielectric spectroscopy of more complex systems such as protein solutions.[34–36] The paucity of simulation work can probably be explained by the fact that usual relaxation times corresponding to the reorganisation of molecular dipoles due to their interaction with electromagnetic radiation at microwaves frequencies are on the order of nanoseconds, or even microseconds for larger molecules. This requires long, computationally expensive simulations in order to obtain statistically accurate results. Another cause for this scarcity in simulation work could be that most atomistic force fields for molecular simulations have been developed to reproduce thermodynamic rather than dynamic properties. Thus, it is unclear how reliably they will be able to reproduce the dynamic dielectric properties of a material.

In this work, we examine the ability of several different force fields to reproduce the dielectric spectra of relatively small molecules, such as water, alcohols, glycols and monoethanolamine (MEA). In order to do so, we perform equilibrium MD simulations for those systems, and apply the methodology developed by Neumann and Steinhauser to obtain their frequency-dependent complex permittivity. Ultimately, our aim is to apply the results of this work to the application of microwaves in regenerating spent adsorbent materials. Equations (1)–(3) indicate this requires good prediction of the dielectric spectra of the materials involved in the process, including the static dielectric constant. In particular, our interest is mainly focused on the regeneration of impregnated materials used for carbon capture within the scope of a 'Wetting Layer Absorption' process.[37,38] This process employs solid adsorbents impregnated with amine compounds to capture carbon dioxide, hence, the inclusion of MEA in this study.

The remainder of this paper is organised as follows. The following section gives the details of the potential models used to describe the different molecules and explains the methodology employed to obtain their dielectric spectra. The results of the simulations are presented and discussed in Section 3. We find that the force fields examined in this work show generally good predictions of dielectric spectra. The estimation of the static dielectric constant can sometimes be problematic though, due to the inaccuracy of some models and the long simulation times required. In this study, we obtain

satisfactory results by employing the experimental value of this parameter in our calculations, instead of the one predicted by the models. This improves the prediction of dielectric spectra while significantly reducing the simulation times required, and hence, will result in more realistic estimations of the heat a dielectric material can absorb from microwaves. Finally, in Section 4, we summarise the main findings of the work and provide directions for future studies.

2. Methodology

In this section, we present the force fields used to describe the molecular systems examined in this paper. In addition, we give details of the simulations and calculations performed, in particular, the method for calculating the dielectric spectrum.

2.1 *Molecular models and interactions*

In this work, we analyse water, a series of alcohols and glycols (i.e. ethanol, ethylene glycol, propylene glycol and glycerol) and MEA. For water, three rigid models (SPC, [39] TIP4P[40] and SPC/E [41]) and two flexible models (F-SPC [42] and Fw-SPC [43]) are examined. For the alcohols and glycols, three force fields are used: Transferable Potentials for Phase Equilibria – United Atom [44,45] (TraPPE-UA), Optimized Potentials for Liquid Simulations [46,47] (OPLS) and Generalized Amber Force Field [47,48] (GAFF). Finally, to model MEA we use the MEAa force field [49] along with the transferable OPLS and GAFF force fields. In the following, we summarise the main characteristics of the different force fields. The parameters used in our simulations are mainly taken from the original papers for each force field, and their values can be found in the appendix.

2.1.1 *Non-bonded interactions*

Non-bonded interactions between atoms are represented as the sum of a Lennard-Jones (LJ) 12–6 pair potential and an electrostatic interaction:

$$U_{\mathrm{nb}}(r_{ij}) = 4\varepsilon_{ij}\left[\left(\frac{\sigma_{ij}}{r_{ij}}\right)^{12} - \left(\frac{\sigma_{ij}}{r_{ij}}\right)^{6}\right] + \frac{q_i q_j}{4\pi\varepsilon_{\mathrm{vac}} r_{ij}}, \quad (4)$$

where r_{ij} is the distance between the atoms i and j, ε_{ij} is the depth of the potential well and σ_{ij} is the distance at which the LJ potential is zero. In the second term, q_i and q_j are the charges of atoms i and j, respectively, and $\varepsilon_{\mathrm{vac}} = 8.85418782 \times 10^{-12}\,\mathrm{F\,m^{-1}}$ is the vacuum permittivity. Non-bonded interactions apply to all intermolecular interactions, but, for intramolecular interactions, they only apply to atoms separated by three or more bonds. This varies, depending on the model, as discussed below.

The Lorentz–Berthelot combination rules are used in the TraPPE-UA, GAFF and MEAa force fields to calculate the interatomic parameters ε_{ij} and σ_{ij} from the atomic parameters ε_i and σ_i:

$$\sigma_{ij} = \frac{1}{2}(\sigma_i + \sigma_j) \quad \varepsilon_{ij} = (\varepsilon_i \varepsilon_j)^{1/2}. \quad (5)$$

Alternatively, the OPLS force field employs a geometric average:

$$\sigma_{ij} = (\sigma_i \sigma_j)^{1/2} \quad \varepsilon_{ij} = (\varepsilon_j \varepsilon_j)^{1/2}. \quad (6)$$

2.1.2 *Bonded interactions*

Bond stretching interactions between atoms separated by one bond are modelled by means of a harmonic potential:

$$U_{\mathrm{b}}(r_{ij}) = \frac{1}{2}k_b(r_{ij} - b_{\mathrm{o}})^2, \quad (7)$$

where k_b is the spring constant bond, and b_0 is the equilibrium bond length. This applies only to bonds in the F-SPC and Fw-PSC water models, and the MEAa force field, because the remaining molecular models use rigid bonds with a fixed bond length b_0.

Similarly to the bond stretching potential, bending of the angle between two adjacent bonds can be represented using a harmonic potential:

$$U_{\mathrm{a}}(\theta) = \frac{1}{2}k_\theta(\theta - \theta_0)^2, \quad (8)$$

where k_θ is the spring constant for bond angle bending, and θ_0 is the equilibrium bond angle.

The last of the bonded interactions considered in most of the models is the internal molecular torsion. In the force fields employed in this work, the potential related to the dihedral angle between four consecutive atoms in a molecule is described either by a Ryckaert–Bellemans or a Fourier function:

Ryckaert–Bellemans dihedral:

$$U_{\mathrm{d}}(\phi) = \sum_{n=0}^{3} c_n \cos^n(\phi - 180^\circ), \quad (9)$$

where ϕ is the dihedral angle (zero-cis convention), and c_n are the different constants defining the model.

Fourier dihedral:

$$U_{\mathrm{d}}(\phi) = \frac{1}{2}[C_1(1 + \cos(\phi)) + C_2(1 - \cos(2\phi)) + C_3(1 + \cos(3\phi))], \quad (10)$$

where ϕ is the dihedral angle (zero-cis convention), and C_n are the different constants defining the model.

2.1.3 *Particularities of the molecular models*

We analyse the performance of five of the most common water models: the simple point charge (SPC) model,[39] the TIP4P model,[40] the SPC/E model,[41] the Flexible SPC (F-SPC) model [42] and the Fw-SPC model [43] (see Figure 1). More details on the models can be found in the appendix. The rationale behind the selection of these particular water models was not that of performing an exhaustive study on the dielectric properties of water, which have already been analysed extensively. We rather want to compare our results with previous simulation work [20,21] in order to validate our methods and extend those to additional systems.

For the remaining molecules, more generalised force fields are used. The TraPPE force field is parameterised to describe phase equilibrium and structural properties of a wide range of compounds. Its United Atom version (TraPPE-UA) [44,45] is used to model ethanol, ethylene glycol and propylene glycol. While the first two molecules have been tested by the original authors, there is no evidence of previous work carried out with propylene glycol. Therefore, based on TraPPE parameters, we decided to build our own TraPPE-UA model for propylene glycol. Glycols require a repulsive potential of the form:

$$U_{\text{rep}}(r_{ij}) = \frac{a}{r_{ij}^{12}}, \tag{11}$$

between hydroxyl hydrogens and oxygens situated four bonds away, where $a = 6.2 \times 10^{-7}$ kJ mol^{-1} nm^{12}. This is needed to avoid the hydrogen atom, not originally protected by a LJ potential, overlapping the oxygen atom which has an opposite charge and will tend to attract it. Both OPLS [46,47] and GAFF [47,48] force fields are all-atom models which consider alkyl hydrogens explicitly. In this work, they have been used to model every studied compound (except water), although model parameters for ethylene and propylene glycols could not be found in the literature and so their topologies are built based on similar molecules (ethanol and glycerol). Finally the MEAa [49] force field is again an all-atom model. It is mainly based on GAFF's MEA model but some corrections were introduced in the charge distribution, the bond flexibility

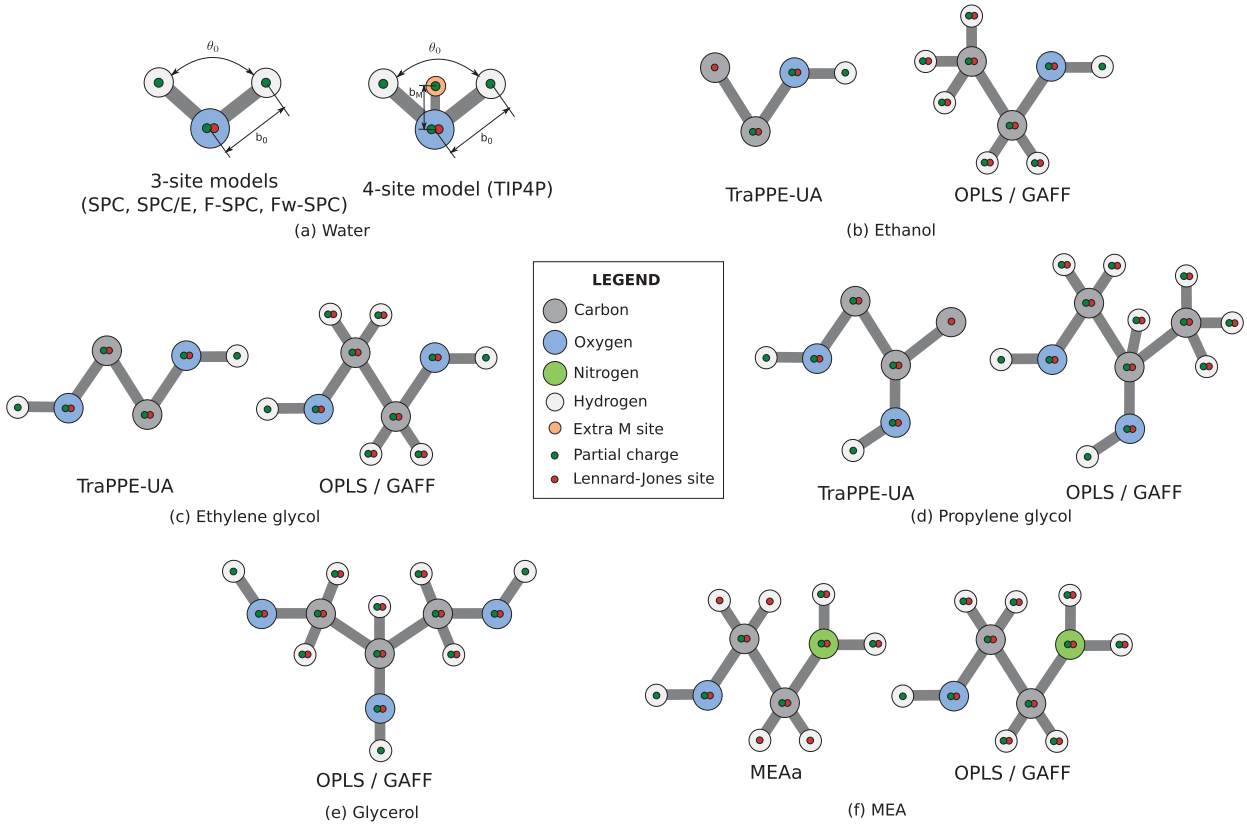

Figure 1. (Colour online) Molecular models used in this study. Carbon, oxygen, nitrogen and hydrogen atoms are represented as grey, blue, green and white circles, respectively. The extra site in the TIP4P water model is shown as a light orange circle. Partial charges appear as dark green dots while LJ interaction sites are represented as red dots.

and the O-C-C-N, C-C-O-H and C-C-N-H dihedrals, in order to improve the prediction of intramolecular interactions, which are believed to have an important effect on the properties of MEA in the liquid phase.

The 1–4 non-bonded interactions are treated differently by the various force fields. The TraPPE-UA model generally excludes these interactions, but in the particular case of ethylene and propylene glycol, Coulombic interactions between atoms separated by three bonds are included, although scaled by a factor of 0.5. OPLS, GAFF and MEAa force fields include both LJ and Coulombic 1–4 interactions with different scaling factors. The OPLS model only considers half of the magnitude of these interactions. The same strategy is used by the GAFF force field regarding LJ interactions; however, Coulombic interactions are scaled by a factor of 5/6 in this case. Finally MEAa fully considers all 1–4 non-bonded interactions.

Figure 1 shows the distribution of charges and LJ interaction sites for the models under consideration. As mentioned previously, the parameters defining the different molecular interactions used in our simulations can be found in the appendix.

2.2 Simulation details

MD simulations are carried out using the GROMACS 4.6.3 [50] package to study the performance of the different force fields in the prediction of dielectric spectra. All the systems consist of simulation boxes containing 1000 molecules and are simulated for 25–100 ns, depending on the time required to obtain a converged value for the static dielectric constant. Starting from independent and equilibrated configurations, four simulations are carried out for every molecular system, and the results are averaged across those four samples. The equations of motion are integrated by means of the leap-frog algorithm [51] with a time step of 1 fs for rigid (SPC, TIP4P and SPC/E) and semi-flexible models (TraPPE-UA, OPLS and GAFF), and 0.2 fs for flexible force fields (F-SPC, Fw-SPC and MEAa). The trajectory of the molecules is read every 100 fs while the energy configuration is recorded every 50 fs. The simulations are performed in the NPT ensemble at 298 K and 1 bar, except for MEA for which a temperature of 293 K is used due to the larger availability of experimental data at that temperature. The Nosé–Hoover thermostat,[52,53] with a time constant of 0.1 ps, is used for temperature coupling while the pressure is controlled by means of a Parrinello–Rahman barostat [54,55] with a compressibility of 4.5×10^{-5} bar^{-1} and a time constant of 1.0 ps. The LINCS algorithm [56] is responsible for constraining the bond length when necessary. A cut-off radius of 0.85 nm is used for the LJ interactions in all the systems, except when the TraPPE-UA or the MEAa force fields are used; for those models, the LJ interaction is truncated at 1.40 nm and 1.00 nm, respectively. Long-range electrostatics are treated with the particle mesh Ewald (PME) method [57] with a truncation at the same distance as the LJ one, and a spacing for the PME grid of 0.12 nm. Analytical tail corrections in potential energy are used to compensate for the truncation in LJ interactions. Finally, cubic and conducting periodic boundary conditions are used in every case.

2.3 Determination of the frequency-dependent dielectric constant

The total dipole moment $\mathbf{M}$ of a polar system corresponds to the sum of the individual dipole moments $\boldsymbol{\mu}_i$ of each of the molecules in the system (i.e. $\mathbf{M} = \sum_i^N \boldsymbol{\mu}_i$). A time series of this quantity can be determined by MD simulation. The fluctuations of the dipole moment can be directly related to the frequency-dependent dielectric response [22]:

$$\frac{\hat{\varepsilon}(\omega) - \varepsilon_\infty}{\varepsilon_0 - \varepsilon_\infty} = 1 + i\omega\hat{\phi}(\omega), \tag{12}$$

where $\hat{\phi}(\omega)$ is the Fourier transform of the total dipole moment autocorrelation function $\phi(t)$, which is given by

$$\phi(t) = \frac{\langle \mathbf{M}(t) \cdot \mathbf{M}(0) \rangle}{\langle \mathbf{M}(0) \cdot \mathbf{M}(0) \rangle}. \tag{13}$$

As defined previously, ε_∞ is the infinite frequency relative permittivity (1 for non-polarisable potential models), and ε_0 is the zero-frequency or static dielectric constant.

To determine the frequency-dependent dielectric constant from Equation (12), it is necessary to obtain the Fourier transform of the dipole moment autocorrelation function $\phi(t)$. In order to obtain this from a finite duration MD simulation, $\phi(t)$ is represented as the sum of a short time contribution $y_{\text{cub}}(t)$ and a long-term exponential decay $y_{\text{exp}}(t)$ (i.e. $\phi(t) = y_{\text{cub}}(t) + y_{\text{exp}}(t)$). The short-time oscillatory portion of the autocorrelation function is fitted with a cubic spline through the initial range of discretely sampled points, and its Fourier transform is obtained analytically.[19,20] For long times, the dipole moment autocorrelation function is fitted to an exponential decay:

$$y_{\text{exp}}(t) = Ae^{-t/\tau_D} \tag{14}$$

in-line with the Debye model, where τ_D is the relaxation time of the exponential decay. The exponential fit was only performed in the region where such a trend was clearly observed, and the same criterion was used for all the systems. This varies for the different models as they show different behaviour. However, we used the same fitting window for the four different runs corresponding to the same model.

3. Results and discussion

3.1 Thermodynamic properties

Table 1 summarises several thermodynamic properties for the systems we study, as determined [47,58] from the MD simulations.

Although thermodynamic properties are not the main focus of this work, we provide these results as a benchmark for the validity of our simulations. The standard errors for the different properties are obtained by averaging across the values obtained for each of the four independent simulations for every system. Most of the force fields used in this study are developed for the prediction of thermodynamic properties. Therefore, as expected, the results are generally in good agreement with experimental data. These are also consistent with previous simulation work by Caleman and coworkers [47], where the over-prediction of the heat capacities is also observed and thought to be due to the neglect of quantum corrections in the calculation of enthalpy fluctuations.

3.2 Dielectric and dynamic properties

3.2.1 Summary of dielectric and dynamic properties

Table 2 summarises the results obtained for the dielectric properties of the compounds, along with additional dynamic properties. The self-diffusion coefficient D is derived from the mean squared displacement of the positions of the atoms. The value of molecular dipole moment $\boldsymbol{\mu}$ presented in Table 2 results from averaging this variable over all the molecules in the system and over the entire trajectory. This property fluctuates due to the flexible nature of most of the molecular models under consideration. Within condensed phases, in addition to flexibility, polarisation effects have a significant effect on the molecular dipole moment, as compared to the gas

Table 1. Summary of thermodynamic properties.

	ρ (kg/m^3)	$10^3\ \alpha_P$ (K^{-1})	κ_T (GPa^{-1})	c_P (J mol^{-1} K^{-1})	ΔH_{vap} (kJ mol^{-1})
Water					
SPC	978.93 ± 0.02	0.733 ± 0.002	0.529 ± 0.002	83.6 ± 0.1	44.168 ± 0.001
TIP4P	998.88 ± 0.04	0.552 ± 0.003	0.512 ± 0.001	87.9 ± 0.1	43.920 ± 0.001
SPC/E	1000.14 ± 0.03	0.506 ± 0.004	0.459 ± 0.001	87.1 ± 0.2	49.239 ± 0.001
F-SPC	995.01 ± 0.02	0.528 ± 0.006	0.457 ± 0.001	112.0 ± 0.2	51.710 ± 0.001
Fw-SPC	1009.70 ± 0.04	0.459 ± 0.006	0.431 ± 0.002	114.1 ± 0.4	46.252 ± 0.002
Experiment	997.1 [59]	0.256 [60]	0.4525 [61]	75.29 [62]	43.87 [63]
Ethanol					
TraPPE-UA	782.4 ± 0.2	1.149 ± 0.006	1.263 ± 0.006	114.4 ± 0.4	46.891 ± 0.004
OPLS	793.21 ± 0.06	1.419 ± 0.004	1.002 ± 0.005	219.0 ± 0.4	45.455 ± 0.003
GAFF	794.16 ± 0.05	1.272 ± 0.005	0.976 ± 0.007	211.7 ± 0.4	47.514 ± 0.003
Experiment	784.8 [64]	1.09 [64]	1.15 [64]	112 [64]	42.32 [64]
Ethylene glycol					
TraPPE-UA	1129.78 ± 0.05	0.62 ± 0.02	0.411 ± 0.002	199 ± 3	80.862 ± 0.007
OPLS	1075.77 ± 0.05	0.80 ± 0.02	0.386 ± 0.003	261 ± 2	69.664 ± 0.005
GAFF	1176.52 ± 0.07	0.709 ± 0.008	0.241 ± 0.002	263.8 ± 0.3	83.911 ± 0.008
Experiment	1113.1 [65]	0.631 [66]	0.3686 [67][a]	148.3425 ± 1.48467 [68]	65.99 ± 0.25 [69]
Propylene glycol					
TraPPE-UA	1042.0 ± 0.2	0.70 ± 0.02	0.591 ± 0.003	238 ± 5	78.85 ± 0.03
OPLS	1097.5 ± 0.2	0.98 ± 0.04	0.390 ± 0.007	334 ± 4	84.69 ± 0.02
GAFF	1120.06 ± 0.04	0.92 ± 0.03	0.307 ± 0.005	344 ± 4	82.318 ± 0.009
Experiment	1032.79 [70]	0.714 [71][b]	–	190.54 ± 3.81 [72]	64.47 ± 0.18 [69]
Glycerol					
OPLS	1251.7 ± 0.2	0.80 ± 0.02	0.273 ± 0.004	361 ± 4	97.57 ± 0.03
GAFF	1302.9 ± 0.4	0.49 ± 0.02	0.166 ± 0.006	332 ± 8	102.57 ± 0.07
Experiment	1257.98 [73]	0.46 [74][c]	0.24 [47][c]	218.90 ± 0.2 [75]	91.7 ± 0.9 [75]
MEA					
MEAa	1053.56 ± 0.02	1.01 ± 0.02	0.356 ± 0.002	376 ± 2	54.140 ± 0.004
OPLS	1024.12 ± 0.06	1.061 ± 0.006	0.457 ± 0.002	280.9 ± 0.6	59.222 ± 0.002
GAFF	1130.6 ± 0.1	0.75 ± 0.02	0.234 ± 0.003	289 ± 3	85.765 ± 0.008
Experiment	1018.0 [76]	0.801 ± 0.016 [77]	0.378 ± 0.038 [77]	144 [78]	64.03 [79]

Note: ρ, density; α_P, thermal expansion coefficient; κ_T, isothermal compressibility; c_P, constant pressure heat capacity; ΔH_{vap}, heat of vaporisation. Simulations are run at 298 K and 1 bar, except for the case of MEA for which the temperature is 293 K.

[a] at 320 K.

[b] at 0.8 bar.

[c] at 293.15 K.

Table 2. Summary of dynamic properties.

	10^9 D (m^2/s)	$\boldsymbol{\mu}$ (D)	ε_0	τ_D (ps)
Water				
SPC	3.96 ± 0.04	2.2740	66.6 ± 0.4	6.7 ± 0.2
TIP4P	3.65 ± 0.04	2.1775	44.5 ± 0.3	5.8 ± 0.2
SPC/E	2.50 ± 0.05	2.3506	70.6 ± 0.6	10.8 ± 0.2
F-SPC	2.64 ± 0.02	2.4580 ± 0.0001	94 ± 1	13.4 ± 0.4
Fw-SPC	2.12 ± 0.03	2.3949 ± 0.0001	80.2 ± 0.8	13.7 ± 0.2
Experiment	2.2999 ± 0.2300 [81]	2.9 ± 0.6 [82]	78.54 [83]	8.22*
Ethanol				
TraPPE-UA	1.15 ± 0.01	2.2625 ± 0.0001	18.1 ± 0.5	136 ± 6
OPLS	1.26 ± 0.03	2.3746 ± 0.0001	17.9 ± 0.3	53 ± 3
GAFF	1.04 ± 0.04	2.1234 ± 0.0002	15.6 ± 0.4	87 ± 3
Experiment	1.07 ± 0.11 [84]	3.43 [85]	25 [76]	187*
Ethylene glycol				
TraPPE-UA	0.0177 ± 0.0009	3.43 ± 0.02	36 ± 2	1000 ± 90
OPLS	0.141 ± 0.003	2.482 ± 0.005	20.3 ± 0.2	58 ± 2
GAFF	0.0146 ± 0.0008	3.209 ± 0.007	35.6 ± 0.5	430 ± 20
Experiment	–	4.02 [85]	40.86 [86]	123*
Propylene glycol				
TraPPE-UA	0.0212 ± 0.0006	3.28 ± 0.02	22.8 ± 0.9	1360 ± 70
OPLS	0.0135 ± 0.0009	4.04 ± 0.02	46 ± 3	2500 ± 300
GAFF	0.0129 ± 0.0005	3.13 ± 0.02	25.1 ± 0.6	600 ± 40
Experiment	0.0051 [87]	3.60 [88]	28.373 ± 0.004 [89]	342*
Glycerol				
OPLS	0.0030 ± 0.0003	4.453 ± 0.003	33 ± 3	2800 ± 300
GAFF	0.00068 ± 0.00003	3.45 ± 0.03	28 ± 5	9200 ± 900
Experiment	0.014 ± 0.004 [90]	4.21 [85]	42.54 [91]	933*
MEA				
MEAa	0.181 ± 0.003	1.994 ± 0.004	10.5 ± 0.2	37.0 ± 0.6
OPLS	0.226 ± 0.004	3.462 ± 0.008	50.7 ± 0.9	87 ± 3
GAFF	0.0048 ± 0.0002	3.002 ± 0.004	40.9 ± 0.9	1320 ± 40
Experiment	0.054 ± 0.003 [92]	2.60 [88]	34.20 [93]	162*

Note: D, self-diffusion coefficient; μ, mean molecular dipole moment; ε_0, static dielectric constant; τ_D, relaxation time. Simulations are run at 298 K and 1 bar, except for the case of MEA for which the temperature is set to 293 K. *Experimental relaxation times τ_D are obtained fitting the experimental data in Figure 4 to the Debye model.

phase.[80] However, polarisable force fields would be required if one wanted to obtain more accurate values of the liquid phase dipole moment. The relaxation time τ_D is obtained from an exponential fit of the long-time behaviour of the dipole moment autocorrelation function, as explained in Section 2.3.

The first conclusion one can deduce from the results is that the prediction of dynamic and dielectric properties is generally not as good as that observed for the thermodynamic properties. This is expected, as the force fields used in this work were developed with the aim of reproducing the latter, and no dynamic properties were involved in their calibration.

3.2.2 *Dynamic response: the dipole moment autocorrelation function*

The dynamics of a molecular system can be analysed in terms of its dipole moment autocorrelation function. The relaxation times corresponding to the rotational and translational modes of a molecule or group of atoms within a larger molecule can be determined from the analysis of the time evolution of the dipole moment. The influence of an external electric field on these processes is believed to be the basis for the microwave heating mechanism. Figure 2 shows the Fourier transform of the dipole moment autocorrelation function $\hat{\phi}(\omega)$ for the different water models under consideration. The experimental data shown in this figure have been obtained using Equation (12) to calculate the real and imaginary parts of $\hat{\phi}(\omega)$ from the experimental dielectric spectrum of water, shown later in Figure 4. In the case of water, it is clear that the flexible models and the SPC/E model overestimate both $\hat{\phi}'(\omega)$ and $\hat{\phi}''(\omega)$ in the microwave region, while SPC and TIP4P models under-predict the response. At higher frequencies, the characteristics of the different models seem to have less influence on the frequency dependence of the dynamic response. The rigid models clearly outperform the flexible ones, with the SPC model showing the best performance. According to the Debye model, the real and imaginary parts of the Fourier transform of the dipole moment autocorrelation function

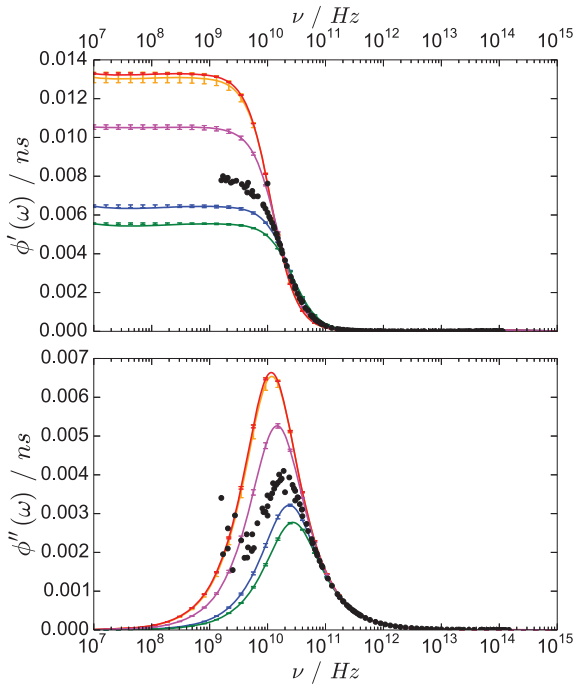

Figure 2. (Colour online) Dynamics of water at 298 K and 1 bar through the Fourier transform of the dipole moment autocorrelation function. Blue, green, magenta, orange and red lines show the results corresponding to the SPC, TIP4P, SPC/E, F-SPC and Fw-SPC models, respectively. Black circles represent experimental values obtained from Equation (12) using dielectric spectrum data from different sources.[9–12]

are given by

$$\begin{aligned} \hat{\phi}'(\omega) &= \frac{\tau_D}{1+\omega^2\tau_D^2} \\ \hat{\phi}''(\omega) &= \frac{\omega\tau_D^2}{1+\omega^2\tau_D^2} \end{aligned} . \qquad (15)$$

This shows how the frequency response of a molecular system is purely dependent on the relaxation time τ_D in the range of frequencies in which the Debye model is applicable. Figure 2 and the values of τ_D in Table 2 confirm the trends predicted by Equation (15) in the case of water, which is a system known to be described accurately by the Debye model. The results for the remaining compounds are shown in the appendix. Analysing the different systems with respect to their frequency response, TraPPE-UA and GAFF force fields seem to provide slower dynamics than OPLS. This tendency is only reversed for propylene glycol. In the case of MEA, the MEAa force field predicts even faster dynamics than OPLS. This is mainly manifested by the positions of low frequency phenomena such as the decay in $\hat{\phi}'(\omega)$ and the corresponding peak in $\hat{\phi}''(\omega)$.

Once the dynamic response of the different systems has been obtained through the dipole moment autocorrelation function, the dielectric response is achieved through Equation (12). To obtain an accurate description of dielectric spectra it becomes essential to have a good estimate of the static dielectric constant ε_0. The importance of the selection of this parameter is discussed in the following sections.

3.2.3 *The static dielectric constant*

The static dielectric constant is calculated using Neumann's formula [22,58] that relates the static dielectric constant to the fluctuations of the total dipole moment of the system:

$$\varepsilon_0 = \varepsilon_\infty + \frac{4\pi}{3k_BTV}\left(\langle \mathbf{M}\cdot\mathbf{M}\rangle - \langle \mathbf{M}\rangle\cdot\langle \mathbf{M}\rangle\right), \qquad (16)$$

where $k_B = 1.3806503\times10^{-23}\,\mathrm{m^2\,kg\,s^{-2}\,K^{-1}}$ is the Boltzmann constant, T is the temperature and V is the volume of the system.

The prediction of the static dielectric constant is poor in most cases (see Table 2), as none of the force fields examined here gives predictions that statistically agree with the experimental values. In the case of water, it would appear flexibility provides an improvement in the prediction of ε_0, particularly in the case of the Fw-SPC model, but this is at the cost of affecting the response at intermediate frequencies, as shown in Section 3.2.2.

The long correlation times in the fluctuations of total dipole moment make the calculation of the static dielectric constant difficult. Previous work has shown the importance of selecting the appropriate block length for the correct calculation of this property of water [94,95]. This is confirmed by the results shown in Figure 3 for the compounds studied in this work. To ensure the convergence of the static dielectric constant, the simulations are extended until the term containing the square of the average dipole moment ($\langle \mathbf{M}\rangle\cdot\langle \mathbf{M}\rangle$) in Equation (16) converges to zero, with a maximum simulation length of 100 ns. In this manner, we obtain converged values of the static dielectric constant for most models. However, this is clearly not valid in the case of glycerol for which longer simulations would be required to obtain the final value predicted by the models. Even ruling out the effect of the simulation length, most potential models do not seem to reach an acceptable agreement with the expected experimental value. It has been reported previously that this property is not well predicted by non-polarisable force fields, such as the ones used in this work.[47]

The consequence of this, through Equation (12) and as shown in the next section, is that the loss factor is also poorly estimated, which in turn would lead to inaccurate estimates of dielectric heating rates. Therefore, due to the

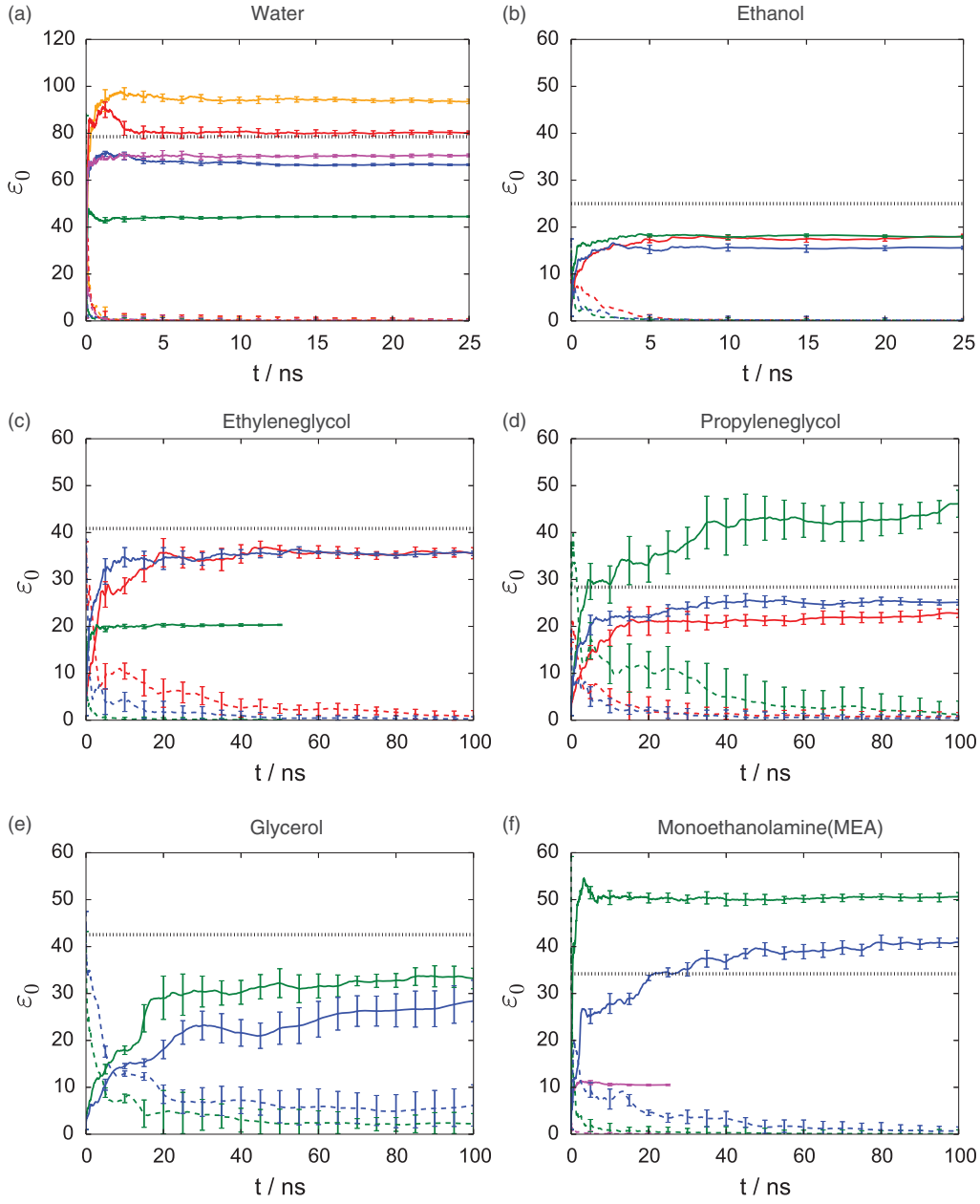

Figure 3. (Colour online) Effect of the block length on the static dielectric constant. The results show running averages started from an energetically equilibrated sample. They are obtained via MD simulations at 298 K and 1 bar, using Neumann's formula (Equation 16). For MEA, the simulations are performed at 293 K. Solid lines represent the results obtained using the different force fields introduced in the text. Dashed lines correspond to the term containing the square of the average dipole moment ($\mathbf{M} \cdot \mathbf{M}$) in Equation (16), which should vanish at long times to consider the static dielectric constant converged. In the particular case of water, blue, green, magenta, orange and red lines show the results corresponding to the SPC, TIP4P, SPC/E, F-SPC and Fw-SPC models, respectively. For the remainder substances, red, green, blue and magenta lines represent results generated using the TraPPE-UA, OPLS, GAFF and MEAa force fields, respectively. Dotted horizontal lines represent experimental values obtained from different sources: water,[83] ethanol,[76] ethylene glycol,[86] propylene glycol,[89] glycerol [91] and MEA.[93]

uncertainty in the prediction of the static dielectric constant, in Section 3.3 it is decided to use the corresponding experimental value in the determination of the dielectric spectra of the different systems under consideration. The effect of this choice on the shape of the dielectric spectra is also discussed in that section.

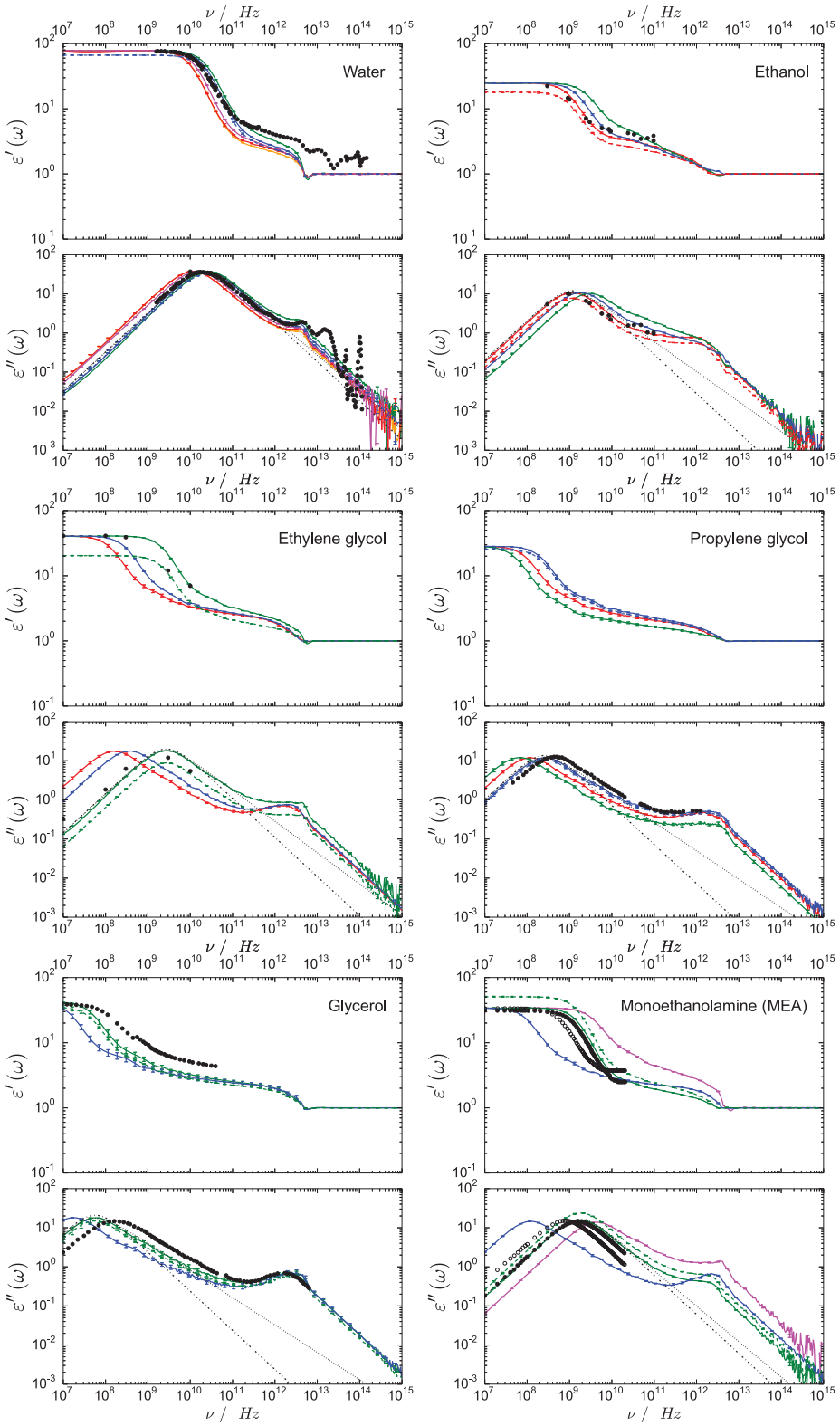

Figure 4. (Colour online) Dielectric response of several organic compounds obtained via MD simulations at 298 K and 1 bar. For MEA, the simulations are performed at 293 K. Solid lines represent the results obtained in our simulations using the different force fields introduced in the text, and employing the experimental static dielectric constant in the calculations. In the particular case of water, blue, green, magenta, orange and red lines show the results corresponding to the SPC, TIP4P, SPC/E, F-SPC and Fw-SPC models, respectively.

3.3 Dielectric spectra

3.3.1 Effect of the static dielectric constant on the dielectric spectrum

Figure 4 summarises the results obtained in the prediction of the dielectric spectra of several organic compounds, applying the methodology explained in Section 2.3. For the different molecules under consideration, dashed lines represent the best dielectric spectra predictions obtained using Equation (12), when the static dielectric constant ε_0 is calculated from simulation data, using Neumann's approach (Equation (16)). In most cases, the low-frequency end of the real part of the dielectric spectrum and the magnitude of the main absorption peak in the dielectric loss do not match the experimental result. Slight differences can be observed in the cases of water, propylene glycol and glycerol, while the results are clearly underestimated for ethanol and ethylene glycol, and over-predicted for MEA. This is related to the value of the static dielectric constant estimated by the different models (see Table 2). This variable acts as a scaling factor for the magnitude of both real and imaginary parts of the dielectric response. However, the dynamics (i.e. the frequency dependence of $\varepsilon'(\omega)$ and $\varepsilon''(\omega)$) are not clearly affected by this fact and follow the experimental trend.

By using the experimental value of the static dielectric constant in Equation (12), instead of the one obtained from the simulations, the dielectric spectra predictions are clearly improved (solid lines in Figure 4). In general, a fairly good agreement with experimental data is reached, with at least one of the models providing an acceptable result. This demonstrates the importance of using a good value for the static dielectric constant. Even though the models may not reproduce the static dielectric constant, they do appear to correctly describe the dipole–dipole autocorrelation function $\phi(t)$. By simply introducing the experimental static dielectric constant in Equation (12), one can obtain good results in the prediction of dielectric spectra. This is clearly the case for the models showing a better performance in the estimation of the dielectric spectra of ethanol (TraPPE-UA), ethylene glycol (OPLS) and MEA (OPLS), as shown in Figure 4. In the cases of propylene glycol (GAFF) and glycerol (OPLS), the improvement is also visible, although not so significant. Finally, the performance of the rigid SPC and TIP4P water models is significantly improved with respect to results obtained by English et al. [20,21]. Therefore, one should not use the static dielectric constant as the only judge of the quality of a molecular model.

Although we recognise the theoretical inconsistency of substituting the calculated ε_0 by the experimental one, we consider this is a useful and practical method to estimate $\varepsilon'(\omega)$ and $\varepsilon''(\omega)$. It avoids the need for extraordinarily long simulations or highly accurate models to determine the static dielectric constant. This becomes particularly important when a good knowledge of the magnitude of the dielectric response is required for the prediction of the heat a molecular system can absorb from a microwave field (see Equation (3)). It seems unlikely that classical force fields of the type used here will ever be satisfactory for production of a wide range of thermodynamic and dynamical phenomena simultaneously, and so methods that can correct for their weaknesses are desirable. In this case, we have shown that prediction of dielectric heating can be systematically improved if the experimental static dielectric constant is known a priori.

3.3.2 Deviations from the Debye model

The main absorption peak observed in the low frequency end of the imaginary part of the dielectric spectrum (see Figure 4) is associated with dipole reorentation as a response to a time-dependent electric field.[7,96,97] It is typically known as the α-relaxation peak, and for relatively small molecules such as the ones studied here, it usually occurs in the microwave or high frequency radio wave region at ambient conditions.

As a description of this process, the Debye model (see Equation (2)) assumes that dipoles relax independently from each other with a common relaxation time. However, in most materials this somehow 'ideal' behaviour does not take place. Cole and Davidson [4] suggested an empirical expression for the complex frequency-dependent permittivity which takes into account deviations from the Debye relaxation model:

$$\hat{\varepsilon}(\omega) = \varepsilon_\infty + \frac{\varepsilon_0 - \varepsilon_\infty}{[1 + i\,\omega\tau_{CD}]^\beta}, \tag{17}$$

where τ_{CD} is the characteristic relaxation time, and β accounts for the asymmetry in the resulting dielectric

For the remaining substances, red, green, blue and magenta lines represent results generated using the TraPPE-UA, OPLS, GAFF and MEAa force fields, respectively. Dashed lines correspond to results using Neumann's formula (Equation 16) to calculate the static dielectric constant, for the force fields showing a better performance in the prediction of the dielectric spectrum in every case (water, SPC; ethanol, TraPPE-UA; ethylene glycol, OPLS; propylene glycol, GAFF; glycerol, OPLS; and MEA, OPLS). Black circles represent experimental values obtained from different sources for the following systems: water,[9–12] ethanol,[16–18,98] ethylene glycol,[99] propylene glycol and [100] glycerol.[96,97,101,102] For MEA, black open and filled circles are experimental values of the dielectric spectrum at 278 K [103] and 308 K,[104] respectively. Black dot-dash and dotted lines in $\varepsilon''(\omega)$ represent the fit of the α-relaxation peak to Debye and Cole–Davidson models, respectively.

Table 3. Cole–Davidson fit parameters.

	τ_{CD}/ps	β		τ_{CD}/ps	β
Water			Propylene glycol		
SPC	7.2 ± 0.2	0.91 ± 0.01	TraPPE-UA	1830 ± 70	0.71 ± 0.02
TIP4P	6.40 ± 0.07	0.895 ± 0.009	OPLS	3100 ± 00	0.77 ± 0.03
SPC/E	11.6 ± 0.2	0.927 ± 0.002	GAFF	810 ± 50	0.71 ± 0.02
F-SPC	14.3 ± 0.4	0.935 ± 0.006			
Fw-SPC	14.8±0.3	0.92±0.01			
Ethanol			Glycerol		
TraPPE-UA	173 ± 7	0.766 ± 0.0.05			
OPLS	75 ± 4	0.67 ± 0.01	OPLS	3700 ± 300	0.72 ± 0.03
GAFF	111 ± 4	0.759 ± 0.002	GAFF	13000 ± 1000	0.74 ± 0.04
Ethylene glycol			MEA		
TraPPE-UA	1300 ± 200	0.74 ± 0.03	MEAa	53 ± 2	0.65 ± 0.02
OPLS	71 ± 2	0.793 ± 0.008	OPLS	97 ± 3	0.891 ± 0.004
GAFF	550 ± 30	0.75 ± 0.02	GAFF	1750 ± 70	0.72 ± 0.02

spectra. In Figure 4 we include the fits of the α-relaxation peak in the imaginary part of the dielectric permittivity to both the Debye and the Cole–Davidson models, for the force fields that show the best performance in the prediction of the dielectric spectrum of each of the compounds. The former uses the values of τ_D shown in Table 2, while for the latter, the fitting parameters τ_{CD} and β are presented in Table 3. These are obtained by fitting the simulation results to the Cole–Davidson equation using the method of least squares. With the goal of making the fitting procedure more uniform, the fit is performed on the data above half height of the main absorption peak. As β approaches unity, Cole and Davidson's model reduces to the Debye model. As deduced from both Figure 4 and the value of the parameters of the Cole–Davidson model, water is the system that conforms most closely to the Debye model. The deviation of β from unity results in an asymmetric broadening of the spectrum or excess wing.[97] This means that the relaxation time predicted by this model will no longer coincide with the relaxation time corresponding to the maximum loss as estimated by the Debye model. This is clearly the case for ethanol OPLS, where τ_{CD} is definitely larger than τ_D. For other systems, the more β differs from 1, the larger is the relaxation time predicted by the Cole–Davidson model with respect to Debye relaxation time.

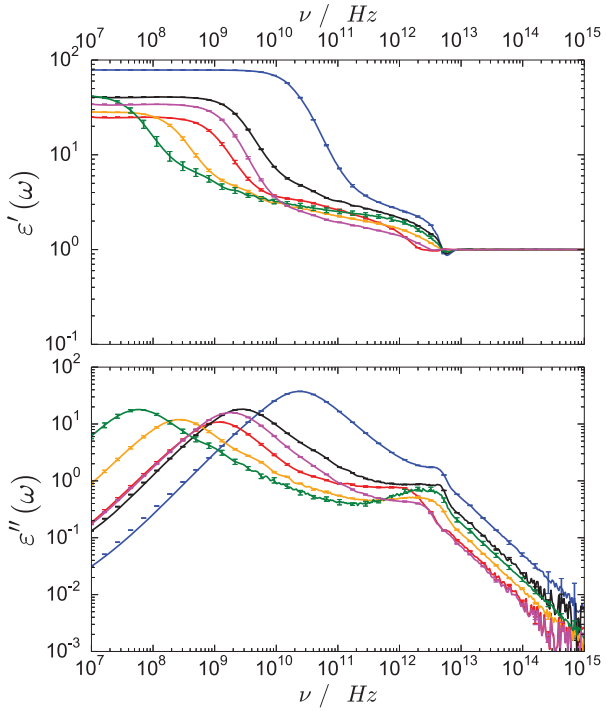

Figure 5. (Colour online) Comparison of the dielectric spectra of different organic substances. The force fields that show a better performance in the prediction of the dielectric response are used in this representation: water, SPC (blue); ethanol, TraPPE-UA (red); ethylene glycol, OPLS (black); propylene glycol, GAFF (orange); glycerol, OPLS (green); and MEA, OPLS (magenta).

3.3.3 *Effect of size and polarity*

Finally, the dielectric spectra of the different substances under consideration are compared in Figure 5, using the results provided by the best force fields in every case. This clearly shows how as the size of the molecule increases the relaxation frequency decreases (i.e. the dynamics slow down). In addition, it is possible to observe the effect of polarity on the maximum of the dielectric loss (i.e. the more polar species show a higher peak and, consequently, have the higher potential to transform electromagnetic energy into heat).

4. Conclusions

In this work, we have examined the ability of MD simulations to predict the dielectric spectra of small molecules in the microwave region. This is an essential feature if one wants to estimate the heat a dielectric material can absorb from an external microwave field. The methodology used here analyses the time fluctuations of the total dipole moment of a molecular system. All-atom and united-atom force fields, which have mainly been developed to accurately reproduce experimental thermodynamic properties, generally give good predictions for the frequency-dependent dielectric constant of a series of alcohols and glycols, as well as for MEA, so long as the correct value of the static dielectric constant is used.

Despite the good performance in describing the dynamics of the dielectric response of the systems under consideration, most of the models have difficulties in predicting the static dielectric constant, which is a crucial parameter in the scaling of dielectric spectra. The use of non-polarisable force fields in our simulations may have an influence on the molecular motion, hence affecting the static dielectric constant. Another limiting factor could be the long time scales required to achieve an accurate value of this property, which corresponds to the magnitude of total dipole moment fluctuations, especially for larger systems.

The solution adopted here is to use the experimental value of this magnitude in conjunction with the dynamics predicted by molecular simulations. This can avoid the need for extraordinarily long simulations for systems for which the static dielectric constant is a well-known property or can be easily measured experimentally.

With these considerations in mind, the models evaluated in this work are able to capture the main experimental features. The simulated dielectric spectra of all the systems we analyse exhibit an α-relaxation peak, characteristic of these types of substances. In addition, while water possesses a Debye-like relaxation, alcohols, glycols and MEA show signs of an excess wing in the high-frequency end of the α-relaxation peak, which has been described in the literature.[97]

Currently, due to limitations in computational hardware, all-atom MD simulations cannot describe interesting features in the dielectric relaxation of a material that occur on times scales greater than or on the order of μs. However, the ability of these simulations to reproduce the characteristics of the dielectric spectra at higher frequencies, as demonstrated here, gives confidence on the possibility of using the force fields studied in this work for the prediction of dielectric spectra of compounds for which experimental data are not available. Together with other recent work in this field, this study opens the possibility to use MD simulations as a powerful tool in areas such as the study of glass-forming materials, the analysis of polymer dynamics or the examination of the dielectric behaviour of mixtures.

Acknowledgements

The authors gratefully acknowledge the support of the Department of Chemical and Process Engineering at the University of Strathclyde and the School of Engineering at the University of Edinburgh, as well as the Engineering and Physical Sciences Research Council (EPSRC).

Disclosure statement

No potential conflict of interest was reported by the authors.

Funding

Results were obtained using the EPSRC funded ARCHIE-WeSt High Performance Computer (www.archie-west.ac.uk) [grant number EP/K000586/1].

References

[1] Cherbański R, Molga E. Intensification of desorption processes by use of microwaves – an overview of possible applications and industrial perspectives. Chem Eng Process: Process Intensification. 2009;48:48–58. doi:10.1016/j.cep.2008.01.004.
[2] Holtzer AM. The collected papers of Peter J. W. Debye. Interscience, New York-London, 1954. Xxi + 700 pp., $9.50. J Polym Sci. 1954;13:548–548. doi:10.1002/pol.1954.120137203.
[3] Cole KS, Cole RH. Dispersion and absorption in dielectrics I. Alternating current characteristics. J Chem Phys. 1941;9:341–351. doi:10.1063/1.1750906.
[4] Davidson DW, Cole RH. Dielectric relaxation in glycerine. J Chem Phys. 1950;18:1417–1417. doi:10.1063/1.1747496.
[5] Havriliak S, Negami S. A complex plane representation of dielectric and mechanical relaxation processes in some polymers. Polymer. 1967;8:161–210. doi:10.1016/0032-3861(67)90021-3.
[6] de la Hoz A, Loupy A, editors. Microwave in organic synthesis. 3rd ed. Hobboken, NJ: Wiley-VCH, 2012.
[7] Kremer F, Schonhals A, editors. Broadband dielectric spectroscopy. Berlin: Springer, 2002.
[8] Ellison WJ. Permittivity of pure water, at standard atmospheric pressure, over the frequency range 0–25. THZ and the temperature range 0–100 °C. J Phys Chem Ref Data. 2007;36:1–18. doi:10.1063/1.2360986.
[9] Kaatze U, Uhlendorf V. The Dielectric Properties of Water at Microwave Frequencies. Z Phys Chem Neue Fol. 1981;126:151–165. doi:10.1524/zpch.1981.126.2.151.
[10] Kaatze U. Complex permittivity of water as a function of frequency and temperature. J Chem Eng Data. 1989;34:371–374. doi:10.1021/je00058a001.
[11] Barthel J, Bachhuber K, Buchner R, Hetzenauer H. Dielectric spectra of some common solvents in the microwave region. Water and lower alcohols. Chem Phys Lett. 1990;165:369–373. doi:10.1016/0009-2614(90)87204-5.
[12] Hasted JB, El Sabeh SHM. The dielectric properties of water in solutions. Faraday Soc. 1953;49:1003–1011. doi:10.1039/tf9534901003.
[13] Davidson DW, Cole RH. Dielectric relaxation in glycerol, propylene glycol, and n-propanol. J Chem Phys. 1951;19:1484–1490. doi:10.1063/1.1748105.
[14] Cole RH, Davidson DW. High frequency dispersion in n-propanol. J Chem Phys. 1952;20:1389–1391. doi:10.1063/1.1700767.
[15] Poley J. Microwave dispersion of some polar liquids, Technische Hogeschool te Delft. 1955.

[16] Rampolla RW, Miller RC, Smyth CP. Microwave absorption and molecular structure in liquids. XXV. Measurements of dielectric constant and loss at 3.1-mm wavelength by an interferometric method. J Chem Phys. 1959;30:566–573. doi:10.1063/1.1729988.

[17] Saxton JA, Bond RA, Coats GT, Dickinson RM. Dispersion at millimeter wavelengths in methyl and ethyl alcohols. J Chem Phys. 1962;37:2132–2138. doi:10.1063/1.1733434.

[18] Buck DE. The dielectric spectra of ethanol-water mixtures in the microwave region. Cambridge, MA: Massachusetts Institute of Technology; 1965.

[19] Rick SW, Stuart SJ, Berne BJ. Dynamical fluctuating charge force fields: Application to liquid water. J Chem Phys. 1994;101:6141–6156. doi:10.1063/1.468398.

[20] English NJ, MacElroy JMD. Atomistic simulations of liquid water using Lekner electrostatics. Mol Phys. 2002;100:3753–3769. doi:10.1080/0026897021000028438.

[21] English NJ. Molecular dynamics simulations of liquid water using various long-range electrostatics techniques. Mol Phys. 2005;103:1945–1960. doi:10.1080/00268970500105003.

[22] Neumann M, Steinhauser O. On the calculation of the frequency-dependent dielectric constant in computer simulations. Chem Phys Lett. 1983;102:508–513. doi:10.1016/0009-2614(83)87455-7.

[23] Neumann M, Steinhauser O. Computer simulation and the dielectric constant of polarizable polar systems. Chem Phys Lett. 1984;106:563–569. doi:10.1016/0009-2614(84)85384-1.

[24] English NJ, MacElroy JMD. Molecular dynamics simulations of microwave heating of water. J Chem Phys. 2003;118:1589–1592. doi:10.1063/1.1538595.

[25] English NJ, MacElroy JMD. Hydrogen bonding and molecular mobility in liquid water in external electromagnetic fields. J Chem Phys. 2003;119:11806–11813. doi:10.1063/1.1624363.

[26] English NJ. Molecular dynamics simulations of microwave effects on water using different long-range electrostatics methodologies. Mol Phys. 2006;104:243–253. doi:10.1080/14733140500352322.

[27] Petravic J, Delhommelle J. Conductivity of molten sodium chloride in an alternating electric field. J Chem Phys. 2003;119:8511–8518. doi:10.1063/1.1613256.

[28] English NJ, Sorescu DC, Karl JK. Effects of an external electromagnetic field on rutile Tio2: A molecular dynamics study. J Phys Chem Solids. 2006;67:1399–1409. doi:10.1016/j.jpcs.2006.01.101.

[29] Desgranges C, Delhommelle J. Estimating the conductivity of a nanoconfined liquid subjected to an experimentally accessible external field. Mol Simulat. 2008;34:177–181. doi:10.1080/08927020801930604.

[30] English NJ, Mooney DA. Very different responses to electromagnetic fields in binary ionic liquid-water solutions. J Phys Chem B. 2009;113:10128–10134. doi:10.1021/jp902500m.

[31] English NJ, Mooney DA. Electromagnetic field effects on binary dimethylimidazolium-based ionic liquid/water solutions. Phys Chem Chem Phys. 2009;11:9370–9374. doi:10.1039/b910462c.

[32] English NJ, Mooney DA, O'Brien SW. Electrical conductivity and dipolar relaxation of binary dimethylimidazolium chloride-water solutions: A molecular dynamics study. J Mol Liq. 2010;157:163–167. doi:10.1016/j.molliq.2010.10.001.

[33] English NJ, Mooney DA, O'Brien S. Ionic liquids in external electric and electromagnetic fields: a molecular dynamics study. Mol Phys. 2011;109:625–638. doi:10.1080/00268976.2010.544263.

[34] Matyushov DV. On the theory of dielectric spectroscopy of protein solutions. J Phys Condensed Matter. 2012;24:325105. doi:10.1088/0953-8984/24/32/325105.

[35] Heyden M, Tobias DJ, Matyushov DV. Terahertz absorption of dilute aqueous solutions. J Chem Phys. 2012;137:235103. doi:10.1063/1.4772000.

[36] Martin DR, Matyushov DV. Hydration shells of proteins probed by depolarized light scattering and dielectric spectroscopy: Orientational structure is significant, positional structure is not. J Chem Phys. 2014;141:22D501. doi:10.1063/1.4895544.

[37] Sweatman MB. Equilibrium behaviour of a novel gas separation process, with application to carbon capture. Chem Eng Sci. 2010;65:3907–3913. doi:10.1016/j.ces.2010.03.016.

[38] Sweatman MB. Improving the equilibrium performance of active carbons for separation processes by co-adsorption with low pressure solvent: application to carbon capture. Adsorption. 2011;17:723–737. doi:10.1007/s10450-011-9351-5.

[39] Berendsen HJC, Postma JPM, Gunsterenvan WF, Hermans J. Intermolecular forces. Dordrecht: Reidel D Publishing Company; 1981. p. 331–342.

[40] Jorgensen WL, Chandrasekhar J, Madura JD, Impey RW, Klein ML. Comparison of simple potential functions for simulating liquid water. J Chem Phys. 1983;79:926–935. doi:10.1063/1.445869.

[41] Berendsen HJC, Grigera JR, Straatsma TP. The missing term in effective pair potentials. J Phys Chem. 1987;91:6269–6271. doi:10.1021/j100308a038.

[42] Ferguson DM. Parameterization and evaluation of a flexible water model. J Comput Chem. 1995;16:501–511. doi:10.1002/jcc.540160413.

[43] Wu Y, Tepper HL, Voth GA. Flexible simple point-charge water model with improved liquid-state properties. J Chem Phys. 2006;124:024503. doi:10.1063/1.2136877.

[44] Chen B, Potoff JJ, Siepmann JI. Monte Carlo calculations for alcohols and their mixtures with alkanes. Transferable potentials for phase equilibria. 5. United-atom description of primary, secondary, and tertiary alcohols. J Phys Chem B. 2001;105:3093–3104. doi:10.1021/jp003882x.

[45] Stubbs JM, Potoff JJ, Siepmann JI. Transferable potentials for phase equilibria. 6. United-atom description for ethers, glycols, ketones, and aldehydes. J Phys Chem B. 2004;108:17596–17605. doi:10.1021/jp049459w.

[46] Jorgensen WL, Tirado-Rives J. Potential energy functions for atomic-level simulations of water and organic and biomolecular systems. Proc Natl Acad Sci USA. 2005;102:6665–6670. doi:10.1073/pnas.0408037102.

[47] Caleman C, Maarenvan PJ, Hong M, Hub JS, Costa LT, Spoelvan der D. Force field benchmark of organic liquids: density, enthalpy of vaporization, heat capacities, surface tension, isothermal compressibility, volumetric expansion coefficient, and dielectric constant. J Chem Theory Comput. 2012;8:61–74. doi:10.1021/ct200731v.

[48] Wang J, Wolf RM, Caldwell JW, Kollman PA, Case DA. Development and testing of a general amber force field. J Comput Chem. 2004;25:1157–1174. doi:10.1002/jcc.20035.

[49] Da silva EF, Kuznetsova T, Kvamme B, Merz KM. Molecular dynamics study of ethanolamine as a pure liquid and in aqueous solution. J Phys Chem B. 2007;111:3695–3703. doi:10.1021/jp068227p.

[50] Hess B, Kutzner C, Spoelvan der D, Lindahl E. GROMACS 4: algorithms for highly efficient, load-balanced, and scalable Molecular Simulation. J Chem Theory Comput. 2008;4:435–447. doi:10.1021/ct700301q.

[51] Hockney R, Goel S, Eastwood J. Quiet high-resolution computer models of a plasma. J Comput Phys. 1974;14:148–158. doi:10.1016/0021-9991(74)90010-2.

[52] Nosé S. A molecular dynamics method for simulations in the canonical ensemble. Mol Phys. 1984;52:255–268. doi:10.1080/00268978400101201.

[53] Hoover WG. Canonical dynamics: equilibrium phase-space distributions. Phys Rev A. 1985;31:1695–1697. doi:10.1103/PhysRevA.31.1695.

[54] Parrinello M, Rahman A. Polymorphic transitions in single crystals: a new molecular dynamics method. J Appl Phys. 1981;52:7182–7190. doi:10.1063/1.328693.

[55] Nosé S, Klein M. Constant pressure molecular dynamics for molecular systems. Mol Phys. 1983;50:1055–1076. doi:10.1080/00268978300102851.

[56] Hess B, Bekker H, Berendsen HJC, Fraaije JGEM. LINCS: A linear constraint solver for molecular simulations. J Comput Chem. 1997;18:1463–1472. doi:10.1002/(SICI)1096-987X(199709)18:12<1463:AID-JCC4>3.0.CO;2-H.

[57] Darden T, York D, Pedersen L. Particle mesh ewald: an N · log(N) method for ewald sums in large systems. J Chem Phys. 1993;98:10089–10092. doi:10.1063/1.464397.

[58] Allen MP, Tildesley DJ. Computer simulation of liquids. Gloucestershire, UK: Clarendon Press, 1989.

[59] Zhang X, Jian C. Liquid-liquid equilibrium for the ternary system methanol + acrylonitrile + water. J Chem Eng Data. 2012;57: 142–147. doi:10.1021/je2009208.

[60] Orekhova Z, Ben-Hamo M, Manzurola E, Apelblat A. Electrical conductance and volumetric studies in aqueous solutions of nicotinic acid. J Solution Chem. 2005;34:687–700. doi:10.1007/s10953-005-4493-2.

[61] Doi H, Tamura K, Murakami S. Thermodynamic properties of aqueous solution of 2-isobutoxyethanol ATT= (293.15, 298.15, and 303.15) K, below and above lcst. J Chem Thermodyn. 2000; 32:729–741. doi:10.1006/jcht.1999.0645.

[62] Kolker AM, Safonova LP. Molar heat capacities of the (water + acetonitrile) mixtures at T=(283.15, 298.15, 313.15, and 328.15) K. J Chem Thermodyn. 2010;42:1209–1212. doi:10.1016/j.jct.2010.04.019.

[63] Antosik M, Gałka M, Malanowski SK. Vapor − liquid equilibrium in a ternary system cyclohexane + ethanol + water. J Chem Eng Data. 2004;49:7–10. doi:10.1021/je025621h.

[64] Marcus Y. The properties of solvents. Hobboken, NJ: Wiley, 1998.

[65] Begum SK, Clarke RJ, Ahmed MS, Begum S, Saleh MA. Densities, viscosities, and surface tensions of the system water + diethylene glycol. J Chem Eng Data. 2011;56:303–306. doi:10.1021/je1009976.

[66] Egorov D, Makarov GI. The bulk properties of ethylene glycol - dimethylsulfoxide mixtures over the temperture range 278-323 K at p=0.1 MPa, Zh. fiz. khim + 82. 2008. p. 1982–1988.

[67] M.G. Technische Hochschule Carl Schorlemmer Leuna-Merseburg, Unpublished data; 1989.

[68] Yang C, Ma P, Jing F, Tang D. Excess molar volumes, viscosities, and heat capacities for the mixtures of ethylene glycol + water from 273.15 K to 353.15 K. J Chem Eng Data. 2003;48:836–840. doi:10.1021/je020140j.

[69] Verevkin SP. Determination of vapor pressures and enthalpies of vaporization of 1,2-alkanediols. Fluid Phase Equilibr. 2004;224: 23–29. doi:10.1016/j.fluid.2004.05.010.

[70] Rodrigues M, Francesconi A. Experimental study of the excess molar volumes of binary and ternary mixtures containing water + (1,2-ethanediol, or 1,2-propanediol, or 1,3-propanediol, or 1,2-butanediol) + (1-N-butyl-3-methylimidazolium bromide) at 298.15 K and atmospheric pressure. J Sol Chem. 2011;40: 1863–1873. doi:10.1007/s10953-011-9756-5.

[71] Zarei HA, Asadi S, Iloukhani H. Temperature dependence of the volumetric properties of binary mixtures of (1-propanol, 2-propanol and 1,2-propanediol) at ambient pressure (81.5 KPA). J Mol Liq. 2008;141:25–30. doi:10.1016/j.molliq.2008.02.006.

[72] Yang C, Ma P, Xia S. Heat capacity of glycol determined by differential scanning calorimeter. Tianjin Daxue Xuebao. 2003;36: 192–196.

[73] Belda Maximino R. Viscosity and density of binary mixtures of alcohols and polyols with three carbon atoms and water: equation for the correlation of viscosities of binary mixtures. Phys Chem Liq. 2009;47:515–529. doi:10.1080/00319100802372114.

[74] Yaws CL. Yaws' Handbook of thermodynamic and physical properties of chemical compounds. New York: McGraw-Hill; 2003.

[75] Bastos M, Nilsson SO, Silva MDR, Silva MAR, Wadsö I. Thermodynamic properties of glycerol enthalpies of combustion and vaporization and the heat capacity at 298.15 K. Enthalpies of solution in water at 288.15, 298.15, and 308.15 K. J Chem Thermodyn. 1988;20:1353–1359. doi:10.1016/0021-9614(88)90173-5.

[76] Lide DR. CRC handbook of chemistry and physics. 90th ed. Boca Raton, FL: CRC Press; 2009.

[77] Kartsev V, Rodnikova M, Tsepulin V, Markova V. Piezometry and densitometry of aqueous solutions of diamines, aminoalcohols, and diols. II. Solutions of monoethanolamine and diols. Russ J Phys Chem. 1988;62:1152–1153.

[78] Liessmann G, Schmidt W, Reiffarth S. Recommended thermophysical data. Data compilation of the Saechsische Olefinwerke Boehlen. Germany; 1995.

[79] DIPPR Design Institute for Physical Properties Research, AIChE. 2010.

[80] Chialvo AA, Moucka F, Vlcek L, Nezbeda I. Vapor-liquid equilibrium and polarization behavior of the GCP water model: Gaussian charge-on-spring versus dipole self-consistent field approaches to induced polarization. J Phys Chem B. 2015;119: 5010–5019 PMID: 25803267. doi:10.1021/acs.jpcb.5b00595.

[81] Holz M, Heil SR, Sacco A. Temperature-dependent self-diffusion coefficients of water and six selected molecular liquids for calibration in accurate 1H NMR PFG measurements. Phys Chem Chem Phys. 2000;2:4740–4742. doi:10.1039/b005319h.

[82] Badyal YS, Saboungi M, Price DL, Shastri SD, Haeffner DR, Soper AK. Electron distribution in water. J Chem Phys. 2000;112: 9206–9208. doi:10.1063/1.481541.

[83] Gente G, La Mesa C. Water-trifluoroethanol mixtures: some physicochemical properties. J Solution Chem. 2000;29: 1159–1172. doi:10.1023/A:1005147318013.

[84] Holz M, Mao Xa, Seiferling D, Sacco A. Experimental study of dynamic isotope effects in molecular liquids: detection of translation-rotation coupling. J Chem Phys. 1996;104:669–679. doi:10.1063/1.470863.

[85] Hanai T, Koizumi N, Gotoh R. Temperature dependence of dielectric constants and dipole moments in polar liquids. Bull Inst Chem Res, Kyoto Univ. 1961;39:195–201.

[86] Kinart CM, Klimczak M. Thermodynamic and structural properties of binary mixtures of some glycols with 2-butoxyethanol at T=(293.15, 298.15 and 303.15) K. J Mol Liq. 2009;148:132–139. doi:10.1016/j.molliq.2009.07.009.

[87] Mitchell M, Tyrrell HJV. Diffusion of benzene, phenol and resorcinol in propane-1,2-diol, and the validity of the Stokes-Einstein equation. J Chem Soc, Faraday Trans. 1972;68:385–399. doi:10.1039/f29726800385.

[88] Gmehling J, Krafczyk J, Ahlers J, Nebig S, Hunecker I, Eisel M, Fischer D, Krentscher B, Beyer K. Pure compound data from DDB.

[89] Sastry NV, Patel MC. Densities, excess molar volumes, viscosities, speeds of sound, excess isentropic compressibilities, and relative permittivities for alkyl (methyl, ethyl, butyl, and isoamyl) acetates + glycols at different temperatures. J Chem Eng Data. 2003;48:1019–1027. doi:10.1021/je0340248.

[90] D'Errico G, Ortona O, Capuano F, Vitagliano V. Diffusion coefficients for the binary system glycerol + water at 25 °C. A velocity correlation study. J Chem Eng Data. 2004;49: 1665–1670. doi:10.1021/je049917u.

[91] Kinart CM, Kinart WJ. Physicochemical properties of glycerol-formamide liquid mixtures and their assumed internal structures. Phys Chem Liq. 1996;33:159–170. doi:10.1080/00319109608039817.

[92] Rodnikova M, Privalov V, Samigullin F, Zhakova V. Rotational and progressive molecules mobility of certain aminoalcohols, Zh. Fiz. Khim + 68. 1994;68:2235–2238.

[93] Undre P, Helambe S, Jagdale S, Khirade P, Mehrotra S. Study of solute-solvent interaction through dielectrics properties of N,N-dimethylacetamide in ethanolamine. J Mol Liq. 2008;137: 147–151. doi:10.1016/j.molliq.2007.06.004.

[94] Gereben O, Pusztai L. On the accurate calculation of the dielectric constant from molecular dynamics simulations: The case of SPC/E and SWM4-DP water. Chem Phys Lett. 2011;507:80–83. doi:10.1016/j.cplett.2011.02.064.

[95] Raabe G, Sadus RJ. Molecular dynamics simulation of the dielectric constant of water: The effect of bond flexibility. J Chem Phys. 2011;134:234501. doi:10.1063/1.3600337.

[96] Schneider U, Lunkenheimer P, Brand R, Loidl A. Dielectric and far-infrared spectroscopy of glycerol. J Non-Cryst Solids. 1998; 235–237:173–179. doi:10.1016/S0022-3093(98)00561-4.

[97] Lunkenheimer P, Schneider U, Brand R, Loid A. Glassy dynamics. Contemp Phys. 2000;41:15–36. doi:10.1080/001075100181259.

[98] Horikoshi S, Matsuzaki S, Mitani T, Serpone N. Microwave frequency effects on dielectric properties of some common solvents and on microwave-assisted syntheses: 2-Allylphenol and the C12-C2-C12 Gemini surfactant. Radiat Phys Chem. 2012;81: 1885–1895. doi:10.1016/j.radphyschem.2012.07.011.

[99] Zahn M, Ohki Y, Fenneman DB, Gripshover R, Gehman J, VH. Dielectric properties of water and water/ethylene glycol mixtures for use in pulsed power system design. Proc IEEE. 1986;74:1182–1221. doi:10.1109/PROC.1986.13611.
[100] Bartoš J, Šauša O, Köhler M, Švajdlenková H, Lunkenheimer P, Krištiak J, Loidl A. Positron annihilation and broadband dielectric spectroscopy: a series of propylene glycols. J Non-Cryst Solids. 2011;357:376–384 384 6th International Discussion Meeting on Relaxation in Complex Systems. doi:10.1016/j.jnoncrysol.2010.07.030.
[101] Lunkenheimer P, Pimenov A, Schiener B, Böhmer R, Loidl A. High-frequency dielectric spectroscopy on glycerol. Europhys Lett. 1996;33:611–616. doi:10.1209/epl/i1996-00387-4.
[102] Lunkenheimer P, Pimenov A, Dressel M, Goncharov YG, Böhmer R, Loidl A. Fast dynamics of glass-forming glycerol studied by dielectric spectroscopy. Phys Rev Lett. 1996;77:318–321. doi:10.1103/PhysRevLett.77.318.
[103] Patil A, Pawar V. Microwave dielectric spectra and molecular interaction in a binary mixture of ethanolamine with diethanolamine. J Mol Liq. 2013;188:1–4. doi:10.1016/j.molliq.2013.09.007.
[104] Patil A, Shinde G, Pawar V. Dielectric relaxation study of hydrogen bonded structures in ethanolamine with diethanolamine using tdr technique. J Mol Liq. 2012;168:42–46. doi:10.1016/j.molliq.2012.01.017.

Appendix A. Force fields parameters

Water models:

- The SPC model [39] is a rigid model in which the water molecule is formed by three Coulomb interaction sites centred on the atomic nuclei and one LJ interaction site situated on the oxygen atom. The SPC model is one of the more broadly used water models, and, despite its simplicity, it provides a good description of most properties of water.
- The TIP4P model [40] is a four-site water model. Its main characteristic is that the partial negative charge of the oxygen atom is moved towards the hydrogen atoms at a point *M* situated along the bisector of the bond angle. As a result, the electrostatic distribution around the molecule is improved. The simple form of this model and its acceptable performance justify its wide implementation in computational chemistry.
- The SPC/E model [41] imposes a change in polarisation with respect to the SPC model by modifying the charges on oxygen and hydrogen atoms. This results in a better prediction of density, as well as diffusion and dielectric constants.
- Based on the SPC model, the Flexible SPC (F-SPC) model [42] adds harmonic and anharmonic terms to describe bond stretching and angle bending. Inclusion of these terms has been shown to lead to improved predictions for thermodynamic, dielectric and dynamic properties.
- Another flexible model showing good results is the Fw-SPC water model [43] which is one of the most accurate non-polarisable models. Its development has shown how important bond stretching and angle bending are for the accurate determination of the self-diffusion coefficient and dielectric constant, respectively.

Table A1. Parameters of water models.

Model	SPC	TIP4P	SPC/E	F-SPC	Fw-SPC
σ_O (nm)	0.316557	0.315365	0.316557	0.318259	0.3165492
ε_O (kJ mol^{-1})	0.650194		0.650194	0.629616	0.6496778
σ_H (nm)	0.000000	0.000000	0.000000	0.0000000	0.000000
ε_H (kJ mol^{-1})	0.000000	0.000000	0.000000	0.0000000	0.000000
σ_M (nm)	–	0.000000	–	–	–
ε_M (kJ mol^{-1})	–	0.000000	–	–	–
b_0 (nm)	0.10000	0.09572	0.10000	0.10000	0.1012
b_M (nm)	–	0.015	–	–	–
k_b (kJ mol^{-1} nm^{-2})	–	–	–	229074[a]	442729.7
k_{cub} (nm^{-1})	–	–	–	− 16.5[a]	–
θ_0 (°)	109.47	104.52	109.47	109.5	113.24
k_a (kJ mol^{-1} rad^{-2})	–	–	–	417.6	317
q_O (e)	− 0.82	–	− 0.8476	− 0.826	− 0.82
q_H (e)	0.41	0.52	0.4238	0.413	0.41
q_M (e)	–	− 1.04	–	–	–

[a] The F-SPC model uses a cubic bond stretching potential of the form: $U_b(r_{ij}) = k_b(r_{ij} - b_0)^2 + k_b k_{cub}(r_{ij} - b_0)^3$.

Table A2. Non-bonded LJ parameters of alcohols and MEA force fields.

		σ(Å)				ε (kJ mol^{-1})		
Atom	TraPPE-UA	OPLS	GAFF	MEAa	TraPPE-UA	OPLS	GAFF	MEAa
CH_3	3.75000	–	–	–	0.814415	–	–	–
CH_2	3.95000	–	–	–	0.382444	–	–	–
CH	4.33000	–	–	–	0.083140	–	–	–
C (CH_3)	–	3.50000	3.39967	–	–	0.276144	0.457730	–
C (CH_2)	–	3.50000	3.39967	3.39967	–	0.276144	0.457730	0.457730
C (CH)	–	3.50000	3.39967	–	–	0.276144	0.457730	–
H (CH_3)	–	2.50000	2.64953	–	–	0.125520	0.0656888	–
H (CH_2)	–	2.50000	2.47135	2.47135	–	0.125520 0.062760[a]	0.0656888	0.0656888
H (CH)	–	2.50000	2.47135	–	–	0.125520	0.0656888	–
O (OH)	3.02000	3.12000 3.07000[b]	3.06647	3.06647	0.773202	0.711280	0.880314	0.880314
H (OH)	0.00000	0.00000	0.00000	0.00000	0.000000	0.000000	0.000000	0.000000
N (NH_2)	–	3.30000	3.25000	3.25000	–	0.711280	0.711280	0.711280
H (NH_2)	–	0.00000	1.06908	–	0.000000	0.0656888	0.0656888	0.0656888

[a] for CH_2-NH_2 in MEA.
[b] for propylene glycol and glycerol.

Table A3. Charge distribution in alcohols and MEA force fields.

		Charge (e)		
Atom	TraPPE-UA	OPLS	GAFF	MEAa
CH_3	0.00000	–	–	–
CH_2	+0.26500	–	–	–
CH	+0.26500	–	–	–
C (CH_3)	–	−0.18	−0.23710	–
C (CH_2)	–	+0.145	+0.51200[a]	0.25000
	–	+0.06 [h]	+0.30500[b]	0.20000 [h]
	–		+0.18590[c]	
	–		+0.23950[d]	
	–		+0.41950[h]	
C (CH)	–	+0.205	+0.41640	–
H (CH_3)	–	+0.06	+0.05950	–
	–		+0.05980[c]	–
H (CH_2)	–	+0.06	−0.08060[a]	0.00000
			−0.00290[b]	
			+0.00480[c]	
			−0.02840[d]	
			−0.00600[h]	
H (CH)	–	+0.06	−0.03390	–
O (OH)	−0.70000	−0.683	−0.69740[a]	−0.60000
		> −0.73[c]	−0.73830[b]	
			−0.76370[c]	
			−0.69200[e]	
			−0.69350[f]	
H (OH)	+0.43500	+0.418	+0.40520[a]	+0.36000
		+0.465[c]	+0.43910[b]	
			+0.46430[d]	
			+0.43880[e]	
			+0.42640[f]	
N (NH_2)	–	−0.9	−1.03480	−0.88000
H (NH_2)	–	+0.36	+0.36000	+0.33500

[a] for ethanol.
[b] for ethylene glycol.
[c] for propylene glycol and glycerol.
[d] for MEA.
[e] for CH_2-OH group in propylene glycol and glycerol.
[f] for CH-OH group in propylene glycol and glycerol.
[h] for CH_2-NH_2 group in MEA.

Table A4. Bond lengths for alcohols and MEA force fields.

		Bond length (Å)			$10^{-5}k_b$ (kJ mol^{-1} nm^{-2})			
Bond	TraPPE-UA	OPLS	GAFF	MEAa	TraPPE-UA	OPLS	GAFF	MEAa
CH_x–CH_y	1.5400	–	–	–	–	–	–	–
C–C	–	1.5290	1.5350	1.5350	–	–	–	2.5363
C–H	–	1.0900	1.0930	1.0930	–	–	–	2.8108
CH_x–O	1.4300	–	–	–	–	–	–	–
C–O	–	1.4100	1.4260	1.4260	–	–	–	2.6284
O–H	0.94500	0.9450	0.97400	0.97400	–	–	–	3.0928
C–N	–	1.4480	1.4700	1.4700	–	–	–	2.6828
N–H	–	1.0100	1.0180	1.0180	–	–	–	3.2978

Table A5. Angle bending parameters for alcohols and MEA force fields.

		θ_0 (°)			k_θ (kJ mol^{-1} rad^{-2})			
Angle	TraPPE-UA	OPLS	GAFF	MEAa	TraPPE-UA	OPLS	GAFF	MEAa
CH_x–CH_y–O	109.50	–	–	–	419.03	–	–	–
CH_x–O–H	108.50	–	–	–	460.60	–	–	–
CH_2–CH–CH_3	112.00	–	–	–	519.63	–	–	–
C–C–C	–	112.700	110.63	–	–	488.273	528.86	–
C–C–O	–	109.500	109.43	109.43	–	418.400	566.51	566.51
C–C–H	–	110.700	110.07	110.07	–	313.800	388.28	388.28
C–O–H	–	108.500	108.16	108.16	–	460.240	394.13	394.13
O–C–H	–	109.500	109.88	109.88	–	292.880	426.77	426.77
H–C–H	–	107.800	109.55 108.35[a]	109.55	–	276.144	328.03 329.70[a]	328.03
C–C–N	–	109.470	110.38	110.38	–	470.281	553.96	553.96
C–N–H	–	109.500	109.92	116.78	–	292.880	394.13	384.93
N–C–H	–	109.500	109.92	109.92	–	292.880	413.38	413.38
H–N–H	–	106.400	107.13	109.50	–	364.845	345.60	292.88

[a] for CH_3 in ethanol.

Table A6. Dihedral torsion parameters for alcohols and MEA force fields (c_i and C_i parameters in kJ mol^{-1}).

TraPPE-UA – Ryckaert–Bellemans dihedral				
Dihedral	c_0	c_1	c_2	c_3
CH_3–CH–O–H	2.51324	5.97851	−0.523117	−5.78388
CH_2–CH–O–H	2.51324	5.97851	−0.523117	−5.78388
O–CH_2–CH_2–O	8.36779	−25.10338	4.183937	33.47117
O–CH_2–CH–O	8.36779	−25.10338	4.183937	33.47117
TraPPE-UA – Fourier dihedral				
Dihedral	C_1	C_2	C_3	
CH_3–CH_2–O–H	3.48736	−0.484826	3.12353	
CH_2–CH_2–O–H	3.48889	−0.485039	3.12490	
CH–CH_2–O–H	3.48889	−0.485039	3.12490	
CH_3–CH–CH_2–O	2.93684	−0.886938	12.8024	
OPLS – Ryckaert-Bellemans dihedral				
Dihedral	c_0	c_1	c_2	c_3
C–C–C–H	0.62760	1.88280	0.00000	−2.51040
H–C–C–H	0.62760	1.88280	0.00000	−2.51040
C–C–C–O	2.87441	0.58158	2.09200	−5.54799
C–C–O–H	−0.44350	3.83255	0.72801	−4.11705
O–C–C–O	18.96607	−18.96607	0.00000	0.00000
H–C–O–H	0.94140	2.82420	0.00000	−3.76560
H–C–C–O	0.97905	2.93716	0.00000	−3.91622
O–C–C–N	16.73600	−16.73600	0.00000	0.00000
H–C–C–N	−4.09614	5.08775	2.96645	−3.95806
C–C–N–H	−1.26775	3.02085	1.74473	−3.49782
H–C–N–H	0.83680	2.51040	0.00000	−3.34720
GAFF – Ryckaert–Bellemans dihedral				
Dihedral	c_0	c_1	c_2	c_3
C–C–C–H	0.65270	1.95811	0.00000	−2.61082
H–C–C–H	0.65270	1.95811	0.00000	−2.61082
C–C–C–O	0.65270	1.95811	0.00000	−2.61082
C–C–O–H	1.71544	0.96232	0.00000	−2.67776
O–C–C–O	0.60250	1.80749	9.83240	−2.40998
H–C–O–H	0.69873	2.09618	0.00000	−2.79491
H–C–C–O	1.04600	−1.04600	0.00000	0.00000
O–C–C–N	0.65270	1.95811	0.00000	−2.61082
H–C–C–N	0.65270	1.95811	0.00000	−2.61082
C–C–N–H	1.25520	3.76560	0.00000	−5.02080
H–C–N–H	1.25520	3.76560	0.00000	−5.02080
MEAa – Ryckaert–Bellemans dihedral				
Dihedral	c_0	c_1	c_2	c_3
H–C–C–H	0.65270	1.95811	0.00000	−2.61082
C–C–O–H	0.00000	0.92048	0.00000	1.17152
H–C–O–H	0.69873	2.09618	0.00000	−2.79491
H–C–C–O	1.04600	−1.04600	0.00000	0.00000
O–C–C–N	0.33472	18.77277	−0.66940	−19.34012
H–C–C–N	0.65270	1.95811	0.00000	−2.61082
C–C–N–H	2.46856	15.69000	−4.93712	−13.72352
H–C–N–H	1.25520	3.76560	0.00000	−5.02080

Appendix B. Dynamic response through the dipole moment autocorrelation function

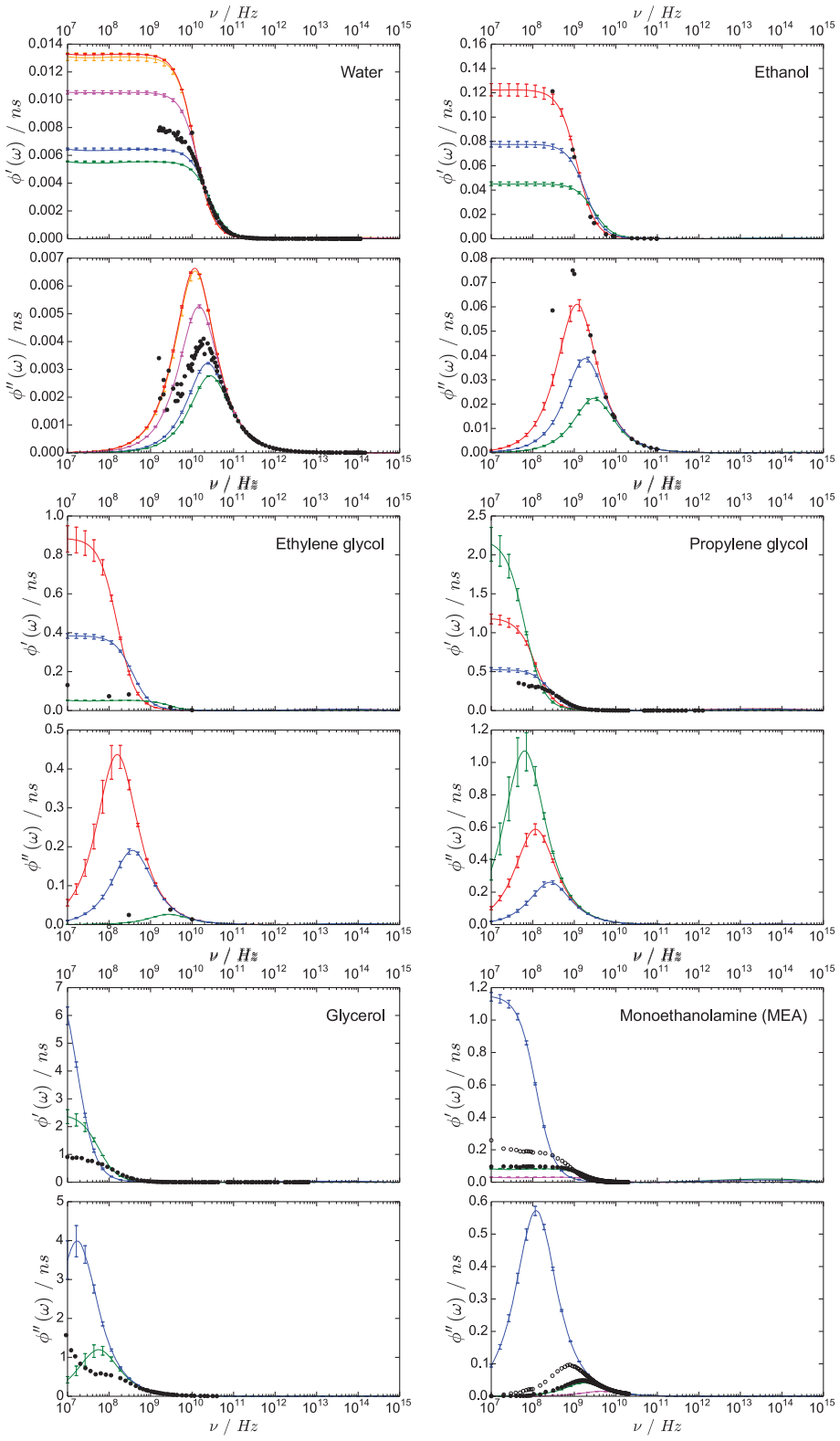

Figure B1. (Colour online) Dynamic response of several organic compounds at 298 K and 1 bar through the Fourier transform of the dipole moment autocorrelation function. For MEA, the simulations are performed at 293 K. Solid lines represent the results obtained in our simulations using the different force fields introduced in the text. In the particular case of water, blue, green, magenta, orange and red lines show the results corresponding to the SPC, TIP4P, SPC/E, F-SPC and Fw-SPC models, respectively. For the remaining substances, red, green, blue and magenta lines represent results generated using the TraPPE-UA, OPLS, GAFF and MEAa force fields, respectively. Black circles represent experimental values obtained from Equation (12) using dielectric spectrum data from different sources for the following systems: water,[9–12] ethanol,[16–18,98] ethylene glycol,[99] propylene glycol and [100] glycerol.[96,97,101,102] For MEA, black open and filled circles are experimental values at 278 K [103] and 308 K,[104] respectively.

Appendix C

Force fields parameters

In this appendix we summarise the parameters that define the force fields we use in our molecular dynamics simulations.

C.1 Water models

- The simple point charge (SPC) model [158] is a rigid model in which the water molecule is formed by three Coulomb interaction sites centred on the atomic nuclei and one LJ interaction site situated on the oxygen atom. The SPC model is one of the more broadly used water models, and, despite its simplicity, it provides a good description of most properties of water.
- The TIP4P model [187] is a 4-site water model. Its main characteristic is that the partial negative charge of the oxygen atom is moved towards the hydrogen atoms at a point M situated along the bisector of the bond angle. As a result, the electrostatic distribution around the molecule is improved. The simple form of this model and its acceptable performance justify its wide implementation in computational chemistry.
- The SPC/E model [188] imposes a change in polarization with respect to the SPC model by modifying the charges on oxygen and hydrogen atoms. This results in a better prediction of density, as well as diffusion and dielectric constants.
- Based on the SPC model, the Flexible SPC (F-SPC) model [189] adds harmonic and anharmonic terms to describe bond stretching and angle bending. Inclusion of these terms has been shown to lead to improved predictions for thermodynamic, dielectric and dynamic properties.
- Another flexible model showing good results is the Fw-SPC water model [190] which is one of the most accurate non-polarizable models. Its development has shown how important bond stretching and angle bending are for the accurate determination of the self-diffusion coefficient and dielectric constant respectively.

TABLE C.1: Parameters of water models

Model	SPC	TIP4P	SPC/E	F-SPC	Fw-SPC
σ_O (nm)	0.316557	0.315365	0.316557	0.318259	0.3165492
ϵ_O (kJ mol^{-1})	0.650194	0.648520	0.650194	0.629616	0.6496778
σ_H (nm)	0.000000	0.000000	0.000000	0.0000000	0.000000
ϵ_H (kJ mol^{-1})	0.000000	0.000000	0.000000	0.0000000	0.000000
σ_M (nm)	—	0.000000	—	—	—
ϵ_M (kJ mol^{-1})	—	0.000000	—	—	—
b_0 (nm)	0.10000	0.09572	0.10000	0.10000	0.1012
b_M (nm)	—	0.015	—	—	—
k_b (kJ mol^{-1} nm^{-2})	—	—	—	229074 [a]	442729.7
k_{cub} (nm^{-1})	—	—	—	−16.5 [a]	—
θ_0 (°)	109.47	104.52	109.47	109.5	113.24
k_a (kJ mol^{-1} rad^{-2})	—	—	—	417.6	317
q$_O$ (e)	−0.82	—	−0.8476	−0.826	−0.82
q$_H$ (e)	0.41	0.52	0.4238	0.413	0.41
q$_M$ (e)	—	−1.04	—	—	—

[a]The F-SPC model uses a cubic bond stretching potential of the form: $U_b(r_{ij}) = k_b(r_{ij} - b_0)^2 + k_b k_{cub}(r_{ij} - b_0)^3$

C.2 Non-bonded interactions parameters

TABLE C.2: Non-bonded LJ parameters of alcohols and MEA force fields

	σ (Å)				ϵ (kJ mol^{-1})			
Atom	TraPPE-UA	OPLS	GAFF	MEAa	TraPPE-UA	OPLS	GAFF	MEAa
CH_3	3.75000	—	—	—	0.814415	—	—	—
CH_2	3.95000	—	—	—	0.382444	—	—	—
CH	4.33000	—	—	—	0.083140	—	—	—
C (CH_3)	—	3.50000	3.39967	—	—	0.276144	0.457730	—
C (CH_2)	—	3.50000	3.39967	3.39967	—	0.276144	0.457730	0.457730
C (CH)	—	3.50000	3.39967	—	—	0.276144	0.457730	—
H (CH_3)	—	2.50000	2.64953	—	—	0.125520	0.0656888	—
H (CH_2)	—	2.50000	2.47135	2.47135	—	0.125520 0.062760 [a]	0.0656888	0.0656888
H (CH)	—	2.50000	2.47135	—	—	0.125520	0.0656888	—
O (OH)	3.02000	3.12000 3.07000 [b]	3.06647	3.06647	0.773202	0.711280	0.880314	0.880314
H (OH)	0.00000	0.00000	0.00000	0.00000	0.000000	0.000000	0.000000	0.000000
N (NH_2)	—	3.30000	3.25000	3.25000	—	0.711280	0.711280	0.711280
H (NH_2)	—	0.00000	1.06908	1.06908	—	0.000000	0.0656888	0.0656888

[a]CH_2-NH_2 in MEA, [b]propylene glycol and glycerol

C.3 Charge distribution

TABLE C.3: Charge distribution in alcohols and MEA force fields

	Charge (e)			
Atom	TraPPE-UA	OPLS	GAFF	MEAa
CH_3	0.00000	—	—	—
CH_2	+0.26500	—	—	—
CH	+0.26500	—	—	—
C (CH_3)	—	−0.18	−0.23710	—
C (CH_2)	—	+0.145	+0.51200 [a]	0.25000
	—	+0.06 [h]	+0.30500 [b]	0.20000 [h]
	—		+0.18590 [c]	
	—		+0.23950 [d]	
	—		+0.41950 [h]	
C (CH)	—	+0.205	+0.41640	—
H (CH_3)	—	+0.06	+0.05950	—
	—		+0.05980 [c]	—
H (CH_2)	—	+0.06	−0.08060 [a]	0.00000
			−0.00290 [b]	
			+0.00480 [c]	
			−0.02840 [d]	
			−0.00600 [h]	
H (CH)	—	+0.06	−0.03390	—
O (OH)	−0.70000	−0.683	−0.69740 [a]	−0.60000
		−0.73 [c]	−0.73830 [b]	
			−0.76370 [c]	
			−0.69200 [e]	
			−0.69350 [f]	
H (OH)	+0.43500	+0.418	+0.40520 [a]	+0.36000
		+0.465 [c]	+0.43910 [b]	
			+0.46430 [d]	
			+0.43880 [e]	
			+0.42640 [f]	
N (NH_2)	—	−0.9	−1.03480	−0.88000
H (NH_2)	—	+0.36	+0.36000	+0.33500

[a]ethanol, [b]ethylene glycol, [c]propylene glycol and glycerol, [d]MEA, [e]CH_2-OH group in propylene glycol and glycerol, [f]CH-OH group in propylene glycol and glycerol, [h]CH_2-NH_2 group in MEA.

C.4 Bonded interactions parameters

TABLE C.4: Bond lengths for alcohols and MEA force fields

	Bond length (Å)				$10^{-5}k_b$ (kJ mol^{-1} nm^{-2})			
Bond	TraPPE-UA	OPLS	GAFF	MEAa	TraPPE-UA	OPLS	GAFF	MEAa
CH_x - CH_y	1.5400	—	—	—	—	—	—	—
C - C	—	1.5290	1.5350	1.5350	—	—	—	2.5363
C - H	—	1.0900	1.0930	1.0930	—	—	—	2.8108
CH_x - O	1.4300	—	—	—	—	—	—	—
C - O	—	1.4100	1.4260	1.4260	—	—	—	2.6284
O - H	0.94500	0.9450	0.97400	0.97400	—	—	—	3.0928
C - N	—	1.4480	1.4700	1.4700	—	—	—	2.6828
N - H	—	1.0100	1.0180	1.0180	—	—	—	3.2978

TABLE C.5: Angle bending parameters for alcohols and MEA force fields

	θ_0 (^{o})				k$_\theta$ (kJ mol^{-1} rad^{-2})			
Angle	TraPPE-UA	OPLS	GAFF	MEAa	TraPPE-UA	OPLS	GAFF	MEAa
CH_x - CH_y - O	109.50	—	—	—	419.03	—	—	—
CH_x - O - H	108.50	—	—	—	460.60	—	—	—
CH_2 - CH - CH_3	112.00	—	—	—	519.63	—	—	—
C - C - C	—	112.700	110.63	—	—	488.273	528.86	—
C - C - O	—	109.500	109.43	109.43	—	418.400	566.51	566.51
C - C - H	—	110.700	110.07	110.07	—	313.800	388.28	388.28
C - O - H	—	108.500	108.16	108.16	—	460.240	394.13	394.13
O - C - H	—	109.500	109.88	109.88	—	292.880	426.77	426.77
H - C - H	—	107.800	109.55	109.55	—	276.144	328.03	328.03
			108.35 [a]				329.70 [a]	
C - C - N	—	109.470	110.38	110.38	—	470.281	553.96	553.96
C - N - H	—	109.500	109.92	116.78	—	292.880	394.13	384.93
N - C - H	—	109.500	109.92	109.92	—	292.880	413.38	413.38
H - N - H	—	106.400	107.13	109.50	—	364.845	345.60	292.88

[a] for CH_3 in ethanol

TABLE C.6: Dihedral torsion parameters for alcohols and MEA force fields (c_i and C_i parameters in kJ mol^{-1})

TraPPE-UA - Ryckaert-Bellemans dihedral

Dihedral	c_0	c_1	c_2	c_3
CH_3 - CH - O - H	2.51324	5.97851	−0.523117	−5.78388
CH_2 - CH - O - H	2.51324	5.97851	−0.523117	−5.78388
O - CH_2 - CH_2 - O	8.36779	−25.10338	4.183937	33.47117
O - CH_2 - CH - O	8.36779	−25.10338	4.183937	33.47117

TraPPE-UA - Fourier dihedral

Dihedral	C_1	C_2	C_3
CH_3 - CH_2 - O - H	3.48736	−0.484826	3.12353
CH_2 - CH_2 - O - H	3.48889	−0.485039	3.12490
CH - CH_2 - O - H	3.48889	−0.485039	3.12490
CH_3 - CH - CH_2 - O	2.93684	−0.886938	12.8024

OPLS - Ryckaert-Bellemans dihedral

Dihedral	c_0	c_1	c_2	c_3
C - C - C - H	0.62760	1.88280	0.00000	−2.51040
H - C - C - H	0.62760	1.88280	0.00000	−2.51040
C - C - C - O	2.87441	0.58158	2.09200	−5.54799
C - C - O - H	−0.44350	3.83255	0.72801	−4.11705
O - C - C - O	18.96607	−18.96607	0.00000	0.00000
H - C - O - H	0.94140	2.82420	0.00000	−3.76560
H - C - C - O	0.97905	2.93716	0.00000	−3.91622
O - C - C - N	16.73600	−16.73600	0.00000	0.00000
H - C - C - N	−4.09614	5.08775	2.96645	−3.95806
C - C - N - H	−1.26775	3.02085	1.74473	−3.49782
H - C - N - H	0.83680	2.51040	0.00000	−3.34720

GAFF - Ryckaert-Bellemans dihedral

Dihedral	c_0	c_1	c_2	c_3
C - C - C - H	0.65270	1.95811	0.00000	−2.61082
H - C - C - H	0.65270	1.95811	0.00000	−2.61082
C - C - C - O	0.65270	1.95811	0.00000	−2.61082
C - C - O - H	1.71544	0.96232	0.00000	−2.67776
O - C - C - O	0.60250	1.80749	9.83240	−2.40998
H - C - O - H	0.69873	2.09618	0.00000	−2.79491
H - C - C - O	1.04600	−1.04600	0.00000	0.00000
O - C - C - N	0.65270	1.95811	0.00000	−2.61082
H - C - C - N	0.65270	1.95811	0.00000	−2.61082
C - C - N - H	1.25520	3.76560	0.00000	−5.02080
H - C - N - H	1.25520	3.76560	0.00000	−5.02080

MEAa - Ryckaert-Bellemans dihedral

Dihedral	c_0	c_1	c_2	c_3
H - C - C - H	0.65270	1.95811	0.00000	−2.61082
C - C - O - H	0.00000	0.92048	0.00000	1.17152
H - C - O - H	0.69873	2.09618	0.00000	−2.79491
H - C - C - O	1.04600	−1.04600	0.00000	0.00000
O - C - C - N	0.33472	18.77277	−0.66940	−19.34012
H - C - C - N	0.65270	1.95811	0.00000	−2.61082
C - C - N - H	2.46856	15.69000	−4.93712	−13.72352
H - C - N - H	1.25520	3.76560	0.00000	−5.02080

Appendix D

Dielectric response of mixtures: additional results

D.1 Component - total

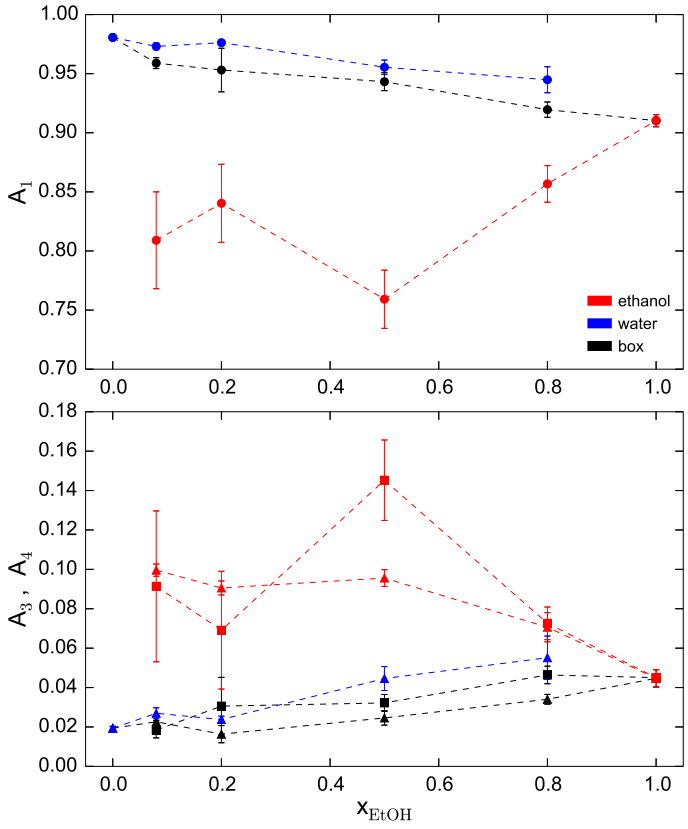

FIGURE D.1: Variation of total component relaxation intensities with concentration in ethanol/water mixtures at 298 K and 1 bar. Filled symbols correspond to the fit of the 1HN + 2Debye model to simulation data. In the case of pure water (x_{EtOH} = 0), a 1HN + 1Debye model is used. Circles represent the intensity of the dominant HN relaxation (1), while squares and triangles correspond to the fast (3) and very fast (4) processes, respectively. Dashed lines are a guide to the eye.

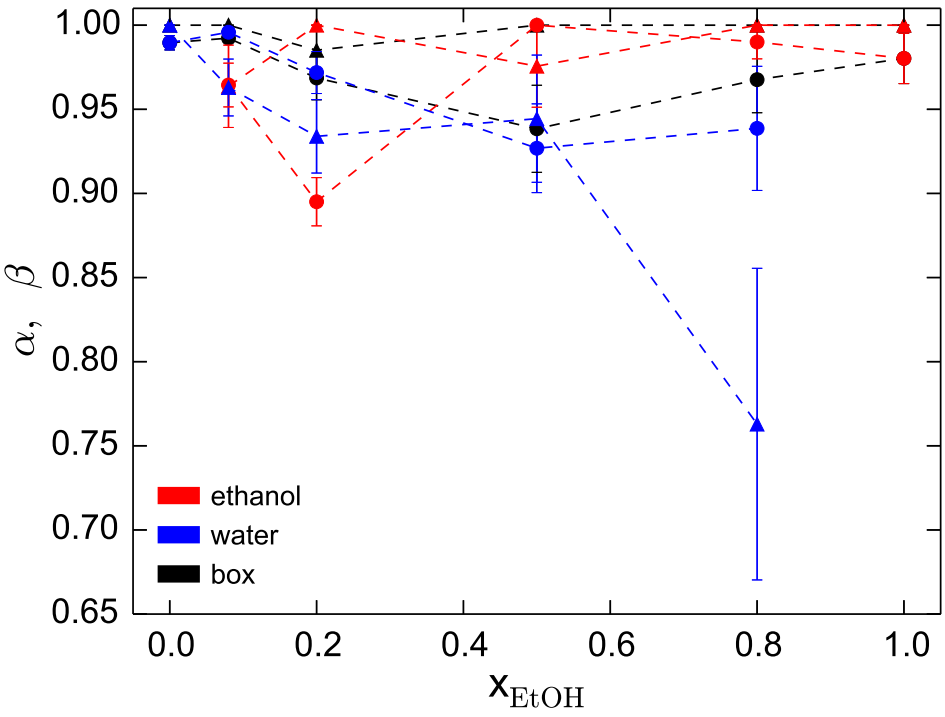

FIGURE D.2: Variation of total component Havriliak-Negami's α and β parameters with concentration in ethanol/water mixtures at 298 K and 1 bar. Filled symbols correspond to the fit of the HN model to the dominant relaxation process. Circles represent values of parameter α, while triangles correspond to parameter β. Dashed lines are a guide to the eye.

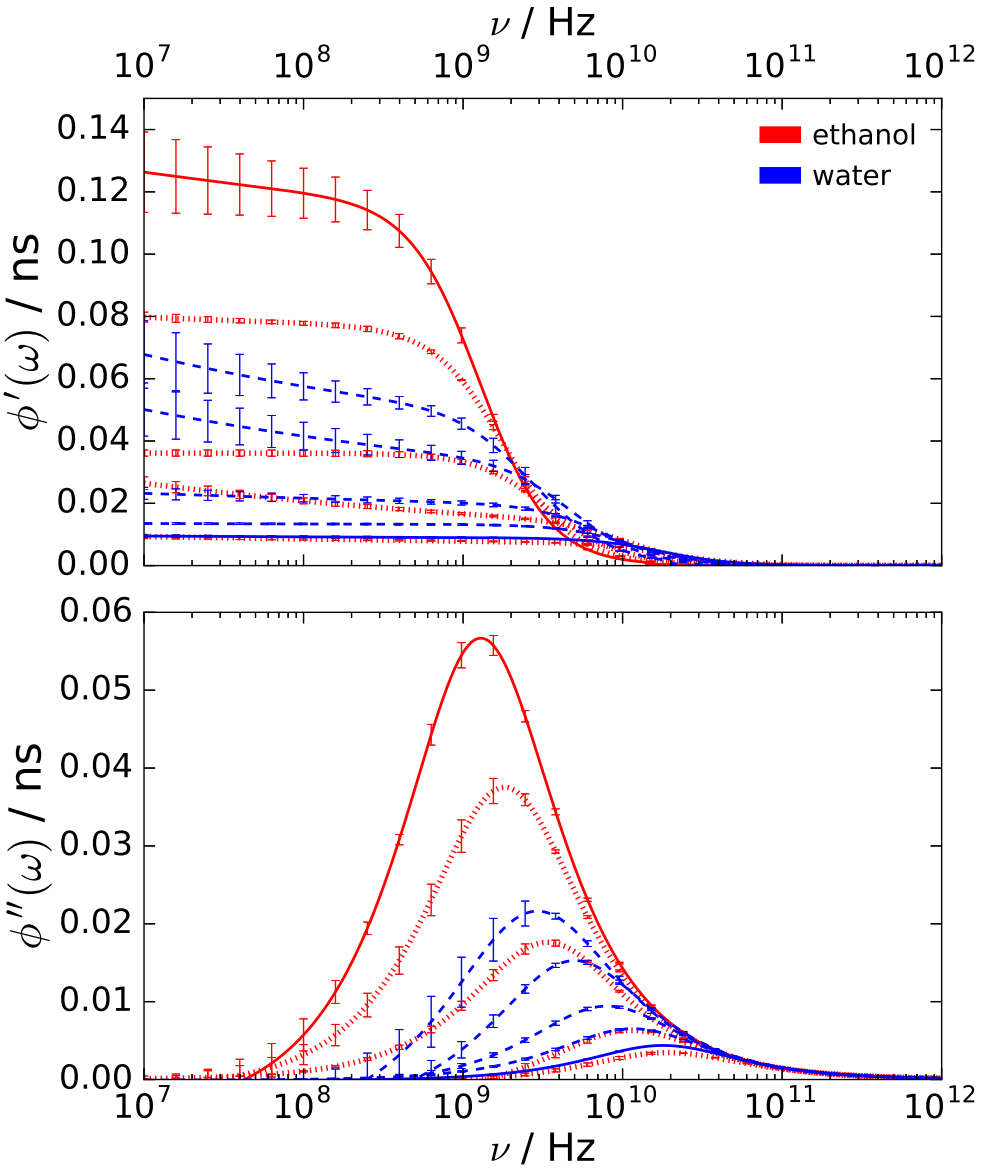

FIGURE D.3: Dynamic response through the dipole moment ACF of individual species in the frequency domain for ethanol/water mixtures at 298 K and 1 bar. Solid lines represent the dipole moment ACF of the pure components: ethanol (red) and water (blue). Dotted (red) lines show the total contribution of ethanol as a component, in mixtures with water of increasing ethanol concentration from top to bottom. Dashed (blue) lines represent the equivalent results for water as a component.

D.2 Component - molecule

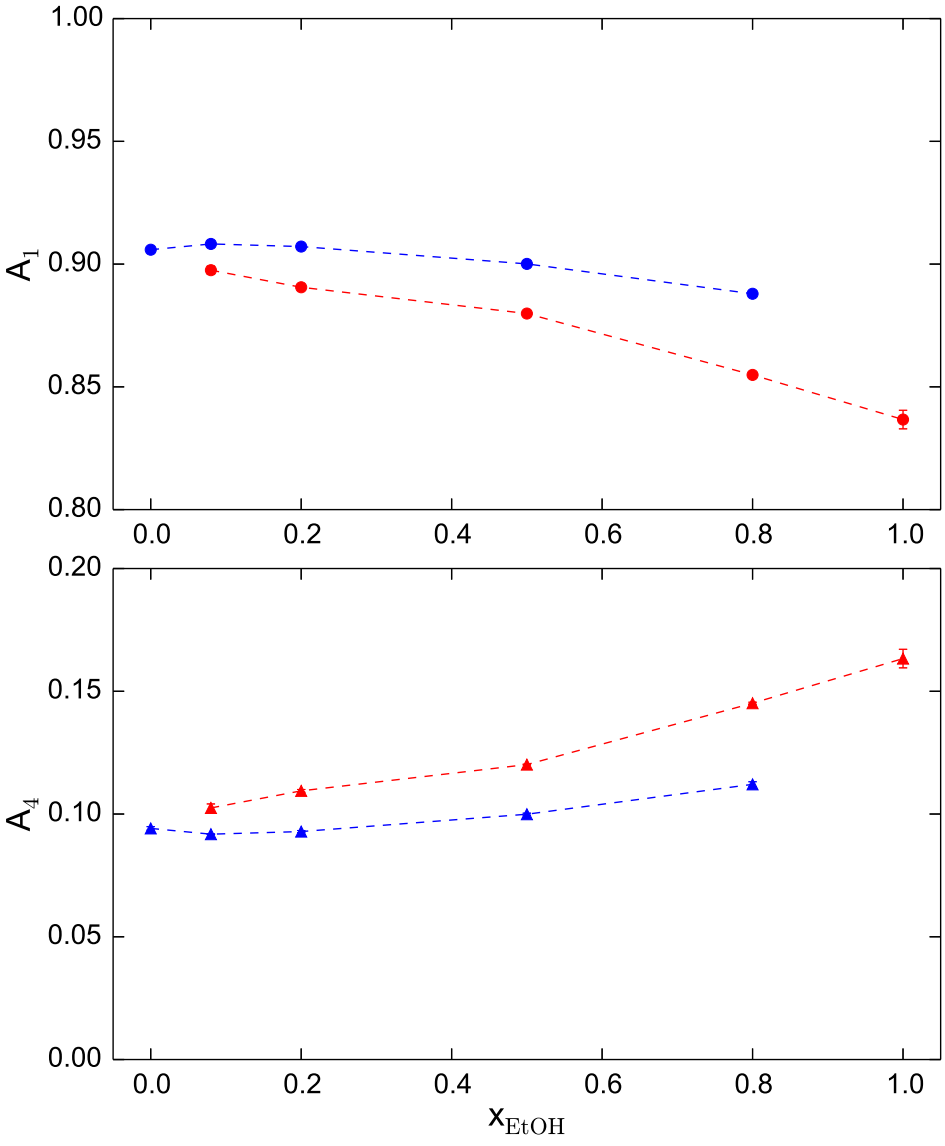

FIGURE D.4: Variation of molecular relaxation intensities with concentration in ethanol/water mixtures at 298 K and 1 bar. Filled symbols correspond to the fit of the 1HN + 1Debye model to simulation data. Circles represent the intensities of the dominant HN relaxation (1), while triangles correspond to the very fast (4) process. Dashed lines are a guide to the eye.

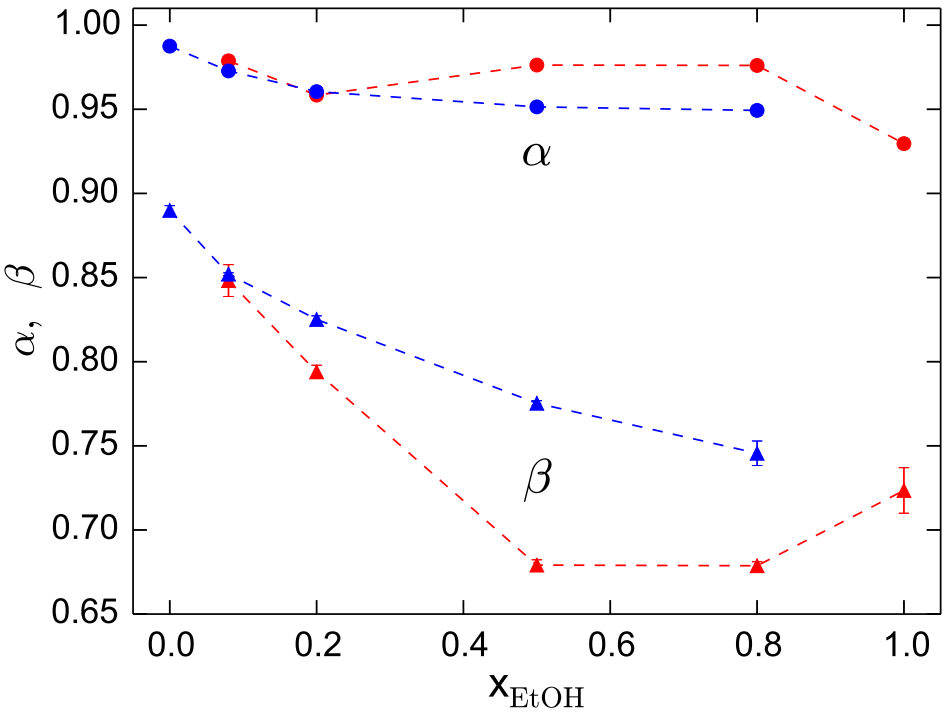

FIGURE D.5: Variation of molecular Havriliak-Negami's α and β parameters with concentration in ethanol/water mixtures at 298 K and 1 bar. Filled symbols correspond to the fit of the HN model to the dominant relaxation process. Circles represent values of parameter α, while triangles correspond to parameter β. Dashed lines are a guide to the eye.

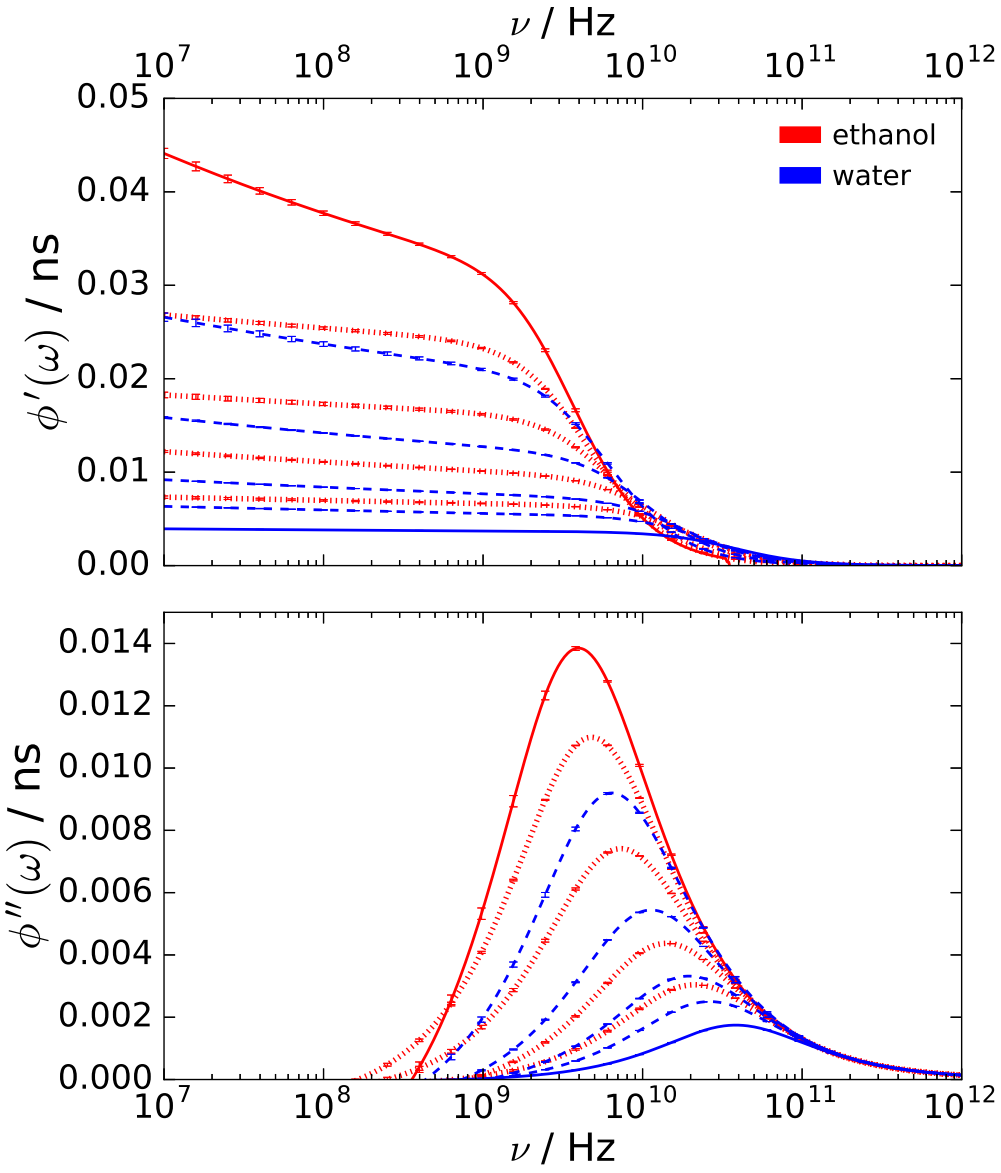

FIGURE D.6: Dynamic response through the dipole moment ACF of separate molecules in the frequency domain for ethanol/water mixtures at 298 K and 1 bar. Solid lines represent the dipole moment ACF of the pure components: ethanol (red) and water (blue). Dotted (red) lines show the total contribution of ethanol as a component, in mixtures with water of increasing ethanol concentration from top to bottom. Dashed (blue) lines represent the equivalent results for water as a component.

Appendix E

Effect of temperature on dielectric spectra: additional results

E.1 One component systems

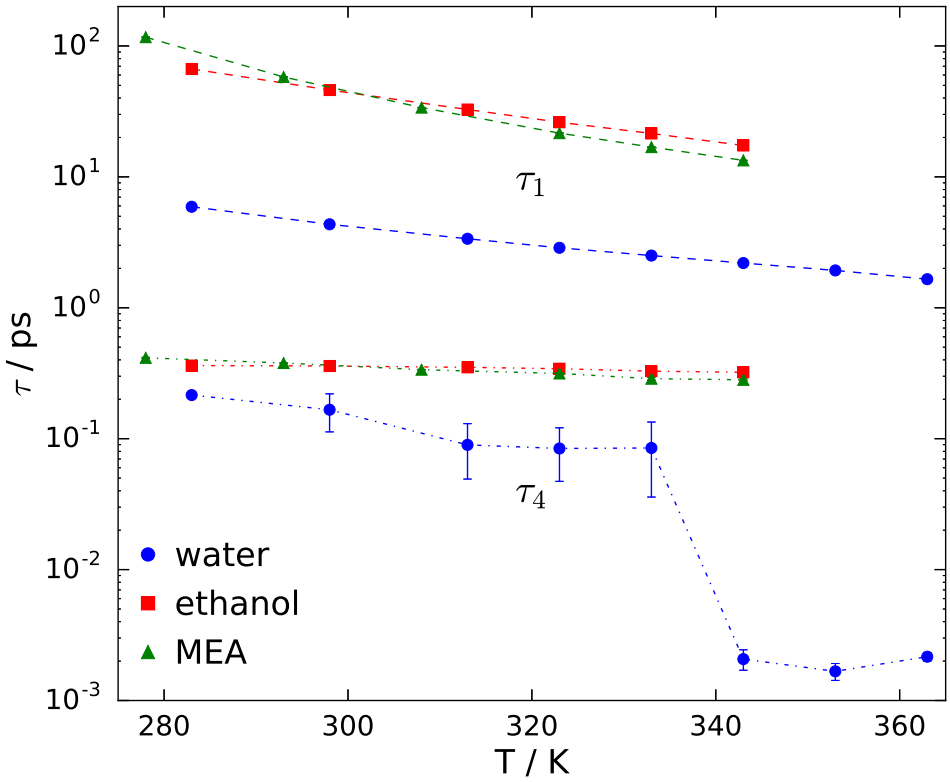

FIGURE E.1: Influence of temperature on molecular relaxation times of water, ethanol and MEA. Blue circles, red squares and green triangles correspond to results obtained from the fit of the 1 HN + 1 Debye model to simulation data for water, ethanol and MEA, respectively. Dashed lines are a guide to the eye.

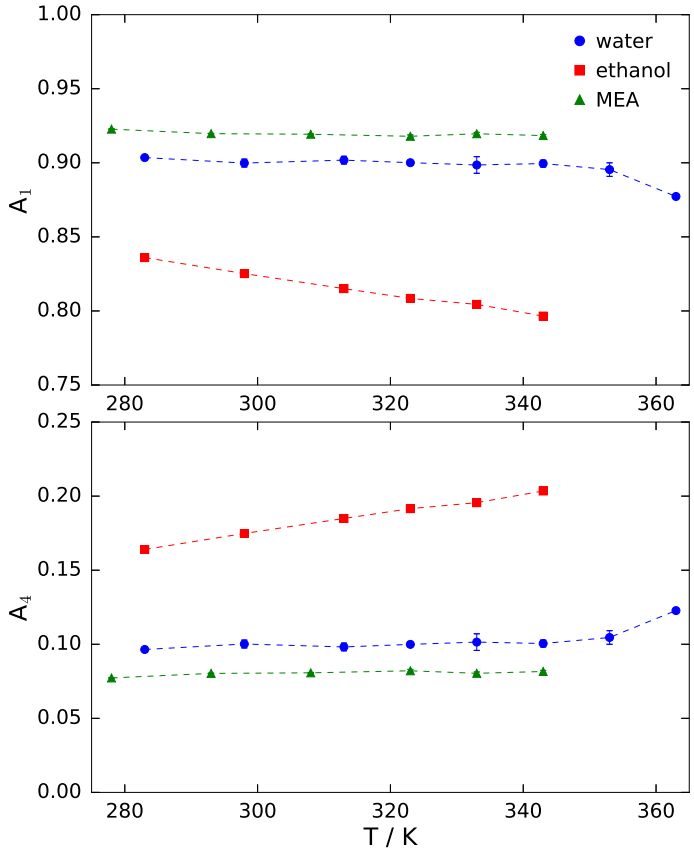

FIGURE E.2: Influence of temperature on the molecular relaxation intensities of water, ethanol and MEA. Blue circles, red squares and green triangles correspond to results obtained from the fit of the 1 HN + 1 Debye model to simulation data for water, ethanol and MEA, respectively. Dashed lines are a guide to the eye.

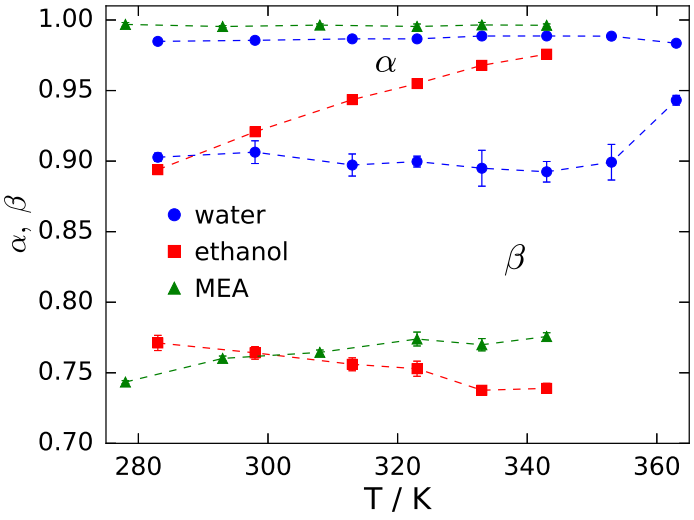

FIGURE E.3: Influence of temperature on Havriliak-Negami's α and β parameters for water, ethanol and MEA. Blue circles, red squares and green triangles correspond to results obtained from the fit of the 1 HN + 1 Debye model to simulation data for water, ethanol and MEA, respectively. Dashed lines are a guide to the eye.

E.2 Mixtures - total

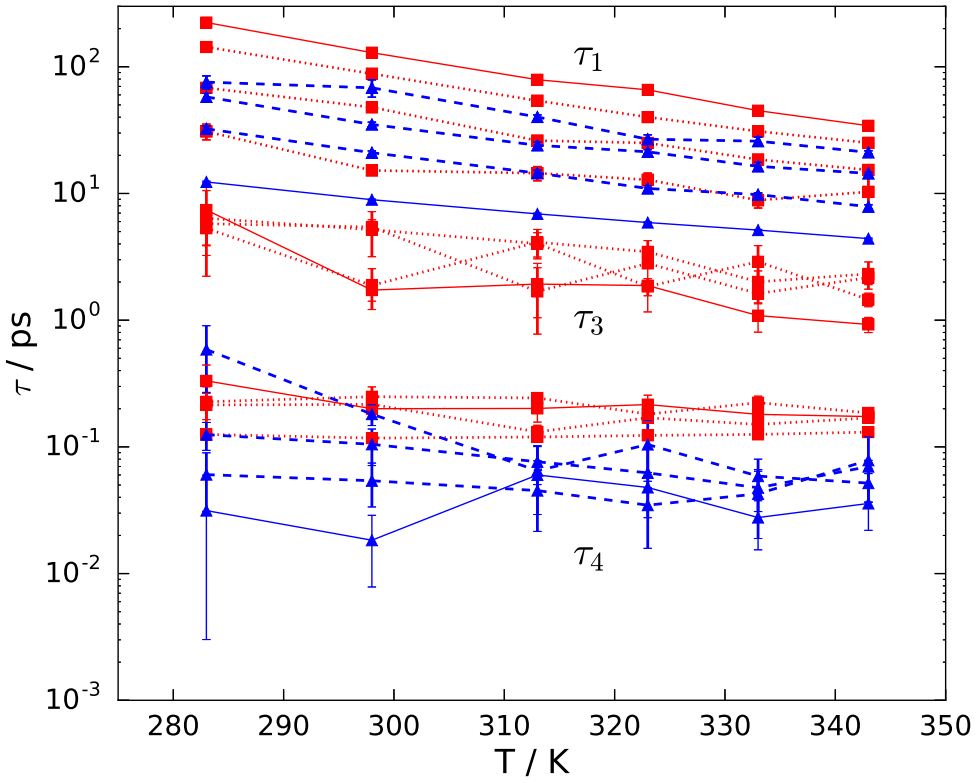

FIGURE E.4: Influence of temperature on relaxation times of each species in ethanol/water mixtures. Red squares correspond to results obtained from the fit of the 1 HN + 2 Debye model to simulation data for ethanol, while and blue triangles represent results obtained from the fit of the 1 HN + 1 Debye model for water. The solid lines are a guide to the eye and correspond to the results obtained for pure components. The dotted and dashed lines are also a guide to the eye and represent the contribution of ethanol and water in mixtures, respectively.

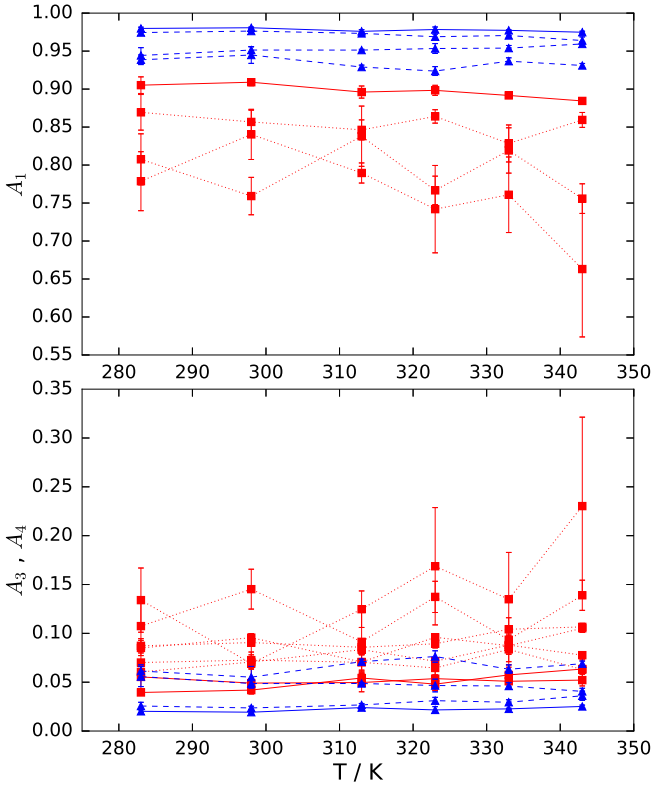

FIGURE E.5: Influence of temperature on relaxation intensities of each species in ethanol/water mixtures. Red squares correspond to results obtained from the fit of the 1 HN + 2 Debye model to simulation data for ethanol, while and blue triangles represent results obtained from the fit of the 1 HN + 1 Debye model for water. The solid lines are a guide to the eye and correspond to the results obtained for pure components. The dotted and dashed lines are also a guide to the eye and represent the contribution of ethanol and water in mixtures, respectively.

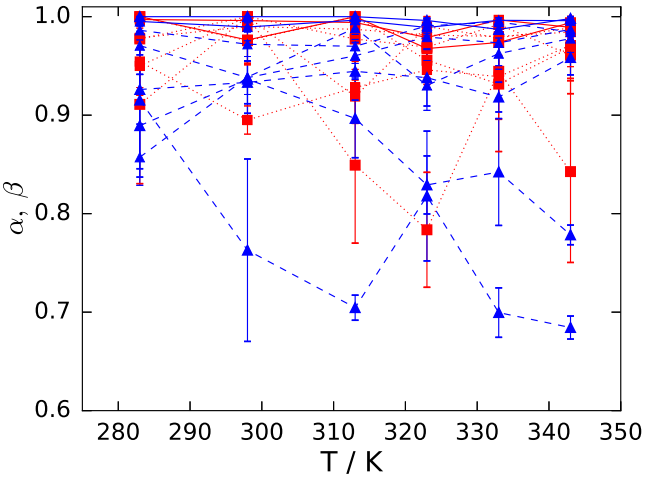

FIGURE E.6: Influence of temperature on Havriliak-Negami's α and β parameters for each species in ethanol/water mixtures. Red squares correspond to results obtained from the fit of the 1 HN + 2 Debye model to simulation data for ethanol, while and blue triangles represent results obtained from the fit of the 1 HN + 1 Debye model for water. The solid lines are a guide to the eye and correspond to the results obtained for pure components. The dotted and dashed lines are also a guide to the eye and represent the contribution of ethanol and water in mixtures, respectively.

TABLE E.1: Variation of dielectric relaxation parameters with temperature for the total contribution of each species in ethanol/water mixtures.

T / K	τ_1/ps	A_1	α	β	τ_3/ps	A_3	τ_4/ps	A_4
Ethanol								
$x_{EtOH} = 0.20$								
283	31 ± 5	0.78 ± 0.04	0.95 ± 0.03	0.91 ± 0.08	5 ± 2	0.13 ± 0.04	0.13 ± 0.01	0.087 ± 0.007
298	15 ± 2	0.84 ± 0.04	0.90 ± 0.02	1.000	1.9 ± 0.7	0.07 ± 0.03	0.117 ± 0.005	0.091 ± 0.004
313	14 ± 2	0.79 ± 0.02	0.928 ± 0.007	0.85 ± 0.08	4 ± 1	0.13 ± 0.02	0.120 ± 0.002	0.086 ± 0.007
323	13 ± 2	0.74 ± 0.06	0.95 ± 0.01	0.78 ± 0.06	3.5 ± 0.8	0.17 ± 0.06	0.123 ± 0.003	0.089 ± 0.004
333	9 ± 2	0.76 ± 0.05	0.94 ± 0.03	0.95 ± 0.05	2.0 ± 0.5	0.14 ± 0.05	0.125 ± 0.004	0.104 ± 0.002
343	10 ± 3	0.66 ± 0.09	0.97 ± 0.03	0.84 ± 0.09	2.3 ± 0.6	0.23 ± 0.09	0.13 ± 0.01	0.107 ± 0.004
$x_{EtOH} = 0.50$								
283	68 ± 6	0.81 ± 0.04	0.95 ± 0.03	1.000	6 ± 2	0.11 ± 0.03	0.21 ± 0.05	0.085 ± 0.008
298	48 ± 3	0.76 ± 0.03	1.000	0.98 ± 0.03	5.4 ± 0.8	0.15 ± 0.02	0.22 ± 0.02	0.096 ± 0.004
313	26 ± 3	0.84 ± 0.04	0.92 ± 0.03	1.000	1.7 ± 0.9	0.09 ± 0.04	0.13 ± 0.02	0.071 ± 0.009
323	25.0 ± 0.6	0.77 ± 0.02	0.990 ± 0.007	0.96 ± 0.03	2.8 ± 0.2	0.14 ± 0.02	0.170 ± 0.003	0.096 ± 0.003
333	19 ± 2	0.82 ± 0.03	0.98 ± 0.02	0.93 ± 0.07	1.6 ± 0.3	0.09 ± 0.03	0.15 ± 0.01	0.087 ± 0.007
343	15.3 ± 0.7	0.76 ± 0.02	0.99 ± 0.01	0.97 ± 0.04	2.2 ± 0.3	0.14 ± 0.02	0.17 ± 0.01	0.105 ± 0.004
$x_{EtOH} = 0.80$								
283	143 ± 9	0.87 ± 0.03	0.98 ± 0.01	0.98 ± 0.03	6 ± 5	0.07 ± 0.02	0.23 ± 0.07	0.060 ± 0.008
298	88 ± 5	0.86 ± 0.02	0.99 ± 0.01	1.000	5 ± 3	0.073 ± 0.008	0.25 ± 0.05	0.071 ± 0.007
313	54 ± 3	0.85 ± 0.02	0.99 ± 0.01	0.98 ± 0.03	4.0 ± 0.9	0.070 ± 0.008	0.24 ± 0.02	0.083 ± 0.005
323	40 ± 2	0.864 ± 0.009	0.98 ± 0.02	0.97 ± 0.04	1.8 ± 0.3	0.065 ± 0.007	0.18 ± 0.01	0.071 ± 0.002
333	30.9 ± 0.9	0.83 ± 0.03	0.98 ± 0.02	0.992 ± 0.008	3 ± 1	0.08 ± 0.02	0.22 ± 0.03	0.088 ± 0.010
343	25 ± 2	0.86 ± 0.01	0.984 ± 0.009	0.96 ± 0.04	1.5 ± 0.2	0.06 ± 0.01	0.19 ± 0.01	0.078 ± 0.002
$x_{EtOH} = 1.00$								
283	224 ± 8	0.91 ± 0.02	0.997 ± 0.003	1.000	8 ± 5	0.039 ± 0.003	0.3 ± 0.2	0.06 ± 0.02
298	129 ± 8	0.909 ± 0.005	0.996 ± 0.004	0.98 ± 0.03	1.7 ± 0.3	0.042 ± 0.004	0.20 ± 0.02	0.049 ± 0.005
313	79 ± 5	0.896 ± 0.008	0.994 ± 0.006	1.000	1.9 ± 0.9	0.054 ± 0.005	0.20 ± 0.04	0.050 ± 0.009
323	66 ± 3	0.898 ± 0.007	0.98 ± 0.02	0.97 ± 0.02	1.9 ± 0.8	0.048 ± 0.006	0.22 ± 0.04	0.05 ± 0.0 2
333	45 ± 4	0.892 ± 0.001	0.997 ± 0.003	0.97 ± 0.03	1.1 ± 0.3	0.057 ± 0.008	0.18 ± 0.03	0.051 ± 0.007
343	34.3 ± 0.5	0.884 ± 0.004	0.99 ± 0.02	0.994 ± 0.006	0.9 ± 0.2	0.063 ± 0.004	0.17 ± 0.01	0.052 ± 0.006

Continued on next page

TABLE E.1 – *Continued from previous page*

T / K	τ_1/ps	A_1	α	β	τ_3/ps	A_3	τ_4/ps	A_4
Water								
$x_{EtOH} = 0.00$								
283	12.3 ± 0.2	0.980 ± 0.002	0.995 ± 0.005	1.000	–	–	0.03 ± 0.03	0.020 ± 0.002
298	8.9 ± 0.1	0.981 ± 0.001	0.990 ± 0.004	1.000	–	–	0.02 ± 0.01	0.019 ± 0.001
313	6.9 ± 0.1	0.976 ± 0.002	0.996 ± 0.003	1.000	–	–	0.06 ± 0.02	0.024 ± 0.002
323	5.90 ± 0.07	0.978 ± 0.003	0.989 ± 0.009	0.996 ± 0.002	–	–	0.05 ± 0.02	0.022 ± 0.003
333	5.14 ± 0.06	0.977 ± 0.001	0.996 ± 0.003	0.987 ± 0.004	–	–	0.03 ± 0.01	0.023 ± 0.001
343	4.40 ± 0.04	0.975 ± 0.001	0.996 ± 0.004	0.998 ± 0.002	–	–	0.04 ± 0.01	0.025 ± 0.001
$x_{EtOH} = 0.20$								
283	32 ± 2	0.974 ± 0.004	0.99 ± 0.01	0.93 ± 0.04	–	–	0.06 ± 0.03	0.026 ± 0.004
298	21.0 ± 0.7	0.976 ± 0.002	0.97 ± 0.02	0.93 ± 0.03	–	–	0.05 ± 0.02	0.024 ± 0.002
313	14.5 ± 0.8	0.973 ± 0.002	0.97 ± 0.02	0.94 ± 0.03	–	–	0.05 ± 0.02	0.027 ± 0.002
323	11.0 ± 0.6	0.969 ± 0.003	0.991 ± 0.008	0.94 ± 0.03	–	–	0.03 ± 0.02	0.031 ± 0.003
333	9.8 ± 0.4	0.971 ± 0.003	0.995 ± 0.004	0.92 ± 0.02	–	–	0.04 ± 0.02	0.029 ± 0.003
343	7.9 ± 0.3	0.964 ± 0.005	0.98 ± 0.01	0.96 ± 0.02	–	–	0.08 ± 0.04	0.036 ± 0.005
$x_{EtOH} = 0.50$								
283	58 ± 4	0.94 ± 0.01	0.97 ± 0.03	0.89 ± 0.06	–	–	0.6 ± 0.3	0.06 ± 0.01
298	35 ± 2	0.951 ± 0.004	0.94 ± 0.02	0.94 ± 0.04	–	–	0.18 ± 0.03	0.049 ± 0.004
313	24 ± 2	0.951 ± 0.001	0.96 ± 0.03	0.90 ± 0.04	–	–	0.06 ± 0.04	0.049 ± 0.001
323	21.3 ± 0.9	0.953 ± 0.006	0.98 ± 0.02	0.83 ± 0.03	–	–	0.10 ± 0.06	0.047 ± 0.006
333	16 ± 2	0.954 ± 0.003	0.97 ± 0.03	0.84 ± 0.06	–	–	0.06 ± 0.02	0.046 ± 0.003
343	14.4 ± 0.3	0.959 ± 0.003	0.987 ± 0.007	0.78 ± 0.01	–	–	0.05 ± 0.02	0.041 ± 0.003
$x_{EtOH} = 0.80$								
283	80 ± 10	0.939 ± 0.006	0.86 ± 0.03	0.92 ± 0.07	–	–	0.12 ± 0.03	0.061 ± 0.006
298	70 ± 10	0.95 ± 0.02	0.94 ± 0.04	0.8 ± 0.1	–	–	0.10 ± 0.03	0.06 ± 0.02
313	40 ± 2	0.929 ± 0.003	0.99 ± 0.02	0.71 ± 0.02	–	–	0.08 ± 0.03	0.071 ± 0.003
323	27 ± 3	0.924 ± 0.006	0.93 ± 0.03	0.82 ± 0.07	–	–	0.06 ± 0.03	0.076 ± 0.006
333	26 ± 2	0.937 ± 0.004	0.96 ± 0.02	0.70 ± 0.03	–	–	0.05 ± 0.02	0.063 ± 0.004
343	21.1 ± 0.6	0.931 ± 0.003	0.98 ± 0.02	0.68 ± 0.02	–	–	0.07 ± 0.01	0.069 ± 0.003

E.3 Mixtures - molecule

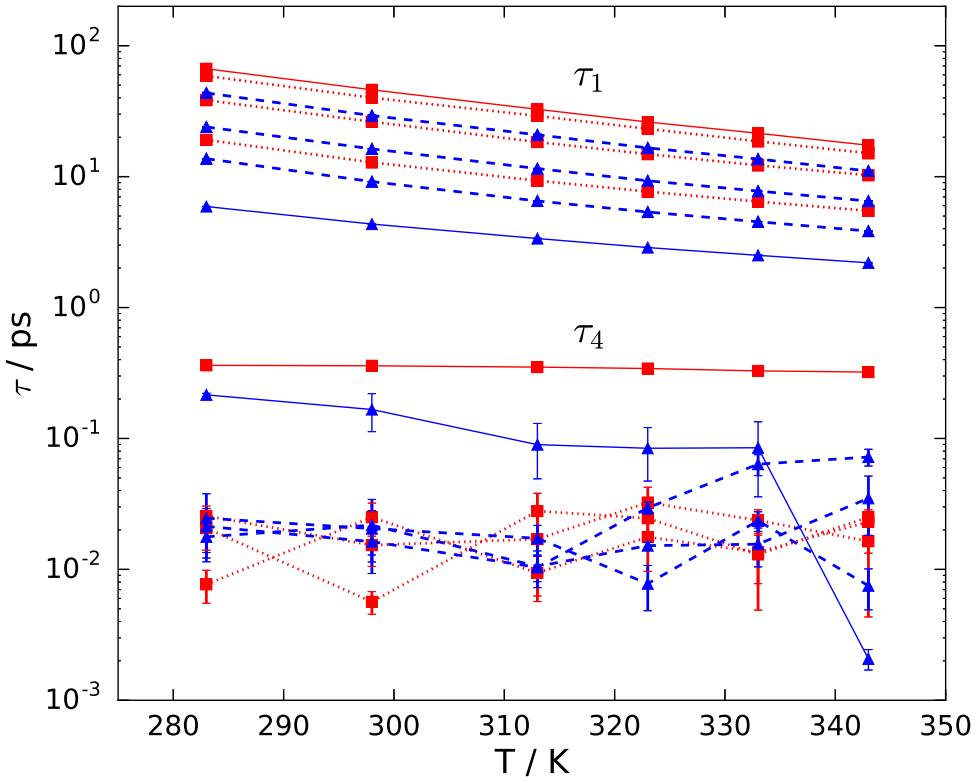

FIGURE E.7: Influence of temperature on molecular relaxation times in ethanol/water mixtures. Red squares and blue triangles correspond to results obtained from the fit of the 1 HN + 1 Debye model to simulation data for ethanol and water, respectively. The solid lines are a guide to the eye and correspond to the results obtained for pure components. The dotted and dashed lines are also a guide to the eye and represent the contribution of ethanol and water in mixtures, respectively.

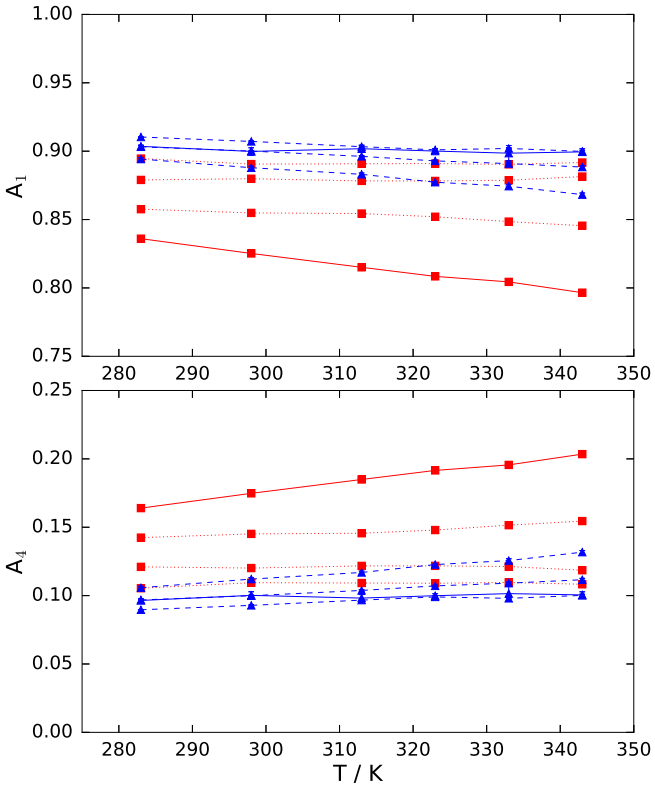

FIGURE E.8: Influence of temperature on molecular relaxation intensities in ethanol/water mixtures. Red squares and blue triangles correspond to results obtained from the fit of the 1 HN + 1 Debye model to simulation data for ethanol and water, respectively. The solid lines are a guide to the eye and correspond to the results obtained for pure components. The dotted and dashed lines are also a guide to the eye and represent the contribution of ethanol and water in mixtures, respectively.

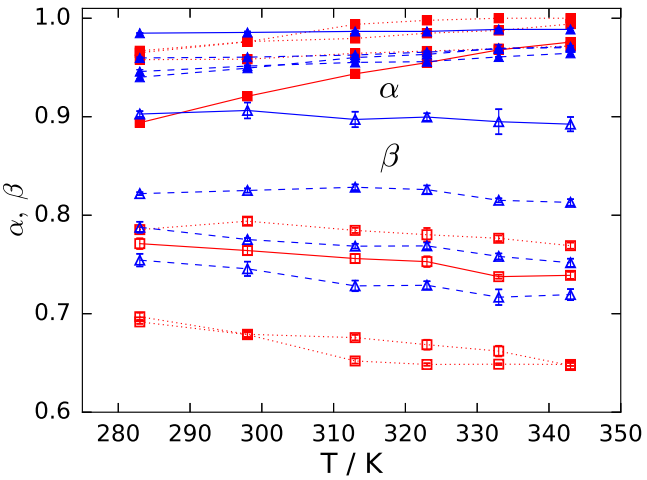

FIGURE E.9: Influence of temperature on Havriliak-Negami's α and β parameters at the molecule level in ethanol/water mixtures. Red squares and blue triangles correspond to results obtained from the fit of the 1 HN + 1 Debye model to simulation data for ethanol and water, respectively. The solid lines are a guide to the eye and correspond to the results obtained for pure components. The dotted and dashed lines are also a guide to the eye and represent the contribution of ethanol and water in mixtures, respectively.

TABLE E.2: Variation of dielectric relaxation parameters with temperature for individual molecules in ethanol/water mixtures.

T / K	τ_1/ps	A_1	α	β	τ_4/ps	A_4
Ethanol						
$x_{EtOH} = 0.20$						
283	19.1 ± 0.2	0.895 ± 0.001	0.958 ± 0.001	0.785 ± 0.003	0.008 ± 0.003	0.105 ± 0.001
298	12.86 ± 0.08	0.891 ± 0.001	0.958 ± 0.001	0.794 ± 0.004	0.03 ± 0.01	0.109 ± 0.001
313	9.32 ± 0.03	0.891 ± 0.001	0.964 ± 0.001	0.785 ± 0.003	0.009 ± 0.004	0.109 ± 0.001
323	7.69 ± 0.07	0.891 ± 0.001	0.967 ± 0.002	0.780 ± 0.007	0.02 ± 0.01	0.109 ± 0.001
333	6.45 ± 0.02	0.890 ± 0.001	0.969 ± 0.001	0.777 ± 0.003	0.01 ± 0.01	0.110 ± 0.001
343	5.48 ± 0.03	0.892 ± 0.001	0.972 ± 0.001	0.769 ± 0.003	0.02 ± 0.01	0.108 ± 0.001
$x_{EtOH} = 0.50$						
283	38.4 ± 0.3	0.879 ± 0.001	0.967 ± 0.002	0.697 ± 0.004	0.02 ± 0.01	0.121 ± 0.001
298	26.3 ± 0.2	0.880 ± 0.001	0.976 ± 0.003	0.679 ± 0.003	0.006 ± 0.002	0.120 ± 0.001
313	18.38 ± 0.07	0.878 ± 0.001	0.979 ± 0.002	0.676 ± 0.003	0.03 ± 0.01	0.122 ± 0.001
323	14.9 ± 0.2	0.878 ± 0.001	0.985 ± 0.002	0.669 ± 0.005	0.02 ± 0.01	0.122 ± 0.001
333	12.2 ± 0.1	0.879 ± 0.001	0.988 ± 0.002	0.662 ± 0.005	0.01 ± 0.01	0.121 ± 0.001
343	10.26 ± 0.07	0.881 ± 0.001	0.994 ± 0.002	0.647 ± 0.004	0.03 ± 0.01	0.119 ± 0.001
$x_{EtOH} = 0.80$						
283	58.8 ± 0.2	0.858 ± 0.001	0.965 ± 0.001	0.692 ± 0.002	0.026 ± 0.005	0.142 ± 0.001
298	40.1 ± 0.2	0.855 ± 0.001	0.976 ± 0.001	0.679 ± 0.002	0.015 ± 0.005	0.145 ± 0.001
313	29.1 ± 0.2	0.854 ± 0.001	0.994 ± 0.001	0.652 ± 0.003	0.02 ± 0.01	0.146 ± 0.001
323	23.18 ± 0.08	0.852 ± 0.001	0.998 ± 0.001	0.648 ± 0.001	0.03 ± 0.01	0.148 ± 0.001
333	18.61 ± 0.02	0.848 ± 0.001	1.000	0.649 ± 0.001	0.024 ± 0.005	0.152 ± 0.001
343	15.09 ± 0.03	0.845 ± 0.001	1.000	0.648 ± 0.001	0.02 ± 0.01	0.155 ± 0.001
$x_{EtOH} = 1.00$						
283	66.7 ± 0.7	0.836 ± 0.001	0.894 ± 0.002	0.771 ± 0.005	0.362 ± 0.003	0.164 ± 0.001
298	46.1 ± 0.5	0.825 ± 0.001	0.921 ± 0.001	0.764 ± 0.004	0.359 ± 0.003	0.175 ± 0.001
313	32.7 ± 0.2	0.815 ± 0.001	0.944 ± 0.001	0.756 ± 0.005	0.351 ± 0.003	0.185 ± 0.001
323	26.1 ± 0.3	0.808 ± 0.001	0.955 ± 0.002	0.753 ± 0.005	0.342 ± 0.002	0.192 ± 0.001
333	21.44 ± 0.06	0.804 ± 0.001	0.968 ± 0.001	0.738 ± 0.002	0.328 ± 0.001	0.196 ± 0.001
343	17.36 ± 0.07	0.797 ± 0.001	0.976 ± 0.001	0.739 ± 0.004	0.321 ± 0.002	0.203 ± 0.001

Continued on next page

TABLE E.2 – *Continued from previous page*

T / K	τ_1/ps	A_1	α	β	τ_4/ps	A_4
Water						
$x_{EtOH} = 0.00$						
283	5.91 ± 0.02	0.904 ± 0.001	0.985 ± 0.001	0.903 ± 0.003	0.22 ± 0.01	0.096 ± 0.001
298	4.34 ± 0.03	0.900 ± 0.003	0.986 ± 0.001	0.906 ± 0.008	0.17 ± 0.05	0.100 ± 0.003
313	3.37 ± 0.03	0.902 ± 0.003	0.987 ± 0.001	0.897 ± 0.008	0.09 ± 0.04	0.098 ± 0.003
323	2.87 ± 0.01	0.900 ± 0.002	0.987 ± 0.001	0.900 ± 0.004	0.08 ± 0.04	0.100 ± 0.002
333	2.51 ± 0.03	0.899 ± 0.006	0.989 ± 0.001	0.90 ± 0.02	0.08 ± 0.05	0.101 ± 0.006
343	2.20 ± 0.02	0.899 ± 0.002	0.989 ± 0.001	0.892 ± 0.007	0.002 ± 0.001	0.101 ± 0.002
$x_{EtOH} = 0.20$						
283	13.71 ± 0.05	0.910 ± 0.001	0.960 ± 0.001	0.822 ± 0.001	0.02 ± 0.01	0.090 ± 0.001
298	9.16 ± 0.04	0.907 ± 0.001	0.960 ± 0.001	0.825 ± 0.002	0.016 ± 0.005	0.093 ± 0.001
313	6.52 ± 0.03	0.903 ± 0.001	0.963 ± 0.001	0.828 ± 0.003	0.010 ± 0.003	0.097 ± 0.001
323	5.37 ± 0.03	0.901 ± 0.001	0.966 ± 0.001	0.826 ± 0.004	0.030 ± 0.004	0.099 ± 0.001
333	4.52 ± 0.01	0.902 ± 0.001	0.969 ± 0.001	0.815 ± 0.002	0.06 ± 0.01	0.098 ± 0.001
343	3.84 ± 0.02	0.900 ± 0.001	0.971 ± 0.001	0.813 ± 0.003	0.07 ± 0.01	0.100 ± 0.001
$x_{EtOH} = 0.50$						
283	24.0 ± 0.2	0.903 ± 0.001	0.946 ± 0.002	0.788 ± 0.006	0.02 ± 0.01	0.097 ± 0.001
298	16.30 ± 0.04	0.900 ± 0.001	0.951 ± 0.001	0.775 ± 0.002	0.02 ± 0.01	0.100 ± 0.001
313	11.52 ± 0.04	0.896 ± 0.001	0.955 ± 0.001	0.769 ± 0.002	0.011 ± 0.004	0.104 ± 0.001
323	9.30 ± 0.05	0.893 ± 0.001	0.956 ± 0.001	0.769 ± 0.003	0.015 ± 0.001	0.107 ± 0.001
333	7.76 ± 0.04	0.891 ± 0.001	0.961 ± 0.001	0.758 ± 0.003	0.02 ± 0.01	0.109 ± 0.001
343	6.51 ± 0.04	0.888 ± 0.001	0.964 ± 0.001	0.752 ± 0.004	0.03 ± 0.02	0.112 ± 0.001
$x_{EtOH} = 0.80$						
283	43.6 ± 0.6	0.894 ± 0.001	0.940 ± 0.002	0.754 ± 0.006	0.02 ± 0.01	0.106 ± 0.001
298	29.3 ± 0.4	0.888 ± 0.001	0.949 ± 0.003	0.746 ± 0.007	0.02 ± 0.01	0.112 ± 0.001
313	20.9 ± 0.3	0.883 ± 0.001	0.960 ± 0.002	0.728 ± 0.005	0.017 ± 0.005	0.117 ± 0.001
323	16.6 ± 0.2	0.877 ± 0.001	0.963 ± 0.002	0.729 ± 0.004	0.008 ± 0.003	0.123 ± 0.001
333	13.6 ± 0.2	0.874 ± 0.001	0.970 ± 0.003	0.717 ± 0.008	0.024 ± 0.005	0.126 ± 0.001
343	11.05 ± 0.09	0.868 ± 0.001	0.970 ± 0.002	0.719 ± 0.006	0.007 ± 0.003	0.132 ± 0.001

Appendix F

Influence of temperature on radial distribution functions in ethanol/water mixtures

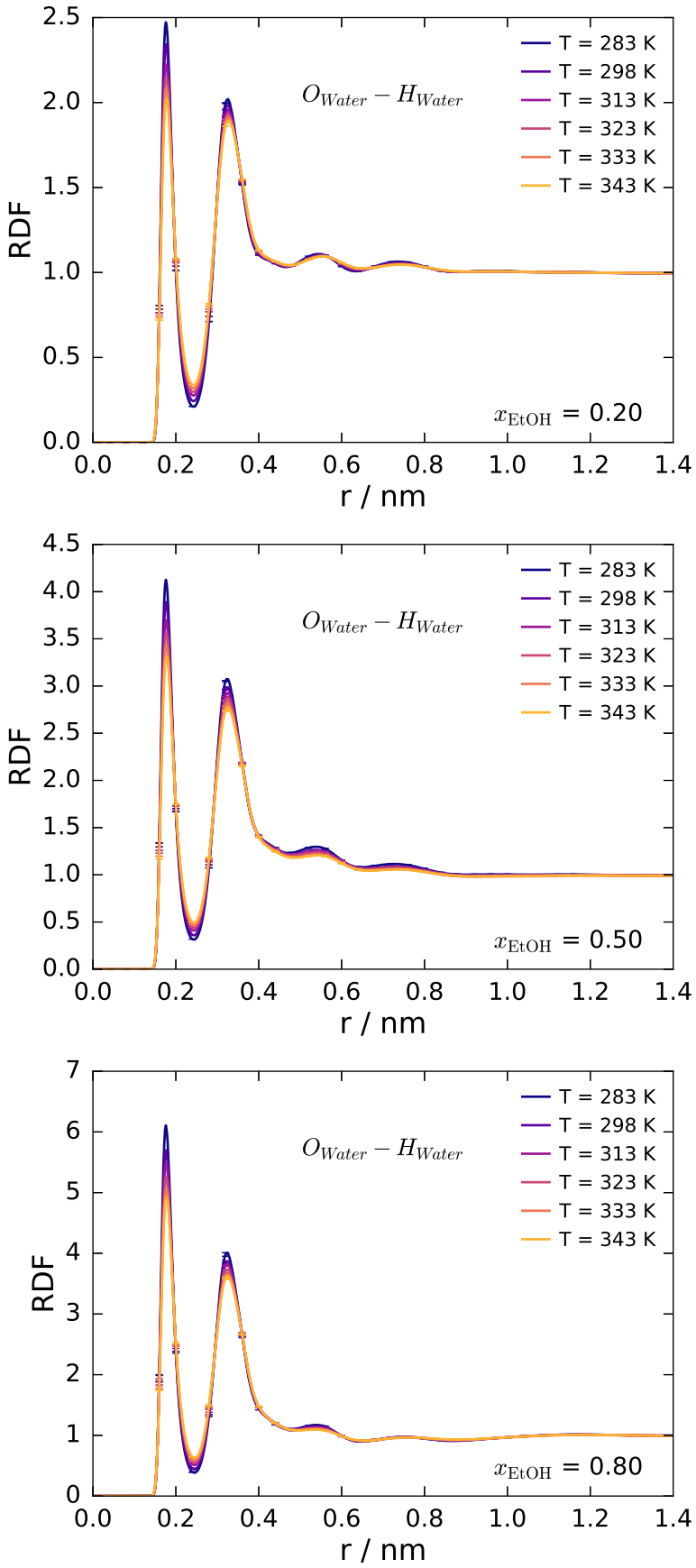

FIGURE F.1: Influence of temperature on O_{Water} – H_{Water} RDF

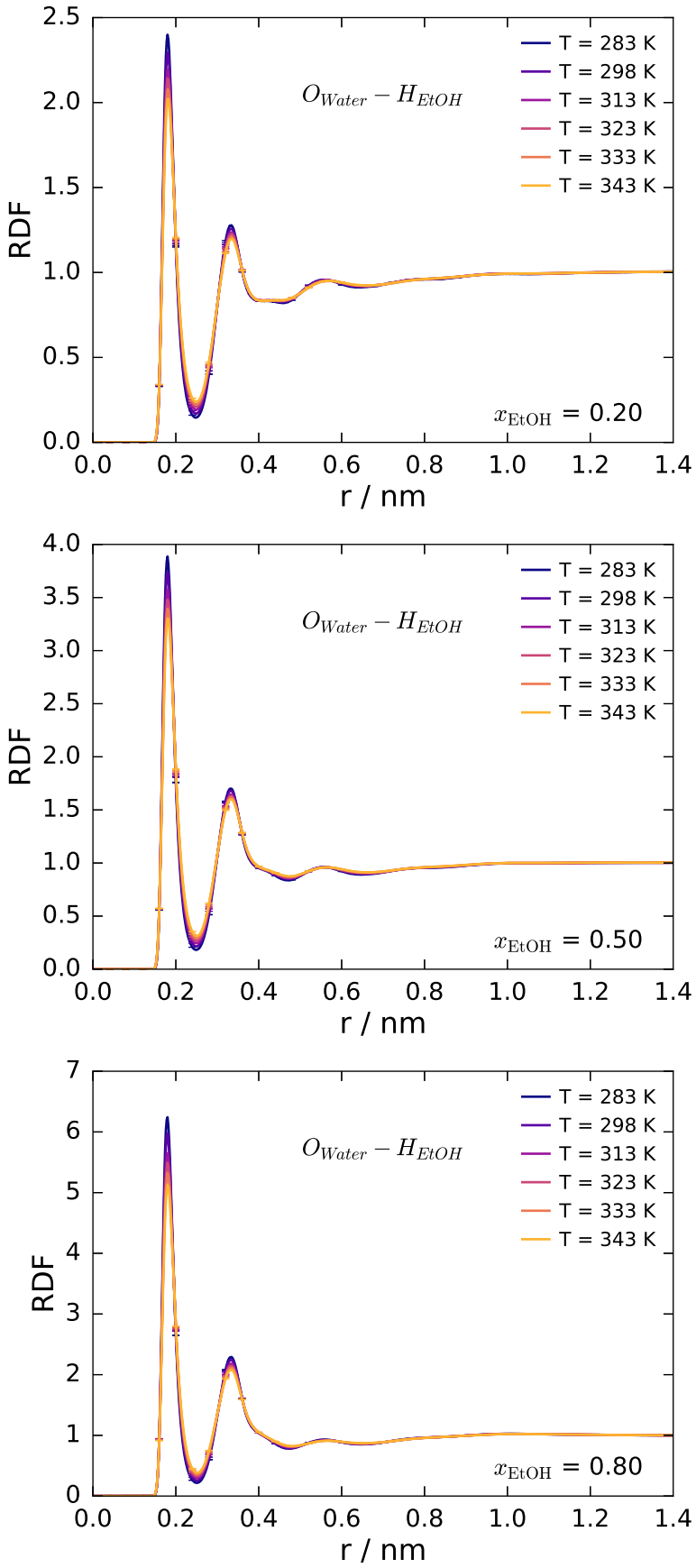

FIGURE F.2: Influence of temperature on $O_{Water} - H_{EtOH}$ RDF

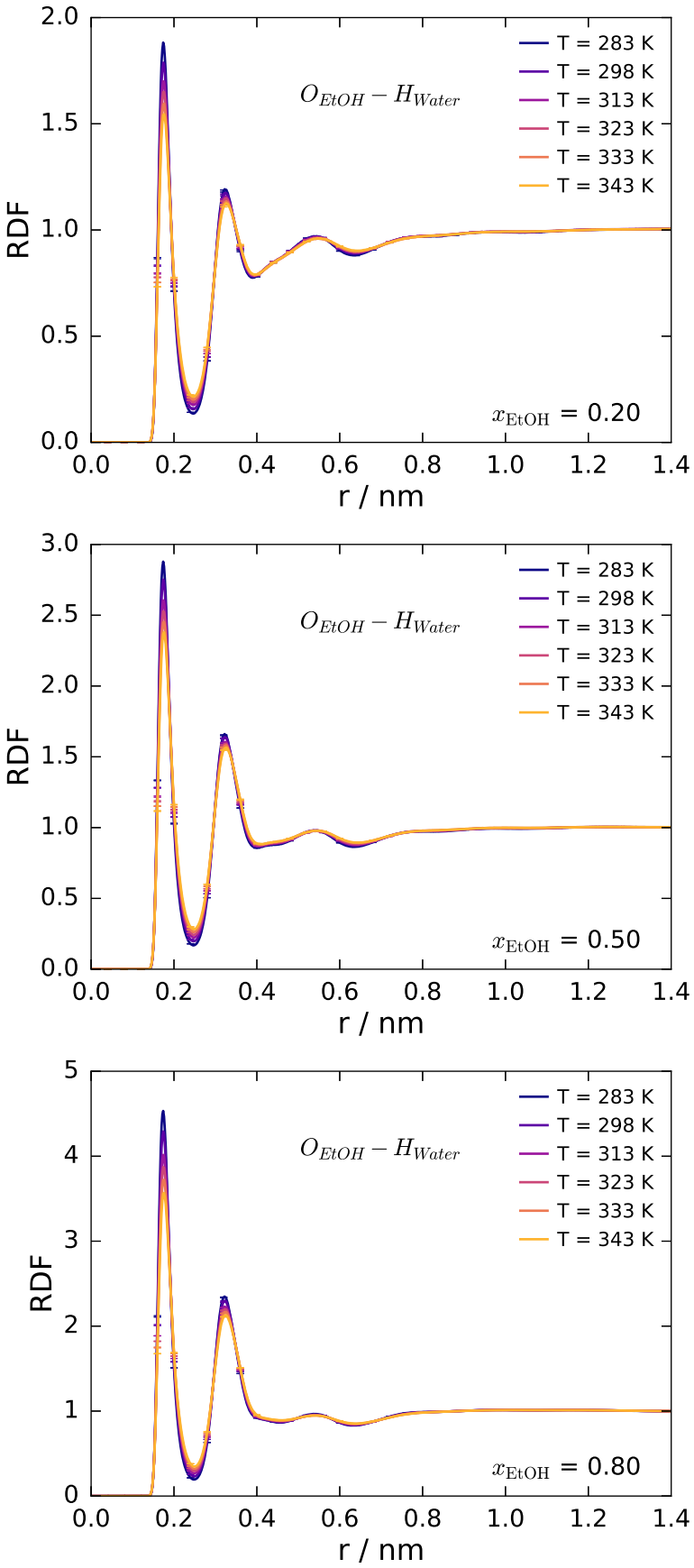

FIGURE F.3: Influence of temperature on $O_{EtOH} - H_{Water}$ RDF

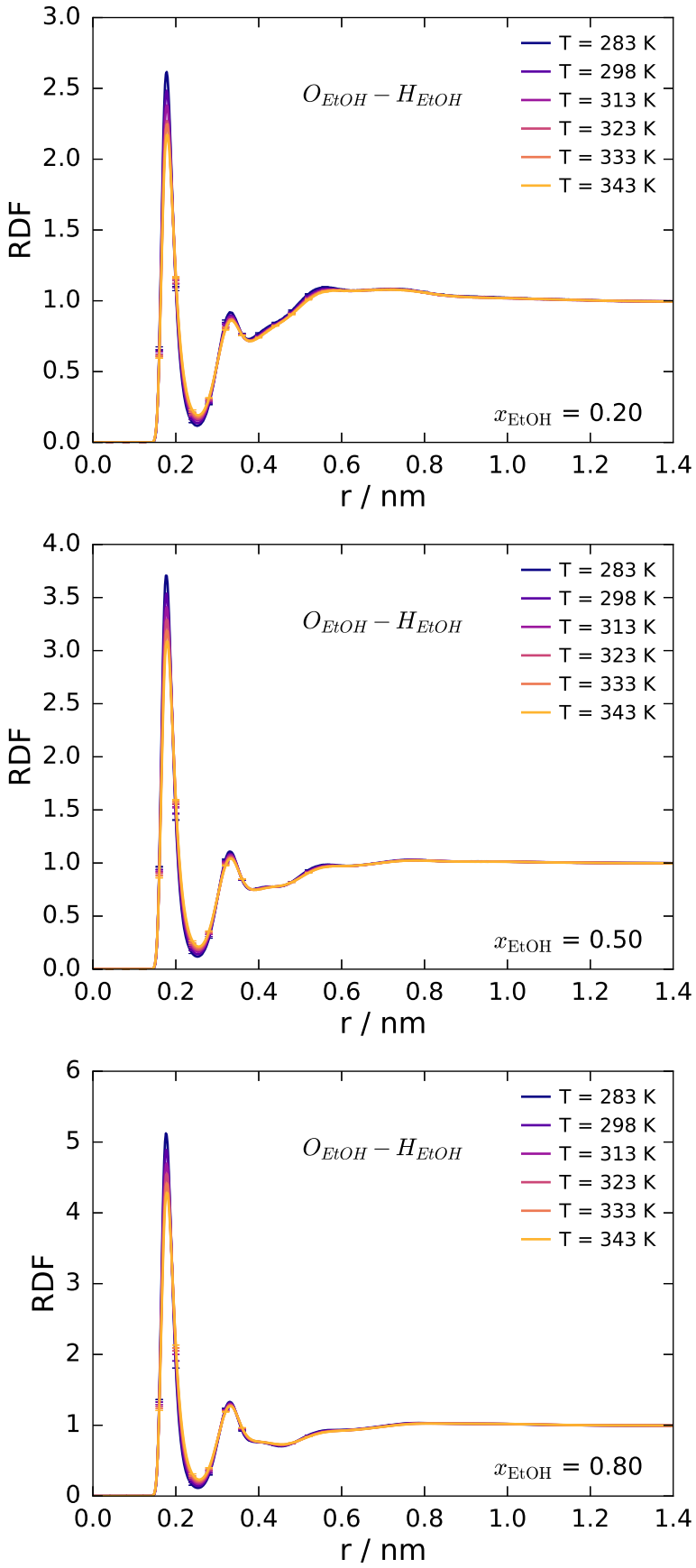

FIGURE F.4: Influence of temperature on $O_{EtOH} - H_{EtOH}$ RDF